UNIVERSITY OF CAMBRIDGE

Novel approaches to MRI of glioma

Dr Fulvio Zaccagna, MD

USN 303034702

Department of Radiology

University of Cambridge School of Clinical Medicine

Gonville & Caius College

University of Cambridge

This dissertation is submitted for the degree of Doctor of Philosophy

September 2019

To my father…

Declaration

This thesis is the result of my own work and includes nothing which is the outcome of work done in collaboration except as declared in the Preface and specified in the text.

It is not substantially the same as any that I have submitted, or, is being concurrently submitted for a degree or diploma or other qualification at the University of Cambridge or any other University or similar institution except as declared in the Preface and specified in the text. I further state that no substantial part of my dissertation has already been submitted, or, is being concurrently submitted for any such degree, diploma or other qualification at the University of Cambridge or any other University or similar institution except as declared in the Preface and specified in the text

It does not exceed the prescribed word limit for the relevant Degree Committee.

Summary

Title of dissertation: Novel approaches to MRI of glioma
Candidate: Dr Fulvio Zaccagna (USN: 303034702)

Gliomas are extremely heterogeneous, both morphologically and biologically, which contributes to a very poor prognosis. Current imaging of glioma is insufficient for a thorough diagnosis, therapy assessment and prognosis prediction. Moreover, refined and more sophisticated imaging technique could help in furthering our knowledge of gliomas.

In order to facilitate proliferation, cancer cells undergo a change in structure and an increase in metabolism that results in distortion and disruption of tissue architecture. Gliomas are characterised by an increase in cells of variable sizes, as well as changes in the tissue microstructure. Diffusion-Weighted Imaging (DWI) and the apparent diffusion coefficient (ADC), have been extensively studied as potential imaging biomarkers for cellularity and tissue architecture. However, several studies have shown partial overlap in the measured values between tumour subtypes. Moreover, ADC is influenced by several factors and does not provide detailed information on the tissue microstructure. The Vascular, Extracellular and Restricted Diffusion for Cytometry in Tumours (VERDICT) is a novel diffusion model that infers tissue microstructure compartment from conventional DWI measurements. This model derives metrics for the intracellular, intravascular and extracellular–extravascular spaces providing a more detailed interpretation of the tissue microstructure. To date, VERDICT has been applied to xenograft models of colorectal cancer, patient studies of prostate cancer and recently its feasibility in glioma has been shown. In this PhD I have applied a shortened version of the VERDICT method

to image intratumoral and intertumoral heterogeneity in glioma. The results have also been validated with histology as part of a prospective study.

Gliomas also exhibit a significant increase in mitotic activity within the tumour. The increased number of mitosis alters cell density which, in turn, affects the total concentration of tissue sodium as the concentration of tissue sodium is approximately ten-fold higher in the extracellular compared to the intracellular space. In addition, there is a decrease in Na^+/K^+-ATPase activity in tumours due to ATP depletion, which contributes to disturb sodium homeostasis. Non-invasive detection of ^{23}Na with MRI has the potential to quantify sodium concentration and therefore could be an imaging probe of cell morphology and membrane function within the tumour microenvironment, as well as a method of probing tissue heterogeneity. During my PhD, a novel ^{23}Na-MRI technique has been used to evaluate sodium distribution within glioma and in the surrounding tissue.

Metabolic reprogramming is one of the major driving forces for determining glioma growth and invasion. Therefore, the non-invasive characterization of metabolic intratumoral, peritumoral and intertumoral heterogeneity *in vivo* could help to better stratify patients and to develop novel therapeutic strategies targeting cancer-specific metabolic pathways. ^{13}C magnetic resonance imaging (MRI) using dynamic nuclear polarization (DNP) is a novel technique that allows non-invasive assessment of the metabolism of hyperpolarized (HP) ^{13}C-labelled molecules *in vivo*, such as the exchange of [1-^{13}C]pyruvate to [1-^{13}C]lactate in tumours (Warburg effect). Part of my PhD has focused on developing and translating HP [1-^{13}C]pyruvate MRI to explore metabolic reprogramming in glioma and the surrounding microenvironment.

The overall aim of my PhD has been to develop novel approaches to imaging glioma with MRI to probe both the architectural and metabolic changes of Glioma. The preliminary evidence suggests that these tools can more deeply phenotype tumours than conventional imaging approaches. Although the main focus of this work has been gliomas, the techniques developed and presented here may be applied to study other pathological conditions within the brain, which raises the possibility of other potential clinical applications for this work.

Table of contents

DECLARATION **3**

SUMMARY **4**

TABLE OF CONTENTS **6**

LIST OF ABBREVIATIONS **10**

LIST OF FIGURES **12**

LIST OF TABLES **13**

CHAPTER 1- INTRODUCTION **16**

1.1 The Warburg effect **18**

1.2 Hallmarks of cancer **18**

1.3 Brain tumours **19**

1.4 Glioma **20**
1.4.1 Epidemiology 21
1.4.2 IDH Mutations and gliomagenesis 21
1.4.3 Treatment 24
1.4.3.1 Lower-grade glioma 24
1.4.3.2 High-grade glioma 25
1.4.4 Treatment evaluation 27

References **30**

CHAPTER 2 - IMAGING OF GLIOMA **35**

2.1 Conventional proton MRI **36**
2.1.1 Morphologic imaging 36
2.1.2 Proton nuclear magnetic resonance spectroscopy 37

2.2 Diffusion weighted imaging **38**
2.2.1 Diffusion Tensor Imaging 41
2.2.2 Intravoxel incoherent motion diffusion imaging 42
2.2.3 Non-Gaussian Diffusion Models 44

2.2.3.1 Vascular, extracellular and restricted diffusion for cytometry in tumours 46

2.3 Sodium MRI 48

2.4 Hyperpolarized ^{13}C MRSI 50
2.4.1 The benefits of metabolic imaging with MRI 51
2.4.1.1 Preclinical imaging 54
2.4.2 Translation into human imaging 55
2.4.3 Clinical imaging studies 57

References 59

CHAPTER 3 - NON-INVASIVE ASSESSMENT OF GLIOMA MICROSTRUCTURE USING VERDICT MRI: CORRELATION WITH HISTOLOGY 69

3.1 Methods and materials 70
3.1.1 Patient selection 70
3.1.2 MRI acquisition 70
3.1.3 VERDICT acquisition and post-processing 71
3.1.4 MRI analysis 72
3.1.5 Pathological analysis 73
3.1.6 Statistical Analysis 73

3.2 Results 74
3.2.1 Histopathological analysis 75
3.2.2 VERDICT analysis 77
3.2.3 Reproducibility analysis 78

3.3 Discussion 79

3.4 Conclusion 82

Supplementary material 84
Short vs. extended protocol 84

References 85

CHAPTER 4 - ^{23}NA-MRI AS A BIOMARKER OF TUMOUR HETEROGENEITY AND SURVIVAL 89

4.1 Methods and materials 95
4.1.1 Patient selection 95
4.1.2 ^{1}H and ^{23}Na MRI acquisitions 96
4.1.3 Image processing and analysis 98
4.1.4 Histopathology 100
4.1.5 Statistical Analysis 101

4.2 Results 105
4.2.1 Characteristic of the cohort 105

4.2.2 Tissue sodium concentration 105
4.2.3 Intracellular-weighted sodium concentration 108
4.2.4 Survival analysis 111

4.3 Discussion 112
4.3.1 Sodium concentration in normal tissue and glioma grading 114
4.3.2 Intralesional and peritumoral heterogeneity 116
4.3.3 Therapy assessment and prognostication 119
4.3.4 Support for drug discovery and assessment of experimental therapies 121

4.4 Conclusion 122

References 123

CHAPTER 5 - METABOLIC PHENOTYPING OF GLIOBLASTOMA WITH MAGNETIC RESONANCE IMAGING OF HYPERPOLARIZED [1-^{13}C]PYRUVATE. 128

5.1 Methods and materials 135
5.1.1 Patient selection, enrolment and clinical monitoring 135
5.1.2 Pyruvate synthesis and hyperpolarization 136
5.1.3 ^{1}H and HP ^{13}C MRI acquisitions 136
5.1.4 Image processing and analysis 138
5.1.5 Histopathology, immunohistochemistry and western blot 140
5.1.5.1 Image-guided biopsy targeting and correlation with pathology 140
5.1.5.2 Histopathology and immunohistochemistry 141
5.1.6 Statistical Analysis 145

5.2 Results 147
5.2.1 Feasibility and technical success 147
5.2.2 Pyruvate dynamics and metabolic heterogeneity 150
5.2.2.1 Comparison between the GBM and the contralateral side 150
5.2.2.2 Intralesional heterogeneity 151
5.2.2.3 Metabolic activity of the non-tumour bearing brain parenchyma 152
5.2.3 GBM cellularity, size and metabolic activity 153
5.2.4 Relationship between HP ^{13}C MRI and tissue biomarkers 154

5.3 Discussion 160
5.3.1 A novel tool for *in vivo* assessment of metabolic activity 160
5.3.2 Intra- and inter- lesional heterogeneity 161
5.3.3 The Warburg effect 164
5.3.4 Reduced bicarbonate in GBM 167
5.3.5 Lesion size and cellularity 169
5.3.6 Limitations and future work 170

5.4 Conclusion 172

Additional tables 174

References **180**

CHAPTER 6 - TOWARDS AN INTEGRATED MOLECULAR IMAGING PLATFORM FOR GLIOMA **187**

6.1 Grading, extension and tumour microenvironment **187**

6.2 Treatment response and prognostication **189**

6.3 The future of HP ^{13}C MRI **190**
6.3.1 MRI hardware developments for hyperpolarisation 190
6.3.2 Pharmacy requirements and developments in formulation 191
6.3.3 New hyperpolarized tracers 192
6.3.4 Image analysis and quantification 193
6.3.5 Hyperpolarized ^{13}C-MRI with PET/MRI 194

6.4 To infinity and beyond **197**

6.5 Future work **198**

6.6 Concluding remarks **199**

REFERENCES **200**

ACHIEVEMENTS **206**

Papers **206**

Book Chapters **209**

Prizes and awards **209**

Grants **210**

Oral presentations at courses and congresses **210**

Posters presentations at courses and congresses **212**

ACKNOWLEDGEMENTS **217**

List of abbreviations

MRI	Magnetic resonance imaging
^{23}Na-MRI	Sodium-23 magnetic resonance imaging
DWI	Diffusion weighted imaging
DKI	Diffusion kurtosis imaging
DTI	Diffusion tensor imaging
HP^{13}C-MRSI	Hyperpolarized Carbon-13 magnetic resonance spectroscopic imaging
WHO	World Health Organization
^{1}H-NMR	Proton nuclear magnetic resonance spectroscopy
GBM	Glioblastoma
LGG	Low-grade glioma
LrGG	Lower-grade glioma
HGG	High-grade glioma
T_2WI	T_2-weighted imaging
FLAIR	T_2 fluid-attenuated inversion recovery
T_1WI	T_1-weighted images
SPGR	Spoiled gradient recalled acquisition
iMRI	Intraoperative MRI
PFS	Progression-free survival
RANO	Response Assessment in Neuro-Oncology
QoL	Quality of life
CR	Complete response
PR	Partial response
SD	Stable disease
PD	Progressive disease
DCE	Dynamic contrast enhancement
ADC	Apparent diffusion coefficient
FA	Fractional anisotropy
MD	Mean diffusivity
DSC	Dynamic susceptibility contrast-enhanced

CBV	Cerebral blood volume
CBF	Cerebral blood flow
kTrans	Endothelial transfer coefficient
ASL	Arterial spin labelling
Cho	Choline
Cr	Creatine
NAA	N-acetyl-aspartate
Lac	Lactate
SNR	Signal-to-noise ratio
PET	Positron-emission tomography
^{18}F-FDG	^{18}F-labelled 2-fluoro 2-deoxyglucose
DNP	Dynamic nuclear polarization
Gd	Gadolinium
SAR	Specific absorption rate
5-ALA	5-aminolevulinic acid
TSC	Tissue sodium concentration
IW SC	Intra-cellular weighted sodium concentration

List of figures

Figure 1.1: Egyptian Ptolemaic mummy. 17
Figure 1.2: Classification of adult gliomas according to histology and IDH status. 21
Figure 2.1: Diffusion signal intensity curve. 39
Figure 2.2: Diagram showing the metabolic fate of glucose and pyruvate. 52
Figure 2.3: Hyperpolarized pyruvate metabolism in human prostate cancer. 55
Figure 2.4: Pharmacy kit for clinical polarisation. 56
Figure 2.5: Schematic of cryostat, magnet and sorption pump; GE SPINlab Diamond Polariser. 57
Figure 3.1: Cell radius at MRI and pathology. 75
Figure 3.2: Representative low grade and high grade glioma. 76
Figure 3.3: Volume fractions for low grade and high grade glioma. 77
Figure 3.4: Apparent diffusion coefficient for low grade and high grade glioma. 78
Figure 4.1: Representative case of lower-grade glioma (LrGG). 103
Figure 4.2: Representative case of high-grade glioma (HGG). 104
Figure 4.3: Boxplot of intracellular-weighted sodium concentration (IW-SC) according to tumour grade. 110
Figure 4.4: Kaplan-Meier survival analysis according to grade and IDH status. 112
Figure 4.5: Kaplan-Meier survival analysis according to tissue sodium concentration. 113
Figure 4.6: Kaplan-Meier survival analysis according to intracellular-weighted sodium concentration. 113
Figure 5.1: Schematic diagrams for models and model-free methods. 131
Figure 5.2: Schematic diagram of a two-site exchange model. 132
Figure 5.3: Representative spectra. 137
Figure 5.4: Diagram showing the conversion of pyruvate into lactate and bicarbonate. 138
Figure 5.5: Example of volume segmentation. 140
Figure 5.6: Hyperpolarised ^{13}C MRI of the entire cohort. 147
Figure 5.7: Hyperpolarised ^{13}C MRI metabolites in the entire cohort. 150
Figure 5.8: ADC values in the entire cohort. 152
Figure 5.9: Relationship between ADC and hyperpolarized ^{13}C MRI. 153
Figure 5.10: Relationship between the volume of the lesion and the hyperpolarized ^{13}C MRI. 155
Figure 5.11: Relationship between the results of the western blots and the hyperpolarized ^{13}C MRI. 156
Figure 5.12: Correlation matrix between the results of the western blots and the hyperpolarized ^{13}C MRI. 156
Figure 5.13: Relationship between the the results of the immunohistochemistry staining and the hyperpolarized ^{13}C MRI. 158
Figure 5.14: Correlation matrix between the results of the immunohistochemistry staining and the hyperpolarized ^{13}C MRI. 159

List of tables

Table 1.1: The RANO criteria used to assess treatment response in gliomas. 28
Table 3.1: Diffusion MRI parameters for the abbreviated VERDICT model. 72
Table 3.2: Demographic data and histopathological characteristics for high grade and low grade tumours. 74
Table 3.3: Comparison between the two observers. 78
Table 3.4: Extended VERDICT MRI protocol compared to the abbreviated protocol. 84
Table 4.1: Inclusion and exclusion criteria for enrolment in the study. 95
Table 4.2: Tissue sodium concentration and intracellular-weighted sodium concentration according to tumour grade (lower-grade glioma - LrGG and high-grade glioma - HGG). 107
Table 4.3: Comparison between sodium concentration in glioma and in normal tissue. 108
Table 4.4: Optimal cut-offs obtained from the receiver operating characteristics curve analysis and Youden's index assessment. 109
Table 5.1: Inclusion and exclusion criteria for enrolment in the study. 133
Table 5.2: Clinical characteristics 134
Table 5.3: Tissue biomarkers 144
Table 5.4: Quality control of the hyperpolarized pyruvate. 149
Table 5.5: Hyperpolarised ^{13}C MRI metabolites in the glioblastoma and in the contralateral non-tumour bearing parenchyma - Mirrored ROI. 174
Table 5.6: Hyperpolarised ^{13}C MRI metabolites in the glioblastoma and in the contralateral non-tumour bearing parenchyma - Multiple ROIs. 175
Table 5.7: Hyperpolarised ^{13}C MRI metabolites in the glioblastoma and in the contralateral non-tumour bearing parenchyma – Hemisphere. 176
Table 5.8: Hyperpolarised ^{13}C MRI metabolites in the glioblastoma. 177
Table 5.9: Hyperpolarised ^{13}C MRI metabolites in the non-tumour bearing brain parenchyma - cancer slice. 178
Table 5.10: Hyperpolarised ^{13}C MRI metabolites in the ipsilateral and contralateral hemisphere. 179
Table 6.1: Some of the tracers currently being investigated and their biological relevance. . 193

Introduction

UNIVERSITY OF CAMBRIDGE

Chapter 1

Introduction

Tumours have traditionally been defined as abnormal masses of tissue that begin when cells in a part of the body proliferate uncontrollably or fail to undergo normal cell death and become immortalised (American Cancer Society, 2011). The uncontrolled proliferation of abnormal cells is one of the commonest shared feature of all tumours and has been considered a hallmark of cancer (Hanahan and Weinberg, 2000).

The simplest tumour classification systems are based on histological aggressiveness. Tumours can be benign (non-cancerous), pre-malignant (pre-cancerous), or malignant (cancerous). Tumours are also commonly labelled as neoplasms: this word derives from the Ancient Greek words *neo*, that means "new", and *plasma*, that means "formation", expressing the concept that a tumour is a new formation, which is usually aberrant. Similarly, the word "cancer" derives from the crab-like nature of cancer that was described by the Greeks around 200 B.C. (David and Zimmerman, 2010). Hippocrates, the "Father of Medicine", used the words *carcinos* (crab) and *carcinoma* in the Hippocratic Corpus to describe a range of swelling that represented tumours. Recent evidence has demonstrated the presence of cancer lesions in mummies, fossils and preserved bodies over a period of several millennia. As an example, a recent CT scan of a Ptolemaic mummy demonstrated osteoblastic metastatic disease (figure 1.1) secondary to prostate cancer (Prates *et al.*, 2011).

Today the most common tumours are lung, breast, prostate and colorectal cancers (Stewart and Wild, 2014). Cancer survival is continuing to increase over the past few decades. However, there are worldwide disparities in cancer incidence and survival which are still significant even within high-income countries (Arnold *et al.*, 2019). Overall, cancer is the major cause of

Figure 1.1: Egyptian Ptolemaic mummy.
Left: X-ray digital extended-view of the upper body, showing the crossed arms mummification position and extensive post-mortem bone fractures.
Right: MDCT MPR (sagittal) of the lumbar spine, showing sclerotic vertebral bone lesions.
From: Prates et al., 2011.

morbidity and mortality with approximately 8 million cancer-related deaths worldwide in 2012 according to the last cancer report produced by the World Health Organization (WHO) in 2014 (Stewart and Wild, 2014). Interestingly, although the report also highlighted a remarkable difference in cancer distribution across the globe, the differences in mortality are less marked (Stewart and Wild, 2014). This heterogeneity in cancer prevalence and

mortality emphasises the wide spectrum of processes that fall under the umbrella of cancer and the importance of understanding the basic principles of cancer biology to determine causation and develop new treatments.

1.1 The Warburg effect

Otto Warburg is one of the most renowned cancer scientists of the past century. Warburg was awarded the Nobel Prize in Physiology or Medicine in 1932 for his doctoral research into oxidation in cancer that led to the so-called Warburg effect which is recognised as a metabolic pathway in most cancer cells (Warburg, 1925; Brand, 2010). The Warburg effect is the conversion of glucose to lactate, even in the presence of ample oxygen (Warburg, 1956). Cancer cells have a predilection for aerobic glycolysis despite the fact that this process is an inefficient way to generate adenosine 5´-triphosphate (ATP), compared to conventional mitochondrial oxidative phosphorylation. This switch towards a less-efficient ATP production may be due to the advantages it confers in facilitating the formation of reducing equivalents and the uptake and incorporation of nutrients into the tumour that are required for proliferation e.g., nucleotides, amino acids, and lipids (Vander *et al.*, 2015). Moreover, the metabolites required to support anabolic growth can themselves be oncogenic, by altering cell signalling and blocking cellular differentiation (Ward and Thompson, 2012). Therefore, aerobic glycolysis is not only a necessary consequence of tumour formation but it also is a driver that promotes proliferation and resistance to cell death (Vander *et al.*, 2015).

1.2 Hallmarks of cancer

In a seminal paper published in Cell in 2000, Hanahan and Weinberg addressed the so-called hallmarks of cancer, i.e. essential alterations in cell biology which result in malignant transformation (Hanahan and Weinberg, 2000). The six original hallmarks were: self-sufficiency in growth signals, insensitivity to growth-inhibitory signals, evasion of apoptosis, limitless replicative potential, sustained angiogenesis, and tissue invasion and metastasis (Hanahan and Weinberg, 2000). Those characteristics are

common to all cancers. Following on from that initial publication, in 2011 the same authors proposed the 2nd generation of these hallmarks which includes two enabling characteristics - genome instability and inflammatory state - and two emerging hallmarks - reprogramming the cellular metabolism and avoiding immunological destruction (Hanahan and Weinberg, 2011). The identification of those characteristics has had a pivotal role in shaping cancer research over the past 15 years. Indeed, the hallmarks became the targets of new drugs as well as new imaging techniques.

The evolution of a normal cell to a neoplastic one is a multistep process that involves these cancer hallmarks with the support of the tumour microenvironment. Cancer is a mixture of complex tissues in which transformed cells exercise their influence over normal cells and the latter contribute to the development and expression of some of the hallmarks. Most of the characteristics of this heterogeneous environment, such as angiogenesis, hypoxia and proliferation, can be assessed with imaging techniques such as Magnetic Resonance Imaging (MRI) or Positron Emission Tomography (PET). Imaging the hallmarks may increase knowledge on cancer biology, which is necessary in order to refine treatment and, eventually, personalise it. In this regard, imaging plays a pivotal role allowing non-invasive detection and evaluation of cancer.

1.3 Brain tumours

Although brain tumours are quite rare, accounting for less than 2% of all cancers, they cause significant morbidity and their prognosis is poor (Walker *et al.*, 2011; Stewart and Wild, 2014). Brain tumours can be both primary and secondary. During the last century, the classification of brain tumours has been largely based upon histopathological features or phenotype with different putative cells of origin. However, the most recent 2016 World Health Organization classification of tumours of the central nervous system takes into account both phenotypic and genotypic parameters (Louis *et al.*, 2016). Markers such as isocitrate dehydrogenase (IDH) mutations, mutations of the alpha-thalassemia/mental retardation syndrome X-linked (ATRX) gene, expression or codeletion of chromosome arms 1p and 19q are now essential

in classifying central nervous system (CNS) tumours. Oligoastrocytoma is, according to the consensus document which defined the updated classification, the best example of how the genotypic characterisation can change lesion classification. Combining genotype (i.e. IDH mutation and 1p/19q codeletion status) and phenotype (combination of astrocytic and oligodendroglial cells population) we can classify most tumours as either astrocytomas or oligodendrogliomas with only a small percentage of tumours defined as not otherwise specified (NOS) (Louis *et al.*, 2016).

Nevertheless, despite numerous primary CNS tumours, gliomas are still the most common, accounting for nearly 70% of central nervous cancers. They arise from glial cells, which form the supporting architecture of the brain, and glioblastoma (GBM) is the most frequent and malignant histologic type among gliomas (Ohgaki, 2009).

1.4 Glioma

Gliomas are a heterogeneous group of tumours that originate from central nervous system precursor epithelial cells (Bigner, 1981; Heppner, 1984). Traditionally, they have been classified according to the prevailing cell lineage as: astrocytic tumours, oligodendroglial tumours or glioblastoma when poorly differentiated (Arevalo *et al.*, 2017). According to the WHO classification, gliomas are given a grade between I and IV; Grade I being the least aggressive and Grade IV the most aggressive anaplastic tumours (Louis *et al.*, 2007a, b, 2016). The incorporation of molecular markers has also contributed to define more homogenous diagnostic categories for treatment purpose based on those biomarkers. Indeed, while in the past the definition of low-grade glioma (LGG) referred to WHO grade II gliomas, the new definition of lower-grade glioma (LrGG) is based upon the presence of the IDH mutation (figure 1.2) as this has been shown to predict survival (Pouratian and Schiff, 2010; Arevalo *et al.*, 2017) This classification determines correct patient management. However, even within the lower-grade gliomas, the management is dramatically different, with some lesions being amenable to surgical resection while the role of surgery in some is still debatable (Carabenciov and Buckner, 2019).

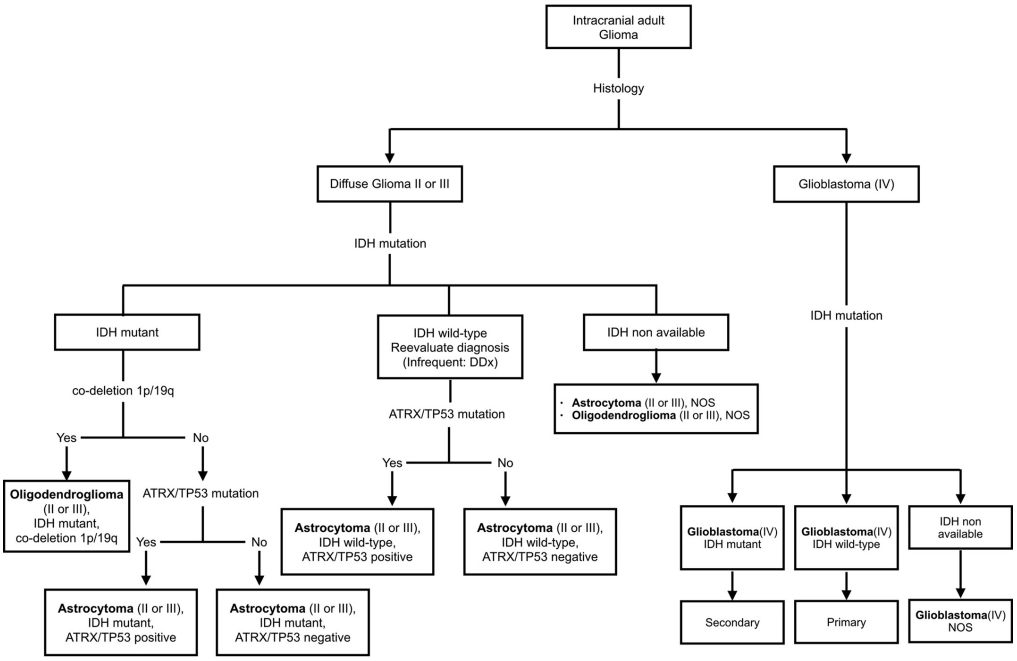

Figure 1.2: Classification of adult gliomas according to histology and IDH status. Oligoastrocytoma is not included because it is very rare.
From: Arevalo et al., 2017

1.4.1 Epidemiology

The overall incidence rate of central nervous cancers in the UK is 12.4 per 100,000 people (CRUK, 2019). Despite some controversy regarding a possible increase in incidence during the 1980s and 1990s (Preston-Martin *et al.*, 1993; Muir *et al.*, 1994), probably due to the introduction of high-resolution imaging modalities which could better detect brain tumours (Ohgaki, 2009), these figures remained stable during the last three decades (CRUK, 2019).

1.4.2 IDH Mutations and gliomagenesis

Isocitrate dehydrogenase (IDH) has become one of the key biomarkers of underlying glioma biology and a cornerstone of the WHO brain tumour classification (Louis *et al.*, 2016). There are three IDH isoforms named IDH1, IDH2 and IDH3, of which the first two are of particular interest in gliomas. IDH converts isocitrate to α-ketoglutarate in the cytosol (IDH1) and in the mitochondria (IDH2) generating reduced nicotinamide adenine dinucleotide phosphate (NADPH) from $NADP^+$ which has a key role in controlling cellular

oxidative damage. In 2008, a seminal paper featured in Science identified IDH1 mutation as un unexpected genetic alteration in patients with glioblastoma (Parsons *et al.*, 2008). The authors extensively sequenced the protein coding genes of a cohort of 22 glioblastomas. In that cohort, all the IDH mutated glioblastomas exhibited the same mutation: a replacement of an arginine with a histidine at amino acid residue 132 (R132H). This site is critical for isocitrate binding to IDH, therefore, a mutation at this level inactivates completely the ability of the protein to bind isocitrate de facto completely arresting its catalytic activity. This results in reduced production of α-ketoglutarate and NADPH. Moreover, the mutated enzyme acquires the new capability of catalysing the reduction of α-ketoglutarate to 2-hydroxyglutarate (2HG), an oncometabolite (Dang *et al.*, 2009). The latter has been associated with increased risk of brain tumours in patients with 2HG dehydrogenase deficiency and its concentration level has been correlated with an increase in reactive oxygen species which in turn contributes to cancer risk (Dang *et al.*, 2009). Moreover, 2HG is also directly toxic by inhibiting enzymes that use glutamate and or α-ketoglutarate. Interestingly, Parsons *et al.* associated this mutation with secondary glioblastomas, younger age of diagnosis and a better prognosis lying the basis for a better understanding of gliomagenesis (Parsons *et al.*, 2008). IDH mutation is also sufficient in establishing glioma CpG island methylator phenotype (G-CIMP) which determines tumour pathogenicity (Turcan *et al.*, 2012).

Further analysis of the presence of IDH mutation in different histological types highlighted that this mutation is an early event in gliomagenesis. Watanabe et al. (Watanabe *et al.*, 2009) demonstrated that low grade diffuse astrocytomas, oligodendrogliomas and oligoastrocytomas share IDH1 mutations as frequent genetic alterations. Interestingly, low grade diffuse astrocytomas usually show TP53 mutations but rarely show loss of 1p/19q. On the contrary, oligodendrogliomas often show loss of 1p/19q but rarely TP53 mutations. Lastly, oligoastrocytomas either have TP53 mutations or 1p/19q codeletion. The heterogeneity in mutation profile bar the presence of IDH1 mutations support the hypothesis that the latter is an earlier event in the gliomagenesis, likely happening in a common precursor, and further

mutations determine the final histological type (Watanabe *et al.*, 2009). The early occurrence of IDH mutations in a common precursor was also confirmed in a large cohort of 939 tumour samples by Yan *et al.* (Yan *et al.*, 2009). Indeed, they demonstrated that astrocytomas and oligodendrogliomas share IDH mutations, but not other genetic alterations, implying that IDH mutations occur relatively early during gliomagenesis. Further supporting evidence is the rarity of IDH mutations in primary glioblastoma (Yan *et al.*, 2009). Some authors therefore have proposed the existence of three separate pathways for gliomagenesis (Cohen *et al.*, 2013). A first pathway would see an early IDH mutation followed by TP53 mutation leading to astrocytic lineage tumours. If the second mutation is the codeletion 1p/19q the resulting lineage would be oligodendrogliomas with the capability of progression to anaplastic oligodendrogliomas if further mutations occur. Lastly, the third pathway leads to IDH wild-type glioblastoma through multiple genetic alterations acquired over a very short time span.

The discovery of the key importance of IDH in glioma tumorigenesis and aggressiveness determined an effort in *non-invasive* detection of the presence of the mutation. As mutation in IDH results in increased concentration of 2HG, measuring the concentration of this metabolite has been proposed as a way to predict IDH mutation. 2HG can be detected with magnetic resonance spectroscopy and dedicated acquisition protocols; its concentration correlates with IDH mutation status (Andronesi *et al.*, 2012; Choi *et al.*, 2012; Pope *et al.*, 2012). The capability of *in vivo* assessment of 2HG concentration has a significant diagnostic and prognostic role. In addition to the possibility of *non-invasively* determining the presence of the mutation without a biopsy, monitoring the 2HG concentration during treatment can predict therapy response earlier than other morphological techniques (Choi *et al.*, 2012). Over the past few years several IDH inhibitors have been proposed with promising results *in vitro* and in animal models (Rohle *et al.*, 2013; Zheng *et al.*, 2013; Turkalp *et al.*, 2014). In particular, Rohle and colleagues developed an IDH1 (R132H) mutation-specific inhibitor that caused a reduction in glioma volume in murine xenografts due to inhibition of proliferating cancer cells (Rohle *et al.*, 2013). More recently, Popovici-Muller *et al.* (Popovici-Muller *et al.*, 2018) developed an inhibitor of the IDH1 mutant

enzyme - AG-120 (ivosidenib) - that lowers the concentration of 2HG without showing any effect on wild-type or mutant isoforms of IDH2. Pre-clinical data in an orthotopic mouse xenograft model of human IDH-mutant glioma demonstrated the capability of ivosidenib to dramatically inhibit the production of 2HG and tumour growth (Nicolay *et al.*, 2017). Ivosidenib was approved by the FDA in 2018 for treatment of acute myeloid leukaemia with IDH1 mutation paving the way to further applications in other malignancies harbouring similar mutations (Dhillon, 2018). A recently concluded open-label multicentre phase 1 study in patients with solid tumours including cholangiocarcinoma and glioma demonstrated promising clinical activity of ivosidenib in those patients with an acceptable toxicity profile (Fan *et al.*, 2020). However, brain penetrance of ivosidenib was low, therefore potentially limiting the efficacy of the drug in patients with glioma. To overcome this limitation, a novel IDH inhibitor (AG-881, vorasidenib) with improved brain penetration and dual efficacy on both IDH1 and IDH2 mutations has been developed (Konteatis *et al.*, 2020). Vorasidenib demonstrated a dramatic inhibition of 2HG production (> 97%) in an orthotopic glioma mouse model (Konteatis *et al.*, 2020). A dedicated phase-1 multi-centre study is currently undergoing in patients with recurrent non-enhancing gliomas with IDH1 mutation (NCT03343197) comparing the concentration of 2HG following treatment with either ivosidenib or vorasidenib with the concentration of 2HG in untreated tumours.

1.4.3 Treatment

Glioma grade is strongly associated with prognosis, thus dictates treatment. MRI is routinely used for the diagnosis and estimation of glioma grade due to its non-invasive nature. Even though it has a high accuracy, in most cases a definite histological diagnosis is required to confirm the suspected diagnosis and evaluate the treatment options.

1.4.3.1 Lower-grade glioma

At present, there is not a common consensus about treatment strategies for LrGG. Indeed a recent Cochrane review underlined the lack of systematic randomised controlled clinical trials on which to base the clinical decision about the clinical management of these patients (Veeravagu *et al.*,

2013). Although common guidelines are still needed, surgical management is widely recognized as a viable treatment strategy, especially for grade II tumours, and the cancer is often resected with or without subsequent fractionated radiotherapy (RT) and chemotherapy using nitrosourea or temozolomide (Nitta *et al.*, 2015; Schucht *et al.*, 2015). Moreover, surgery is also indicated in patients with large lesions or with neurologic symptoms (Carabenciov and Buckner, 2019). After surgery, patients are followed up using serial MRIs in order to detect recurrence and/or progression.

Beside surgery, conventional radiation therapy is a well-established treatment strategy for lower-grade gliomas. A combination of radiation and chemotherapy is currently supported as therapy in post-surgical patients as soon as there is a risk for tumour recurrence (Carabenciov and Buckner, 2019). Early radiotherapy is especially warranted in patients with histology suggestive of astrocytoma and subtotal resection after surgery. However, the timing of radiotherapy is still very controversial especially in patients with lower risk of transformation due to the potential significant side effects. A potential new avenue for treatment of low-grade glioma are IDH inhibitors such as ivosidenib and vorasidenib described in paragraph 1.4.2. A phase 1 study comparing those two compounds is currently ongoing.

It is important to highlight that even grade II gliomas are an incurable chronic disease with malignant progression toward a high-grade glioma being almost granted at some stage of follow-up.

1.4.3.2 High-grade glioma

The role of surgery in HGG is less debatable. Although some older studies failed to demonstrate a survival benefit for resection, this was probably due to the inadequate assessment of the tumour boundaries and the extent of resection (Schucht *et al.*, 2015). Several current guidelines, including the NICE guidelines, advocate maximal resection as a primary target in the management of patients with HGG (Sanai, 2012; Talibi *et al.*, 2014; NICE, 2015). The optimal extent of resection depends on several characteristics, including the tumour size and location, general and neurological status, and the experience of the surgeon. However, to achieve a gross-total resection it

is mandatory to understand the exact location and extent of tumour, which is often challenging with currently available methods.

Since the introduction of neuronavigation based on pre-surgical imaging, there has been a significant improvement in surgical accuracy, and this is now standard-of-care. New techniques such as 5-aminolevulinic acid (5-ALA)-guided surgery and intraoperative MRI (iMRI) have been developed in order to overcome these limitations. Indeed, a recently published review, confirmed that these new techniques have an individual benefit in terms of extent of resection (Barone *et al.*, 2014). In particular, the introduction of 5-ALA in the clinical setting has had a striking effect in achieving gross total resection; patients in which the resection was carried out using 5-ALA experienced a longer progression-free survival and less enhancement in the tumour bed after resection, when compared with white light alone (Tonn and Stummer, 2008; Stummer *et al.*, 2014). From a biological point of view, 5-ALA is an amino acid that is normally present in the human body being a metabolite of heme. Its production is strictly regulated by a negative feedback inhibition of the heme on the enzyme 5-ALA synthase. When exogenous 5-ALA is administered the feedback is bypassed and it starts to accumulate. 5-ALA elicits the synthesis of the protoporphyrin IX which is fluorescent if exposed to the appropriate wavelengths of light and is usually converted in heme. The uncontrolled increase in protoporphyrin IX due to the 5-ALA therefore results in a build-up of fluorescence inside malignant cells. The tumour can be then better visualised using a surgical microscope equipped with dedicated optical filters (Stummer *et al.*, 1998; Tonn and Stummer, 2008). This characteristic helps neurosurgeons in identifying malignant tissue and, combined with neuronavigation, may significantly improve gross total resection (Tonn and Stummer, 2008; Barone *et al.*, 2014). Nevertheless, a complete resection is very often unachievable either due to unfavourable lesion characteristics or an underestimation of the tumour spread.

Radiotherapy is an integral component in the treatment of HGG (Ludmir *et al.*, 2019). It confers a survival advantage in patients with glioblastoma (Cabrera *et al.*, 2016a). Although the specific approach depends on characteristics specific to tumour and patient (such as age and performance status) radiotherapy is recommended for patients with

glioblastoma both after the initial surgery/biopsy and at recurrence in the American Society for Radiation Oncology (ASTRO) guidelines (Cabrera *et al.*, 2016b). Moreover, thanks to recent technological advantages such as intensity-modulated radiotherapy (IMRT) and image-guided radiotherapy (IGRT), it is possible to reduce the dose delivery to normal tissues without sacrificing the treatment of the glioblastoma (Burnet *et al.*, 2014). Therefore, the combination of these technologies is the state-of-the-art of radiotherapy for patients with glioblastoma.

1.4.4 Treatment evaluation

Whilst neurosurgery is focused on obtaining the so-called maximum-achievable resection in order to boost the prognosis, there is a compelling need for proper treatment evaluation. Currently, this evaluation relies either on the duration of patient survival or on the radiographic response rate or progression-free survival (PFS). In order to improve the assessment of the radiographic response, the RANO Working Group (an international panel consisting of neuro-oncologists, neurosurgeons, radiation oncologists, neuroradiologists, neuropsychologists, and experts in QoL measures) proposed in 2010 a set of criteria that do not rely anymore only on two-dimensional measurements of the enhancing tumour area but on a more elaborate set of characteristics that takes into account multiple sequences and parameters (table 1.1) (Wen *et al.*, 2010). Although the RANO criteria perform significantly better compared to traditional response assessment strategies, they fall short of definitively distinguishing tumour progression, pseudoresponse, and pseudoprogression (Huang *et al.*, 2015).

RANO criteria defined pseudoprogression as an increase in contrast enhancement which is evident at the first post radiation MRI and subsequently subsides without any change in therapy at the following scan (Wen *et al.*, 2010). This phenomenon usually occurs within 12 weeks after the completion of radiotherapy in 20-30% of patients (Wen *et al.*, 2010). To partially mitigate the risk of misinterpreting an enhancing area and labelling it as progression within 12 weeks from radiotherapy, the criteria define as true progression only contrast enhancing areas that are outside the radiation field, unless a sample

is obtained from the enhancing area to confirm the presence of viable tissue (Wen *et al.*, 2010). A similar solution has been proposed for pseudoresponse: antiangiogenic agents may produce a significant decrease in contrast enhancement as early as 2 days after initiation of therapy therefore potentially resulting in overcalling of radiological response; RANO criteria only claim response if the radiological appearance persists for at least 4 weeks to overcome this (Wen *et al.*, 2010). It is evident that the approach taken by the RANO panel has been quite conservative, resulting in uncertainties for up to 12 weeks after therapy.

	CR	PR	SD	PD
T1 post Gadolinium	None	≥ 50% ↓	< 50% ↓ < 25% ↑	≥ 25% ↑*
T2/FLAIR	Stable or ↓	Stable or ↓	Stable or ↓	↑*
New lesion	None	None	None	Present*
Corticosteroids	None	Stable or ↓	Stable or ↓	NA **
Clinical Status	Stable or ↑	Stable or ↑	Stable or ↑	↓*
Requirement for response	All	All	All	Any **

Table 1.1: The RANO criteria used to assess treatment response in gliomas. Abbreviations are as follow: CR = complete response; PR = partial response; SD = stable disease; PD = progressive disease.

** Progression occurs when any of these criteria is present. ** NA = Not applicable. Despite the other criteria, an increase in steroid dose alone is not sufficient to classify a patient as a progressive disease.*

In the past few years, a number of advanced techniques, such as perfusion MRI or spectroscopy have been proposed to help with this, however a consensus is still to be reached (Huang *et al.*, 2015). Dynamic susceptibility contrast-magnetic resonance imaging (DSC-MRI) has been proposed as a quantitative tool to assess pseudoprogression: using the relative cerebral blood volume, a sensitivity of 90% and a specificity of 60% have been reported whilst perfusion maps demonstrated slightly lower figures with sensitivity of 85.7% and a specificity of 89.2% (Huang *et al.*, 2015). Despite the good performance of DSC-MRI, this technique has important limitations. Its characteristic sensitivity to susceptibility for instance, leads to a low signal-to-noise level in areas near bone surfaces, air interface or blood products (as in case of haemorrhage) and the disruption of the blood-brain barrier resulting in vascular leakage. Some studies have demonstrated that dynamic contrast enhanced- magnetic resonance imaging (DCE-MRI) could effectively detect

pseudo response with a sensitivity of approximately 100% and specificity of around 80%, but the pharmacokinetic models are complex to use leading to difficulty in standardization (Huang *et al.*, 2015).

Magnetic resonance spectroscopy (MRS) is a promising technique for pseudo progression evaluation: a higher choline-to-creatine and choline-to-NAA ratios are observed in tumour progression compared to normal parenchyma or treatment necrosis; in particular, using the choline-to-NAA ratio the sensitivity and specificity are 88% and 86% (Huang *et al.*, 2015). However, MRS requires an operator to properly select the region in which the ratio has to be computed and to set the saturation bands; this results in low reproducibility of results and high inter-operator variability. Reproducibility is also jeopardised by the equipment, pulse sequences, parameters, and post-processing methods used in different sites.

Despite the potential utility of these techniques in helping characterising pseudo progression from true progression their adoption into the routine clinical environment faces many challenges due to issues with acquisition, post-processing and analysis. Many are still considered research techniques rather than clinical tools. Nevertheless, a prompt assessment of therapy would be desirable to better define management at the earliest stage possible. Therefore, it is necessary to develop more advanced imaging techniques to allow a better understanding of tumour physiology which will improve primary detection and tumour characterisation, as well as early therapy assessment and long-term follow-up in a routine clinical environment.

References

American Cancer Society. The History of Cancer [Internet]. Cancer 2011Available from: www.cancer.net/patient/Advocacy and Policy/Treatment_Advances_Timeline.pdf

Andronesi OC, Kim GS, Gerstner E, Batchelor T, Tzika AA, Fantin VR, et al. Detection of 2-hydroxyglutarate in IDH-mutated glioma patients by in vivo spectral-editing and 2D correlation magnetic resonance spectroscopy. Sci Transl Med 2012; 4

Arevalo OJ, Valenzuela R, Esquenazi Y, Rao M, Tran B, Zhu J, et al. The 2016 World Health Organization Classification of Tumors of the Central Nervous System: A Practical Approach for Gliomas, Part Part 1. Basic Tumor Genetics. Neurographics 2017; 7: 334–343.

Arnold M, Rutherford MJ, Bardot A, Ferlay J, Andersson TM-L, Myklebust TÅ, et al. Progress in cancer survival, mortality, and incidence in seven high-income countries 1995–2014 (ICBP SURVMARK-2): a population-based study. Lancet Oncol 2019; 2014: 1–13.

Barone DG, Lawrie T a, Hart MG, Dg B, Ta L, Mg H. Image guided surgery for the resection of brain tumours. Cochrane database Syst Rev 2014; 1: CD009685.

Bigner D. Biology of gliomas: potential clinical implications of glioma cellular heterogeneity. Neurosurgery 1981; 9: 320–326.

Brand R a. Biographical sketch: Otto Heinrich Warburg, PhD, MD. Clin Orthop Relat Res 2010; 468: 2831–2832.

Burnet NG, Jena R, Burton KE, Tudor GSJ, Scaife JE, Harris F, et al. Clinical and practical considerations for the use of intensity-modulated radiotherapy and image guidance in neuro-oncology. Clin Oncol 2014; 26: 395–406.

Cabrera AR, Kirkpatrick JP, Fiveash JB, Shih HA, Koay EJ, Lutz S, et al. Radiation Therapy for Glioblastoma: An ASTRO Evidence-Based Clinical Practice Guideline. Pract Radiat Oncol 2016: 1–58.

Cabrera AR, Kirkpatrick JP, Fiveash JB, Shih HA, Koay EJ, Lutz S, et al. Radiation therapy for glioblastoma: Executive summary of an American Society for Radiation Oncology Evidence-Based Clinical Practice Guideline. Pract Radiat Oncol 2016; 6: 217–225.

Carabenciov ID, Buckner JC. Controversies in the Therapy of Low-Grade Gliomas. Curr Treat Options Oncol 2019; 20: 25.

Choi C, Ganji SK, DeBerardinis RJ, Hatanpaa KJ, Rakheja D, Kovacs Z, et al. 2-Hydroxyglutarate detection by magnetic resonance spectroscopy in IDH-mutated patients with gliomas. Nat Med 2012; 18: 624–629.

Cohen AL, Holmen SL, Colman H. IDH1 and IDH2 Mutations in Gliomas. Curr Neurol Neurosci Rep 2013: 13:345.

CRUK. Brain, other CNS and intracranial tumours incidence statistics | Cancer Research UK [Internet]. 2019[cited 2019 Mar 24] Available from: https://www.cancerresearchuk.org/health-professional/cancer-statistics/statistics-by-cancer-type/brain-other-cns-and-intracranial-tumours/incidence#collapseTen

Dang L, White DW, Gross S, Bennett BD, Bittinger MA, Driggers EM, et al. Cancer-associated IDH1 mutations produce 2-hydroxyglutarate. Nature 2009; 462: 739–744.

David AR, Zimmerman MR. Cancer: An old disease, a new disease or something in between? Nat Rev Cancer 2010; 10: 728–733.

Dhillon S. Ivosidenib: First Global Approval. Drugs 2018; 78: 1509–1516.

Fan B, Mellinghoff IK, Wen PY, Lowery MA, Goyal L, Tap WD, et al. Clinical pharmacokinetics and pharmacodynamics of ivosidenib, an oral, targeted inhibitor of mutant IDH1, in patients with advanced solid tumors. Invest New Drugs 2020; 38: 433–444.

Hanahan D, Weinberg R a. The hallmarks of cancer. Cell 2000; 100: 57–70.

Hanahan D, Weinberg R a. Hallmarks of cancer: The next generation. Cell 2011; 144: 646–674.

Heppner G. Tumor heterogeneity. Cancer Res 1984; 44: 2259–2265.

Huang RY, Neagu MR, Reardon DA, Wen PY. Pitfalls in the Neuroimaging of Glioblastoma in the Era of Antiangiogenic and Immuno/Targeted Therapy - Detecting Illusive Disease, Defining Response. Front Neurol 2015; 6: 33.

Konteatis Z, Artin E, Nicolay B, Straley K, Padyana AK, Jin L, et al. Vorasidenib (AG-881): A First-in-Class, Brain-Penetrant Dual Inhibitor of Mutant IDH1 and 2 for Treatment of Glioma. ACS Med Chem Lett 2020; 11: 101–107.

Louis D, Ohgaki H, Wiestler O, Cavenee W. WHO ClassiWcation of tumours of the central nervous system. [Internet]. 4th ed. Lyon: IARC - International Agency for Research on Cancer; 2007Available from: http://apps.who.int/bookorders/anglais/detart1.jsp?codlan=1&codcol=70&codcch=4001

Louis DN, Ohgaki H, Wiestler OD, Cavenee WK, Burger PC, Jouvet A, et al. The 2007 WHO classification of tumours of the central nervous system. Acta Neuropathol 2007; 114: 97–109.

Louis DN, Perry A, Reifenberger G, von Deimling A, Figarella-Branger D, Cavenee WK, et al. The 2016 World Health Organization Classification of Tumors of the Central Nervous System: a summary. Acta Neuropathol 2016; 131: 1–18.

Ludmir EB, Mahajan A, Ahern V, Ajithkumar T, Alapetite C, Bernier-Chastagner V, et al. Assembling the brain trust: the multidisciplinary imperative in neuro-oncology. Nat Rev Clin Oncol 2019; 16: 521–522.

Muir CS, Storm HH, Polednak A. Brain and other nervous system tumors. Cancer Surv 1994; 19/20: 369–392.

NICE. Brain cancers overview. 2015

Nicolay B, Narayanaswamy R, Aguado E, Nagaraja R, Murtie J, Liu G, et al. The IDH1 mutant inhibitor AG-120 shows strong inhibition of 2-HG production in an orthotopic IDH1 mutant glioma model in vivo [abstract no. EXTH-59 plus poster]. Neuro Oncol 2017; 19: vi86.

Nitta M, Muragaki Y, Maruyama T, Ikuta S, Komori T, Maebayashi K, et al. Proposed therapeutic strategy for adult low-grade glioma based on aggressive tumor resection. Neurosurg Focus 2015; 38: E7.

Ohgaki H. Epidemiology of Brain Tumors. Humana Press; 2009

Parsons DW, Jones S, Zhang X, Lin JCH, Leary RJ, Angenendt P, et al. An integrated genomic analysis of human glioblastoma multiforme. Science (80-) 2008; 321: 1807–1812.

Pope WB, Prins RM, Thomas MA, Nagarajan R, Yen KE, Bittinger MA, et al. Non-invasive detection of 2-hydroxyglutarate and other metabolites in IDH1 mutant glioma patients using magnetic resonance spectroscopy. J Neurooncol 2012; 107: 197–205.

Popovici-Muller J, Lemieux RM, Artin E, Saunders JO, Salituro FG, Travins J, et al. Discovery of AG-120 (Ivosidenib): A First-in-Class Mutant IDH1 Inhibitor for the Treatment of IDH1 Mutant Cancers. ACS Med Chem Lett 2018; 9: 300–305.

Pouratian N, Schiff D. Management of low-grade glioma. Curr Neurol Neurosci Rep 2010; 10: 224–31.

Prates C, Sousa S, Oliveira C, Ikram S. Prostate metastatic bone cancer in an Egyptian Ptolemaic mummy, a proposed radiological diagnosis. Int J Paleopathol 2011; 1: 98–103.

Preston-Martin S, Lewis S, Winkelmann R, Borman B, Auld J, Pearce N. Descriptive epidemiology of primary cancer of the brain, cranial nerves, and cranial meninges in New Zealand, 1948 – 88. Cancer Causes Control 1993; 4: 529–538.

Rohle D, Popovici-Muller J, Palaskas N, Turcan S, Grommes C, Campos C, et al. An inhibitor of mutant IDH1 delays growth and promotes differentiation of glioma cells. Science (80-) 2013; 340: 626–630.

Sanai N. Emerging operative strategies in neurosurgical oncology. Curr Opin Neurol 2012;

25: 756–66.

Schucht P, Beck J, Seidel K, Raabe a. Extending resection and preserving function: modern concepts of glioma surgery. Swiss Med Wkly 2015: 1–11.

Stewart BW, Wild C. World cancer report 2014. Geneva WHO 2014

Stummer W, Stocker S, Novotny A, Heimann A, Sauer O, Kempski O, et al. In vitro and in vivo porphyrin accumulation by C6 glioma cells after exposure to 5-aminolevulinic acid. J Photochem Photobiol B 1998; 45: 160–9.

Stummer W, Tonn JC, Goetz C, Ullrich W, Stepp H, Bink A, et al. 5-Aminolevulinic acid-derived tumor fluorescence: The diagnostic accuracy of visible fluorescence qualities as corroborated by spectrometry and histology and postoperative imaging. Neurosurgery 2014; 74: 310–319.

Talibi SS, Talibi SS, Aweid B, Aweid O. Prospective therapies for high-grade glial tumours: A literature review. Ann Med Surg 2014; 3: 55–59.

Tonn JC, Stummer W. Fluorescence-guided resection of malignant gliomas using 5-aminolevulinic acid: practical use, risks, and pitfalls. Clin Neurosurg 2008; 55: 20–26.

Turcan S, Rohle D, Goenka A, Walsh LA, Fang F, Yilmaz E, et al. IDH1 mutation is sufficient to establish the glioma hypermethylator phenotype. Nature 2012; 483: 479–483.

Turkalp Z, Karamchandani J, Das S. IDH Mutation in Glioma New Insights and Promises for the Future. JAMA Neurol 2014; 71: 1319.

Vander MG, Cantley LC, Thompson CB, Thompson CB, Heiden MG Vander, Cantley LC. Understanding The Metabolic the Warburg Effect : of Requirements Cell Proliferation. 2015; 324: 1029–1033.

Veeravagu A, Jiang B, Ludwig C, Chang SD, Black KL, Patil CG. Biopsy versus resection for the management of low-grade gliomas. Cochrane database Syst Rev 2013; 4: CD009319.

Walker C, Baborie A, Crooks D, Wilkins S, Jenkinson MD. Biology, genetics and imaging of glial cell tumours. Br J Radiol 2011; 84: S90–S106.

Warburg O. The Metabolism of Carcinoma Cells. J Cancer Res 1925; 9: 148–163.

Warburg O. On the Origin of Cancer Cells. Science (80-) 1956; 123: 309–14.

Ward PS, Thompson CB. Metabolic Reprogramming: A Cancer Hallmark Even Warburg Did Not Anticipate. Cancer Cell 2012; 21: 297–308.

Watanabe T, Nobusawa S, Kleihues P, Ohgaki H. IDH1 mutations are early events in the development of astrocytomas and oligodendrogliomas. Am J Pathol 2009; 174: 1149–1153.

Wen PY, Macdonald DR, Reardon D a., Cloughesy TF, Sorensen a. G, Galanis E, et al. Updated response assessment criteria for high-grade gliomas: Response assessment in neuro-oncology working group. J Clin Oncol 2010; 28: 1963–1972.

Yan H, Parsons DW, Jin G, McLendon R, Rasheed BA, Yuan W, et al. Mutations in Gliomas. N Engl J Med 2009; 360: 765–773.

Zheng B, Yao Y, Liu Z, Deng L, Anglin JL, Jiang H, et al. Crystallographic investigation and selective inhibition of mutant isocitrate dehydrogenase. ACS Med Chem Lett 2013; 4: 542–546.

Imaging of glioma

UNIVERSITY OF CAMBRIDGE

Chapter 2

Imaging of glioma

Gliomas may present clinically with neurological disturbance such as headaches, seizures or focal neurological deficits depending on the location of the tumour. Despite the routine clinical use of conventional proton Magnetic Resonance Imaging (^{1}H-MRI) in the assessment of glioma, the technique cannot fully assess infiltrative growth or response to therapy (Villanueva-Meyer *et al.*, 2017). Therefore, anatomic imaging of gliomas can be complemented by more advanced techniques to assess tumour biology (Brindle *et al.*, 2017). For example, the use of diffusion-weighted imaging (DWI) to evaluate tissue water movement has been extensively applied to imaging cancer and has found a wide range of routine applications. DWI is frequently used in glioma imaging and recently an advanced form of DWI, diffusion kurtosis imaging (DKI), has emerged as a new potential tool to demonstrate tumour heterogeneity (Van Cauter *et al.*, 2012, 2014).

MRI largely measures the signal from hydrogen nuclei (or protons ^{1}H) in water or to a lesser extent in fat given the natural abundance of these molecules. MRI can also be used to detect other nuclei, the so-called X-nuclei: these nuclei can be used to explore metabolic processes *in vivo* and include sodium (^{23}Na) (Maudsley and Hilal, 1984; Madelin, 2013; Madelin and Regatte, 2013) or carbon (^{13}C) containing compounds (Gallagher *et al.*, 2008, 2011a). Research in multi-nuclei MRI has increased over the last decade due to the potential of these approaches to unlock new biology. However, the signal from nuclei such as ^{23}Na, ^{13}C or ^{31}P is much lower compared to protons due to their lower concentration, different gyromagnetic ratio and nuclear polarisation and therefore until recently, multi-nuclei imaging with conventional MRI systems has been a great challenge. Nevertheless, with the widespread adoption of higher-field magnets and the improvement in coil technology and

acquisition sequences, these nuclei can now be successfully imaged at high resolution within a clinically practical timescale. These techniques may provide useful data to complement conventional multi-parametric MRI protocols comprising standard morphological and dynamic contrast enhanced sequences, to better stratify tumours and response to treatment.

2.1 Conventional proton MRI

The current standard of practice in Europe for glioma imaging is based on conventional proton MRI. The standard protocol includes T_2W, FLAIR, DWI and pre- and post- gadolinium-based contrast agent T_1W with 80% of centres using 3D imaging (Thust *et al.*, 2018). This simple protocol is in line with the recommendation of the Response Assessment in Neuro-Oncology (RANO) Criteria for glioma, based on changes in tumour size and blood-brain barrier breakdown seen on post-contrast imaging (Wen *et al.*, 2010). However, conventional imaging has significant limitations in assessing tumour response in the first 3 months after treatment. During this time window, contrast enhancement can increase for many reasons, such as therapy induced damage to normal brain tissue or simulated tumour progression (pseudo progression). Therefore, during these 3 months there is a significant delay in accurately assessing the response of the tumour which could result in missing the optimal treatment window for these patients with a dismal prognosis.

2.1.1 Morphologic imaging

MRI is the modality of choice to investigate patients with sudden presentation of neurological disturbances and has a high sensitivity for detecting brain tumours. Routine MRI of brain tumours typically involves T_2-weighted images (T_2WI), T_2 fluid-attenuated inversion recovery (FLAIR), T_1-weighted images (T_1WI), acquired pre- and post- gadolinium-based contrast agent administration and Diffusion Weighted Imaging (DWI) (Brindle *et al.*, 2017). Often a post-contrast high-resolution T1 isovolumetric sequence is performed preoperatively for use with intraoperative navigational software (i.e. Stealth System and Brainlab) (Elhawary *et al.*, 2011; Khoshnevisan and Allahabadi, 2012). Together these sequences have a role in detection and

localisation of the lesion, identification of mass effect on the brain parenchyma and distant spread, assessment of the ventricular system and vasculature, and to some extent can be used to characterize the lesion according to its imaging phenotype. Certain features, such as contrast enhancement, signs of mass effect and significant peri-tumoral oedema, strongly suggest a high-grade tumour, whilst others, such as a poorly defined mass, are more in keeping with lower-grade tumours. However, making a diagnosis of a specific tumour type is challenging due to the fact that some characteristics associated with high grade tumours may be expressed by low grade tumours and vice versa (Mabray *et al.*, 2015). In these cases, MRI cannot be specific.

Another limitation of conventional imaging is the evaluation of peri-tumoral oedema: high grade gliomas spread through oedema with tumour cells infiltrating regions of non-enhancing T_2WI/FLAIR signal hyperintensity as well as in regions of up to 2.5 cm beyond the area of T_2WI/FLAIR signal change (Watanabe *et al.*, 1992; Price and Gillard, 2011). This leads to a sub-optimal resection with potential residual tumour and risk of recurrence (Lu *et al.*, 2003; Cha, 2006; Barajas *et al.*, 2013).

2.1.2 Proton nuclear magnetic resonance spectroscopy

Both benign and malignant tumours show an increased metabolism compared to the normal surrounding tissue and produce high levels of lactate. Proton MR spectroscopy (^{1}H-MRS) can non-invasively measure brain metabolites *in vivo*, including the steady-state concentration of lactate. Several biological processes can be measured using ^{1}H-MRS, such as glucose consumption, variation in membrane turnover and proliferation (Price and Gillard, 2011; Zhang *et al.*, 2014). Proton spectroscopy is current in use for many clinical applications in neurological, cardiac, and oncological imaging (Constantine *et al.*, 2004; Sahraian and Eshaghi, 2010; Radbruch and Bendszus, 2015).

MRS has been used to differentiate brain tumours of different grades and secondary from primary lesions using metabolite concentrations; however clear cut-off values to discriminate tumour grades have not been identified. In addition, there is also an overlap of some metabolites between different

lesions: for example, Cho/Cr values are similar in grade IV astrocytoma and metastatic deposits (Möller-Hartmann *et al.*, 2002). Despite the lack of accuracy in grading brain tumours, some researchers have demonstrated benefits in adding spectroscopic imaging to conventional MR techniques for target selection in brain biopsies (Martin *et al.*, 2001). To date, most of the studies are single centre with variations in scan qualities. Different inpatient populations and study designs may produce heterogeneity in the results. Although ^{1}H-MRS may be a non-invasive method for assessing brain tumours, it has to be interpreted by an experienced reader and has not to date been shown to clearly discriminate between high and low grade tumours (Wang *et al.*, 2014).

2.2 Diffusion weighted imaging

Diffusion-Weighted Imaging (DWI) is an MRI technique based on the Brownian motion of water within tissue. Any molecule in a fluid is displaced as the molecule is agitated by thermal energy into random motion. In normal tissue the motion of water molecules is relatively free and random - it is limited only by the boundaries of the tissue itself; the effect of this erratic motion has been termed *displacement distribution*. Analysing this distribution at two time-points using diffusion-sensitive gradients, information can be obtained about the medium in which water molecules are moving. DWI is the general term given for such sequences and can be seen as the unprocessed result of the application of a pulsed gradient spin echo sequence (Stejskal and Tanner, 1965; Hagmann *et al.*, 2006).

The degree of diffusion weighting of the pulsed gradient spin echo sequence is termed the *b*-factor, and is determined through manipulation of the gradients (Stejskal and Tanner, 1965; McRobbie *et al.*, 2017). The *b*-factor is given by the equation:

$$b = \gamma^2 G^2 \delta^2 (\Delta - \frac{\delta}{3}) \text{ [1]}$$

where G is the amplitude of the gradients, δ is the time of applied gradients and Δ duration between the paired gradients. Having defined the *b*-factor, the diffusion signal strength can be defined according to the following equation:

$$S(b) = S_0 \exp(-bD) \text{ [2]}$$

where S(*b*) is the diffusion signal at a specific *b* value and D is the self-diffusion constant of the specific tissue. To simplify DWI evaluation, a map which depicts the magnitude of diffusion is generated using at least two DWI acquisitions with different b-values; this map is called the apparent diffusion coefficient (ADC) map. The apparent diffusion coefficient is calculated according to the following equation:

$$ADC\ image = -\frac{1}{b}\ln\left(\frac{DW\ image}{T_2W\ image}\right) \text{ [3]}$$

where the T_2W signal is provided by the images acquired with *b* set to 0. The ADC map will also eliminate any interpretation uncertainties deriving from the so-called T2 shine through effect which is due to the long TE used for DWI acquisitions and the subsequent T_2W signal. A high ADC value reflects

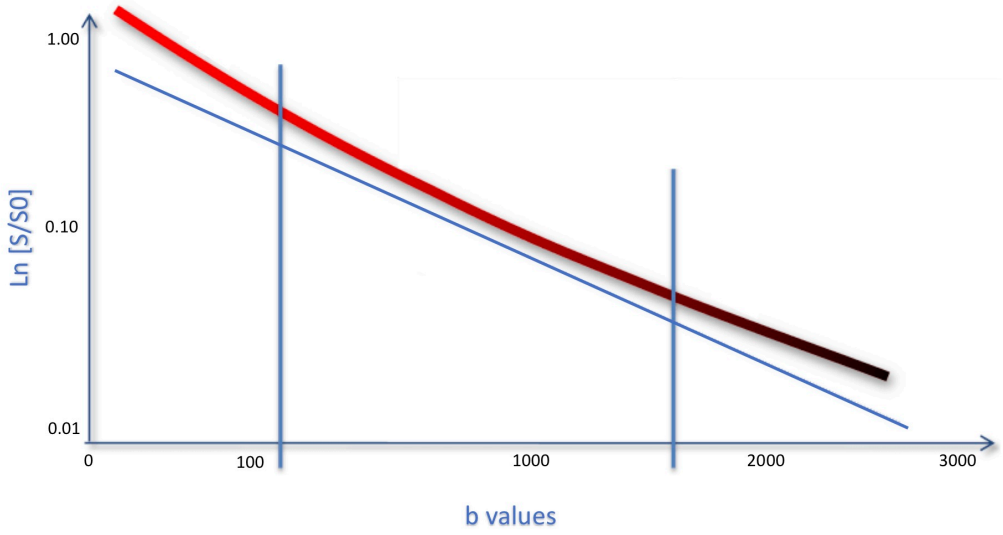

Figure 2.1: Diffusion signal intensity curve.

Log signal intensity versus b-values, the apparent diffusion coefficient (ADC) is the absolute value of the slope of the curves. The theoretical curve of signal decay for the mono-exponential model is represented in blue. This is based on the assumption that the water molecules within a voxel diffuse in the same way. However, this is not true in reality as more than one tissue will be present within a voxel represented by a biexponential curve (represented in red). At low b-values (< 150 s/mm^2), the signal is dominated by the blood microcirculation with a resulting higher signal than expected. This perfusion component is exploited with the intravoxel incoherent motion imaging (IVIM – see paragraph 2.2.1). At high b values the signal is dominated by hindrance effects (notably from water/membranes interaction). The heterogeneity of the signal due to the different interactions, results in the so-called diffusion kurtosis (DKI) with a large deviation of the measured signal compared to the expected signal. As IVIM informs on perfusion, DKI has greater sensitivity to tissue features.

Figure adapted from R. G. Figueiras – RSNA 2014

unrestricted random motion, and it will result in a hyperintense region on the map; conversely, in the presence of restricted motion, it will appear hypointense, such as an acute stroke or in the presence of a cellular tumour.

DWI is a very powerful sequence routinely used in the assessment of many disease processes, such as acute stroke and solid cancers. Several papers have addressed the importance of DWI and ADC in evaluation of gliomas. As tumour proliferation increases cellularity, it is expected that higher grade malignant tumours should exhibit lower ADC values due to reduction of the extracellular matrix and consequent hindrance to water diffusion (Chen *et al.*, 2013). Indeed, higher grade gliomas tend to have lower ADC values compared to lower grade gliomas (Bulakbasi *et al.*, 2004). Moreover, a worse prognosis is associated with lower ADC values (Hilario *et al.*, 2014). However, the ADC values of certain gliomas types, such as grade II astrocytoma and glioblastoma, overlap significantly and therefore a clear cut-off for discriminating higher grade and lower grade tumours is still undefined (Kono *et al.*, 2001). Interestingly, ADC values have also been reported to be higher in the infiltrative peri-tumoral oedema seen in glioblastoma, although this has not been found consistently in all studies (Kono *et al.*, 2001; Oh *et al.*, 2005; Server *et al.*, 2009; Lee *et al.*, 2011; Hilario *et al.*, 2014).

ADC has also been proven capable of subtyping lower grade gliomas. Astrocytomas and oligodendrogliomas exhibit characteristic features on pathology: astrocytomas have low to moderate cell density with variable cellular morphology, whilst oligodendroglioma are more hypercellular with more uniform cellular morphology. Therefore, astrocytomas tend to have higher ADC values compared to oligodendroglioma due to greater diffusion of the molecules of water within the extracellular matrix (Tozer *et al.*, 2007). Interestingly although, both astrocytomas and oligodendrogliomas are more cellular than normal brain parenchyma, the ADC values are higher than normal brain. This hints to the possibility that the presence of macromolecules in the extracellular matrix of those tumours may have a significant effect in reducing the diffusion of molecule of waters. The extracellular matrix of astrocytomas and oligodendrogliomas is known to contain a high concentration of glycosaminoglycans, in particular hyaluronan, which positively correlates with ADC (Tozer *et al.*, 2007).

Nevertheless, despite the potential applications in neuro-oncology and the vast body of published literature, clear cut-offs for quantitative assessment of ADC are still lacking, mostly due to the high variability of ADC values reported in the literature. This variability on ADC can be related both to biological and technical factors. For instance, some ADC values have been calculated without taking into account the IVIM affect, therefore resulting in a higher value than expected, especially using clinical protocols including *b* values of 0 and 1000 s/mm^2. Moreover, the diffusion of molecules of water in tissues can be influenced by several biological factors such as cell density, cell size, cell shape, membrane permeability and subcellular architecture (Panagiotaki *et al.*, 2014). Diffusion weighted imaging is also highly sensitive to technical parameters. As per equation 1 and 2, it is clear that the gradients and field strength have a significant effect on the *b* values. Moreover, different coils and magnets will have different technical characteristics resulting in lower reproducibility between different vendors (Chen *et al.*, 2013). The *b* value is a key determiner of the ADC values, but there is no consensus on which *b* value should be used and despite the fact that a *b* value of 1000 s/mm^2 is the most used in neuro applications, this is not a standardized approach.

2.2.1 Diffusion Tensor Imaging

The assumption that water diffusion is the same in every direction (isotropic) inside the brain parenchyma is an oversimplification. The brain parenchyma is highly structured, and the axonal bundles present a specific orientation; therefore, the diffusion of water between these will follow those paths having different diffusion coefficients along different directions (anisotropic diffusion). Anisotropic diffusion is described using a 3x3 matrix which is called a diffusion tensor (DT):

$$DT = \begin{bmatrix} D_{xx} & D_{xy} & D_{xz} \\ D_{yx} & D_{yy} & D_{yz} \\ D_{zx} & D_{zy} & D_{zz} \end{bmatrix} \text{[4]}$$

In this matrix, D_{xx}, D_{yy} and D_{zz} represent the diffusion along the reference axis (x, y and z) while the six off-diagonal elements represent the correlation of random motions between each pair of principal directions. Assuming that

diffusion in the directions x → y and y →x is the same, the mirror elements of the matrix should be identical and therefore only 6 unique elements are needed to fill the matrix. This means that to calculate the tensor, 7 measurements are needed: one baseline value (b0) and 6 data sets oriented in 6 different directions. The technique that has been developed to probe this directionality is named Diffusion Tensor Imaging (DTI) (Moseley *et al.*, 1990; Basser *et al.*, 1994; Le Bihan, 1995; Poupon *et al.*, 2000). DTI can provide information on anisotropic diffusion characterized by eigenvectors (direction – expressed as fractional anisotropy [FA]) and eigenvalues (magnitude – expressed as mean diffusivity [MD]). The fractional anisotropy is of particular interest in brain imaging and is defined according to the following equation:

$$FA = \sqrt{\frac{3}{2}} \cdot \sqrt{\frac{(\lambda_1-\bar{\lambda})^2+(\lambda_2-\bar{\lambda})^2+(\lambda_3-\bar{\lambda})^2}{\lambda_1^2+\lambda_2^2+\lambda_3^2}} \text{ [5]}$$

where λ represent the principal eigenvalues. The mean diffusivity (MD) is derived according to the following equation:

$$MD = \frac{\lambda_1\lambda_2\lambda_3}{3} \text{ [6]}$$

Gliomas tend to spread along white matter tracts, therefore they cause a significant disruption of white matter regions that can be visualized using DTI (Price and Gillard, 2011). The visualisation of these changes can be used to improve surgical planning by giving neurosurgeons a better understanding of tumour location, proliferation and surrounding normal axonal bundles (Price *et al.*, 2004). Lastly, DTI has been demonstrated to predict recurrence in GBM patients thanks to a deeper insight into tumour pattern of infiltration (Price *et al.*, 2007).

2.2.2 Intravoxel incoherent motion diffusion imaging

In the 1980s, Le Bihan introduced the concept that the movement of protons caused by blood flow within capillaries (namely microperfusion) can mimic a random walk (namely pseudo-diffusion) (Le Bihan *et al.*, 1986). This can be observed at low b values and can influence the signal of diffusion weighted imaging (Le Bihan *et al.*, 1986; Higaki *et al.*, 2018; Le Bihan, 2019). Shortly after describing this phenomenon, Le Bihan also introduced a method to assess tissue perfusion and diffusion using specific *b* values, also due to

the fact that the blood microcirculation component decays 10 times faster than the diffusion component (Le Bihan *et al.*, 1986; Le Bihan, 2019). The overall signal intensity from the combination of the tissue diffusion and the blood flow component, is described as:

$$S/S_0 = f_{IVIM} \exp[-b\ (D^* + D_{blood})] + (1 - f_{IVIM}) \exp(-bD_{tissue})\ [7]$$

where f_{IVIM} is the blood flow fraction, D_{blood} is the diffusion coefficient in the blood and D_{tissue} is the diffusion coefficient in the tissue. Performing a diffusion acquisition with multiple *b* values of which at least half are below the IVIM effect threshold (believed to be 250 s/mm²) allows for estimating both the perfusion and diffusion using the equation above. Theoretically, as few as 3 low *b* values are sufficient to derive the IVIM signal (i.e. *b* = 0, 100 and 200 s/mm²), however, the long acquisition time and the subsequent sensibility to motion artifacts jeopardized the adoption of IVIM until echo planar imaging was coupled with echo-planar imaging (Le Bihan *et al.*, 1988; Turner *et al.*, 1990; Yamada *et al.*, 1999).

The capability of informing on perfusion without the need of a gadolinium-based contrast agent and almost with no penalties in terms of acquisition time, sparked significant interest in the potential application of IVIM imaging in neuro-oncology. Over the past few years, several reports demonstrated that IVIM imaging can improve glioma grading providing information on perfusion (assessed at low *b* values) and tissue diffusion (assessed at high *b* values). Bisdas *et al.* for example (Bisdas *et al.*, 2013) observed higher diffusion values in high-grade glioma and increased perfusion fraction in keeping with perfusion studies of gliomas. Those results were also confirmed by other reports (Federau *et al.*, 2014; Shen *et al.*, 2016). Response to therapy has also been evaluated with IVIM diffusion imaging. Gadolinium-based contrast agent enhanced perfusion imaging is routinely used to assess pseudo-progression by the use of cerebral blood volume maps. However, this requires injection of a gadolinium-based contrast agent which is now recognized as potentially harmful due to dose-dependent gadolinium deposition in the brain (Kanda *et al.*, 2014). Moreover, contrast agents are known to leak through the disrupted blood-brain barrier potentially limiting the accuracy of conventional contrast enhanced perfusion techniques.

IVIM diffusion imaging exploits the intrinsic properties of the tissue providing, at the same time, information on perfusion and structural architecture of the tissue. Kim et al. (Kim *et al.*, 2014) demonstrated that the evaluation of the heterogeneity of the IVIM-derived parameters can differentiate between pseudo-progression and true progression with higher accuracy than conventional perfusion imaging. Interestingly, Puig *et al*. (Puig *et al.*, 2016) demonstrated that the perfusion fraction and the pseudo-diffusion component of the contrast enhancing regions of glioblastomas can significantly predict survival at 6-months in newly diagnosed glioblastomas.

2.2.3 Non-Gaussian Diffusion Models

DWI and the derived ADC have been shown to be useful in evaluating the cellularity of gliomas and Diffusion Tensor Imaging (described in paragraph 2.2.1) is a valuable tool to evaluate tumour invasiveness. However, DWI and DTI both approximate the Brownian motion of water using a Gaussian distribution. This model is an over-simplification: the brain is a complex microenvironment structurally, in which movements are restricted by the parenchymal architecture which is highly heterogeneous. The non-Gaussian diffusion effects are particular evident at high *b* values (Iima and Le Bihan, 2016) where the ADC simplified model reaches its limits. To overcome these limitations, over the last two decades several models have been proposed.

The first model proposed to handle the non-Gaussian behaviour of the diffusion signal was the bi-exponential model (Niendorf *et al.*, 1996). However, this model is simplistic and assumes that the signal was due to two different pools of water molecules which demonstrate Gaussian diffusion. Despite the simplistic nature of this model, the idea of employing non-monoexponential models to analyse diffusion data to fully harness the potentiality of the technique lead to the development of several models based on the non-Gaussian distribution of water movement (Mulkern *et al.*, 2009). One of the most popular model is Diffusional Kurtosis Imaging (DKI) (Jensen and Helpern, 2003, 2010; Jensen *et al.*, 2005; Rosenkrantz *et al.*, 2015)

Originally introduced by Jensen and Helpern in 2003 (Jensen and Helpern, 2003), this technique was proposed to estimate the excess of kurtosis of water diffusion using pulsed-field gradient sequences and *b* values up to 2000 s/mm^2. Subsequent formulation of the technique was based on the following equation:

$$\ln [S(b)] = \ln[S(0)] - bD_{app} + \frac{1}{6}b^2 D_{app}^2 K_{app} + O(b^3) \text{ [8]}$$

where S(b) is the signal intensity at a given echo time, D_{app} is the apparent diffusion coefficient in the direction parallel to the diffusion sensitizing gradients, and K_{app} is the apparent diffusional kurtosis in the same direction (Jensen *et al.*, 2005). The parameter *b* is function of the gradient strength (defined as *g*) and the time parameters δ and Δ according to the following equation:

$$b = (\gamma \delta g)^2 \, (\Delta - \frac{\delta}{3}) \text{ [9]}$$

Equation 7 defines diffusional kurtosis as dependent on the direction of the diffusion sensitizing gradients. As the directional dependence of the conventional diffusion coefficient is described by a diffusion tensor with 6 components (see equation 4, paragraph 2.2.1), the directional dependence of the diffusional kurtosis can be defined by a diffusional kurtosis tensor with 15 components according to the following equation:

$$W_{ijkl}(t) = 9 \frac{\langle s_i s_j s_k s_l \rangle - \langle s_i s_j \rangle \langle s_k s_l \rangle - \langle s_i s_k \rangle \langle s_j s_l \rangle - \langle s_i s_l \rangle \langle s_j s_k \rangle}{\langle s \cdot s \rangle^2} \text{ [10]}$$

where s_i is a component of the displacement vector s.

DKI could be a more accurate tool to assess water diffusion *in vivo* enabling a better evaluation of structural architecture and heterogeneity. In comparison with conventional DWI, DKI has shown improved performance for discriminating between high-grade and low-grade gliomas, hence being a potential non-invasive biomarker in the grading of gliomas (Raab *et al.*, 2010; Van Cauter *et al.*, 2012, 2014). In 2010 Raab *et al.* demonstrated that DKI could have a role in glioma grading (Raab *et al.*, 2010). They used a diffusion sequence with six non-zero *b* values and calculated the mean kurtosis (MK) as the average of the apparent kurtosis coefficient over all the directions they acquired. In the 34 patients which completed the study, MK was significantly different between lower grade and higher-grade gliomas. Van Cauter *et al.*

used a different acquisition technique based on 3 non-zero *b* values from which they derived axial, radial and mean kurtosis (Van Cauter *et al.*, 2012, 2014). They confirmed the findings of Raab and proposed a decision path based on mean kurtosis which used the most significant values derived from diffusion kurtosis. Although those studies successfully highlighted the utility of diffusion kurtosis in glioma imaging, more refined methods to estimate the diffusion kurtosis tensor that were proposed by Tabesh *et al.* in 2011 have not yet been applied to gliomas (Tabesh *et al.*, 2011); this model should increase the robustness of diffusion kurtosis reducing noise, motion and imaging artifacts. Moreover, this approach allows the estimation of more parameters derived from the kurtosis tensor including fractional anisotropy of diffusion kurtosis. Tabesh *et al.* derived a tensor equation to estimate the mean kurtosis moving away from the directional averaging used in the previously published papers.

2.2.3.1 Vascular, extracellular and restricted diffusion for cytometry in tumours

The different approaches to diffusion imaging described above are mostly based on different ways of modelling the diffusion signal without any assumption related to the biological properties of the tissue that determine that signal. To explore tissue architecture and functioning, biophysical modelling is necessary (Novikov *et al.*, 2018). Several methods have been proposed to disentangle the effect of the different structures contained in each voxel in order to harness the full potential of diffusion MRI (Panagiotaki *et al.*, 2012). Some of those models were built on the geometry and architecture of the structures contained within the target tissue, other models are built around the different tissue compartments and the exchange of molecules between them. The Neurite Orientation Dispersion and Density Imaging is an example of a model based on the geometric characteristics of the target tissue (Zhang *et al.*, 2012). In this model, Zhang et al adapted the previously proposed orientation-dispersed cylinder model (Zhang *et al.*, 2011) to estimate neurite density and orientation dispersion.

A more recent and potentially relevant model for assessing brain tumours is the Vascular, Extracellular and Restricted Diffusion for Cytometry in Tumours (VERDICT). This novel advanced model-based diffusion-weighted

MRI technique can quantify microstructural features of tumours *in vivo*. As previously mentioned, ADC is the most commonly used metric to summarize the water mobility under the assumption that low ADC values correspond to increased cellularity. However, ADC is a composite biomarker that conflates several biological parameters in a single metric. Cell density, size, shape, permeability, subcellular architecture and perfusion all influence the ADC measurement making them difficult to separate (Panagiotaki *et al.*, 2014). Biophysical models such as VERDICT can estimate the effects of specific histologic features through the implementation of complex algorithms, and could potentially disentangle the effects of the different components and provide more accurate metrics.

VERDICT MRI has been developed for prostate cancer, with the objective of providing information on the size of the cancer cells, the vascular compartment, the extracellular and the intracellular volume (Panagiotaki *et al.*, 2014). The model was proposed by Panagiotaki *et al.* in 2014 as a way to obtain as assessment of the microstructure of the whole-tumour as opposed to conventional histology that is limited in sample number and, therefore, limited in assessing the structural heterogeneity of cancer. Technically, the model is actually the sum of three models characterising diffusion in the intracellular compartment (S_1), extracellular compartment (S_2), and arising from the microcirculation (S_3). The overall model does not account for any potential exchange between the three compartment and is represented by the following equation:

$$S = \sum_{i=1}^{3} f_i S_i \quad [11]$$

where f_i is the signal at b = 0 from water molecules in population i, $0 \leq f_i \leq 1$, $\sum_{i=1}^{3} f_i = 1$. Over the past few years, this technique has been successfully translated into human and applied to patients with prostate cancer with brilliant results in terms of differentiating tumour from benign areas and assessing therapy response to cytotoxic drugs (Panagiotaki *et al.*, 2015; Bonet-Carne *et al.*, 2018).

Previous data obtained with conventional ADC and IVIM imaging proveides some evidence that grade correlates with extracellular space volume and cell density (Vargová *et al.*, 2003; Bisdas *et al.*, 2013). Moreover,

as mentioned in paragraph 2.2.1, tissue perfusion measured with IVIM imaging was shown to be significantly different between glioma grade (Bisdas *et al.*, 2013), in line with a significant body of literature based on perfusion MRI. The capability of VERDICT MRI to probe intracellular, extracellular and vascular compartments in prostatic cancer suggests that this technique could also be used in glioma. Our group has recently translated this technique to brain imaging, albeit with some modifications as detailed in chapter 3, and published the first proof-of-concept study on the use of VERDICT in patients with glioma. The results of that study are presenting in this thesis, chapter 3.

2.3 Sodium MRI

An increase in cell metabolic activity is also associated with changes in Na^+/K^+-ATPase activity. In particular, when the consumption of ATP for proliferation is higher, the function of the sodium pump may be reduced and, as a consequence of this, changes in the extracellular and intracellular concentration of these ions will be affected (Madelin and Regatte, 2013). Malignant tumours show an increase in intracellular sodium concentration that if detectable and could be used to distinguish low-grade and high-grade gliomas (Ouwerkerk *et al.*, 2003). Gliomas are characterized by angiogenesis and cell proliferation as well as increased lactate formation; these factors, in addition to the changes in Na^+/K^+ transport, produce an acidic extracellular environment. Therefore, Sodium MRI (^{23}Na MRI) could also be a surrogate for non-invasive assessment of pH.

Sodium is a quadrupolar nucleus with spin 3/2 that yields the second strongest nuclear magnetic resonance signal from biological tissues, after protons (Madelin and Regatte, 2013). Although natural abundance sodium is detectable with ^{23}Na-MRI, the sensitivity for sodium is 9.2% of the proton sensitivity and therefore sodium MRI (^{23}Na-MRI) has an average signal-to-noise ratio (SNR) which is up to 20,000 times lower than that for protons. However, with the advent of high-field scanners, improved radiofrequency coils, as well as optimized sequences, ^{23}Na-MRI is now feasible with a temporal and spatial resolution that is clinically useful (Konstandin and Nagel, 2014). Several ^{23}Na-MRI studies have already been performed in the brain to

evaluate its possible use for assessing tumours or neurodegenerative diseases both qualitatively and quantitatively (Ouwerkerk *et al.*, 2003; Mellon *et al.*, 2009; Thulborn *et al.*, 2009; Inglese *et al.*, 2010, 2013; Nagel *et al.*, 2011; Reetz *et al.*, 2012; Zaaraoui *et al.*, 2012; Yushmanov *et al.*, 2013; Haneder *et al.*, 2015). MRI is able to detect and quantify both intracellular and extracellular sodium, thus providing a powerful tool to assess tumour metabolism and homeostasis (Ouwerkerk *et al.*, 2003; Thulborn *et al.*, 2009; Zaaraoui *et al.*, 2012).

Historically, brain tumours have been of primary interest as a potential application for sodium imaging. In the paper that established this field, Maudsley postulated why sodium MRI could detect the different components within gliomas but was able only to show images of an animal model of stroke (Maudsley and Hilal, 1984). The interest in glioma imaging was revamped in the nineties by Schuierer *et al.* and Thulborn *et al.* (Schuierer *et al.*, 1991; Thulborn *et al.*, 1999). Despite the growing interest and the potential utility of sodium MRI in primary brain tumours, at present less than 15 studies have evaluated this technique in patients with gliomas. This may in part be attributed to the technical challenges both in terms of acquisition and post-processing.

Sodium Imaging has been performed on patients with gliomas using a resolution of up to 4 mm^3 isotropic at both 1.5 T (Ouwerkerk *et al.*, 2003) and 3 T (Haneder *et al.*, 2015), 5.5 mm^3 isotropic at 7 T (Nagel *et al.*, 2011) and 3 mm^3 isotropic at 9.4 T (Mirkes *et al.*, 2014). We have developed within the group some high-resolution sequences with a nominal resolution of 2 x 2 x 4 mm^3 and 3 mm^3 isotropic which are feasible on a clinical 3 T scanner in approximately 10 minutes. The higher resolution we have achieved allows a more accurate localization of areas expressing alteration in sodium concentration. Moreover, we may have a more accurate sodium map that may improve biopsy accuracy, therapeutic planning and may assist with better tumour stratification. Ouwerkerk *et al.* in 2003 demonstrated that sodium concentration could differentiate normal parenchyma from malignant tissue; however, their study was a proof–of-concept study and did not correlate sodium concentration with different pathological subtypes (Ouwerkerk *et al.*, 2003). Acquiring sodium-targeted biopsies would allow a deeper

understanding of tumour heterogeneity with the possibility to correlate an increase in sodium concentration with other biomarkers such as IDH1 or ATRX.

2.4 Hyperpolarized ^{13}C MRSI

Tumours metabolise glucose very differently from normal tissue, generating lactate even in the presence of oxygen, a process known as the Warburg effect (Warburg, 1956). Other metabolic pathways, such as amino acid utilisation and fatty acid synthesis, are also reprogrammed in tumours compared to normal tissue (Yoshimoto *et al.*, 2001; Kuhajda, 2006; Menendez and Lupu, 2007). A number of non-invasive imaging methods have been used to probe these alterations in cancer metabolism. A novel technique for studying this metabolism is currently under development and has been termed hyperpolarized carbon-13 Magnetic Resonance Spectroscopic Imaging (MRSI) (Weissleder and Mahmood, 2001).

Positron Emission Tomography (PET) is an extremely sensitive technique for studying molecular processes without disrupting normal physiology, with tracer detection in the nano- to picomolar range (Culver *et al.*, 2008; Kurhanewicz *et al.*, 2011). PET imaging in conjunction with [^{18}F]2-fluoro-2-deoxy-D-glucose (^{18}F-FDG), is an established clinical tool to probe altered glucose metabolism in cancer patients (Czernin *et al.*, 2013). Whole body ^{18}F-FDG PET is superior to standard Computed Tomography for the assessment of tumour stage in many malignancies (Hicks, 2012), however it is limited by a relatively low clinical spatial resolution (of the order of 5 mm), poor soft tissue contrast, exposure of patients to ionizing radiation and the inability to discriminate between different metabolites or the compartment from which the signal arises e.g. extracellular vs intracellular (Gallagher *et al.*, 2011b; Ehman *et al.*, 2017).

Magnetic Resonance Spectroscopy (MRS) may also play a useful role in probing cancer metabolism by detecting the resonant frequencies of nuclei within distinct molecules (such as that of hydrogen, ^{1}H, or protons), therefore it can be used to non-invasively discriminate between metabolites (Kwock *et al.*, 2006; García-Figueiras *et al.*, 2016). However, in comparison to PET, MRI

is a very insensitive technique utilising only a small number of the available nuclei to generate an image or spectrum. At clinical field strengths, only a few of the available hydrogen nuclei in every million are used to generate these images (Kurhanewicz and Vigneron, 2008; Van Der Graaf, 2010). This low sensitivity is due to the low polarisation of the nuclei at thermal equilibrium and consequently, only molecules at relatively high concentration can be probed with MRS. Despite the great potential of MRS as a tool to study biochemistry *in vivo*, it is not used routinely in the clinic due to both the low spatial and molecular sensitivity of the technique, and difficulty in subsequent data interpretation (Kwock *et al.*, 2006; Gallagher *et al.*, 2011b).

Dynamic Nuclear Polarisation (DNP) is a technique based in solid state physics which greatly increases the signal-to-noise ratio (SNR) achieved on MR by significantly increasing the polarisation of nuclear spins and therefore enabling a much larger proportion of them to be utilised for imaging (Overhauser, 1953). In 2003 DNP was combined with an efficient method to transfer the substrate from the solid (~1 K) to liquid (~300 K) state, a process which is now known as 'Dissolution DNP'. This technique opened up new possibilities for the method to be translated into biological systems such as cell studies and *in vivo* animal imaging (Ardenkjaer-Larsen *et al.*, 2003). The technique, termed Hyperpolarized Carbon-13 Magnetic Resonance Spectroscopic Imaging (HP ^{13}C-MRSI), has now been translated into humans (Nelson *et al.*, 2013). This paragraph provides a brief overview of the technique, its applications in pre-clinical imaging, an outline of the current human trials that are ongoing as well as future potential applications.

2.4.1 The benefits of metabolic imaging with MRI

An alternative approach to the steady state measurement of tissue metabolites, is to probe dynamic changes in metabolites during enzymatic reactions, which can be assessed through the exogenous administration of labelled metabolites. A physiologically-active substrate labelled with a nucleus that can be detected with MRI, allows spectral discrimination between the substrate and its subsequent downstream metabolic products; when applied to imaging it allows the spatial distribution of both the substrate and the

product to be detected. However, MRS requires long acquisition times which in turn makes it difficult to discriminate rapid changes in real-time metabolism *in vivo*. ^{13}C is ideal for labelling endogenous metabolic molecules which are mostly carbon based, as its low natural abundance (1.1%) results in a low level of background noise. ^{13}C-MRS acquisition from either a single voxel or a small number of voxels has been used to successfully analyse many

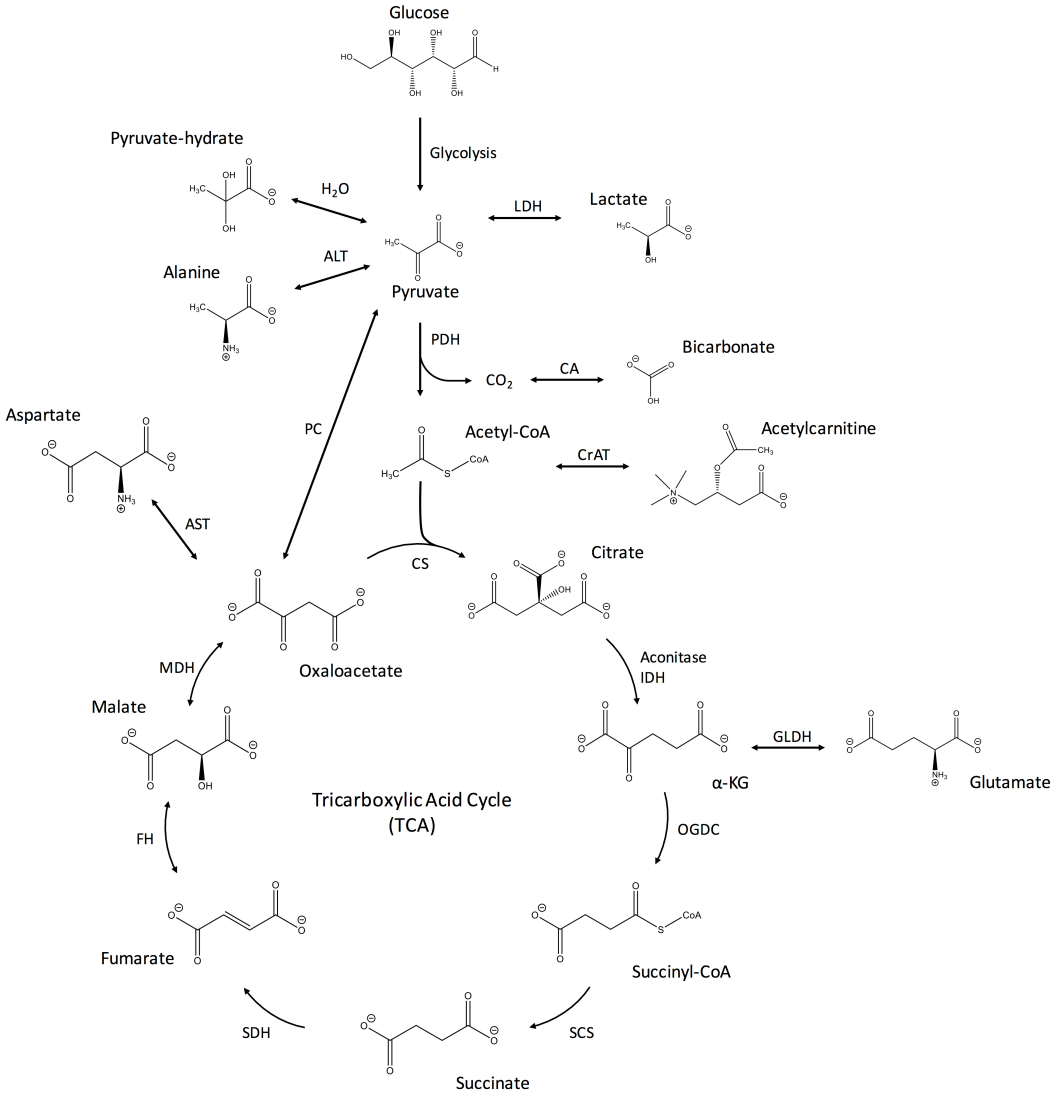

Figure 2.2: Diagram showing the metabolic fate of glucose and pyruvate.
Abbreviations: LDH - lactate dehydrogenase, ALT - alanine transaminase, PDH - pyruvate dehydrogenase, CA - carbonic anhydrase, PC - pyruvate carboxylase, CAT - carnitine acyltransferase, CS - citrate synthase, IDH - isocitrate dehydrogenase, GLDH - glutamate dehydrogenase, OGDC – oxoglutarate (α-ketoglutarate) dehydrogenase complex, SCS - succinyl coenzyme A synthetase, SDH – succinate dehydrogenase (part of succinate-coenzyme Q reductase), FH - fumarate hydratase, MDH - malate dehydrogenase, AST - aspartate transaminase.

physiological processes in organs such as in the brain, as well as pathological processes including cancer (Neeman *et al.*, 1990; Morris and Bachelard, 2003; Abrantes *et al.*, 2014). Although ^{13}C-MRS has been used to detect early changes in cancer metabolism as a biomarker for response to treatment (Neeman *et al.*, 1990), its utility is limited by very low SNR as well as poor temporal and spatial resolution. Therefore the increase in SNR afforded by DNP has opened up the possibility of applying ^{13}C-MRS in new ways, allowing for rapid acquisition of imaging to probe real-time metabolism (Ardenkjaer-Larsen *et al.*, 2003; Hurd *et al.*, 2012).

There are several methods that have been described for increasing nuclear polarisation and generically they are termed hyperpolarisation techniques; for example, there are a number of approaches for the hyperpolarisation of gases used in ventilation imaging (Couch *et al.*, 2015; Kruger *et al.*, 2016; Ebner *et al.*, 2017). DNP was first postulated as a hyperpolarisation method by Overhauser in 1953 (Overhauser, 1953), and has now been applied to ^{13}C-labelled physiologically substrates which are rapidly transported and metabolised by the cells. To facilitate the process, labelled molecules are mixed with a free-radical containing agent, frozen in a glass state, and then cooled to approximately 1 Kelvin in a magnetic field e.g. 3.35 T or 5 T. At these extreme physical conditions, the electron pool in the free radical becomes fully polarised and the transfer of polarisation from the electron pool to the nuclear pool is facilitated by microwave irradiation. Increasing the polarisation to levels required for *in vivo* imaging takes approximately two hours and following this the sample is removed from the field and quickly dissolved with superheated water (Ardenkjaer-Larsen *et al.*, 2011; Jähnig *et al.*, 2016). This hyperpolarized sample has an increase in signal of 10,000 to 100,000-fold and can be used to probe the real-time dynamics of enzymatic activity *in vitro* in cell culture or *in vivo* in animal models, using rapid spectroscopy or imaging (Day *et al.*, 2007; Merritt *et al.*, 2007; Lerche *et al.*, 2010; Nielsen *et al.*, 2017). The term spectroscopic imaging is used where spectra are acquired from multiple voxels to generate an image of the metabolic distribution across the tissue.

One of the challenges of the technique is that the signal from the hyperpolarized carbon is very transient and decays with a half-life that is

commonly 20-30 s *in vivo*; therefore perfusion, transport and metabolism must occur during approximately 5 half-lives or 2-3 mins. This limits the number of *in vivo* molecules and reactions that can be probed with the technique and necessitates very rapid and efficient imaging strategies.

2.4.1.1 Preclinical imaging

To date, [1-^{13}C]pyruvate has been the most widely used metabolite for hyperpolarized ^{13}C MRSI, due to its relatively long polarisation half-life (the time it takes for a compound to lose half of its initial hyperpolarized signal), rapid distribution and uptake, and the central role it plays in many metabolic pathways (figure 2.1) (Brindle *et al.*, 2011; Lumata *et al.*, 2015). Pyruvate is at an important metabolic crossroad between the formation of lactate on one hand, and entry into the tricarboxylic acid cycle (TCA) with the formation of carbon dioxide on the other.

In cancer, the ^{13}C label on [1-^{13}C]pyruvate is predominantly exchanged to [1-^{13}C]lactate via the enzyme lactate dehydrogenase (LDH) but some will also be exchanged to [1-^{13}C]alanine via alanine aminotransferase (ALT), or irreversibly converted to $^{13}CO_2$ via pyruvate dehydrogenase (PDH) (Merritt *et al.*, 2007). The production of lactate in tumour tissue, even in the presence of oxygen, is termed the 'Warburg effect' and has been observed using HP ^{13}C-MRSI in a variety of preclinical cancer models. There is evidence that the labelling of lactate correlates with tumour grade, with higher lactate labelling present in more aggressive tumours (Warburg, 1956; Albers *et al.*, 2008). HP ^{13}C-MRSI has also been used to demonstrate a consistent decrease in the ^{13}C exchange between [1-^{13}C]pyruvate and [1-^{13}C]lactate during tumour responses, regardless of treatment type in various *in vitro* and *in vivo* models, with changes seen as early as 24 hours after the initiation of therapy, and sometimes earlier than conventional imaging modalities such as diffusion-weighted imaging (Day *et al.*, 2007, 2011; Witney *et al.*, 2009, 2010; Ward *et al.*, 2010; Bohndiek *et al.*, 2012). HP ^{13}C-MRSI may also have a role in the early detection of preneoplastic changes, as demonstrated in a pancreatic model evaluating LDH activity with increased HP ^{13}C label exchange between ^{13}C-pyruvate and endogenous lactate present with the onset of neoplastic transformation (Serrao *et al.*, 2016).

2.4.2 Translation into human imaging

The first human study using HP ^{13}C-MRSI was completed in 2013 at the University of California San Francisco (UCSF) (Nelson *et al.*, 2013). This study demonstrated the safety and feasibility of HP ^{13}C-MRSI with [1-^{13}C]pyruvate in thirty one male subjects with biopsy-proven prostate cancer. Patients were injected with hyperpolarized ^{13}C-pyruvate. Signals from pyruvate and lactate were observed in the vasculature, tumour and normal prostate at the 3 dose levels considered (0.14, 0.28 and 0.43 mL/kg actual body weight of 230 mM pyruvate solution) and uptake in the prostate was observed approximately 20 seconds after injection.

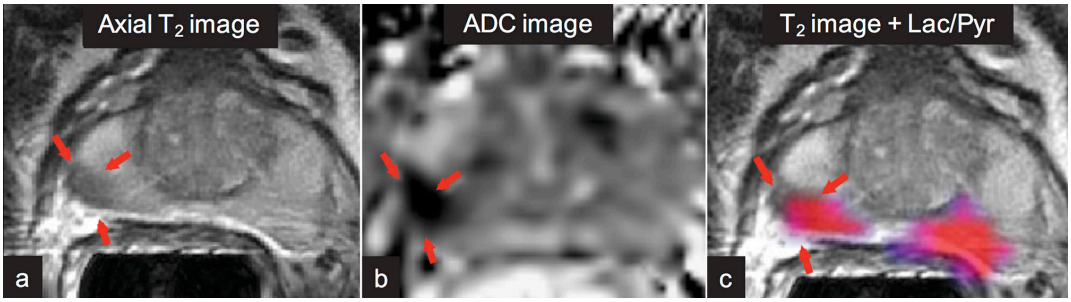

Figure 2.3: Hyperpolarized pyruvate metabolism in human prostate cancer.
Images from a patient with bilateral biopsy-proven Gleason grade 3+3 prostate cancer. (a) Axial T_2 weighted image and (b) apparent diffusion coefficient map showing a peripheral zone tumour (red arrows). (c) False colour metabolic map superimposed over the the proton image showing voxels with an elevated ratio of hyperpolarized [1-^{13}C]lactate/[1-^{13}C]pyruvate bilaterally in the prostate and highlighted in pink, obtained after administration of hyperpolarized [1-^{13}C]pyruvate. Adapted from Nelson et al 2013.

A few mild adverse events such as dysgeusia (5/31 patients) were reported but none of them were considered to be dose-limiting toxicities. Two single events of dizziness and grade 2 diarrhoea reported in the phase 2 component, were attributed to concomitant medications. The highest dose tested, 0.43 mL/kg of ^{13}C-pyruvate solution, showed the highest SNR for ^{13}C-pyruvate as expected. The study also demonstrated an elevated ^{13}C-lactate/^{13}C-pyruvate ratio on HP ^{13}C-MRSI in one patient where no abnormality was detectable on conventional ^{1}H-MRI; this patient was subsequently shown to have a biopsy-proven low-grade tumour (figure 2.2). The study concluded that the data confirmed both the safety of the agent and

that an elevated ^{13}C-lactate/^{13}C-pyruvate may be seen in regions that were otherwise undetectable with standard methods, opening up the possibility of using metabolic imaging to detect occult tumours.

This initial study required a sterile room for the production and hyperpolarisation of the ^{13}C pyruvate prior to dissolution and injection. Wider

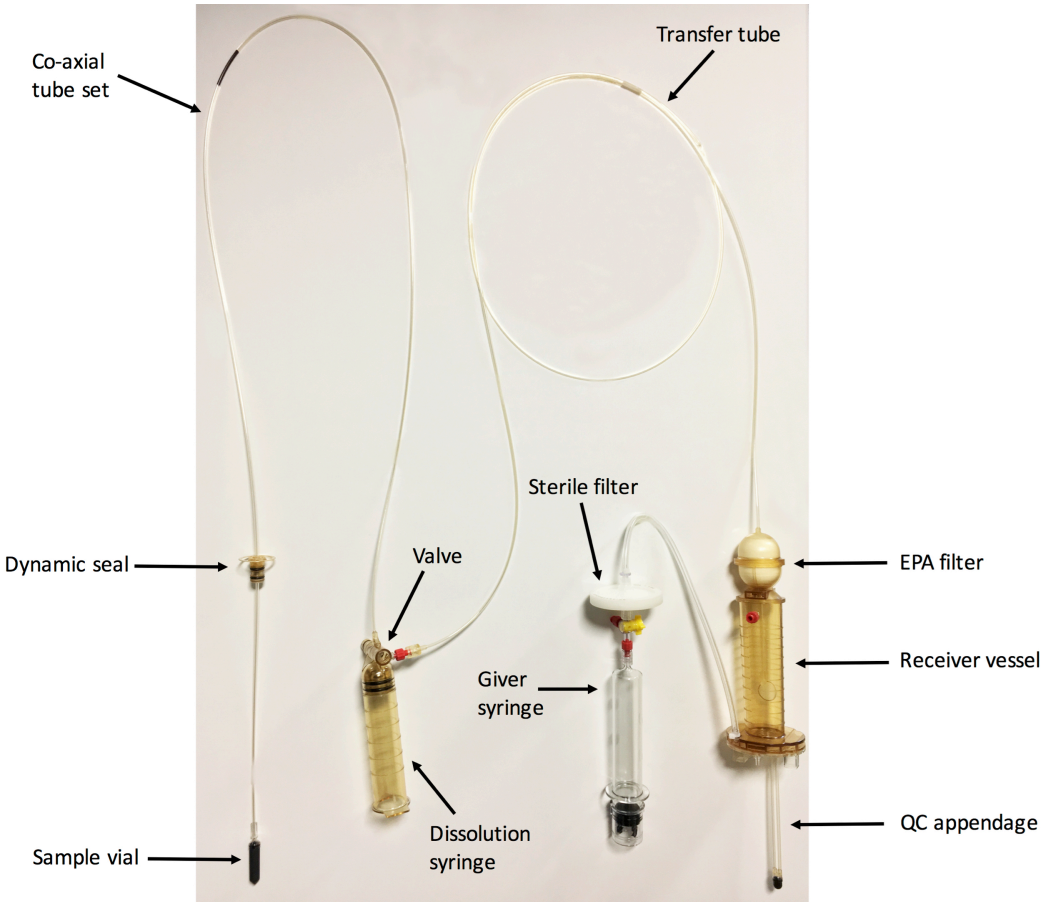

Figure 2.4: Pharmacy kit for clinical polarisation.
The kit contains pyruvate sealed within a closed sterile environment. The kit includes: a sample vial, the concentric tube assembly, the multi-position inlet/outlet valve, a syringe for dissolution medium, a filter and a receiver unit.

application of the technology was made possible by the design of a new platform which utilises an integral, disposable and sterile fluid path or pharmacy kit (figure 2.3) (Ardenkjaer-Larsen *et al.*, 2011). The SPINlab hyperpolarizer, produced by GE Healthcare, uses a closed-cycle cryogenic system and has multi-sample capability (figure 2.4). The pharmacy kit is prefilled and sealed in a sterile environment, before being transferred to the clinical hyperpolarizer, thus enabling the hyperpolarisation of a pyruvate sample within a routine clinical environment such as a radiology department,

whilst maintaining the sample sterility. Filled pharmacy kits can either be used on the day of production or stored frozen depending on the method that is used.

2.4.3 Clinical imaging studies

There are currently six sites that have undertaken clinical imaging with the technique, although several other facilities will commence human imaging

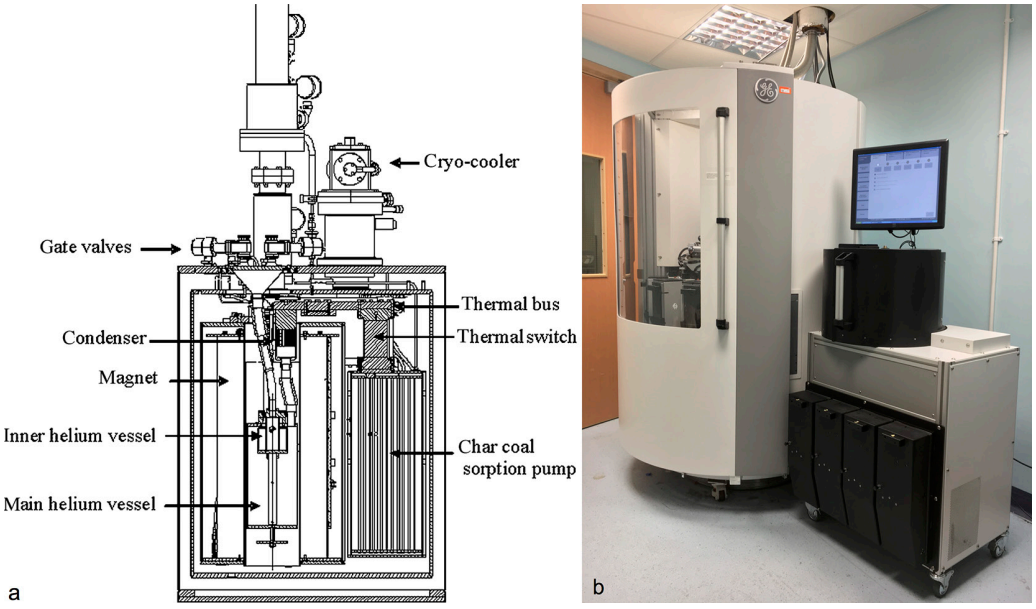

Figure 2.5: Schematic of cryostat, magnet and sorption pump; GE SPINlab Diamond Polariser.

(a) Schematic of cryostat, magnet and sorption pump. The 3.35 T magnet is located within a helium-filled cryostat and suspended within an external vacuum vessel. Reproduced from Ardenkjaer-Larsen et al[37] with permission. (b) Photograph of the SPINlab Diamond Polariser for clinical use in Cambridge (GE Healthcare). This clinical SPINlab uses a 5T magnet.

in the near future. Current studies in human HP ^{13}C-MRSI research are exploring pyruvate metabolism in a number of organs such as the brain, heart, liver and breast and in a variety of disease processes. Several of these studies are evaluating HP ^{13}C-MRSI derived biomarkers in addition to tissue samples in order to understand and validate the biophysical nature of signal generation with HP ^{13}C-MRSI. Another important aim is to establish the reproducibility and repeatability of the technique.

A significant objective of the current clinical studies is to investigate HP ^{13}C-MRSI as an imaging biomarker of early treatment response. Many of these studies are being run in parallel with other conventional imaging tests for measuring treatment response, as well as functional MR imaging techniques, such as dynamic contrast-enhanced (DCE) MRI. Changes in tumour metabolism in response to therapy have been shown to occur before anatomical changes can be detected and potentially could be earlier than functional imaging alterations. The use of the technique as a response biomarker has been demonstrated in several animal studies and is now being translated into humans (Day *et al.*, 2007, 2011; Witney *et al.*, 2009; Aggarwal *et al.*, 2017). An exciting area for future research is how changes in metabolism measured by HP ^{13}C-MRSI following treatment relate to circulating tumour biomarkers such as cell-free DNA (Dawson *et al.*, 2013; Bettegowda *et al.*, 2014), as this would increase the ability to non-invasively interrogate tumour activity and responses to therapies, and spare patients the complications associated with serial biopsies. Potentially, HP ^{13}C-MRSI may provide a specific pharmacodynamic downstream imaging biomarker of both conventional and novel agents, and could also be used to detect early changes following therapy which are predictive of long-term response. This could therefore provide a novel non-invasive precision medicine approach to drug development, permitting early cessation of ineffective drugs and providing a cost saving in terms of patient time and toxicities.

References

Abrantes AM, Tavares LC, Pires S, Casalta-Lopes J, Mendes C, Simões M, et al. Metabolic effects of hypoxia in colorectal cancer by ^{13}C NMR isotopomer analysis. Biomed Res Int 2014; 2014: 759791.

Aggarwal R, Vigneron DB, Kurhanewicz J. Hyperpolarized 1-[^{13}C]-Pyruvate Magnetic Resonance Imaging Detects an Early Metabolic Response to Androgen Ablation Therapy in Prostate Cancer. Eur Urol 2017; 72: 1028–1029.

Albers MJ, Bok R, Chen AP, Cunningham CH, Zierhut ML, Zhang VY, et al. Hyperpolarized ^{13}C lactate, pyruvate, and alanine: noninvasive biomarkers for prostate cancer detection and grading. Cancer Res 2008; 68: 8607–8615.

Ardenkjaer-Larsen JH, Fridlund B, Gram A, Hansson G, Hansson L, Lerche MH, et al. Increase in signal-to-noise ratio of > 10,000 times in liquid-state NMR. Proc Natl Acad Sci U S A 2003; 100: 10158–63.

Ardenkjaer-Larsen JH, Leach AM, Clarke N, Urbahn J, Anderson D, Skloss TW. Dynamic nuclear polarization polarizer for sterile use intent. NMR Biomed 2011; 24: 927–932.

Barajas RF, Hess CP, Phillips JJ, Von Morze CJ, Yu JP, Chang SM, et al. Super-resolution track density imaging of glioblastoma: Histopathologic correlation. Am J Neuroradiol 2013; 34: 1319–1325.

Basser P, Mattiello J, LeBihan D. Estimation of the effective self-diffusion tensor from the NRM spin echo. J Magn Reson 1994; 103: 247–254.

Bettegowda C, Sausen M, Leary RJ, Kinde I, Wang Y, Agrawal N, et al. Detection of circulating tumor DNA in early- and late-stage human malignancies. Sci Transl Med 2014; 6: 224ra24.

Le Bihan D. Molecular diffusion, tissue microdynamics and microstructure. NMR Biomed 1995; 8: 375–386.

Le Bihan D. What can we see with IVIM MRI? Neuroimage 2019; 187: 56–67.

Le Bihan D, Breton E, Lallemand D, Aubin M, Vignaug J, Laval-Jeantet M. Separation of diffusion and perfusion in intravoxel incoherent motion MR Imaging. Radiology 1988; 168: 497–505.

Le Bihan D, Breton E, Lallemand D, Grenier P, Cabanis E, Laval-Jeantet M. MR imaging of intravoxel incoherent motions: application to diffusion and perfusion in neurologic disorders. Radiology 1986; 161: 401–407.

Bisdas S, Koh TS, Roder C, Braun C, Schittenhelm J, Ernemann U, et al. Intravoxel incoherent motion diffusion-weighted MR imaging of gliomas: Feasibility of the method and initial results. Neuroradiology 2013; 55: 1189–1196.

Bohndiek SE, Kettunen MI, Hu DE, Brindle KM. Hyperpolarized ^{13}C spectroscopy detects early changes in tumor vasculature and metabolism after VEGF neutralization. Cancer Res 2012; 72: 854–864.

Bonet-Carne E, Johnston E, Daducci A, Jacobs JG, Freeman A, Atkinson D, et al. VERDICT-

AMICO: Ultrafast fitting algorithm for non-invasive prostate microstructure characterization. NMR Biomed 2018: 1–15.

Brindle KM, Bohndiek SE, Gallagher FA, Kettunen MI. Tumor imaging using hyperpolarized ^{13}C magnetic resonance spectroscopy. Magn Reson Med 2011; 66: 505–519.

Brindle KM, Izquierdo-García JL, Lewis DY, Mair RJ, Wright AJ. Brain Tumor Imaging. J Nucl Med 2017; 35: 2432–2438.

Bulakbasi N, Guvenc I, Onguru O, Erdogan E, Tayfun C, Ucoz T. The added value of the apparent diffusion coefficient calculation to magnetic resonance imaging in the differentiation and grading of malignant brain tumors. J Comput Assist Tomogr 2004; 28: 735–46.

Van Cauter S, De Keyzer F, Sima DM, Sava AC, D'Arco F, Veraart J, et al. Integrating diffusion kurtosis imaging, dynamic susceptibility-weighted contrast-enhanced MRI, and short echo time chemical shift imaging for grading gliomas. Neuro Oncol 2014; 16: 1010–1021.

Van Cauter S, Veraart J, Sijbers J, Peeters RR, Himmelreich U, De Keyzer F, et al. Gliomas: Diffusion Kurtosis MR Imaging in Grading. Radiology 2012; 263: 492–501.

Cha S. Update on brain tumor imaging: from anatomy to physiology. Am J Neuroradiol 2006; 27: 475–487.

Chen L, Liu M, Bao J, Xia Y, Zhang J, Zhang L, et al. The correlation between apparent diffusion coefficient and tumor cellularity in patients: A meta-analysis. PLoS One 2013; 8

Constantine G, Shan K, Flamm SD, Sivananthan MU. Role of MRI in clinical cardiology. Lancet 2004; 363: 2162–2171.

Couch MJ, Blasiak B, Tomanek B, Ouriadov A V., Fox MS, Dowhos KM, et al. Hyperpolarized and Inert Gas MRI: The Future. Mol Imaging Biol 2015; 17: 149–162.

Culver J, Akers W, Achilefu S. Multimodality molecular imaging with combined optical and SPECT/PET modalities. J Nucl Med 2008; 49: 169–172.

Czernin J, Allen-Auerbach M, Nathanson D, Herrmann K. PET/CT in Oncology: Current Status and Perspectives. Curr Radiol Rep 2013; 1: 177–190.

Dawson S-J, Tsui DWY, Murtaza M, Biggs H, Rueda OM, Chin S-F, et al. Analysis of circulating tumor DNA to monitor metastatic breast cancer. N Engl J Med 2013; 368: 1199–209.

Day SE, Kettunen MI, Cherukuri MK, Mitchell JB, Lizak MJ, Morris HD, et al. Detecting response of rat C6 glioma tumors to radiotherapy using hyperpolarized [1-^{13}C]pyruvate and ^{13}C magnetic resonance spectroscopic imaging. Magn Reson Med 2011; 65: 557–563.

Day SE, Kettunen MI, Gallagher FA, Hu D-E, Lerche M, Wolber J, et al. Detecting tumor response to treatment using hyperpolarized ^{13}C magnetic resonance imaging and spectroscopy. Nat Med 2007; 13: 1382–1387.

Ebner L, Kammerman J, Driehuys B, Schiebler ML, Cadman R V., Fain SB. The role of hyperpolarized 129xenon in MR imaging of pulmonary function. Eur J Radiol 2017; 86: 343–352.

Ehman EC, Johnson GB, Villanueva-Meyer JE, Cha S, Leynes AP, Larson PEZ, et al. PET/MRI: Where might it replace PET/CT? J Magn Reson Imaging 2017: 1–16.

Elhawary H, Liu H, Patel P, Norton I, Rigolo L, Papademetris X, et al. Intraoperative real-time querying of white matter tracts during frameless stereotactic neuronavigation. Neurosurgery 2011; 68: 506–16; discussion 516.

Federau C, Meuli R, O'Brien K, Maeder P, P. H. Perfusion measurement in brain gliomas with intravoxel incoherent motion MRI. Am J Neuroradiol 2014; 35: 256–262.

Gallagher F a., Kettunen MI, Brindle KM. Imaging pH with hyperpolarized ^{13}C. NMR Biomed 2011; 24: 1006–1015.

Gallagher FA, Bohndiek SE, Kettunen MI, Lewis DY, Soloviev D, Brindle KM. Hyperpolarized ^{13}C MRI and PET: In Vivo Tumor Biochemistry. J Nucl Med 2011; 52: 1333–1336.

Gallagher FA, Kettunen MI, Day SE, Hu D-E, Ardenkjaer-Larsen JH, Zandt R in 'T, et al. Magnetic resonance imaging of pH in vivo using hyperpolarized ^{13}C-labelled bicarbonate. Nature 2008; 453: 940–943.

García-Figueiras R, Baleato-González S, Padhani AR, Oleaga L, Vilanova JC, Luna A, et al. Proton magnetic resonance spectroscopy in oncology: The fingerprints of cancer? Diagnostic Interv Radiol 2016; 22: 75–89.

Van Der Graaf M. In vivo magnetic resonance spectroscopy: Basic methodology and clinical applications. Eur Biophys J 2010; 39: 527–540.

Hagmann P, Jonasson L, Maeder P, Thiran J, Wedeen VJ, Meuli R. Understanding Diffusion MR Imaging Techniques : From Scalar Imaging to Diffusion. Radio Graph 2006; 26: 205–224.

Haneder S, Giordano F a., Konstandin S, Brehmer S, Buesing K a., Schmiedek P, et al. 23Na-MRI of recurrent glioblastoma multiforme after intraoperative radiotherapy: technical note. Neuroradiology 2015; 57: 321–326.

Hicks RJ. Should positron emission tomography/computed tomography be the first rather than the last test performed in the assessment of cancer? Cancer Imaging 2012; 12: 315–23.

Higaki T, Nakamura Y, Tatsugami F, Kaichi Y, Akagi M, Akiyama Y, et al. Introduction to the technical aspects of computed diffusion-weighted imaging for radiologists. Radiographics 2018; 38: 1131–1144.

Hilario a., Sepulveda JM, Perez-Nuñez a., Salvador E, Millan JM, Hernandez-Lain a., et al. A prognostic model based on preoperative MRI predicts overall survival in patients with diffuse gliomas. Am J Neuroradiol 2014; 35: 1096–1102.

Hurd RE, Yen Y-F, Chen A, Ardenkjaer-Larsen JH. Hyperpolarized ^{13}C metabolic imaging using dissolution dynamic nuclear polarization. J Magn Reson Imaging 2012; 36: 1314–1328.

Iima M, Le Bihan D. Clinical intravoxel incoherent motion and diffusion MR imaging: Past, present, and future. Radiology 2016; 278: 13–32.

Inglese M, Madelin G, Oesingmann N, Babb JS, Wu W, Stoeckel B, et al. Brain tissue sodium concentration in multiple sclerosis: a sodium imaging study at 3 tesla. Brain 2010; 133: 847–57.

Inglese M, Oesingmann N, Zaaraoui W, Ranjeva JP, Fleysher L. Sodium imaging as a marker of tissue injury in patients with multiple sclerosis. Mult Scler Relat Disord 2013; 2: 263–9.

Jähnig F, Kwiatkowski G, Ernst M. Conceptual and instrumental progress in dissolution DNP. J Magn Reson 2016; 264: 22–29.

Jensen J, Helpern J. Quantifying non-Gaussian water diffusion by means of pulsed-field-gradient MRI. In: Proceedings of the 11th Annual Meeting of ISMRM. Toronto (Canada); 2003. p. 2154

Jensen JH, Helpern J a., Ramani A, Lu H, Kaczynski K. Diffusional kurtosis imaging: The quantification of non-gaussian water diffusion by means of magnetic resonance imaging. Magn Reson Med 2005; 53: 1432–1440.

Jensen JH, Helpern JA. MRI quantification of non-Gaussian water diffusion by kurtosis analysis. NMR Biomed 2010; 23: 698–710.

Kanda T, Ishii K, Kawaguchi H, Kitajima K, Takenaka D. High signal intensity in the dentate

nucleus and globus pallidus on unenhanced T1-weighted MR images: Relationship with increasing cumulative dose of a gadoliniumbased contrast material. Radiology 2014; 270: 834–841.

Khoshnevisan A, Allahabadi NS. Neuronavigation: principles, clinical applications and potential pitfalls. Iran J Psychiatry 2012; 7: 97–103.

Kim HS, Suh CH, Kim N, Choi CG, Kim SJ. Histogram analysis of intravoxel incoherent motion for differentiating recurrent tumor from treatment effect in patients with glioblastoma: Initial clinical experience. Am J Neuroradiol 2014; 35: 490–497.

Kono K, Inoue Y, Nakayama K, Shakudo M, Morino M, Ohata K, et al. The role of diffusion-weighted imaging in patients with brain tumors. AJNR Am J Neuroradiol 2001; 22: 1081–8.

Konstandin S, Nagel AM. Measurement techniques for magnetic resonance imaging of fast relaxing nuclei. Magn Reson Mater Physics, Biol Med 2014; 27: 5–19.

Kruger SJ, Nagle SK, Couch MJ, Ohno Y, Albert M, Fain SB. Functional imaging of the lungs with gas agents. J Magn Reson Imaging 2016; 43: 295–315.

Kuhajda FP. Fatty Acid Synthase and Cancer: New Application of an Old Pathway. Cancer Res 2006; 66: 5977–5980.

Kurhanewicz J, Vigneron DB. Advances in MR Spectroscopy of the Prostate. Magn Reson Imaging Clin N Am 2008; 16: 697–710.

Kurhanewicz J, Vigneron DB, Brindle K, Chekmenev EY, Comment A, Cunningham CH, et al. Analysis of cancer metabolism by imaging hyperpolarized nuclei: prospects for translation to clinical research. Neoplasia 2011; 13: 81–97.

Kwock L, Smith JK, Castillo M, Ewend MG, Collichio F, Morris DE, et al. Clinical role of proton magnetic resonance spectroscopy in oncology: brain, breast, and prostate cancer. Lancet Oncol 2006; 7: 859–868.

Lee EJ, TerBrugge K, Mikulis D, Choi DS, Bae JM, Lee SK, et al. Diagnostic value of peritumoral minimum Apparent Diffusion Coefficient for differentiation of Glioblastoma Multiforme from solitary metastatic lesions. Am J Roentgenol 2011; 196: 71–76.

Lerche MH, Meier S, Jensen PR, Baumann H, Petersen BO, Karlsson M, et al. Study of molecular interactions with ^{13}C DNP-NMR. J Magn Reson 2010; 203: 52–56.

Lu S, Ahn D, Johnson G, Cha S. Peritumoral diffusion tensor imaging of high-grade gliomas and metastatic brain tumors. Am J Neuroradiol 2003; 24: 937–941.

Lumata L, Yang C, Ragavan M, Carpenter N, DeBerardinis RJ, Merritt ME. Hyperpolarized ^{13}C Magnetic Resonance and its use in metabolic assessment of cultured cells and perfused organs [Internet]. 1st ed. Elsevier Inc.; 2015Available from: http://dx.doi.org/10.1016/bs.mie.2015.04.006

Mabray MC, Barajas RF, Cha S. Modern brain tumor imaging. Brain tumor Res Treat 2015; 3: 8–23.

Madelin G. Sodium Magnetic Resonance Imaging : Biomedical Applications. J Magn Reson Imaging 2013

Madelin G, Regatte RR. Biomedical applications of sodium MRI in vivo. J Magn Reson Imaging 2013; 38: 511–529.

Martin a J, Liu H, Hall W a, Truwit CL. Preliminary assessment of turbo spectroscopic imaging for targeting in brain biopsy. AJNR Am J Neuroradiol 2001; 22: 959–68.

Maudsley AA, Hilal SK. Biological aspects of Sodium-23 imaging. Br Med Bull 1984; 40: 165–166.

McRobbie DW, Moore EA, Graves MJ. To BOLDly Go: fMRI, Perfusion and Diffusion. In: MRI from Picture to Proton. Cambridge: Cambridge University Press; 2017. p. 303–325

Mellon EA a, Pilkinton DTT, Clark CMM, Elliott MA a, Witschey WRR, Borthakur a, et al. Sodium MR imaging detection of mild Alzheimer disease: preliminary study. AJNR Am J Neuroradiol 2009; 30: 978–984.

Menendez JA, Lupu R. Fatty acid synthase and the lipogenic phenotype in cancer pathogenesis. Nat Rev Cancer 2007; 7: 763–777.

Merritt ME, Harrison C, Storey C, Jeffrey FM, Sherry AD, Malloy CR. Hyperpolarized ^{13}C allows a direct measure of flux through a single enzyme-catalyzed step by NMR. Proc Natl Acad Sci U S A 2007; 104: 19773–19777.

Mirkes CC, Hoffmann J, Shajan G, Pohmann R, Scheffler K. High-resolution quantitative sodium imaging at 9.4 tesla. Magn Reson Med 2014; 25096: 25393.

Möller-Hartmann W, Herminghaus S, Krings T, Marquardt G, Lanfermann H, Pilatus U, et al. Clinical application of proton magnetic resonance spectroscopy in the diagnosis of intracranial mass lesions. Neuroradiology 2002; 44: 371–381.

Morris P, Bachelard H. Reflections on the application of ^{13}C-MRS to research on brain metabolism. NMR Biomed 2003; 16: 303–12.

Moseley ME, Cohen Y, Kucharczyk J, Mintorovitch J, Asgari HS, Wendland MF, et al. Diffusion-weighted MR imaging of anisotropic water diffusion in cat central nervous system. Radiology 1990; 176: 439–445.

Mulkern R V., Haker SJ, Maier SE. On high b diffusion imaging in the human brain: ruminations and experimental insights. Magn Reson Imaging 2009; 27: 1151–1162.

Nagel AM, Bock M, Hartmann C, Gerigk L, Neumann J-O, Weber M-A, et al. The Potential of Relaxation-Weighted Sodium Magnetic Resonance Imaging as Demonstrated on Brain Tumors. Invest Radiol 2011; 46: 539–547.

Neeman M, Eldar H, Rushkin E, Degani H. Chemotherapy-induced changes in the energetics of human breast cancer cells; ^{31}P- and ^{13}C-NMR studies. BBA - Mol Cell Res 1990; 1052: 255–263.

Nelson SJ, Kurhanewicz J, Vigneron DB, Larson PEZ, Harzstark AL, Ferrone M, et al. Metabolic imaging of patients with prostate cancer using hyperpolarized [1-^{13}C]pyruvate. Sci Transl Med 2013; 5

Nielsen PM, Eldirdiri A, Bertelsen LB, Jørgensen HS, Ardenkjaer-Larsen JH, Laustsen C. Fumarase activity: an in vivo and in vitro biomarker for acute kidney injury. Sci Rep 2017; 7: 40812.

Niendorf T, Dijkhuizen RM, Norris DG, Van Lookeren Campagne M, Nicolay K. Biexponential diffusion attenuation in various states of brain tissue: Implications for diffusion-weighted imaging. Magn Reson Med 1996; 36: 847–857.

Novikov DS, Kiselev VG, Jespersen SN. On modeling. Magn Reson Med 2018; 79: 3172–3193.

Oh J, Cha S, Aiken AH, Han ET, Crane JC, Stainsby J a., et al. Quantitative apparent diffusion coefficients and T_2 relaxation times in characterizing contrast enhancing brain tumors and regions of peritumoral edema. J Magn Reson Imaging 2005; 21: 701–708.

Ouwerkerk R, Bleich K, Gillen J. Tissue sodium concentration in human brain tumors as measured with ^{23}Na MR imaging. Radiology 2003; 23: 529–537.

Overhauser AW. Polarization of nuclei in metals. Phys Rev 1953; 92: 411–415.

Panagiotaki E, Chan RW, Dikaios N, Ahmed HU, O'Callaghan J, Freeman A, et al. Microstructural characterization of normal and malignant human prostate tissue with vascular, extracellular, and restricted diffusion for cytometry in tumours magnetic resonance imaging. Invest Radiol 2015; 50: 218–227.

Panagiotaki E, Schneider T, Siow B, Hall MG, Lythgoe MF, Alexander DC. Compartment models of the diffusion MR signal in brain white matter: A taxonomy and comparison. Neuroimage 2012; 59: 2241–2254.

Panagiotaki E, Walker-Samuel S, Siow B, Johnson SP, Rajkumar V, Pedley RB, et al. Noninvasive quantification of solid tumor microstructure using VERDICT MRI. Cancer Res 2014; 74: 1902–1912.

Poupon C, Clark CA, Frouin V, Régis J, Bloch I, Le Bihan D, et al. Regularization of diffusion-based direction maps for the tracking of brain white matter fascicles. Neuroimage 2000; 12: 184–195.

Price SJ, Burnet NG, Carpenter TA, Pickard JD, Gillard JH. Predicting patterns of glioma recurrence using diffusion tensor imaging. Eur Radiol 2007; 17: 1675–1684.

Price SJ, Burnet NG, Green HAL, Carpenter TA, Pickard JD, Gillard JH. Tissue signature characterisation of diffusion tensor abnormalities in cerebral gliomas. Eur Radiol 2004; 14: 1909–1917.

Price SJ, Gillard JH. Imaging biomarkers of brain tumour margin and tumour invasion. Br J Radiol 2011; 84: S159–S167.

Puig J, Sánchez-González J, Blasco G, Daunis-I-Estadella P, Federau C, Alberich-Bayarri Á, et al. Intravoxel incoherent motion metrics as potential biomarkers for survival in glioblastoma. PLoS One 2016; 11: 1–14.

Raab P, Hattingen E, Franz K, Zanella FE, Lanfermann H. Cerebral gliomas: diffusional kurtosis imaging analysis of microstructural differences. Radiology 2010; 254: 876–881.

Radbruch A, Bendszus M. Advanced MR Imaging in Neuro-oncology. Clin Neuroradiol 2015; 25: 143–149.

Reetz K, Romanzetti S, Dogan I, Saß C, Werner CJ, Schiefer J, et al. Increased brain tissue sodium concentration in Huntington's Disease - a sodium imaging study at 4 T. Neuroimage 2012; 63: 517–24.

Rosenkrantz AB, Padhani AR, Chenevert TL, Koh D-M, De Keyzer F, Taouli B, et al. Body diffusion kurtosis imaging: Basic principles, applications, and considerations for clinical practice. J Magn Reson Imaging 2015: n/a-n/a.

Sahraian MA, Eshaghi A. Role of MRI in diagnosis and treatment of multiple sclerosis. Clin Neurol Neurosurg 2010; 112: 609–615.

Schuierer G, Ladebeck R, Barfuß H, Hentschel D, Huk WJ. Sodium-23 imaging of supratentorial lesions at 4.0 T. Magn Reson Med 1991; 22: 1–9.

Serrao EM, Kettunen MI, Rodrigues TB, Dzien P, Wright AJ, Gopinathan A, et al. MRI with hyperpolarised [1- ^{13}C]pyruvate detects advanced pancreatic preneoplasia prior to invasive disease in a mouse model. Gut 2016; 65: 465–475.

Server A, Kulle B, Mæhlen J, Josefsen R, Schellhorn T, Kumar T, et al. Quantitative Apparent Diffusion Coefficients in the characterization of brain tumors and associated peritumoral edema. Acta radiol 2009; 50: 682–689.

Shen N, Zhao L, Jiang J, Jiang R. Intravoxel Incoherent Motion Diffusion- Weighted Imaging Analysis of Diffusion and Microperfusion in Grading Gliomas and Comparison With Arterial Spin Labeling for Evaluation of Tumor Perfusion. J Magn Reson Imaging 2016; 44: 620–32.

Stejskal EO, Tanner JE. Spin diffusion measurements: Spin echoes in the presence of a time-dependent field gradient. J Chem Phys 1965; 42: 288–292.

Tabesh A, Jensen JH, Ardekani BA, Helpern JA. Estimation of tensors and tensor-derived measures in diffusional kurtosis imaging. Magn Reson Med 2011; 65: 823–36.

Thulborn KR, Davis D, Adams H, Gindin T, Zhou J. Quantitative Tissue Sodium Concentration Mapping of the Growth of Focal Cerebral Tumors With Sodium Magnetic Resonance Imaging. Cell 1999; 359: 351–359.

Thulborn KR, Lu A, Atkinson IC, Damen F, John V. Quantitative Sodium MR Imaging and Sodium Bioscales for the Management of Brain Tumors. Neuroimaging Clin N Am 2009; 19: 615–624.

Thust SC, Heiland S, Falini A, Jäger HR, Waldman AD, Sundgren PC, et al. Glioma imaging in Europe: A survey of 220 centres and recommendations for best clinical practice. Eur Radiol 2018: 1–12.

Tozer DJ, Jager HR, Danchaivijitr N, Benton CE, Tofts PS, Rees JH, et al. Apparent diffusion coefficient histograms may predict low-grade glioma subtype. NMR Biomed 2007; 20: 304–325.

Turner R, Le Bihan D, Maier J, Vavrek R, Hedges LK, Pekar J. Echo-planar imaging of intravoxel incoherent motion. Radiology 1990; 177: 407–414.

Vargová L, Homola A, Zámečník J, Tichý M, Beneš V, Syková E. Diffusion parameters of the extracellular space in human gliomas. Glia 2003; 42: 77–88.

Villanueva-Meyer JE, Mabray MC, Cha S. Current clinical brain tumor imaging. Clin Neurosurg 2017; 81: 397–415.

Wang W, Hu Y, Lu P, Li Y, Chen Y, Tian M, et al. Evaluation of the diagnostic performance of magnetic resonance spectroscopy in brain tumors: a systematic review and meta-analysis. PLoS One 2014; 9: e112577.

Warburg O. On the Origin of Cancer Cells. Science (80-) 1956; 123: 309–14.

Ward CS, Venkatesh HS, Chaumeil MM, Brandes AH, VanCriekinge M, Dafni H, et al. Noninvasive detection of target modulation following phosphatidylinositol 3-kinase inhibition using hyperpolarized ^{13}C magnetic resonance spectroscopy. Cancer Res 2010; 70: 1296–1305.

Watanabe M, Tanaka R, Takeda N. Magnetic resonance imaging and histopathology of cerebral gliomas. Neuroradiology 1992; 34: 463–469.

Weissleder R, Mahmood U. Molecular Imaging. Radiology 2001; 219: 316–333.

Wen PY, Macdonald DR, Reardon D a., Cloughesy TF, Sorensen a. G, Galanis E, et al. Updated response assessment criteria for high-grade gliomas: Response assessment in neuro-oncology working group. J Clin Oncol 2010; 28: 1963–1972.

Witney TH, Kettunen MI, Day SE, Hu D, Neves AA, Gallagher FA, et al. A comparison between radiolabeled fluorodeoxyglucose uptake and hyperpolarized ^{13}C-labeled pyruvate utilization as methods for detecting tumor response to treatment. Neoplasia 2009; 11: 574–82.

Witney TH, Kettunen MI, Hu D, Gallagher FA, Bohndiek SE, Napolitano R, et al. Detecting treatment response in a model of human breast adenocarcinoma using hyperpolarised [1-^{13}C]pyruvate and [1,4-^{13}C2]fumarate. Br J Cancer 2010; 103: 1400–1406.

Yamada I, Aung W, Himeno Y, Nakagawa T, Shibuya H. Diffusion coefficients in abdominal organs and hepatic lesions: Evaluation with intravoxel incoherent motion echo-planar MR

imaging. Radiology 1999; 210: 617–623.

Yoshimoto M, Waki A, Yonekura Y, Sadato N, Murata T, Omata N, et al. Characterization of acetate metabolism in tumor cells in relation to cell proliferation: Acetate metabolism in tumor cells. Nucl Med Biol 2001; 28: 117–122.

Yushmanov VE, Kharlamov A, Yanovski B, LaVerde G, Boada FE, Jones SC. Correlated sodium and potassium imbalances within the ischemic core in experimental stroke: a ^{23}Na MRI and histochemical imaging study. Brain Res 2013; 1527: 199–208.

Zaaraoui W, Konstandin S, Audoin B, Nagel a. M, Rico a., Malikova I, et al. Distribution of Brain Sodium Accumulation Correlates with Disability in Multiple Sclerosis: A Cross-sectional ^{23}Na MR Imaging Study. Radiology 2012; 264: 859–867.

Zhang H, Hubbard PL, Parker GJM, Alexander DC. Axon diameter mapping in the presence of orientation dispersion with diffusion MRI. Neuroimage 2011; 56: 1301–1315.

Zhang H, Ma L, Wang Q, Zheng X, Wu C, Xu B. Role of magnetic resonance spectroscopy for the differentiation of recurrent glioma from radiation necrosis: a systematic review and meta-analysis. Eur J Radiol 2014; 83: 2181–9.

Zhang H, Schneider T, Wheeler-Kingshott CA, Alexander DC. NODDI: Practical in vivo neurite orientation dispersion and density imaging of the human brain. Neuroimage 2012; 61: 1000–1016.

Non-invasive assessment of glioma microstructure using VERDICT MRI: correlation with histology

UNIVERSITY OF CAMBRIDGE

Chapter 3

Non-invasive assessment of glioma microstructure using VERDICT MRI: correlation with histology

Gliomas are primary brain tumours characterised by diffuse infiltration and a poor prognosis (Paulus and Peiffer, 1989; Louis *et al.*, 2016). Genetic and phenotypic heterogeneity contribute to both poor therapy response and tumour recurrence (Anjum *et al.*, 2017; Daher and de Groot, 2018). Magnetic Resonance Imaging (MRI) is the imaging modality of choice but is limited in assessing tumour subtypes and intratumoral heterogeneity (Sottoriva *et al.*, 2013; Mabray *et al.*, 2015; Ceccarelli *et al.*, 2016; Aihara *et al.*, 2017). In addition, conventional imaging is ineffective in evaluating the spread of tumour into the peritumoral region which may lead to sub-optimal resection and recurrence (Langen *et al.*, 2017). Consequently, new imaging biomarkers are required to improve the assessment of glioma.

Several studies have addressed the importance of Diffusion-Weighted Imaging (DWI) and the apparent diffusion coefficient (ADC) in evaluating gliomas but have shown partial overlap in the measured values between subtypes (Kono *et al.*, 2001; Bulakbasi *et al.*, 2004; Hilario *et al.*, 2014). The ADC may have a role in differentiating high grade glioma from metastases and in assessing peritumoral oedema, but it cannot accurately differentiate primary brain tumour subtypes (Kono *et al.*, 2001; Oh *et al.*, 2005; Server *et al.*, 2009; Lee *et al.*, 2011; Hilario *et al.*, 2014).

The Vascular, Extracellular and Restricted Diffusion for Cytometry in Tumours (VERDICT) is a model that infers tissue microstructure from DWI measurements (Panagiotaki *et al.*, 2014). This model derives multiple compartments (intracellular, intravascular and extracellular–extravascular

spaces) and has been applied to xenograft models of colorectal cancer, patient studies of prostate cancer and has recently been shown to be feasible in glioma (Panagiotaki *et al.*, 2014, 2015a; Bailey *et al.*, 2018; Roberts *et al.*, 2018). Here we have applied this method to image intratumoral and intertumoral heterogeneity in glioma and validated with histology as part of a prospective study. The primary aims of this prospective study were to demonstrate the use of the technique in the human brain for the first time and to show feasibility in a clinical environment. The secondary aim was to validate VERDICT parameters with histopathologic analysis on a patient-by-patient basis. Exploratory aims of this study were to evaluate the potential utility of the modelled parameters as biomarkers of glioma heterogeneity and subtype as well as the presence of tumour in the peritumoral environment.

3.1 Methods and materials

3.1.1 Patient selection

Fourteen consecutive treatment-naïve patients (6 men, 8 women; age 43.5 ± 15.1 years) were recruited into this prospective ethically-approved study (East of England, Cambridge South Research Ethics Committee, REC reference number 16/EE/0184) from a neuro-oncology multidisciplinary team meeting or clinic. Subjects were scheduled for for image-guided biopsy or resection and gave written informed consent.

3.1.2 MRI acquisition

MRI examinations were performed using a 3.0 T clinical scanner and a 12-channel head coil (Discovery MR750; GE Healthcare). Imaging included: 3D T_2-weighted imaging (T^2W; repetition time/echo time [TR/TE] 2500/79 ms; 248 slices; slice thickness 1.2 mm; acquisition matrix 320x320; field of view [FOV] 240x240 mm), 2D T_2W fluid-attenuated inversion recovery (FLAIR; TR/TE 8000/126ms; inversion time [TI] 2128 ms; slice thickness 6 mm; acquisition matrix 384x224; FOV 240x240 mm) and DWI (TR/TE 2841-3867/83.3-87.4 ms; slice thickness 5mm; b-values 0,1000 s/mm^2; matrix 128x128; FOV 240x240 mm). 3D T_1-weighted Fast SPoiled GRadient echo (T_1W FSPGR;

252 slices; 0.94x0.94x1.5 mm reconstructed to 0.94x0.94x1 mm; TR/TE 8.2/3.2; slice thickness 1.5 mm; matrix 256x256; FOV 240x240 mm) was performed before and after injection of a gadolinium-based contrast agent (Gadobutrol 1.0 mmol/mL; Schering). ADC maps were generated as per clinical standard.

3.1.3 VERDICT acquisition and post-processing

VERDICT is a model-based diffusion MRI proposed in 2014 to quantify tumour microstructure (Panagiotaki *et al.*, 2014). The model assumes that a wide range of tumours can be characterised by assessing three different compartments: the vascular compartment, the extracellular-extravascular space and the intracellular space. Technically, as also described in chapter 2, the model is the sum of three models characterising diffusion in the intracellular compartment (S_1), extracellular compartment (S_2), and arising from the microcirculation (S_3). The overall model does not account for any potential exchange between the three compartments and is represented by the following equation:

$$S = \sum_{i=1}^{3} f_i S_i \quad [11]$$

where f_i is the signal at b = 0 from water molecules in population i, $0 \leq f_i \leq 1$, $\sum_{i=1}^{3} f_i = 1$.

The parameters for DWI and VERDICT modelling used in this study are shown in table 3.1, the spatial resolution was 2 mm isotropic (Panagiotaki *et al.*, 2015a). For each b-value, a separate b=0 image was acquired to compensate for varying T2-weighting. To assess the robustness of the 5 b-value abbreviated acquisition, an extended protocol using 40 b-values was undertaken in one patient within the limits of the clinical gradient system (G_{max}, 45 mT/m; slew rate, 200 mT/m/s). The echo time (TE) scaled as a consequence of an increase of the diffusion time (the time between the diffusion sensitising gradients, expressed as Δ in table 3.1), thus in turn increasing the total time between excitation and refocussing leading to longer echo times. Each scan was normalised with their respective own unweighted image to account for the echo time dependence of the diffusion signal.

***b* value (s/mm^2)**	**Δ /∂(ms)**	**Echo Time (ms)**	**|G| mT/m**	**Number of averages**	**Acceleration factor**	**Full readout bandwidth (Hz)**
90	23.5/4.7	49.3	49.4	8	2	200000
500	31.3/12.2	64.3	41.5	8	2	200000
1500	43.4/25.8	91.4	30.1	8	2	200000
2000	32.1/16.5	72.7	75.8	8	2	200000
3000	43.8/24.8	89.4	43.9	8	2	200000

Table 3.1: Diffusion MRI parameters for the abbreviated VERDICT model.
Parameters used for the shortened protocol: Δ is the time separation between the gradient pulses; ∂ Is the duration of the pulses; |G| is the combined gradient strength of the diffusion encoding.

The tumours were located on T_2W and then 16 axial DWI slices were acquired over the region-of-interest (ROI) for VERDICT modelling. The acquisition time for each b-value was 66 s, with a total time of 330 s. Tumour cell radius, intracellular (IC) and combined extracellular/vascular volume (EC) were calculated (MATLAB 2016b, the MathWorks) using a framework based on linearization and convex optimization which provides an acceleration factor of 1500 (Daducci *et al.*, 2015; Bonet-Carne *et al.*, 2016). Intracellular and extracellular spaces were modelled separately and therefore the sum of both compartments was only approximately 100%. Parameter maps were registered to 3D T_1W obtained after gadolinium-based contrast agent injection and 3D T_2W sequences (SPM12, UCL).

3.1.4 MRI analysis

A neuroradiologist with 6 years of experience in neuro-imaging outlined ROIs on axial T_2W and axial 3D-T_1W post-contrast sequences using OsiriX (V.8.5.2, Pixmeo SARL). To assess the reproducibility of the ROI definition, a second observer with 3 years of experience in neuro-imaging, blind to the clinical data, performed a second analysis using the same software. ROIs were drawn around the entire lesion including the surrounding oedema using a combined evaluation of T_1W and T_2W imaging. The 3D-T_1W images obtained after injection of a gadolinium-based contrast agent were used to

better define the enhancing tissue and the necrosis (if present) whilst the T_2WI were used to better highlight the oedema boundaries. ADC and VERDICT maps were co-registered to the anatomical imaging to calculate the microstructural parameters.

3.1.5 Pathological analysis

All enrolled patients underwent image-guided biopsy or resection using the 3D-T_1W imaging obtained after injection of a gadolinium-based contrast agent as per clinical routine and to facilitate retrospective correlation with imaging. Screenshots of the neuro-navigation system were saved during the procedure to guide pathological analysis. Histopathology was used to determine the tumour grade and type using WHO-2016 classification (Louis *et al.*, 2016). A neuropathologist with 7 years of experience evaluated tumour photomicrographs from a x600 FOV and a fixed matrix of 184x138 μm to assess cellularity and cell size using semi-automated software (Image-Pro Insight). Average tumour cell size was assessed by measuring the short and long axes of 20 cancer cells in each FOV for patient-by-patient correlation with the cell size obtained processing the VERDICT data. To determine if shrinkage post fixation affected these measurement, red blood cell size was compared between a blood smear and a stained section in the same patient (Hsu *et al.*, 2007; Tran *et al.*, 2015).

3.1.6 Statistical Analysis

Statistical analysis was performed using a mathematical analytical software (Matlab Statistics and Machine Learning Toolbox, Matlab 2017a, Mathworks). A Kolmogorov–Smirnov test was used as a goodness-of-fit test comparing our data to a standard normal distribution to confirm the appropriateness of using non-parametric tests for the statistical analysis. Comparisons between pathological analysis and VERDICT parameters were performed using the Wilcoxon rank-sum test. The same non-parametric statistical test was used to assess the difference in cell size and density and to compare the results obtained by the two observers. A statistical significance of $p \leq 0.05$ was used. The Dice similarity coefficient (DSC) was

used to assess the reproducibility of the segmentation performed by the two observers (Dice, 1945); a coefficient > 0.70 indicates good overlap between the ROIs (Zijdenbos *et al.*, 1994; Zou *et al.*, 2004).

3.2 Results

The demographics and tumour characteristics are shown in Table 3.2. VERDICT fitting was successfully performed for all patients. The time window between imaging and surgery was 17.5 ± 12.3 (median ± standard deviation; range: 4 – 46) days in patients with LGG and 5.2 ± 6.4 (1 – 17) days in patients with HGG. Patients included: seven low grade gliomas (LGG: four diffuse, isocitrate dehydrogenase 1 [IDH1] R132H mutant astrocytomas; three IDH1 R132H mutant, 1p19q co-deleted oligodendrogliomas) and seven high grade gliomas (HGG: six IDH-wildtype glioblastomas; one IDH-wildtype astrocytoma).

	Low Grade Glioma	**High Grade Glioma**	**p**
Age in years	33.2 ± 9.2 (24 – 45)	55.3 ± 11.9 (44 – 78)	< 0.01
Men, n (%)	2 (28.6%)	4 (57.1%)	0.59
Lesion size in mm	44.4 ± 19.1 (23.1 – 68.7)	27.1 ± 17.2 (6.4 – 56.4)	0.13
IDH1 R132H, n (%)			
- **Present**	7 (100%)	0 (0%)	< 0.01
- **Absent**	0 (0%)	7 (100%)	
MIB-1 (a.u.)	4.2 ± 3.0 (1 – 8.8)	19.2 ± 6.7 (12 – 31)	< 0.001

Table 3.2: Demographic data and histopathological characteristics for high grade and low grade tumours.
IDH1 R132H: mutations involving isocitrate dehydrogenase 1. The monoclonal antibody MIB-1 was used to determine the Ki-67 labelling index as a marker of proliferation. Continuous values are expressed as mean ± SD with range in parentheses.

3.2.1 Histopathological analysis

The histopathological measure of cell radius (Figure 3.1) was not significantly different in HGG compared to LGG: 5.7 ± 1.4 μm (range: 4.5 – 8.1) vs. 4.6 ± 1.6 μm (3.1 – 8.1) respectively ($p = 0.16$). The red blood cell size was 5.5 ± 0.7 μm (range 4.4 – 6.9) on fixed sections and 7.6 ± 0.6 μm (6.6 – 8) on the cell smear ($p < 0.001$) demonstrating a reduction in size following fixation.

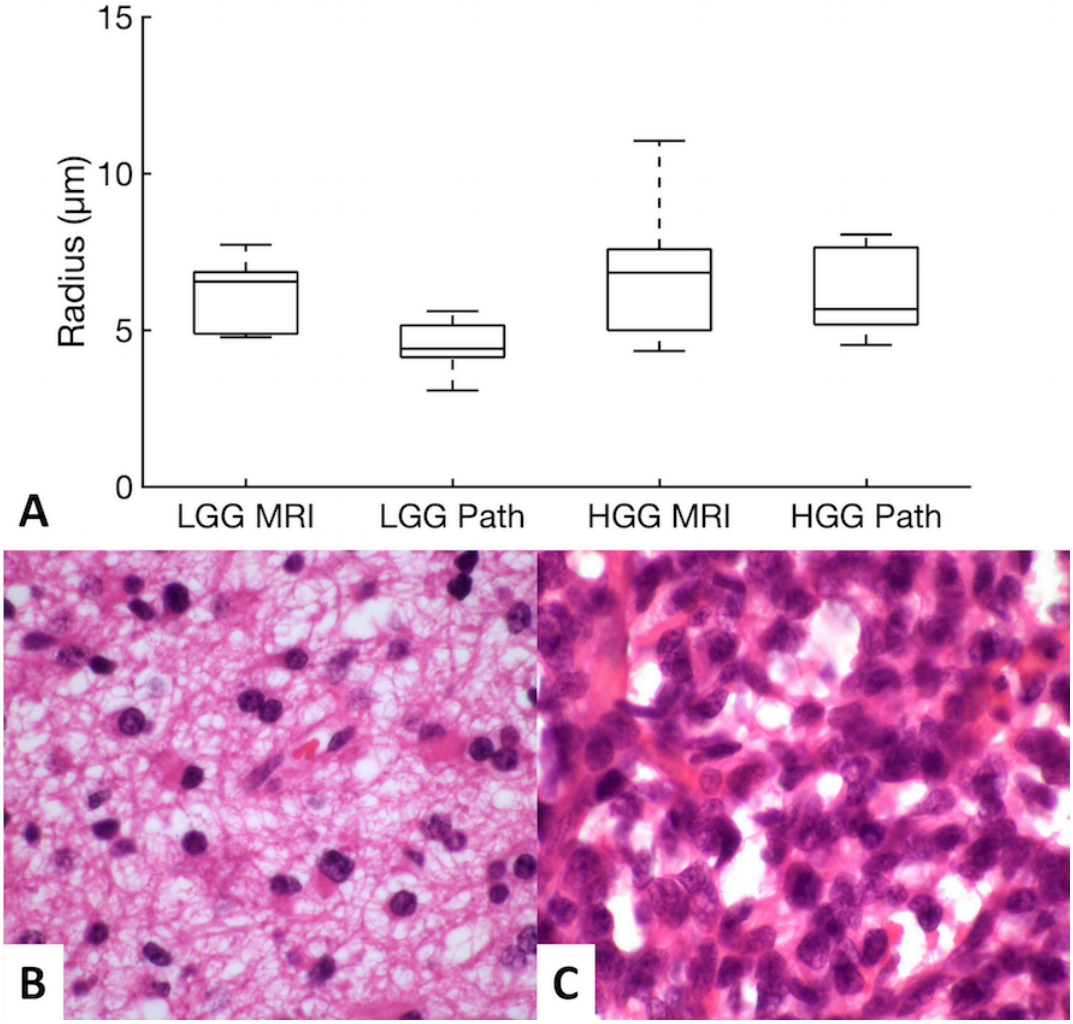

Figure 3.1: Cell radius at MRI and pathology.
(A) Box-and-whisker plot illustrating the cell radius as measured by VERDICT MRI and pathology for low grade glioma (LGG) and high grade glioma (HGG). (B) H&E staining from a low grade glioma shown in Fig. 2. (C) H&E staining from a high grade glioma also shown in Fig. 3.2.

There was a trend towards a higher histological cell density in HGG compared to LGG: 104 ± 43 cells/FOV (range: 67 – 170) vs. 51 ± 66.4 cells/FOV (35 – 210) respectively; the difference was not significant (p = 0.21).

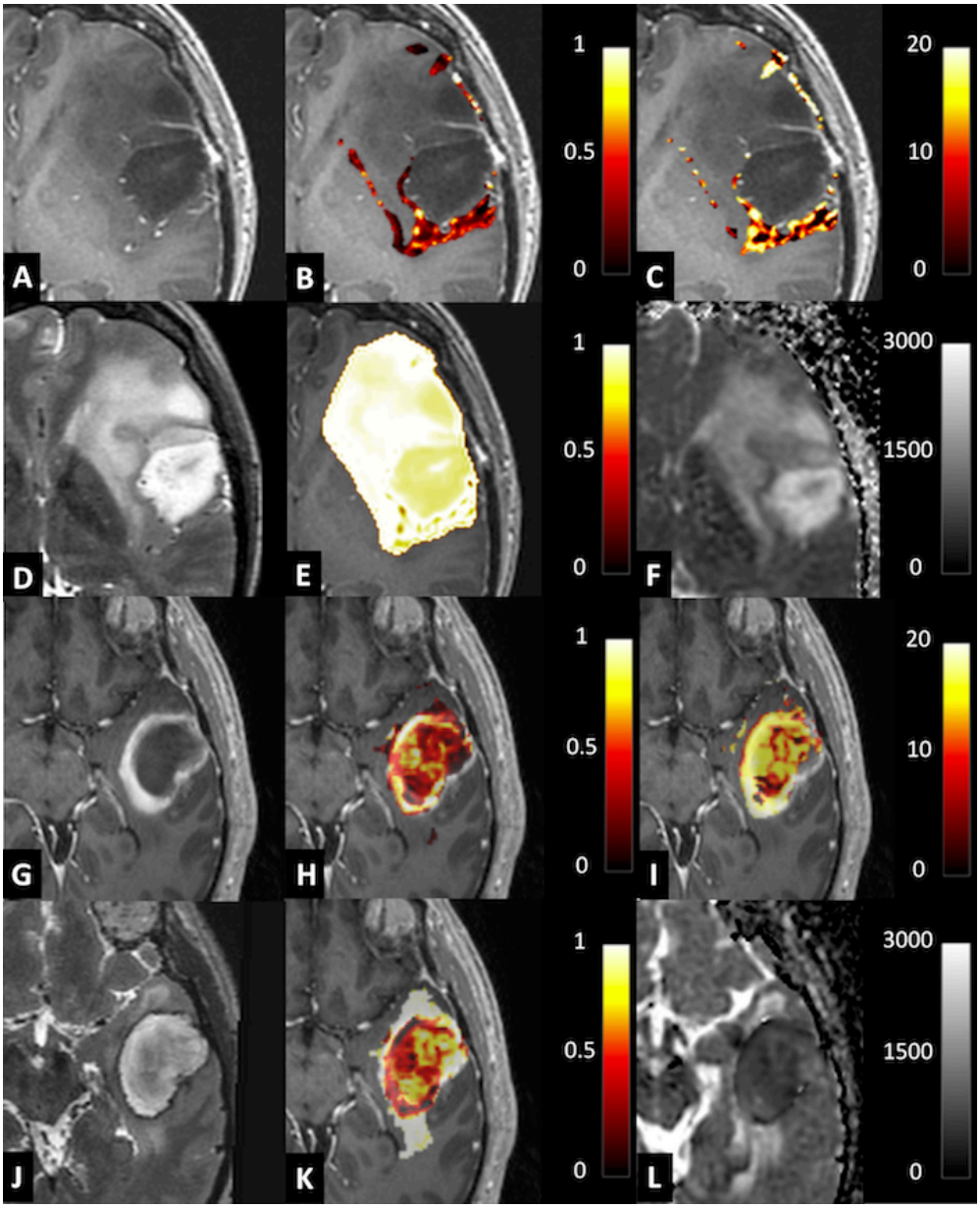

Figure 3.2: Representative low grade and high grade glioma.
(A) - (F) Representative images from a low grade glioma: (A) axial post gadolinium 3D T_1WI; (B) intracellular volume fraction; (C) cell radius maps; (D) axial T_2WI; (E) extracellular volume fraction; (F) ADC map; scale shown x10-6 mm^2/s. Colour maps for B, C and E have been superimposed on the grayscale image from A with the colour scale shown for each image. (G) - (N) Representative images from a high grade glioma: (G) axial post gadolinium 3D T_1WI; (H) intracellular volume fraction; (I) cell radius maps; (J) axial T_2WI; (K) extracellular volume fraction; and (L) ADC map, scale shown x 10-6 mm^2/s. Colour maps for H, I and K have been superimposed on the greyscale image from A with the colour scale shown for each image.

3.2.2 VERDICT analysis

VERDICT parametric maps for LGG and HGG are shown in Figure 3.2. The calculated cell radius was similar in both groups: 6.8 ± 2.3 μm for HGG (range 4.3 – 11) and 6.7 ± 1.2 μm for LGG (4.8 – 7.8); Figure 3.1. There were no significant differences between VERDICT radius measurements and those from pathological sections for either LGG ($p = 0.09$) or HGG ($p = 0.80$). The intracellular volume fraction was higher in HGG compared to LGG: 0.13 ± 0.07 (range 0.08 – 0.27) vs. 0.08 ± 0.02 (0.07 – 0.14) respectively; $p = 0.05$. The extracellular/vascular volume fraction showed the opposite trend with a higher EC volume fraction in LGG compared to HGG but this was not significant: 0.92 ± 0.04 (range 0.85 – 0.95) vs. 0.88 ± 0.07 (0.75 – 0.92) respectively; $p = 0.10$, Figure 3.3. DWI as per clinical standard was obtained in 12/15 patients. The conventional ADC was higher in LGG compared to HGG: 1.22 ± 0.13 x 10^{-3}mm^2/s (range 1.13 – 1.44) vs. 0.98 ± 0.38 x 10^{-3}mm^2/s (0.77 – 1.74); however, the difference was not statistically significant ($p = 0.18$); Figure 3.4.

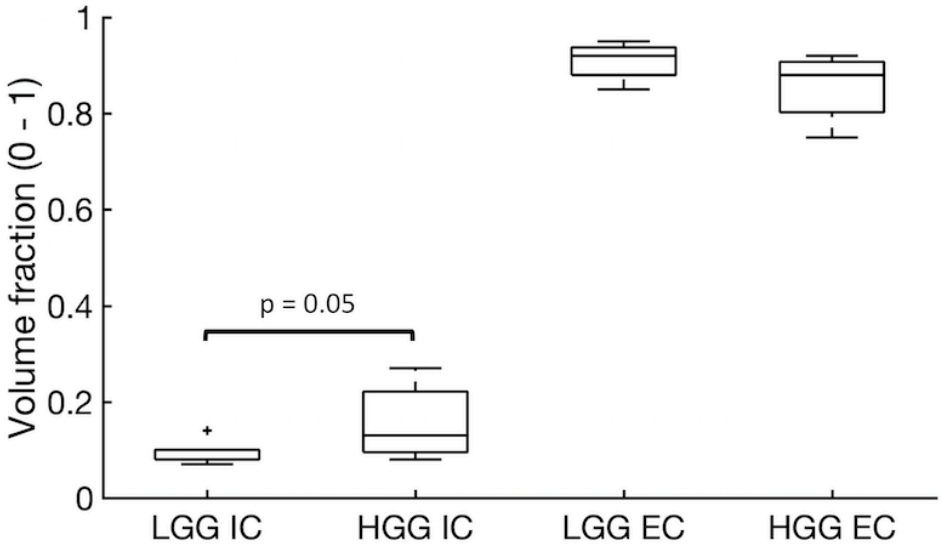

Figure 3.3: Volume fractions for low grade and high grade glioma.
Box-and-whisker plot showing intracellular volume fraction (IC) and extracellular volume fraction (EC) for both low grade gliomas (LGG) and high grade gliomas (HGG) derived from the VERDICT MRI model.

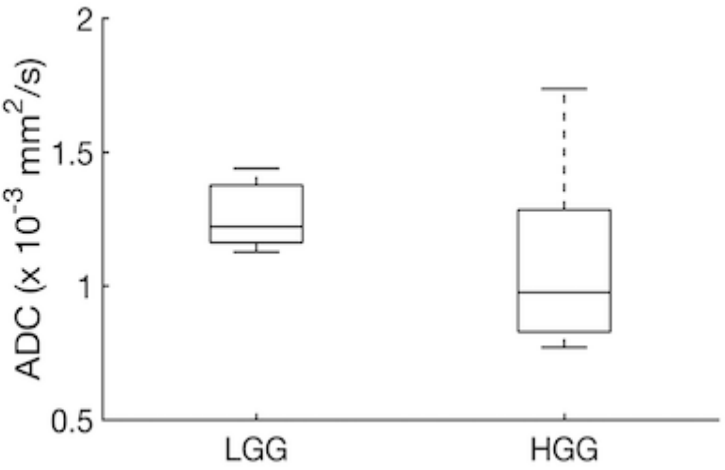

Figure 3.4: Apparent diffusion coefficient for low grade and high grade glioma.
Apparent diffusion coefficient (ADC) values for low grade glioma (LGG) and high grade glioma (HGG) as derived from conventional DWI.

3.2.3 Reproducibility analysis

The assessment of the reproducibility in the ROIs segmentation for the entire tumour region performed by the two observers resulted in high reproducibility demonstrated by a DSC of 0.89 ± 0.06 (0.80 - 0.99). A sub analysis performed according to grading demonstrated similar results with a DSC of 0.89 ± 0.05 (0.82 - 0.94) for LGG and 0.89 ± 0.08 (0.80 - 0.99) for HGG.
The results of the analysis performed by the second observer are shown in Table 3.3.

	LGG			HGG		
	Obs 1	**Obs 2**	**p**	**Obs 1**	**Obs 2**	**p**
Cell radius (μm)	6.7±1.2	6.7±1.5	0.53	6.8±2.3	6.1±2.1	1
IC volume fraction	0.08±0.02	0.11±0.03	0.07	0.13±0.07	0.12±0.06	0.93
EC volume fraction	0.92±0.04	0.91±0.05	0.60	0.88±0.07	0.89±0.05	0.94

Table 3.3: Comparison between the two observers.
Comparison between the VERDICT parameters derived by the analysis performed by the two observers. Values are expressed as median ± SD.

3.3 Discussion

VERDICT is an advanced diffusion method which has previously been applied to pre-clinical models of cancer showing microstructural differences between tumours and a decrease in cell volume following chemotherapy (Panagiotaki *et al.*, 2014). The method has also been shown to differentiate benign prostate tissue from tumour in patients (Panagiotaki *et al.*, 2015a). In this study we have compared VERDICT to histopathological findings at surgery and correlated with tumour grade. Non-invasive grading of glioma is a major challenge for conventional MRI and biopsied tissue is limited by sampling error as the tumour is very heterogeneous (Langen *et al.*, 2017). Conventional ADC has a sensitivity and specificity for differentiating high and low grade tumours of only 85% and 80% respectively and there is a large overlap in ADC between grades (Zhang *et al.*, 2017). Therefore, additional imaging methods are required to accurately differentiate tumour subtypes and to demonstrate tumour heterogeneity (Kono *et al.*, 2001).

VERDICT parameters showed a higher intracellular volume fraction in HGG compared to LGG and a trend towards a smaller extracellular/vascular volume fraction. As IC and EC are independently derived, their complementarity demonstrates intra-model consistency. Moreover, these results were validated with the histological findings where there was a higher cell density in HGGs compared to LGGs. Importantly, although the conventional ADC was higher in LGG compared to HGG, this was not statistically significant. Therefore, VERDICT could provide important additional information which is complementary to conventional DWI. Moreover, the capability of VERDICT to explore micro-architectural changes through assessing the relative volume fraction has a significant potential role in evaluating tumour infiltration in the peritumoral region. Indeed, visual assessment of the maps revealed significant heterogeneity in the peritumoral zone both in LGG and HGG. For instance, in the representative case of LGG depicted in Figure 3.2, there were areas of increased intracellular volume fraction and increased cell radius not corresponding to areas of suspicion on conventional imaging. Similarly, the representative case of HGG showed an increased intracellular volume fraction and increased cell radius within the

peritumoral region but outside the boundaries of the contrast enhancing lesions. However, targeted biopsies were not obtained from these areas, warranting future studies to explore the significance of those findings.

VERDICT-derived maps showed a higher degree of heterogeneity compared to the corresponding ADC maps. This phenomenon was particularly evident in HGG (Figure 3.2) where regional differences in the VERDICT maps were not visible on ADC. The areas of high IC volume largely corresponded to the independently-derived areas of low EC volume, which again provides evidence that the model is internally consistent. Future studies can validate this heterogeneity using multiregional biopsies and the technique could be used as a tool to assess changes in this heterogeneity with treatment as well as a method to assess the resection cavity following surgery (Panagiotaki *et al.*, 2014).

The range of cell size was larger for HGG compared to LGG on both VERDICT and histopathology in keeping with the more heterogeneous nature of the higher-grade tumours. The patient-by-patient validation of cell size measured with VERDICT against the pathological assessment demonstrated no statistically significant difference between the two techniques for both HGG ($p = 0.80$) and LGG ($p = 0.09$). However, a one-to-one comparison with pathology is difficult to achieve due to several limiting factors. Sampling errors are a major potential confounding factor given that only a small proportion of the tumour was biopsied and this may not represent the whole tumour (Panagiotaki *et al.*, 2014). Moreover, brain shift during surgery and the different scale of pathology and imaging (μm vs mm) also contribute to potential mis-registration. It is also worth noting that the model used in this study was optimized for the assessment of gliomas. Indeed, the model requires an average expected cell size as input information and has been fine-tuned on a specific cell shape. With the aims of assessing the feasibility of the technique and obtain preliminary validation data, the model was optimized to embrace a wide spread of gliomas, however, different tumours have different histological characteristics, therefore it would be desirable to optimize a pool of models in order to harness the full potential of the technique. For example, astrocytomas have low to moderate cell density with variable cellular morphology, whilst oligodendroglioma are more hypercellular

with more uniform cellular morphology thus they would be better assessed with dedicated models.

The slight reduction in cell size measurements on histopathology compared to the *in vivo* measurements may be accounted for by shrinkage following fixation which is a known phenomenon both at the macroscopic and microscopic and level. Shrinkage is accounted for by a combination of dehydration and direct effects of formalin. In particular, formalin fixation is a two-step process characterised by initial diffusion in the tissue and accumulation followed by the binding phase in which chemical bounds between protein and nucleic acids are promoted by formalin (Hsu *et al.*, 2007). Macroscopically, several authors reported shrinkage of the cerebrum, cerebellum and brain stem (Quester and Schröder, 1997). More interesting and pertinent to this study is that microscopic shrinkage after fixation was observed in a plethora of different cancers including breast cancer (Pritt *et al.*, 2005), non-small cell lung cancer (Hsu *et al.*, 2007; Park *et al.*, 2017), renal tumours (Tran *et al.*, 2015), oral squamous cella carcinoma (Umstattd *et al.*, 2017) and melanoma (Friedman *et al.*, 2019). Therefore, caution must be applied when comparing pathological specimens and image-derived biomarkers. In this study the comparison between VERDICT-derived biomarkers and pathology was aimed at validating the imaging measurements as correlative biomarkers to the reference standard. However, direct correspondence was not expected due to the effects of fixation. To assess this effect, we collected blood smears to assess the magnitude of shrinkage in our cohort: we found a good correspondence between image-derived and pathological biomarkers, especially taking into account the magnitude of shrinkage we observed in the red blood cells. Although there is no ground truth for cell size the aim was to correlate relative cell size measurements on histology and imaging, rather than to assess absolute cell size.

Rapid acquisition and data analysis are necessary for clinical translation of the method and the abbreviated VERDICT MRI protocol proposed by Panagiotaki *et al.* (Panagiotaki *et al.*, 2015b) was performed in 5.5 min representing a reduction of 45 min compared to the extended protocol. A single case was acquired with both the abbreviated and extended protocol (results presented in the supplementary material) to explore the

magnitude of change in the imaging biomarker derived with those two different approaches. The estimation of the intracellular and extracellular volume fractions were similar, although a formal statistical analysis was not performed as both protocols were performed on a single case. However, the similarity in resulting parameters suggest the abbreviated protocol can be successfully applied to explore cellularity in gliomas by adding only few minutes to a standard brain protocol. In addition, the data fitting was combined with a post-processing algorithm based on linearization and convex optimization which reduced the computing by more than 1500-fold to allow the analysis to be made available within a clinically applicable timescale: 25.5±5.3 min for acquisition and post-processing (Daducci *et al.*, 2015; Bonet-Carne *et al.*, 2016).

The primary objective of the work was to assess the feasibility of using VERDICT MRI to investigate the tissue microstructure in glioma in a clinical setting. The limitations of the study include a small sample size which may have reduced the statistical power of the study. Also, the original VERDICT model is designed to compute the intracellular, intravascular and extracellular–extravascular spaces in an animal model of prostate cancer at a pre-clinical field strength of 9.4T which has significantly higher diffusion gradient capabilities of ~300 mT/m. The computational modelling can become unstable with the noise and time constraints experienced at clinical field strength which can compromise the computational fit of the intravascular compartment (Panagiotaki *et al.*, 2015a). Correlation between histology and imaging is also challenging as 2 mm thick imaging slices were compared to 4 μm pathological slides which could introduce sampling errors, particularly given the heterogeneous nature of glioma. Future larger studies are needed to more fully validate the technique against histopathology and to explore its potential applications as a routine clinical tool.

3.4 Conclusion

In conclusion, VERDICT MRI could be a promising technique to assess the tissue microenvironment within glioma using a clinically applicable protocol. The derived parameters demonstrated larger cells and a trend

towards a smaller extracellular space in high grade tumours compared to low grade tumours. This approach may provide additional information compared to conventional diffusion weighted imaging.

Supplementary material

Short vs. extended protocol

The extended protocol duration was 49.5 min and the post-processing required 16 min; the abbreviated protocol was 5.5 min and the post-processing required 20 ± 5.3 min (Table 4). The computing time to perform the fit without linearization and convex optimization was estimated to be more than 343 hours for a single patient and was not deemed feasible. The cell radius was 4.1 ± 0.6 μm using the extended protocol and 3.4 ± 0.7 μm with the abbreviated protocol; the average cell radius at pathology was 4.1 ± 1.3 μm.

	Extended protocol	**Abbreviated protocol**
Scan time (min)	49.5	5.5
Cell radius (μm)	4.1 ± 0.6	3.4 ± 0.7
IC volume fraction	0.12 ± 0.02	0.11 ± 0.01
EC volume fraction	0.88 ± 0.02	0.81 ± 0.02

Table 3.4: Extended VERDICT MRI protocol compared to the abbreviated protocol. Comparison between the scanning time and derived metrics for the full and the abbreviated protocols for the single patient that underwent both approaches. Values are expressed as mean ± SD.

References

Aihara K, Mukasa A, Nagae G, Nomura M, Yamamoto S, et al. Genetic and epigenetic stability of oligodendrogliomas at recurrence. Acta Neuropathol Commun 2017; 5: 18.

Anjum K, Shagufta BI, Abbas SQ, Patel S, Khan I, Shah SAA, et al. Current status and future therapeutic perspectives of glioblastoma multiforme (GBM) therapy: A review. Biomed Pharmacother 2017; 92: 681–689.

Bailey C, Collins DJ, Tunariu N, Orton MR, Morgan VA, Feiweier T, et al. Microstructure Characterization of Bone Metastases from Prostate Cancer with Diffusion MRI: Preliminary Findings. Front Oncol 2018; 8: 26.

Bonet-Carne E, Daducci A, Panagiotaki E, Johnston E, Stevens N, Atkinson D, et al. Non-invasive quantification of prostate cancer using AMICO framework for VERDICT MR. In: International Society for Magnetic Resonance in Medicine (ISMRM). 2016. p. 5–8

Bonet-Carne E, Johnston E, Daducci A, Jacobs JG, Freeman A, Atkinson D, et al. VERDICT-AMICO: Ultrafast fitting algorithm for non-invasive prostate microstructure characterization. NMR Biomed 2018: 1–15.

Bulakbasi N, Guvenc I, Onguru O, Erdogan E, Tayfun C, Ucoz T. The added value of the apparent diffusion coefficient calculation to magnetic resonance imaging in the differentiation and grading of malignant brain tumors. J Comput Assist Tomogr 2004; 28: 735–46.

Ceccarelli M, Barthel FP, Malta TM, Sabedot TS, Salama SR, Murray BA, et al. Molecular profiling reveals biologically discrete subsets and pathways of progression in diffuse glioma. Cell 2016; 164: 550–563.

Daducci A, Canales-Rodríguez EJ, Zhang H, Dyrby TB, Alexander DC, Thiran JP. Accelerated Microstructure Imaging via Convex Optimization (AMICO) from diffusion MRI data. Neuroimage 2015; 105: 32–44.

Daher A, de Groot J. Rapid identification and validation of novel targeted approaches for Glioblastoma: A combined ex vivo-in vivo pharmaco-omic model. Exp Neurol 2018; 299: 281–288.

Dice LR. Measures of the Amount of Ecologic Association Between Species. 1945; 26: 297–302.

Friedman EB, Dodds TJ, Lo S, Ferguson PM, Beck M, Saw RPM, et al. Correlation Between Surgical and Histologic Margins in Melanoma Wide Excision Specimens. Ann Surg Oncol 2019; 26: 25–32.

Hilario a., Sepulveda JM, Perez-Nuñez a., Salvador E, Millan JM, Hernandez-Lain a., et al. A prognostic model based on preoperative MRI predicts overall survival in patients with diffuse gliomas. Am J Neuroradiol 2014; 35: 1096–1102.

Hsu P-K, Huang H-C, Hsieh C-C, Hsu H-S, Wu Y-C, Huang M-H, et al. Effect of formalin fixation on tumor size determination in stage I Non-Small Cell Lung Cancer. Ann Thorac Surg 2007; 84: 1825–1829.

Kono K, Inoue Y, Nakayama K, Shakudo M, Morino M, Ohata K, et al. The role of diffusion-weighted imaging in patients with brain tumors. AJNR Am J Neuroradiol 2001; 22: 1081–8.

Langen K-J, Galldiks N, Hattingen E, Shah NJ. Advances in neuro-oncology imaging. Nat Rev Neurol 2017; 13: 279–289.

Lee EJ, TerBrugge K, Mikulis D, Choi DS, Bae JM, Lee SK, et al. Diagnostic value of peritumoral minimum Apparent Diffusion Coefficient for differentiation of Glioblastoma

Multiforme from solitary metastatic lesions. Am J Roentgenol 2011; 196: 71–76.

Louis DN, Perry A, Reifenberger G, von Deimling A, Figarella-Branger D, Cavenee WK, et al. The 2016 World Health Organization Classification of Tumors of the Central Nervous System: a summary. Acta Neuropathol 2016; 131: 1–18.

Mabray MC, Barajas RF, Cha S. Modern brain tumor imaging. Brain tumor Res Treat 2015; 3: 8–23.

Oh J, Cha S, Aiken AH, Han ET, Crane JC, Stainsby J a., et al. Quantitative apparent diffusion coefficients and T2 relaxation times in characterizing contrast enhancing brain tumors and regions of peritumoral edema. J Magn Reson Imaging 2005; 21: 701–708.

Panagiotaki E, Chan RW, Dikaios N, Ahmed HU, O'Callaghan J, Freeman A, et al. Microstructural characterization of normal and malignant human prostate tissue with vascular, extracellular, and restricted diffusion for cytometry in tumours magnetic resonance imaging. Invest Radiol 2015; 50: 218–227.

Panagiotaki E, Ianus A, Johnston E, Chan R, Atkinson D, Punwani S, et al. Optimised VERDICT MRI protocol for prostate cancer characterisation. In: Proceedings of the 23rd meeting of the International society for magnetic resonance in medicine 2015. 2015. p. 2872

Panagiotaki E, Walker-Samuel S, Siow B, Johnson SP, Rajkumar V, Pedley RB, et al. Noninvasive quantification of solid tumor microstructure using VERDICT MRI. Cancer Res 2014; 74: 1902–1912.

Park HS, Lee S, Haam S, Lee GD. Effect of formalin fixation and tumour size in small-sized non-small-cell lung cancer: a prospective, single-centre study. Histopathology 2017; 71: 437–445.

Paulus W, Peiffer J. Intratumoral histologic heterogeneity of gliomas. A quantitative study. Cancer 1989; 64: 442–447.

Pritt B, Tessitore JJ, Weaver DL, Blaszyk H. The effect of tissue fixation and processing on breast cancer size. Hum Pathol 2005; 36: 756–760.

Quester R, Schröder R. The shrinkage of the human brain stem during formalin fixation and embedding in paraffin. J Neurosci Methods 1997; 75: 81–89.

Roberts T, Hyare H, Hipwell B, Ianus A, Breen-norris J, Panagiotaki E, et al. Quantification of tumour microstructure in low and high-grade brain tumours using VERDICT MRI: an initial feasibility study. Neuro Oncol 2018; 20: i16.

Server A, Kulle B, Mæhlen J, Josefsen R, Schellhorn T, Kumar T, et al. Quantitative Apparent Diffusion Coefficients in the characterization of brain tumors and associated peritumoral edema. Acta radiol 2009; 50: 682–689.

Sottoriva A, Spiteri I, Piccirillo SGM, Touloumis A, Collins VP, Marioni JC, et al. Intratumor heterogeneity in human glioblastoma reflects cancer evolutionary dynamics. Proc Natl Acad Sci U S A 2013; 110: 4009–14.

Tran T, Sundaram CP, Bahler CD, Eble JN, Grignon DJ, Francesca Monn M, et al. Correcting the shrinkage effects of formalin fixation and tissue processing for renal tumors: Toward standardization of pathological reporting of tumor size. J Cancer 2015; 6: 759–766.

Umstattd LA, Mills JC, Critchlow WA, Renner GJ, Zitsch RP. Shrinkage in oral squamous cell carcinoma: An analysis of tumor and margin measurements in vivo, post-resection, and post-formalin fixation. Am J Otolaryngol - Head Neck Med Surg 2017; 38: 660–662.

Zhang L, Min Z, Tang M, Chen S, Lei X, Zhang X. The utility of diffusion MRI with quantitative ADC measurements for differentiating high-grade from low-grade cerebral gliomas: Evidence from a meta-analysis. J Neurol Sci 2017; 375: 103–106.

Zijdenbos a P, Dawant BM, Margolin R a, Palmer a C. Morphometric analysis of white matter lesions in MR images: method and validation. IEEE Trans Med Imaging 1994; 13: 716–24.

Zou KH, Warfield SK, Bharatha A, Tempany CMC, Kaus MR, Haker SJ, et al. Statistical validation of image segmentation quality based on a spatial overlap index. Acad Radiol 2004; 11: 178–89.

^{23}Na-MRI as a biomarker of tumour heterogeneity and survival

UNIVERSITY OF CAMBRIDGE

Chapter 4

^{23}Na-MRI as a biomarker of tumour heterogeneity and survival

Gliomas are tumours that arise from the cells that surround and support the neurons termed glial cells which include astrocytes (origin of astrocytomas and glioblastomas), oligodendrocytes (origin of oligonderoglioma), and ependymocytes (origin of ependymomas). Among primary brain tumours, gliomas are the most common, accounting for nearly 70% of central nervous cancers, of which glioblastoma (GBM) is the most frequent and malignant histologic type (Ohgaki, 2009; Dolecek *et al.*, 2013; Ostrom *et al.*, 2015; Tamimi and Juweid, 2017). Gliomas are a heterogeneous group (Bigner, 1981; Heppner, 1984) and according to the WHO 2016 classification of tumours of the central nervous system, are currently classified by integrating phenotypic and genotypic parameters into groups with similar prognosis and treatments (Louis *et al.*, 2016). In order to determine the malignancy and select the best treatment, gliomas are given a grade between I and IV: grade I being the least aggressive (virtually non-existent in adults) and grade IV the most aggressive anaplastic tumours (Louis *et al.*, 2016). Based on the histological appearances, gliomas are divided into: diffuse glioma (grade II or III), also termed lower-grade glioma (LrGG); and glioblastoma (Grade IV), also termed high-grade glioma (HGG) (Arevalo *et al.*, 2017). There has been a recent shift in classification with an increasing role for molecular biomarkers, which highlights the biological complexity of gliomas.

The contribution of ion channel expression and ion imbalance in cancer formation and development is increasingly being understood: several ions have been shown to be key in a number of fundamental cancer processes (Prevarskaya *et al.*, 2010). Among others, sodium is critical for normal cellular function and its dysregulation has been observed in several cancers. For

instance, prostate, breast and ovarian cancers with high metastatic phenotypes have increased expression of embryonic forms of voltage-gated sodium channels (VGSCs) and a striking increase in sodium concentration within the tumours (Diss *et al.*, 2005; Fraser *et al.*, 2005; N Ahmed *et al.*, 2007). Similarly, high-grade glioma cells have been shown to overexpress non-voltage-gated sodium channels of the degenerin superfamily, which are normally absent in astrocytes, and their knockdown inhibits glioma growth and cell migration opening up new potential treatment strategies for malignant gliomas (Vila-Carriles et al., 2006; Kapoor et al., 2009). Moreover, an increase in the tissue sodium concentration may also be a consequence of increased extracellular interstitial fluid volume: this can be due to several processes including protein leakage into the interstitium secondary to permeable blood brain barrier or cell death with the sudden release of the intracellular fluid (Leslie *et al.*, 2019). Gliomas are typically associated with oedema which is due to an enlarged interstitial fluid compartment (Papadopoulos *et al.*, 2004). Furthermore, HGGs are characterized by the presence of necrosis, which contributes to the expansion of the extracellular fluid compartment and increases the extracellular sodium concentration. Despite the mounting evidence that sodium may play a significant role in tumours and that its concentration is raised is several malignancies, a tool or technique for routine, non-invasive, *in vivo* measurements of sodium concentration in patients is lacking (Leslie *et al.*, 2019).

Sodium-23 (^{23}Na) is the only stable sodium isotope. ^{23}Na has a quadrupolar nucleus with spin 3/2 that yields the second strongest nuclear magnetic resonance signal from biological tissues, after protons (Madelin and Regatte, 2013). Although natural abundance sodium is detectable with MRI, the sensitivity for sodium is 9.2% of the proton sensitivity and therefore sodium MRI (^{23}Na-MRI) has an average signal-to-noise ratio (SNR), which is up to 20,000 times lower than that for proton. Since the first paper on sodium MRI (Maudsley and Hilal, 1984), brain neoplasms have been a topic of great interest for potential applications of the technique. Although Maudsley and Hilal (Maudsley and Hilal, 1984) showed only images of a healthy cat brain and of a middle cerebral artery ischaemic stroke (induced by manual ligation), their postulation about the signal changes in neoplasms laid the foundation for the subsequent

research in brain tumours. As mentioned above, an increase in cell metabolic activity is associated with changes in Na^+/K^+-ATPase activity: when ATP utilisation for cellular proliferation is increased, the function of the sodium pump may be reduced and, as a consequence of this, changes in the extracellular and intracellular concentration of these ions will be seen (Madelin and Regatte, 2013). Gliomas are characterized by angiogenesis, cell proliferation and increased lactate formation; these factors, in combination with the changes in Na^+/K^+ transport, foster the production of an acidic extracellular environment. Therefore, ^{23}Na-MRI could potentially be a surrogate for non-invasive assessment of mitochondrial ATP production and pH.

In 1991 Schuierer and colleagues (Schuierer *et al.*, 1991) reported the first application of sodium MRI to study human brain tumours using a 4 T whole-body MR scanner. Their cohort of 27 patients comprised gliomas (n = 17, both low and high grade), meningiomas (n = 4) as well as other supratentorial lesions (n = 6). Feasibility and tolerability were confirmed in all patients, however 2 of the smallest meningioma were not visible on the sodium MRI due to the lack of spatial resolution. Moreover, as compared to conventional proton MRI, Sodium MRI failed to show any additional information above that provided by histology, grading, size, and differentiation from the surrounding oedema. However, this was as a result of the technical limitations of these early studies In 2003 Ouwerkerk *et al*. published a seminal paper using improved sodium MRI methodology on a 1.5 T clinical scanner (Ouwerkerk *et al.*, 2003). Although the study claimed to enrol only malignant brain tumours, 6 of the 20 cases were WHO grade II and only 7 were grade IV. Ouwerkerk *et al.* demonstrated that the sodium concentration could differentiate normal parenchyma from malignant tissue. Moreover, they were able to observe high sodium concentration in FLAIR hyperintense but non-enhancing regions confirming a sodium increase both in tumours and oedema. The signal increase was attributed to a combination of changes in the extracellular volume fraction and intracellular sodium concentration, but the two compartments could not be disentangled given the technique used at that time. Interestingly, the signal heterogeneity found in the peritumoral region hinted at potential additional information provided by sodium MRI as compared to conventional proton MRI.

In an attempt to disentangle the effect on the sodium signal due to its extracellular and intracellular component, Nagel *et al.* (Nagel *et al.*, 2011) explored the use of relaxation-weighted ^{23}Na sequences (^{23}NaR) to quantify the intracellular compartment. This sequence used an inversion recovery preparation pulse to exploit the T_1W differences of sodium ions. In their paper, Nagel et al used an inversion time of 41 ms and a repetition time of 185 ms that allowed for suppression of the sodium signal arising from compartments with longitudinal relaxation times such as the CSF. Therefore, the signal that was obtained was supposed to be derived from the intracellular compartment. Their cohort was comprised of low- (7) and high- grade primary brain tumours (7) and 2 metastases. An increased ^{23}NaR signal intensity was observed only in 4 of the 5 glioblastomas and in 1 of the 2 cerebral metastases. This finding was deemed in keeping with the higher proliferation activity seen in high-grade gliomas and in metastases, and was also confirmed by a strong correlation between ^{23}NaR imaging and MIB-1, a known marker of proliferation rate.

The following year, Laymon *et al.* (Laymon *et al.*, 2012) evaluated sodium MRI in combination with [^{18}F]FLT-PET, acquired as separate studies, as imaging biomarkers for therapy evaluation in patients with glioblastoma. The rationale behind this combination is that [^{18}F]FLT-PET is a marker for DNA synthesis and consequently cellular proliferation which does not cross the blood-brain barrier. In contrast, sodium MRI is also a marker of cellular proliferation and viability but as it relies on intrinsic contrast it is not influenced by the blood-brain barrier. Therefore, those two techniques may have a synergic effect providing complementary information. Laymon and colleagues demonstrated that sodium MRI and [^{18}F]FLT-PET imaging biomarkers have some similarities and differences in assessing therapy response of glioblastoma suggesting that the two modalities are complementary. Indeed, assessing the degree of complementarity and overlap of the two modalities in a voxel-wise analysis, they showed a significant heterogeneity across the lesion and were able to identify 4 clusters: increase in [^{18}F]FLT and increase in sodium, increase in [^{18}F]FLT and decrease in sodium, decrease in [^{18}F]FLT and increase in sodium and decrease in [^{18}F]FLT and decrease in sodium. The envisaged that changes in [^{18}F]FLT can be secondary to blood-brain barrier damage (i.e. an increase in [^{18}F]FLT may be due to an increase in breakdown of the blood-brain

barrier) whilst the sodium signal has no relation with the blood brain barrier and it is only due to biological differences. However, the significance of the clusters was deemed to be undetermined.

Sodium MRI has also been investigated as an indirect biomarker of IDH mutation and as a prognostic factor by Biller *et al.* (Biller *et al.*, 2016). Following on from previous work by Nagel *et al.* (Nagel *et al.*, 2011), in this study the ratio between the relaxation-weighted sodium signal (^{23}NaR, deemed to be derived from the intracellular sodium) and the total sodium signal (^{23}NaT) was investigated. Biller and colleagues demonstrated a strong correlation between the proposed ratio and IDH mutation, however they also showed that sodium MRI is superior to IDH mutation status in predicting progression-free survival and improves the accuracy of brain tumour classification. Thus, they concluded that sodium MRI is a promising tool for non-invasive outcome prediction and tumour diagnosis, with the potential to improve patient management.

Neto *et al.* (Neto *et al.*, 2018) proposed a three-compartment model to determine pseudo-intracellular sodium concentration: 1. extracellular volume fraction, 2. apparent intracellular sodium concentration, and 3. apparent total sodium concentration. As expected the solid components of all the tumours showed higher values of apparent total sodium concentration than the normal appearing white matter (Madelin and Regatte, 2013; Madelin *et al.*, 2014). However, the extracellular volume fraction was consistently increased in all the cases and the authors deemed this to be the dominant factor responsible for the apparent total sodium concentration increase. The apparent intracellular sodium concentration was lower than in the normal-appearing white matter in all the cases bar the single glioblastoma recruited (Nagel *et al.*, 2011; Biller *et al.*, 2016). The model presented in this study clearly showed the ability to differentiate between the different compartments; however, as highlighted by the authors, the necessity to assume that the water fraction is constant in the brain parenchyma despite the known differences between grey and white matter, constitutes a significant limitation of this study.

More recently, Thulborn *et al*. (Thulborn *et al.*, 2018) assessed the potential utility of sodium MRI as early biomarker of therapy response in patients with glioblastoma undergoing fractionated chemoradiation. Using a two-compartment model they converted what they called tissue sodium

concentration (TSC; essentially the ^{23}NaT described by Nigel) maps into Cell Volume Fraction maps from which they subsequently derived the Residual Tumour Volume and the Tumour Cell Kill. Interestingly, changes in Cell Volume Fraction, Residual Tumour Volume and Tumour Cell Kill were seen during the course of the 6-week regimen, but they were not correlated with prognosis; over the same period of time, there was little biological variation in the normal appearing tissue ruling out the possibility of inaccurate measurement. The lack of a correlation with prognosis may reflect the heterogeneity of glioblastoma with its extremely high response variability to treatments. Nevertheless, the capability of sodium imaging to detect changes during treatment, whilst the lesion size remains stable in size, highlighted the potential use of sodium imaging as an early biomarker for therapy assessment.

Thanks to the technical advances in scanner technology, in particular the wider availability of high-performance ≥ 3 T magnets, and acquisition strategies, such as the 3D-cones trajectory (Gurney *et al.*, 2006; Riemer *et al.*, 2014), over the past three decades, sodium MRI is now feasible in a clinical environment with 3 T clinical scanners. Moreover, the development of new sequences has allowed accurate measurements of sodium in both the intracellular and extracellular compartments, enabling a deeper understanding of both the lesion and the surrounding microenvironment. Gliomas are known to have an increase in cell mitotic activity, this should later the intracellular sodium concentration that is detectable with sodium imaging. Furthermore, changes in the ^{23}Na-MRI signal in the region surrounding gliomas can be an indirect measure of the presence of cancer cells in the peritumoral brain zone, with the possibility of radically changing the management of patients with glioma. Therefore, the primary aim of this study was to non-invasively measure the distribution of tissue sodium concentration and intracellular-weighted sodium concentration within gliomas and in the peritumoral brain parenchyma. Additionally, as we hypothesised that sodium is a biomarker for cell proliferation, our secondary aim was to assess the capability of sodium MRI to predict overall survival in patients with LrGG and HGG.

4.1 Methods and materials

4.1.1 Patient selection

Inclusion criteria
- 18 years or older; - Be scheduled for biopsy or resection of a presumed glioma of any grade (based on imaging features consisting with glioma); - Be aware of, and understand the diagnosis; - Be able to provide written informed consent according to ICH/GCP, national and local regulations; - Be willing and able to comply with scheduled visits, laboratory tests, imaging and other study procedure; - Patients of childbearing potential must have a negative urinary or blood pregnancy test prior to enrolment if there is a possibility they could be pregnant.
Exclusion Criteria
Clinical contraindications to MR imaging will apply to each patient and include, but are not limited to: - Pacemakers, non-MR compatible heart valves or cardiac stent or other vascular stent; - Renal impairment; - Known allergic reactions to Gd contrast agent; - Intracranial aneurysm clips that are not MR safe; - Intracranial programmable shunt; - History of intra-orbital metal fragments that have not been removed; - Inner ear implants; - Artificial joint/limb prosthesis not MR safe; - Neuro-stimulator or other under the skin devices; - False eye; - Claustrophobia; - Inability to give informed consent.

Table 4.1: Inclusion and exclusion criteria for enrolment in the study.

Patients presented in this work were enrolled under three prospective studies approved by our local Research Ethics Committee (East of England, Cambridge South Research Ethics Committee; REC reference numbers 16/EE/0184, 15/EE/0378 and 07/H0308/245) as part of a larger brain tumour imaging initiative. Between October 2015 and October 2018 sixty-five

treatment-naïve patients (36 males, 29 females; 54.8 ± 16.9 years) with a presumed diagnosis of a glioma of any grade were recruited from the weekly Multidisciplinary Team (MDT) meeting and/or from the Neuro-oncology clinic. Only patients scheduled for stereotactic biopsy or resection of a glioma, based on previous imaging featuring a lesion in keeping with a glioma with MDT consensus of the likely diagnosis, were screened to assess eligibility by a member of the research team. The inclusion and exclusion criteria used to assess eligibility are shown in table 4.1. During the Neuro-oncology clinic appointment, all the eligible patients received a detailed participant information sheet, describing the study rationale and procedure, and had a dedicated encounter with a member of the research team to discuss the study rationale, potential involvement and expected outcome. Written informed consent was signed by all the participants before enrolling in the study and after ample time for reflection and questioning.

4.1.2 ^{1}H and ^{23}Na MRI acquisitions

All the MRI examinations were performed using a 3 T clinical scanner (GE Discovery MR750; GE Healthcare, Waukesha, WI, USA) using a dual-tuned ^{23}Na/^{1}H quadrature transmit/receive head coil (Rapid Biomedical, Rimpar, Germany) for the ^{23}Na MRI and a 12-channel head coil for the ^{1}H imaging.

Sodium imaging was performed using two independent acquisition both based on an ultra-short echo time sequence with 3D-Cones readout (Riemer *et al.*, 2014); acquisition parameters were as follow: TE = 0.5 ms, TR = 100 ms, 3 mm nominal isotropic resolution, FOV = 28 cm. The intracellular weighted sodium images were obtained with similar parameters using fluid suppression by inversion recovery (IR). The two sequences exploit the different T_1 effect of sodium in the intracellular and extracellular spaces. In particular, the IR sequence eliminates the signal from extracellular fluid exploiting the T_1 relaxation differences between CSF and tissues. To achieve fluid suppression, the T_1 value for CSF was firstly established and then an IR pulse was set accordingly. The suppression of the extracellular fluid leads to an estimation of the concentration of the sodium contained within the intracellular space. Scan duration was between 12 and 16 minutes according to scan coverage and

individual specific absorption rate (SAR). To convert the signal intensity into apparent sodium concentration, external calibrants with a known concentration of sodium are needed. For this study, the calibration phantoms were made from a stock of 20 mM and 80 mM sodium chloride (NaCl) in water with 4% agar and 1% nickel sulphate ($NiSO_4$). Each of the phantoms were cylindrical tubes of 30 ml capacity filled with the stock solution. During the acquisition, those were strapped to the headphones worn by the subjects so they were included in the imaging field of view (FOV). Phantoms were changed regularly to exclude the possibility of dehydration. Nevertheless, the mathematical method used to create the map is independent of the phantom concentration. The formula uses the signal intensities of the phantoms as a reference for the signal intensities within the body, therefore as long as the phantom concentration is within the physiological range there is not a detrimental effect on the quantitative maps. It is worth mentioning that there are other potential methods to separate the signal of the intracellular (bound) sodium and the extracellular (free) sodium. In particular, a hybrid technique combining diffusion and sodium imaging would aid in distinguishing the two pools of sodium molecules. Advanced model-based diffusion imaging (i.e. neurite orientation dispersion and density imaging [NODDI] or VERDICT, discussed in chapters 2 and 3) could be used to calculate the compartmentalisation of tissue within each voxel (intracellular vs extracellular volume fraction) and in turn, this information could be combined with the total sodium concentration to disentangle the sodium concentration in the different compartments.

The ^{23}Na MRI acquisition was followed by conventional proton imaging including: 3D T_2-weighted imaging (T_2W; repetition time/echo time [TR/TE] 2500/79 ms; 248 slices; slice thickness 1.2 mm; acquisition matrix 320 x 320; field of view [FOV] 240 x 240 mm), 2D T_2W fluid-attenuated inversion recovery (T_2W FLAIR; TR/TE 8000/126 ms; inversion time [TI] 2128 ms; slice thickness 6 mm; acquisition matrix 384 x 224; FOV 240 x 240 mm) and Diffusion-Weighted Imaging (DWI, TR/TE 2841-3867/83.3-87.4 ms; slice thickness 5 mm; b-values 0, 1000 s/mm^2; matrix 128 x 128; FOV 240 x 240 mm). 3D T_1-weighted Fast SPoiled GRadient echo (3D T_1W FSPGR; 252 slices; 0.94 x 0.94 x1.5 mm reconstructed to 0.94 x 0.94 x 1 mm; TR/TE 8.2/3.2; slice thickness 1.5 mm;

matrix 256 x 256; FOV 240 x 240 mm) was performed before and after gadolinium-based contrast injection (Gadobutrol 1.0 mmol mL^{-1}; Schering).

4.1.3 Image processing and analysis

The post processing was performed in Matlab (Matlab 2017a, the MathWorks, Natick, MA) using in-house scripts allowing for the automatic segmentation of the phantoms, including erosion of the voxels at the periphery of the phantoms to avoid partial volume due to intensity thresholding. Tissue sodium concentration (TSC) and intracellular-weighted sodium concentration maps were subsequently generated using Matlab as previously described by Inglese *et al.* (Inglese *et al.*, 2010). Briefly, the signal intensity of the calibrants was used to create a two-point linear calibration curve that was then used to convert signal intensity to sodium concentration voxel-wise. Noise compensation was performed by subtracting the average signal intensities derived from regions of interest (ROIs) drawn within air inside the FOV.

In order to facilitate image analysis and ROI drawing, the sodium images were registered to their corresponding T_2WI and T_1WI post-contrast images using SPM8 (The Wellcome Trust Centre for Neuroimaging, University College London, London, UK). Due to the different head positioning within the dual-tuned $^{23}Na/^{1}H$ quadrature transmit/receive head coil and the ^{1}H 12-channel head coil, the first step of the registration process involved the realignment of the 3D T_2WI and the post gadolinium 3D T_1W FSPGR to the sodium images. Firstly, the 3D T_2W sequence was warped and realigned to the tissue sodium concentration maps. Those two sequences were chosen as pivotal for realignment, warping and, subsequently, co-registration due to the similar contrast intensity. The CSF contains the highest concentration of sodium in the head and is hyperintense on the maps and on the T_2WI. Once the alignment and warping of the T_2WI was deemed satisfactory, the 3D T_2WI and the post gadolinium 3D T_1W FSPGR were co-registered. Subsequently, the 3D T_2WI and the tissue sodium concentration maps were registered propagating the translational parameters to the associated 3D T_1W FSPGR and intracellular-weighted sodium concentration. Re-alignment, warping and registration of the ^{1}H and ^{23}Na images was an iterative process that required intensive

computation and carefully evaluation by a trained neuroradiologist to ensure the highest quality of registration. The choice of performing most of the re-alignment, warping and registration on the ^{1}H images was made to avoid excessive manipulation of the quantitative sodium maps to ensure that the measured values on the images corresponded to the acquired data and not biased by interpolation.

A neuroradiologist with 7 years of experience in neuro-imaging outlined all the ROIs to generate the volumes of interest (VOIs) using OsiriX (V.8.5.2, Pixmeo SARL, Bernex, Switzerland). The unenhanced, registered, 3D T_1W FSPGR acquired with the dual-tuned $^{23}Na/^{1}H$ coil and the registered 3D T_2W acquired with the ^{1}H coil were used to define the ROIs. The T_2W hyperintense lesion was defined on the T_2WI as the region including the lesion and the hyperintense peritumoral brain zone. The same sequence was used also for the normal-appearing white matter (NAWM) that was assessed in the contralateral corona radiata. The enhancing lesion and the non-enhancing core were evaluated on the post gadolinium 3D T_1WI; as per conventional definition, the former was defined as the contrast enhancing component of the lesion whilst the latter was defined as the non-enhancing core tissue using the signal intensity on the T_2WI as additional guidance.

The normal-appearing grey matter (NAGM) was assessed in the contralateral basal ganglia on the post gadolinium 3D T_1W FSPGR. Those structures were chosen, as opposed to the cortical white matter, to maximise the reliability of the analysis while minimizing the risk of partial volume from the CSF contained in the sulci. Automatic segmentation of white matter and grey matter is challenging in patients with large space-occupying lesions due to mass effect and distortion of the normal anatomy. Moreover, the cortex is usually thin measuring between 1 and 4.5 mm (Fischl and Dale, 2000). The nominal isotropic resolution of our sodium imaging is 3 mm, therefore the measured sodium concentration in the cortical grey matter would have been heavily influenced by the high sodium concentration in the CSF. However, the basal ganglia can be reliably identified on the post gadolinium 3D T_1W images and segmented allowing for enough distance from the lateral ventricles to avoid any partial volume effect.

The generated VOIs were stored and applied to the corresponding registered tissue sodium concentration and intracellular-weighted sodium concentration maps using OsiriX. Mean, standard deviation, minimum and maximum values were extracted for every voxel using a custom plugin and recorded in dedicated spreadsheets.

Due to the exploratory nature of this study, the inter-observer agreement was not tested, in line with the previously published data on this technique.

4.1.4 Histopathology

All the enrolled patients underwent surgery (either stereotactic burr hole biopsy or debulking resection) and tissue samples were analysed by a neuropathologist with 7 years of experience to determine tumour type and grade according to the WHO 2016 classification of tumours of the central nervous system (Louis *et al.*, 2016). Patients enrolled before the new classification came into force were reassessed and re-classified according to the new classification. Accounting for the new WHO 2016 classification, the molecular biomarkers and the recent guidelines for management, gliomas were classified as lower-grade (LrGG) and high-grade (HGG) (Louis *et al.*, 2016).

Haematoxylin and eosin staining (H&E) was performed as per clinical standard. Analysis of the isocitrate dehydrogenase 1 (IDH1 R132H) and O^6-methylguanin-DNA-methyltransferase (MGMT) methylation status were performed in all cases. In addition, ATP-dependent helicase (ATRX), glial fibrillary acidic protein (GFAP), deletion of 1p36 and amplification of 19q13 chromosomal locus were tested as determined by the pathologist according to the tumour grade and type or if the MDT deemed this necessary to better plan the treatment. The monoclonal antibody MIB-1 was used to measure the Ki-67 expression which in turn determined the Ki-67 labelling index as a marker of proliferation. MIB-1 staining was assessed on tumour photomicrographs from a x600 FOV and a fixed matrix of 184x138 μm using a semi-automated software (Image-Pro Insight) and expressed in percentage.

4.1.5 Statistical Analysis

All data were recorded in digital spreadsheets (Excel 16.16.7 for Mac OS; Microsoft Corporation, Redmond, WA, USA) and the statistical analysis was performed using a dedicated statistical analytical software (SPSS 18.0 statistical package; SPSS Inc, Chicago, IL, USA). The Shapiro–Wilk test was used to test for normality of data. Continuous data are expressed as mean ± standard deviation [minimum – maximum] for normally distributed data and median [minimum - maximum] for non-parametric data; categorical data are expressed an *n* (%).

Paired and unpaired t-test were used to compare the sodium concentration between LrGGs and HGGs and to assess differences in concentration among brain tumours and normal appearing brain parenchyma as appropriate according to the nature of the data. To determine the statistical significance of all the tests, a base set value of $p = 0.05$ was initially chosen and subsequently corrected for multiple comparison. The false discovery rate (FDR) method using the Benjamini-Hochberg procedure was applied to test significance (Benjamini and Hochberg, 1995). The FDR represents the proportion of significant results that are actually false positives. Carefully consideration has been given to which proportion of false positive we were willing to accept for this study. An FDR of 5% is generally believed too low for many experiments having multiple correlations because this is applied on top of a p value which is usually already chosen as low as 0.05 lead to an over rejection rate (McDonald, 2014). However, considering the strong significance on the determined p values and deeming the n of this study ample enough to explore the relationship between sodium concentration in brain tumours and normal appearing tissue, we choose the strictest FDR (5%) to ensure that significant results of this study would be most likely to be significant in further following studies. Of note, the p values that are presented in this study are raw p values and only the significance is stated according to the Benjamini-Hochberg procedure. No Benjamini-Hochberg adjusted p values have been provided to avoid the potential confusion that those modified p values could generate in readers not familiar with the procedure.

A survival analysis was performed to explore the prognostication capability of sodium imaging. IDH status and tumour grade after pathology were also analysed for prognostication to provide a comparison with current clinical reference standards and confirm the generalisability of the recruited cohort. The Kaplan-Meier survival analysis was used for each of the assessed parameters.

A total of 20 imaging parameters derived from sodium imaging were chosen for the analysis: TSC and IW-SC for T_2W hyperintense VOI, enhancing lesion, non-enhancing core, ratio between T_2W hyperintense VOI and NAWM, ratio between enhancing lesion and NAWM, ratio between T_2W hyperintense VOI and basal ganglia, ratio between enhancing lesion and basal ganglia and ratio between T_2W hyperintense VOI and non-enhancing core; ratio between TSC and IW-SC and between IW-SC and TSC for both the T_2W hyperintense VOI and the enhancing lesion. The optimal cut-offs to divide the cohort in two groups according to their survival was chosen performing a receiver operating characteristic (ROC) analysis and determining the best Youden's index for each parameter. The Youden's index is a single statistic that captures the performance of a dichotomous diagnostic test (W. J. Youden, 1950). The index is designed to maximise the number of correctly classified results, either positive or negative, attributing equal weight to false positive and false negative results. In this context, the Youden's index would maximise the chance of sodium imaging to predict prognosis either as survival or death. The index was computed with a custom SPSS script for all points of each ROC curves; the maximum value was used for selecting the optimum cut-off point to be the threshold for the Kaplan-Meier analysis in the following steps. Kaplan-Meier curves dividing patients according to the optimal threshold were generated to facilitate the visualization of the survival trend of the two populations. The curves with the most significant capability of predicting the survival status are shown in this chapter.

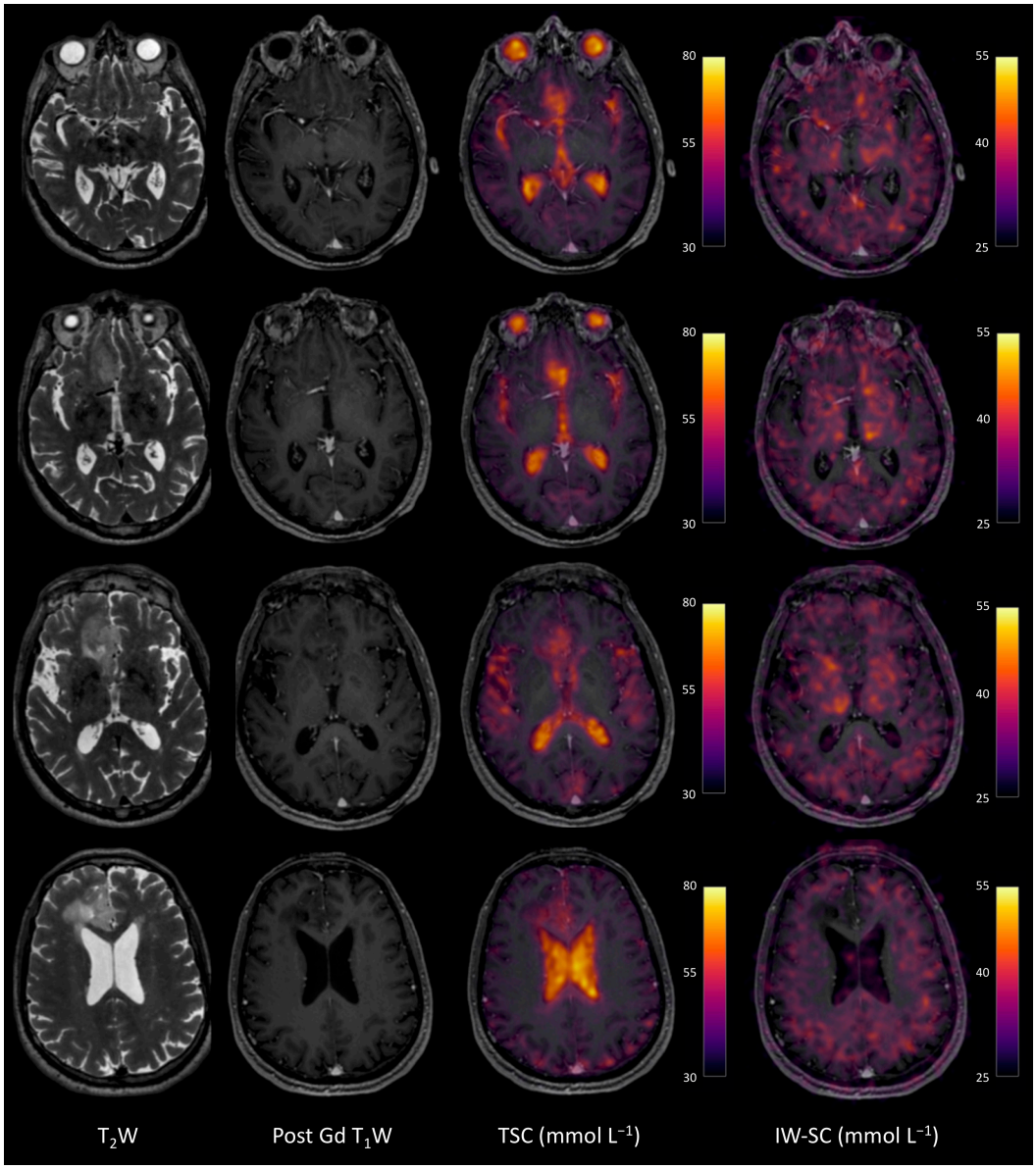

Figure 4.1: Representative case of lower-grade glioma (LrGG).
Axial T_2-weighted images (T_2W; axial post gadolinium 3D T_1-weighted Fast SPoiled GRadient echo images (Post Gd T_1W); axial post Gd T_1W overlaid with tissue sodium concentration overlaid (TSC); and axial post Gd T_1W overlaid with intracellular-weighted sodium concentration (IW-SC). A heterogenous T_2-weighted hyperintense lesion in the right superior frontal gyrus is shown extending downwards towards the frontal pole; no contrast enhancement is seen after gadolinium injection. The lesion does not have mass effect on the adjacent parenchyma although there is sulcal effacement. On the proton images the corpus callosum appears spared. The TSC images demonstrates the lesion with similar conspicuity as on the T_2W, however, the increase in sodium concentration is seen extending beyond the T_2W hyperintensity, particularly downwards and within the corpus callosum. Of note, the high sodium concentration within the ventricles, sylvian fissures and eye globes confirming the accurate registration of sodium imaging with the conventional proton MRI. The IW-SC images show almost complete suppression of the sodium concentration within the T_2W hyperintense lesion suggesting that the increase in sodium within the lesion is mostly due to an enlarged interstitial matrix. However, some foci of increased IW-SC could represent areas of potential higher grade cancer cells within the LrGG that might be targets for image-guided biopsies.

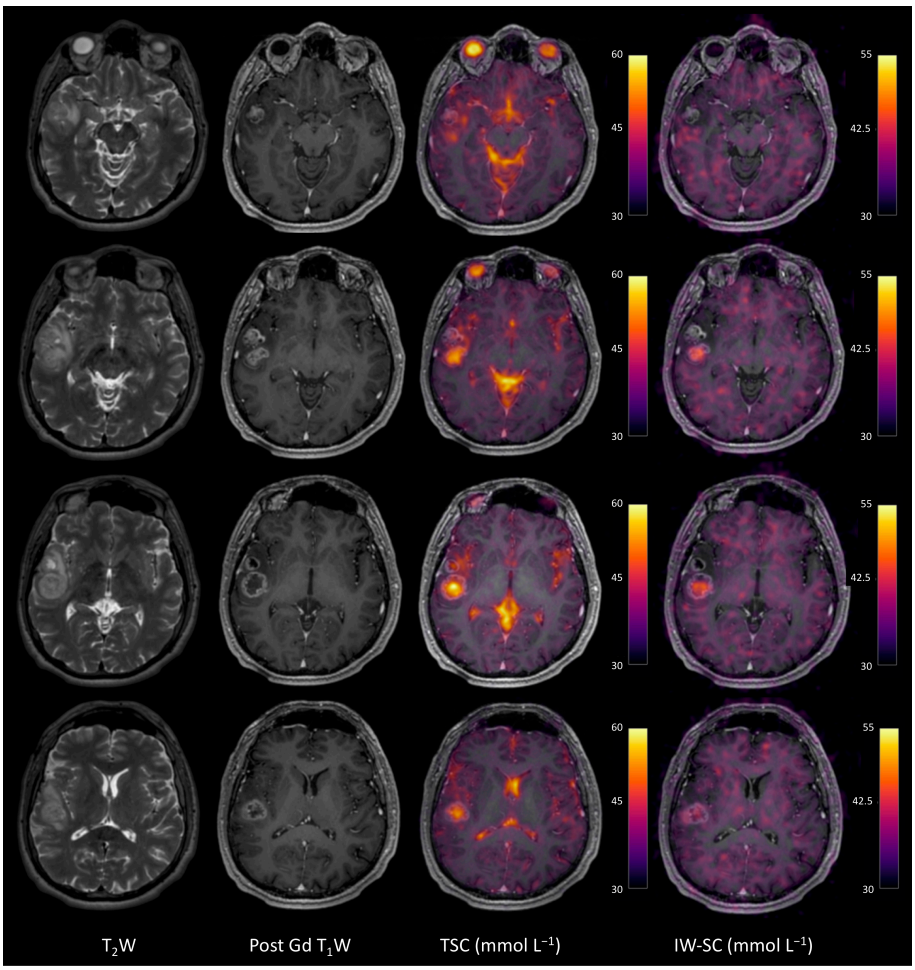

Figure 4.2: Representative case of high-grade glioma (HGG).
Axial T_2-weigthed images (T_2W); axial post gadolinium injection 3D T_1-weighted Fast SPoiled GRadient echo images (Post Gd T_1W); axial post Gd T_1W overlaid with tissue sodium concentration overlaid (TSC); and axial post Gd T_1W overlaid with intracellular-weighted sodium concentration (IW-SC). Large heterogenous T_2-weighted hyperintense lesion in the right middle and superior temporal lobe with mild peritumoral oedema. Gadolinium enhanced images demonstrate the presence of two round lesions with complete ring enhancement and hypointense central core in keeping with multifocal GBM. Adjacent sulci are effaced and there is mild expansion of the temporal lobe with mild compressive effects on the right insula. The TSC images demonstrates diffuse heterogeneity within the T_2W hyperintense area with the posterior lesion exhibiting a higher tissue sodium concentration when compared with the anterior one. There is increased sodium concentration in the non-enhancing T_2W hyperintense area between the smaller lesion and the sylvian fissure. Interestingly, on the IW-SC images the anterior lesion shows complete suppression whilst the larger one still has a discreet signal corresponding to increased intracellular sodium concentration. This could be due to the different content of the tissue with the anterior core being entirely necrotic (hence the suppression) and the core of the posterior lesion containing tumour and inflammatory cells. Of note, the discrepancy could be appreciated also on the T_2W images showing higher signal intensity in the anterior lesion, and on the post Gd T_1W images showing intermediate signal within the core of the larger signal. This case clearly demonstrates the potential of sodium imaging to detect necrosis and therefore therapy response. Moreover, the heterogenous sodium signal within the area of T_2W hyperintensity and the discrepancy between the TSC and IW-SC could help in differentiating oedema from cancer/inflammation and aid in the planning of biopsies, surgery and radiotherapy.

4.2 Results

4.2.1 Characteristic of the cohort

Of the sixty-five recruited patients, 2 patients were not able to tolerate the scan due to claustrophobia and in 3 cases the acquisition failed due to technical reasons, therefore 60 patients (34 male, 55.7%) successfully completed the research MRI. Mean age at diagnosis of the successfully scanned cohort was 55.3 ± 17.2 (18 - 79) years; patients with LrGG were significantly younger (38.7 ± 15.9 vs 64 ± 9.9, $p < 0.001$). All the enrolled patients underwent surgery (either burr hole biopsy or debulking resection) and tissue was analysed according to the WHO 2016 classification of tumours of the central nervous system (Louis *et al.*, 2016). At pathology, 36 patients were classified as higher-grade (WHO grade IV) primary CNS tumours, 19 as lower-grade (Grade II and III) primary CNS tumours and 3 cases were classified as metastases (high-grade serous carcinoma, renal cell carcinoma and lung cancer); 2 cases were reported as non-diagnostic from a consensus of neuro-pathologists and were excluded from the analysis. The 55 primary CNS tumours were: 32 (58.2%) glioblastoma IDH1 R132H wild type, 8 (14.5%) diffuse astrocytoma IDH mutant, 5 (9.1%) anaplastic oligodendroglioma IDH-mutant and 1p/19q co-deleted, 3 (5.5%) gliosarcoma, 1 (1.8%) anaplastic astrocytoma IDH-wildtype, 1 (1.8%) anaplastic astrocytoma IDH mutated, 1 (1.8%) anaplastic ependymoma, 1 (1.8%) oligodendroglioma non otherwise specified, 1 (1.8%) Anaplastic pleomorphic xanthoastrocytoma, 1 (1.8%) gangliocytoma and 1 (1.8%) anaplastic ganglioglioma.

The tissue sodium concentration and the intracellular-weighted sodium concentration for the 3 metastases are reported separately; these 3 cases were not included in the survival analysis. Therefore, the survival analysis was performed in 55 patients with primary brain tumours.

4.2.2 Tissue sodium concentration

Figure 4.1 shows a representative case of LrGGs (patient GS-56, a diffuse astrocytoma IDH mutant) and figure 4.2 shows a representative case of

HGGs (patient MGS-09, Glioblastoma IDH1 R132H wild type). Detailed description of the imaging findings is provided in the respective captions of the two figures.

The tissue sodium concentration in LrGGs, HGGs and metastases is shown in table 4.3. Briefly, the tissue sodium concentration in T_2W hyperintense lesions was higher in the HGGs (58 ± 13 mmol L^{-1} vs 55 ± 1.5 mmol L^{-1} in the LrGGs). The tissue sodium concentration in the enhancing component and in the non-enhancing core were higher in the LrGGs than in the HGGs (66 ± 15 mmol L^{-1} vs 62 ± 17 mmol L^{-1} and 84 ± 11 mmol L^{-1} vs 76 ± 21 mmol L^{-1} respectively). However, there were no statistically significant differences between LrGGs and HGGs. The tissue sodium concentration in the basal ganglia and in the normal appearing white matter was not significantly different between the two groups ($p = 0.45$ and $p = 0.97$ respectively).

Table 4.3 shows the comparison between the sodium concentration in the lesions and the normal appearing brain parenchyma. Both in LrGGs and in HGGs, the tissue sodium concentration in the T_2W hyperintense lesion and in the enhancing lesion were significantly higher compared to basal ganglia (p values < 0.01) and normal appearing white matter (p values < 0.001).

The metastases showed an average tissue sodium concentration of 62 ± 30 mmol L^{-1} in the T_2W hyperintense lesion and 76 ± 37 mmol L^{-1} in the enhancing lesion. Only a single case showed a non-enhancing core.

Region of interest	Tissue Sodium Concentration (mmol L^{-1})			Intracellular-weighted Sodium concentration (mmol L^{-1})			Metastases (n = 3)	
	LrGG (n = 19)	HGG (n = 36)	p values	LrGG (n = 19)	HGG (n = 36)	p values	TSC (mmol L^{-1})	IW-SC (mmol L^{-1})
T_2W hyperintense lesion	55 ± 15	58 ± 13	0.54	21 ± 7	27 ± 15	0.04*	62 ± 30	17 ± 11
Enhancing lesion	66 ± 15	62 ± 17	0.60	18 ± 9	29 ± 15	0.03*	76 ± 37	25 ± 6
Non-enhancing core	84 ± 11	76 ± 21	0.35	10 ± 7	32 ± 17	0.01*	67‡	25‡
Basal ganglia	34 ± 5	33 ± 8	0.45	29 ± 10	32 ± 12	0.29	40 ± 8	29 ± 6
Normal appearing white matter	32 ± 6	32 ± 8	0.97	26 ± 8	28 ± 12	0.61	33 ± 4	24 ± 5

Table 4.2: Tissue sodium concentration and intracellular-weighted sodium concentration according to tumour grade (lower-grade glioma - LrGG and high-grade glioma - HGG).

*Concentration values are shown as mean ± standard deviation (minimum - maximum) and expressed in mmol L-1. The level of significance was assessed using unpaired sample t-tests and was set at 0.05. Correction for multiple comparison was performed using a false discovery rate method (FDR) according to the Benjamini-Hochberg procedure. Significant p values are indicated with *. ‡ non-enhancing core was present only in a single case of brain metastasis therefore no SD or range is given.*

4.2.3 Intracellular-weighted sodium concentration

The intra-cellular weighted sodium concentration in LrGGs, HGGs and metastases is shown in table 4.2. The intra-cellular weighted sodium concentration was significantly higher in all the three VOIs of the HGGs as compared to the LrGGs ($p = 0.04$ for the T_2W hyperintense lesion, $p = 0.03$ for the enhancing lesion and $p = 0.01$ for the non-enhancing core). The intra-cellular weighted sodium concentration in the normal appearing tissue did not significantly differ ($p = 0.29$ for the basal ganglia and $p = 0.61$ for the normal appearing white matter).

	p values for LrGG		**p values for HGG**	
	TSC	**IW-SC**	**TSC**	**IW-SC**
T_2W hyperintense lesion vs basal ganglia	< 0.001*	< 0.001*	< 0.0001**	0.01*
T_2W hyperintense lesion vs normal appearing white matter	< 0.0001**	< 0.0001**	< 0.0001**	0.86
Enhancing lesion vs basal ganglia	0.01*	0.01*	< 0.0001**	0.14
Enhancing lesion vs normal appearing white matter	< 0.001*	0.11	< 0.0001**	0.36

Table 4.3: Comparison between sodium concentration in glioma and in normal tissue.
The table shows the p values for the comparison between tissue sodium concentration (TSC) and intracellular-weighted sodium concentration (IW-SC) in gliomas (lower-grade gliomas - LrGG and high-grade glioma - HGG) and in the normal appearing tissue assessed at the level of the contralateral basal ganglia and contralateral corona radiata. The level of significance was assessed using unpaired sample t-tests and was set at 0.05. Correction for multiple comparison was performed using a false discovery rate method (FDR) according to the Benjamini-Hochberg procedure.

As shown in Table 4.3, for the LrGGs, the intra-cellular weighted sodium concentration in the T_2W hyperintense lesion and in the enhancing lesion were significantly lower compared to basal ganglia (p values < 0.001 and $p = 0.01$, respectively); but only the T_2W hyperintense lesion was significantly lower than normal appearing white matter ($p = 0.01$). The intra-cellular weighted sodium concentration in the HGGs was significantly different only when comparing the T_2W hyperintense lesion with the basal ganglia ($p = 0.01$).

	Cut-off	p value
Tissue sodium concentration		
T_2W hyperintense VOI	50.6	0.04*
Enhancing lesion	56.2	0.87
Non-enhancing core	74.5	0.81
Ratio between T_2W hyperintense VOI and NAWM	1.7	0.43
Ratio between enhancing lesion and NAWM	1.4	0.60
Ratio between T_2W hyperintense VOI and basal ganglia	1.6	0.03*
Ratio between enhancing lesion and basal ganglia	1.4	0.58
Ratio between T_2W hyperintense VOI and Non-enhancing core	0.9	< 0.001**
Intracellular-weighted sodium concentration		
T_2W hyperintense VOI	74.5	0.27
Enhancing lesion	24.8	< 0.01*
Non-enhancing core	25.4	0.13
Ratio between T_2W hyperintense VOI and NAWM	0.9	0.02*
Ratio between enhancing lesion and NAWM	1	< 0.01*
Ratio between T_2W hyperintense VOI and basal ganglia	1.1	0.02*
Ratio between enhancing lesion and basal ganglia	1.1	< 0.001**
Ratio between T_2W hyperintense VOI and Non-enhancing core	0.9	0.98
T_2W hyperintense VOI		
Ratio between TSC and IW-SC	2.9	0.11
Ratio between IW-SC and TSC	0.45	0.12
Enhancing lesion		
Ratio between TSC and IW-SC	7.4	0.09
Ratio between IW-SC and TSC	0.3	< 0.01*

Table 4.4: Optimal cut-offs obtained from the receiver operating characteristics curve analysis and Youden's index assessment.

The table shows the best cut-off obtained from the Youden's index assessment, performed on the receiver operating characteristic curve analysis. The cut-offs shown here were used for the Kaplan-Meier survival analysis and the p values are relative to the survival analysis, i.e. if a p value is significant the corresponding cut-off is able to correctly predict survival status. The level of significance was set at 0.05.

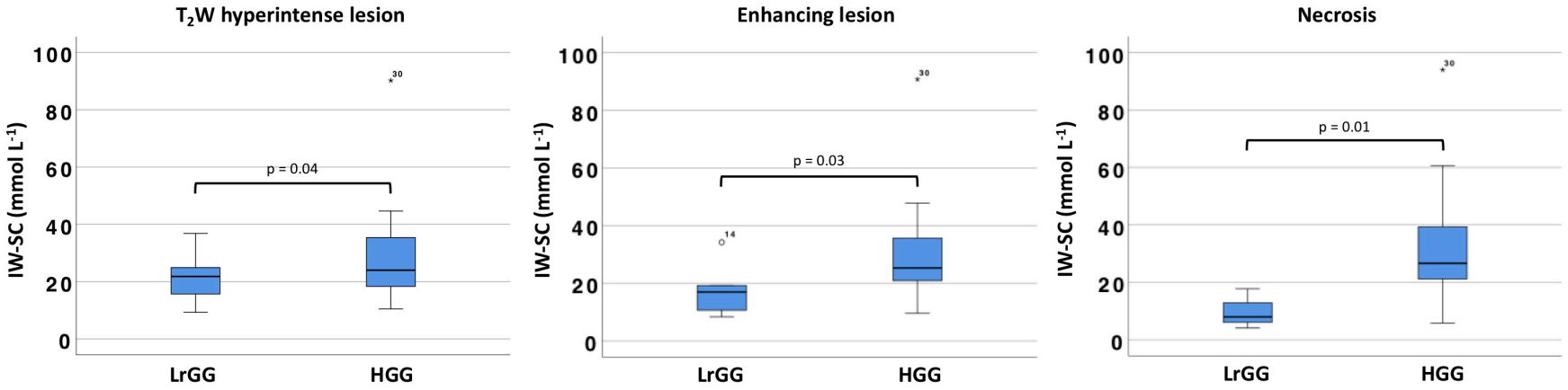

Figure 4.3: Boxplot of intracellular-weighted sodium concentration (IW-SC) according to tumour grade.

The boxplot show minimal overlap between the IW-SC of the T_2W hyperintense lesion between lower-grade gliomas (LrGG) and high grade gliomas (HGG). Negligible overlap is demonstrated for the enhancing component of the lesion and for the necrotic core. The level of significance was assessed using unpaired sample t-tests and was set at 0.05. Correction for multiple comparison was performed using a false discovery rate method (FDR) according to the Benjamini-Hochberg procedure.

The metastases showed an average intracellular weighted sodium concentration of 17 ± 11 mmol L^{-1} in the T_2W hyperintense lesion and 25 ± 6 mmol L^{-1} in the enhancing lesion. The intracellular weighted sodium concentration in the single case with central non-enhancing core was 25 mmol L^{-1}.

4.2.4 Survival analysis

Table 4.4 shows the best cut-off obtained from the ROC analysis and subsequent Youden's index assessment paired with the p values resulting from their use in the Kaplan-Meier analysis. Figures 4 to 6 show the Kaplan-Meier curves for: the current clinical reference standard (IDH and WHO 2016 grading; figure 4.4), tissue sodium concentration (figure 4.5) and intracellular-weighted sodium concentration (figure 4.6).

As expected, higher-grade primary brain tumours according to the WHO 2016 criteria and the absence of the IDH1 R132H mutation (IDH wildtype) are strong predictor of worse prognosis ($p < 0.0001$ for both the biomarkers).

The tissue sodium concentration in the T_2W hyperintense lesion is a significant prognostic predictor (figure 4.5), with sodium concentration values higher than 50.6 mmol L^{-1} predicting a shorter overall survival ($p = 0.04$). Similarly, a ratio between the tissue sodium concentration in the T_2W hyperintense lesion and the basal ganglia greater than 1.6 was indicative of a worst prognosis ($p = 0.03$; figure 4.5). The strongest prognostic predictor based on the tissue sodium concentration was the ratio between the T_2W hyperintense lesion and the necrotic component (threshold 0.9, $p < 0.001$; figure 4.5).

The most representative Kaplan-Meier curves for the biomarkers derived from the intracellular-weighted sodium concentration are shown in figure 4.6. A ratio greater than 1 between the intracellular-weighted sodium concentration in the T_2W hyperintense lesion and the basal ganglia was indicative of the worst prognosis ($p = 0.02$). The enhancing component was more strongly associated with survival. An intracellular-weighted sodium concentration greater than 24.8 in the enhancing component was a strong predictor of survival both as an independent biomarker ($p <0.01$) and as ratio over the basal ganglia (threshold 1.1; $p < 0.001$; figure 6).

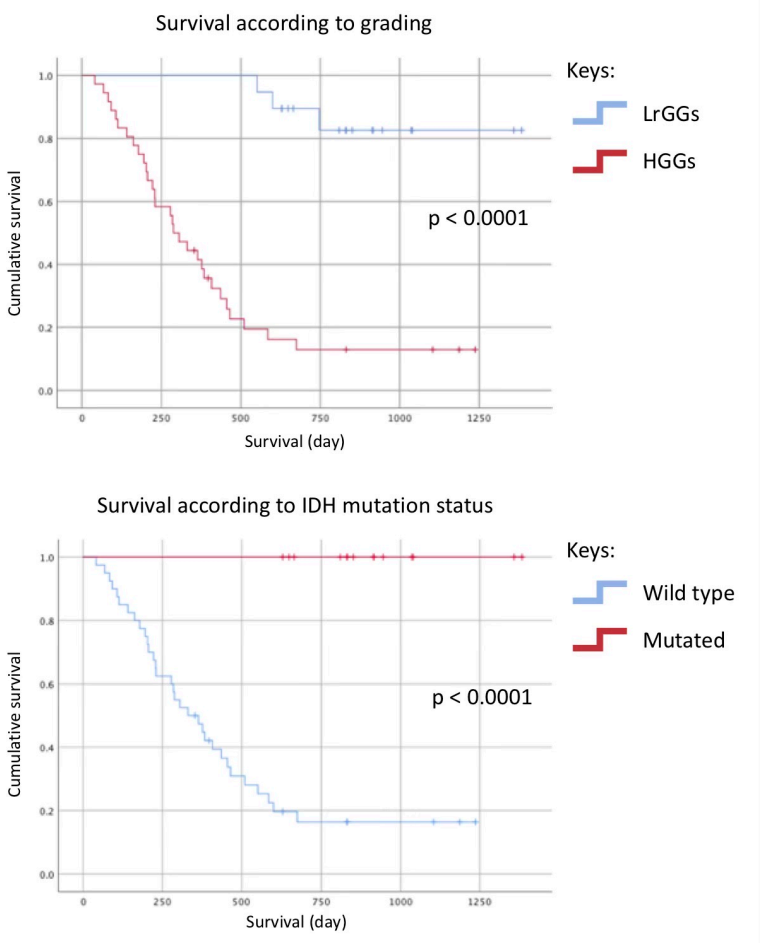

Figure 4.4: Kaplan-Meier survival analysis according to grade and IDH status.
The survival analysis comparing lower-grade gliomas (LrGG) to high grade gliomas (HGG) shows a significant longer survival for LrGG ($p < 0.0001$). As expected, the presence of IDH mutation is indicative of longer survival ($p < 0.0001$) irrespective of other clinical parameters.

4.3 Discussion

This study aimed to explore the total tissue sodium concentration and the intracellular concentration as predictors of survival in patients with gliomas. Over the three-year recruitment window, we recruited the largest cohort of brain tumours patient in a sodium MRI study. Indeed, with a total cohort of 65 recruited patients, we breached the current record of Weber *et al.* that recruited a cohort of 61 patients for their study (Weber *et al.*, 2010). Of interest, in both the studies a small amount of lesions turned out to not be a glioma, highlighting how challenging can be the differential diagnosis if even in very selected and sophisticated studies there is a proportion of misdiagnosed cases. Moreover,

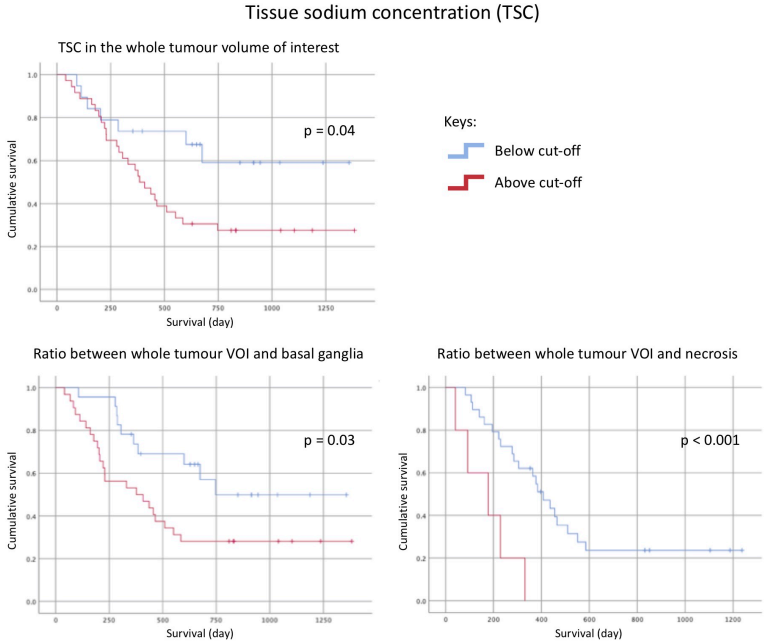

Figure 4.5: Kaplan-Meier survival analysis according to tissue sodium concentration.

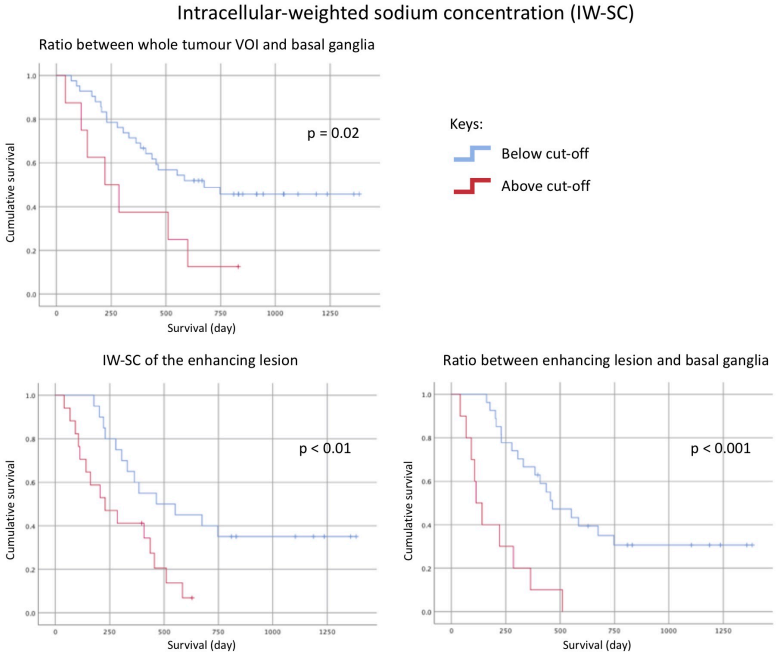

Figure 4.6: Kaplan-Meier survival analysis according to intracellular-weighted sodium concentration.

we obtained clinical follow-up for the entire cohort, almost double the current largest published cohort (34 patients) with follow-up previously reported by Biller *et al.* (Biller *et al.*, 2016). The size of the study allows important results to be derived and provides a basis for future work in this area.

4.3.1 Sodium concentration in normal tissue and glioma grading

The tissue sodium concentration in our cohort was consistent with published literature. Despite the wide ranges of estimated tissue sodium concentration previously reported for both white matter (20 - 60 mmol L^{-1}) and grey matter / basal ganglia (30-70 mmol L^{-1}), most published reports fall within a similar range to this study (Madelin and Regatte, 2013). Madelin *et al.* reported an overall average for combined white and grey matter of around 35 mmol L^{-1}, whilst the most recent paper published by Neto *et al.* reported an average of 30.30 ± 3.53 mmol L^{-1} for white matter and 34.95 ± 4.16 mmol L^{-1} for the putamen (Madelin *et al.*, 2014; Neto *et al.*, 2018). In particular, the latter is very close to the 34 ± 5 mmol L^{-1} detected in the contralateral basal ganglia reported here. The similarity between published results in normal brain parenchyma highlights the robustness of the technique and the limited variance across different sites that we have recently estimated to be below 5% (Riemer *et al.*, 2019). Technical validation and reproducibility of the technique is a mandatory and key component of potential clinical implementation and translation. The current study did not include an *ex vivo* correlate for the sodium concentration. The possibility of *ex vivo* quantifying the sodium concentration from tumour biopsies was explored in depth with input from the Department of Chemistry and the MRC Nutritional Unit. However, this was not deemed feasible due to logistical and technical issues and therefore was not performed. The strict similarity between our results and previously published data would suggest that our measurements are accurate and reproducible, however future studies may correlate *ex vivo* measurements with imaging biomarkers to confirm the validity of the *in vivo* technique.

In our cohort, the tissue sodium concentration was not able to differentiate lower-grade glioma and higher-grade glioma. However, the intracellular-weighted sodium concentration was significantly different in the T_2W hyperintense lesion ($p = 0.04$), the enhancing component ($p = 0.03$) and the non-enhancing core ($p = 0.01$). This discrepancy is likely to be a consequence of the different contributions of the intracellular and extracellular compartments to the total sodium concentration in lower-grade glioma and

higher-grade glioma. The sodium concentration in the extracellular matrix is known to be an order of magnitude higher than the intracellular concentration and therefore an increase in the tissue sodium concentration may be due to both an increase in the intracellular concentration and/or an increase in the volume of the extracellular fluid relative to the volume of intracellular fluid (Leslie *et al.*, 2019). In HGGs the sodium concentration is increased in both compartments. The larger cancer cells and the known increase in intracellular sodium concentration in malignant cancer cells paired with the necrotic core and the oedema in the peritumoral tumour zone produce a parallel increase in the total and intracellular sodium concentrations. This is supported by the lower degree of suppression of the sodium signal in the intracellular-weighted sequence in HGGs as opposed to the LrGG: lower-grade gliomas are less cellular than their higher-grade counterparts. This striking difference could potentially be used for early detection of LrGG malignant transformation in secondary GBMs where an increase in the IW-SC may be a biomarker for malignant transformation. Moreover, as sodium homeostasis dysregulation contributes to imbalance in metabolic activity, proliferation, migration and invasion, a shift in sodium concentration towards an increase in the intracellular compartment may affect the integrity of the blood-brain barrier resulting in gadolinium enhancement. A simple metric such as the ratio between the tissue sodium concentration and the intracellular-weighted sodium concentration of the T_2W hyperintense lesion could represent a simple index to monitor LrGG over time. At present, the relative cerebral blood volume (rCBV) obtained from gadolinium-enhanced perfusion MRI is a valid indicator of tumour progression when it is at least 2.6-fold higher than the contralateral normal appearing tissue (Langen *et al.*, 2017). This is particularly useful when there is an increase over time of the rCBV in patient under close surveillance. However, the lack of standardization of image acquisition and processing, the difficult in interpreting the results and the susceptibility to artifacts have somewhat limited a widespread use of the technique. An index based on sodium imaging could provide additional information to Dynamic Susceptibility Contrast perfusion imaging and could complement its assessment. The few published papers have shown similar ranges of sodium concentration in the normal grey and white matter proving the reproducibility and repeatability of the results. Once a

threshold for optimal progression prediction is established, this could be automatically analysed due to the high contrast-to-background ratio of sodium MR images. In this cohort, that threshold turned out to be 2.9, however, this is a report from a single institution study and, albeit this is the largest cohort of patients with both tissue sodium concentration and intracellular-weighted sodium concentration, further investigation on the optimal thresholds is warranted.

Sodium imaging can also have a role in the detection of gliomas. Figure 4.1 and 4.2 show a representative case of LrGG and HGG. In both the cases the conspicuity of the lesions over the background on the tissue sodium concentration images is clearly appreciated. On the intracellular-weighted sodium concentration, the contrast is mostly negative with the lesion appearing hypointense as compared to the background. Quantitatively, the lower-grade glioma tissue sodium concentration in the T_2W hyperintense lesion and enhancing component were significantly different compared to the basal ganglia ($p < 0.001$ and $p = 0.01$, respectively) and to the normal appearing white matter ($p < 0.0001$ and $p < 0.001$, respectively). Interestingly, whilst the tissue sodium concentration of the HGGs was significantly different compared with both the basal ganglia and normal appearing white matter ($p < 0.0001$ for all the combinations), only the difference between the intracellular-weighted sodium concentration in the T_2W hyperintense lesion and the basal ganglia was significantly different ($p = 0.01$). The comparison with the basal ganglia appears to be a reliable reference for comparison with the tumour to be chosen as biomarker in future larger studies. It is worth mentioning that age-related iron deposition in the basal ganglia is a known phenomenon. The presence of iron causes shortening of the T_1 and T_2 relaxation times on conventional ^{1}H imaging, however, this does not affect sodium imaging as the gyromagnetic ratio for ^{23}Na, is approximately four times lower than that for ^{1}H.

4.3.2 Intralesional and peritumoral heterogeneity

Gliomas are highly heterogenous with areas containing different gene expression profiles, hence different grades within the same lesion. Heterogeneity is particularly important in lower-grade gliomas, where foci of

higher-grade tumour can avoid detection through conventional imaging. Therefore stereotactic biopsies must be aimed at areas reflecting the biologic most active region of the tumour and thus of higher-grade (Jacobs *et al.*, 2005). Imaging can play a significant role in selecting suitable targets for stereotactic biopsies exploiting the metabolic heterogeneity *in vivo*. Complex approaches combining a plethora of MRI and positron emission tomography (PET) techniques, such as diffusion, perfusion and spectroscopy with ^{18}F-fluorothymidine-PET have been evaluated. However, despite the improvement in grading assessment the incorporation of many of these advanced techniques in a clinical setting is not feasible (Weber *et al.*, 2010). Sodium MRI could be a potential viable solution to this problem as it is relatively straightforward to implement.

Comparing the tissue sodium concentration and the intracellular-weighted sodium concentration maps with the corresponding T_2WI and post-gadolinium 3D T_1WI in figure 4.1 and 4.2, it appears that the sodium signal is heterogenous with changes that do not correspond to the proton signal. In lower-grade gliomas, sodium imaging is able to highlights region of potential higher-grade that the post-gadolinium 3D T_1WI, currently used in many centres as the reference sequence for intraoperative guidance, is not able to highlight. Indeed, only a minority of LrGGs enhance and when the enhancement is detected it often corresponds to an area which has already transformed to higher-grade tumour. Hence, it is too late to make a significant impact on the long-term survival. The tissue sodium concentration maps in all the LrGG recruited in this study were highly heterogenous, depicting several areas with different sodium concentration even within homogenously T_2W hyperintense regions. As previously mentioned, those areas are likely to correspond to cells that are proliferating, migrating and actively consuming more ATP. Therefore, we could postulate that areas of higher TSC and IW-SC would be the best target for stereotactic biopsies in LrGG. Similarly, sodium imaging highlights greater heterogeneity within GBMs than found on conventional imaging. Contrast enhancement in GBMs is deemed to be secondary to gadolinium leakage through the damaged blood-brain barrier, and therefore may not entirely represent viable tissue. Comparing the TSC and the IW-SC, sodium offers the possibility to disentangle areas where there is loss of cellular integrity

(signal is suppressed on the IW-SC) from the viable tissue providing a better target for tissue biopsy and treatment.

Furthermore, on the TSC maps there are areas of increased sodium concentration outside the tumour boundaries defined by the T_2W hyperintensity both in LrGGs and in HGGs. The sodium concentration has been shown to be increased also in the presence of inflammation (Leslie *et al.*, 2019). Although sodium concentration measurements have not yet been studied in tumour inflammation, it is reasonable to believe that this will also be associated with elevated sodium. Therefore, the areas of increased sodium concentration outside the tumour boundaries could either represent foci of migrated cancer cells or peritumoral inflammation and further histological assessment of those regions is warranted. Areas of increased TSC could be additional targets for more aggressive resection or radiotherapy treatment with potential survival benefit.

Interestingly, sodium is also used intraoperatively as fluorescein sodium (FL) for real-time intraoperative guidance during microsurgery. Fluorescein sodium is a biosafe green-fluorescing dye that accumulates in areas of malignancy, vascular leakage, pooling defects or abnormal vasculature. This compound has been evaluated as an alternative to 5-aminolevulinic acid (5-ALA) for several years although its precise mechanism of action is still unravelled (D'Amico *et al.*, 2017). Fluorescein sodium is believed to passive stain the extracellular space in the presence of a disrupted blood-brain barrier (Chen *et al.*, 2012; Höhne *et al.*, 2019). However, recent studies have demonstrated that non-enhancing gliomas show fluorescence and this extends beyond the tumour margins (Neira *et al.*, 2017; Bowden *et al.*, 2018). The fluorescent regions can be shown to have a higher cell density and proliferative activity, similarly to what seen with sodium imaging (Bowden *et al.*, 2018). However, despite the fact that the extent of resection is an independent predictor of prognosis in patients with gliomas and fluorescein sodium increases the extent of resection, the dose used to maximise the resection can induce an anaphylactic reaction and therefore the wide adoption of this technique is halted (Fan *et al.*, 2018). Sodium MRI could complement fluorescein sodium: its non-invasive nature, safety and high resolution (up to 2 mm isotropic) could be applied clinically. Sodium maps could be used in guidance systems fused with

other convectional images technique providing the same information of fluorescein sodium without the need of the injection. Moreover, if safety concerns are addressed, sodium imaging could be the natural complement for fluorescein sodium. Liu *et al.* demonstrated that combining advanced imaging and fluorescein sodium can increase the gross total resection rate, decrease surgical morbidity and improve quality of life (Liu *et al.*, 2013). Sodium MRI could be the natural complement for this technique and the combination of the two may lead to the identification of more foci of cancer cells that are presently not identified.

4.3.3 Therapy assessment and prognostication

In the clinic, therapy assessment for brain tumours usually assesses size and contrast enhancement, but is limited by the fact that gliomas are highly heterogenous and lack of contrast enhancement may not represent complete response as enhancing tissue may not indicate recurrence/residual disease (Wen *et al.*, 2010). A more accurate way of assessing therapy response could include evaluation of tissue viability and metabolic activity rather than morphology alone.

Sodium MRI is particularly sensitive to necrosis due to the abundance of free sodium ions in the necrotic tissue. Moreover, the availability of intracellular-weighted sequences can aid the identification of areas of loss of cellular integrity. In previous work on stroke, it has been demonstrated that an increase of tissue sodium concentration of ~50% greater than the contralateral tissue (corresponding to a threshold of 70mM), corresponds to infarct (Madelin and Regatte, 2013). In our group, the non-enhancing areas of both the LrGGs and the HGGs were above this threshold (84 ± 11 for the LrGG and 76 ± 21 for the HGG). Furthermore, we observed a suppression of sodium signal greater than 50% on the IW-SC maps. The capability of detecting necrosis would be extremely effective in serial follow-up studies to monitor therapy efficacy and assess therapy response at an early stage. Indeed, an increase in the TSC with an associated decrease in IW-SC during treatment would be indicative of loss of cellular integrity and therefore potential therapy response. On the contrary, if the TSC remains stable and/or the IW-SC increases, the tumour may be still

proliferating and therefore a change of therapy would be warranted. Further studies are required to evaluate further.

Looking beyond therapy response assessment, the capability of predicting long term survival with a scan at baseline would be invaluable to better manage patients with glioma. Previously, Biller and colleagues demonstrated in a cohort of 34 patients that sodium imaging is able to predict IDH mutation status and tumour progression (Biller *et al.*, 2016). IDH mutation is the strongest predictor of prognosis in glioma. Since the most recent update of the WHO classification of tumours of the central nervous system, IDH mutational status has been shown to play a key role in classifying and grading glioma. Unsurprisingly, in our cohort it was the strongest predictor of long-term survival with a significant shorter survival if no mutation was detected. Sodium imaging did not offer any additional prognostic information over IDH measurements. This was expected as IDH is currently the key determining biomarker for treatment and survival of patients with glioma. Nonetheless, tissue is required to test for the presence of the mutation and, given the high degree of heterogeneity present within gliomas, a wild-type result may not be accurate if the biopsy was taken in the highest-grade area of the lesion. Therefore, the role of sodium imaging could be as a potential aid for targeting biopsies or in selected cases in which a tissue biopsy is not deemed feasible.

Sodium MRI is a potential candidate for non-invasive, *in vivo*, assessment of long-term prognosis. Several biomarkers were statistically significant predictor of survival: the tissue sodium concentration in the T_2W hyperintense lesion ($p = 0.04$), the ratio between the tissue sodium concentration in the T_2W hyperintense lesion and the basal ganglia ($p = 0.03$) and the ratio between he tissue sodium concentration in the T_2W hyperintense lesion and the non-enhancing core ($p < 0.001$). The latter was the strongest predictor among the biomarkers derived from the tissue sodium concentration results. This may be explained considering that the higher the quantity of necrosis, the greater the aggressiveness of the tumour, growing so rapidly that it outpaces the neovascularization. The intracellular-weighted sodium concentration and the ratio between the enhancing tissue and the basal ganglia were the strongest predictors of survival ($p < 0.01$ and $p < 0.001$). Also, the ratio

between the sodium concentration in the T_2W hyperintense lesion and the basal ganglia was a significant predictor, albeit weaker ($p = 0.02$).

4.3.4 Support for drug discovery and assessment of experimental therapies

Primary brain tumours are challenging to treat due to heterogeneity (Aldape *et al.*, 2019). Indeed, despite recent progress in the treatment of many other cancer types, the survival of patients with primary brain tumours remains poor. Sodium imaging can play a significant role in fostering drug research. The identification of new targets in primary brain tumours requires a deeper understanding of tumour biology. Ion channels are one of those novel targets that could be exploited as new therapeutic approach.

Several ions have been shown to be dysregulated in cancer cells and are involved in most of the hallmarks of cancer (Prevarskaya *et al.*, 2010). Imaging can aid in determining if the channel is under- or over-expressed in a specific cancer, how specific is the dysregulation of the channel to the tumour as well as the functional significance of any change in expression. Sodium has been shown to be increased in malignancy and involved in several pathways, therefore direct or indirect manipulation of its concentration may either complement existing therapeutic approaches or be evaluated as primary therapy (Leslie *et al.*, 2019). High-grade gliomas overexpress non-voltage-gated sodium channel of the degenerin superfamily that are commonly absent in normal astrocytes and in lower-grade tumours. Several studies have demonstrated that the inhibition of some of those channels, namely ASIC 1 and 2, results in a decrease in growth and glioma cells migration (Vila-Carriles *et al.*, 2006; Kapoor *et al.*, 2009). Sodium imaging can be instrumental in trials aimed at evaluating the efficacy of those drugs *in vivo*. The possibility of profiling the individual cancer before any intervention will allow the selection of patients who are most likely to benefit from a therapy, maximising the survival whilst also limiting the adverse effects. In this instance, on top of the above-mentioned key role in assessing therapy response to conventional therapies, evaluating the concentration of tissue sodium concentration and intracellular-weighted sodium concentration could aid in the selection of patients that are more likely to benefit

from the inhibition of non-voltage-gated sodium channels. Moreover, sodium imaging of the ion concentration in the extracellular and intracellular compartments, can be used to provide an assessment of the efficacy of those drugs in inhibiting the sodium current through the channels. A more accurate means of evaluating the efficacy of treatment would also allow for therapy to be switched or modulated and therefore reducing adverse effects, improving quality of life and potentially maximising the survival. However, sodium channels are ubiquitous and therefore accurately targeting cancer cells is a challenge. Moreover, voltage-gated sodium channels play a significant role in regulating immune cell function, therefore there is a risk of impairing innate immunity by targeting these channels (Leslie *et al.*, 2019).

4.4 Conclusion

Sodium homeostasis is disrupted in primary brain tumours. Here I have demonstrated that sodium MRI is a reliable technique to measure both the total sodium concentration and the concentration in the intracellular compartment. In particular, the quantification of the intracellular fraction could help in grading gliomas and in early detection of malignant transformation. Sodium imaging significantly correlates with survival and could be used as a novel imaging technique for early metabolic response assessment and prognostication.

References

Aldape K, Brindle KM, Chesler L, Chopra R, Gajjar A, Gilbert MR, et al. Challenges to curing primary brain tumours [Internet]. Nat Rev Clin Oncol 2019; 16Available from: http://dx.doi.org/10.1038/s41571-019-0177-5

Arevalo OJ, Valenzuela R, Esquenazi Y, Rao M, Tran B, Zhu J, et al. The 2016 World Health Organization Classification of Tumors of the Central Nervous System: A Practical Approach for Gliomas, Part Part 1. Basic Tumor Genetics. Neurographics 2017; 7: 334–343.

Benjamini Y, Hochberg Y. Controlling the False Discovery Rate : A Practical and Powerful Approach to Multiple Testing. J R Stat Soc 1995; 57: 289–300.

Bigner D. Biology of gliomas: potential clinical implications of glioma cellular heterogeneity. Neurosurgery 1981; 9: 320–326.

Biller A, Badde S, Nagel A, Neumann JO, Wick W, Hertenstein A, et al. Improved brain tumor classification by sodium MR imaging: Prediction of IDH mutation status and tumor progression. Am J Neuroradiol 2016; 37: 66–73.

Bowden SG, Neira JA, Gill BJA, Ung TH, Englander ZK, Zanazzi G, et al. Sodium fluorescein facilitates guided sampling of diagnostic tumor tissue in nonenhancing gliomas. Neurosurgery 2018; 82: 719–727.

Chen B, Wang H, Ge P, Zhao J, Li W, Gu H, et al. Gross total resection of glioma with the intraoperative fluorescence- Guidance of fluorescein sodium. Int J Med Sci 2012; 9: 708–714.

D'Amico RS, Englander ZK, Canoll P, Bruce JN. Extent of Resection in Glioma–A Review of the Cutting Edge. World Neurosurg 2017; 103: 538–549.

Diss JKJ, Stewart D, Pani F, Foster CS, Walker MM, Patel A, et al. A potential novel marker for human prostate cancer: Voltage-gated sodium channel expression in vivo. Prostate Cancer Prostatic Dis 2005; 8: 266–273.

Dolecek TA, Propp JM, Stroup NE, Kruchko C. CBTRUS Statistical Report: Primary Brain and Central Nervous System Tumors Diagnosed in the United States in 2005 – 2009. Neuro Oncol 2013; 15: ii1–ii56.

Fan C, Jiang Y, Liu R, Wu G, Wu G, Xu K, et al. Safety and feasibility of low-dose fluorescein-guided resection of glioblastoma. Clin Neurol Neurosurg 2018; 175: 57–60.

Fischl B, Dale AM. Measuring the thickness of the human cerebral cortex from magnetic resonance images. Proc Natl Acad Sci U S A 2000; 97: 11050–5.

Fraser SP, Diss JKJ, Chioni AM, Mycielska ME, Pan H, Yamaci RF, et al. Voltage-gated sodium channel expression and potentiation of human breast cancer metastasis. Clin Cancer Res 2005; 11: 5381–5389.

Gurney PT, Hargreaves BA, Nishimura DG. Design and analysis of a practical 3D cones trajectory. Magn Reson Med 2006; 55: 575–582.

Heppner G. Tumor heterogeneity. Cancer Res 1984; 44: 2259–2265.

Höhne J, Schebesch KM, de Laurentis C, Akçakaya MO, Pedersen CB, Brawanski A, et al. Fluorescein Sodium in the Surgical Treatment of Recurrent Glioblastoma Multiforme. World Neurosurg 2019; 125: e158–e164.

Inglese M, Madelin G, Oesingmann N, Babb JS, Wu W, Stoeckel B, et al. Brain tissue sodium concentration in multiple sclerosis: a sodium imaging study at 3 tesla. Brain 2010; 133: 847–57.

Jacobs AH, Kracht LW, Gossmann A, Rüger MA, Thomas A V., Thiel A, et al. Imaging in neurooncology. NeuroRx 2005; 2: 333–347.

Kapoor N, Bartoszewski R, Qadri YJ, Bebok Z, Bublen JK, Fuller CM, et al. Knockdown of ASIC1 and epithelial sodium channel subunits inhibits glioblastoma whole cell current and cell migration. J Biol Chem 2009; 284: 24526–24541.

Langen K-J, Galldiks N, Hattingen E, Shah NJ. Advances in neuro-oncology imaging. Nat Rev Neurol 2017; 13: 279–289.

Laymon CM, Oborski MJ, Lee VK, Davis DK, Wiener EC, Lieberman FS, et al. Combined imaging biomarkers for therapy evaluation in glioblastoma multiforme: Correlating sodium MRI and F-18 FLT PET on a voxel-wise basis. Magn Reson Imaging 2012; 30: 1268–1278.

Leslie TK, James AD, Zaccagna F, Grist JT, Deen S, Kennerley A, et al. Sodium homeostasis in the tumour microenvironment. Biochim Biophys Acta - Rev Cancer 2019; 1872: 188304.

Liu JG, Yang SF, Liu YH, Wang X, Mao Q. Magnetic resonance diffusion tensor imaging with fluorescein sodium dyeing for surgery of gliomas in brain motor functional areas. Chin Med J (Engl) 2013; 126: 2418–2423.

Louis DN, Perry A, Reifenberger G, von Deimling A, Figarella-Branger D, Cavenee WK, et al. The 2016 World Health Organization Classification of Tumors of the Central Nervous System: a summary. Acta Neuropathol 2016; 131: 1–18.

Madelin G, Kline R, Walvick R, Regatte RR. A method for estimating intracellular sodium concentration and extracellular volume fraction in brain in vivo using sodium magnetic resonance imaging. Sci Rep 2014; 4: 4763.

Madelin G, Regatte RR. Biomedical applications of sodium MRI in vivo. J Magn Reson Imaging 2013; 38: 511–529.

Maudsley AA, Hilal SK. Biological aspects of Sodium-23 imaging. Br Med Bull 1984; 40: 165–166.

McDonald JH. Handbook of Biological Statistics. 3rd ed. Baltimore, Maryland: Sparky House Publishing; 2014

N Ahmed, E. W. Thompson, M. A. Quinn. Epithelial–Mesenchymal Interconversions in Normal Ovarian Surface Epithelium and Ovarian Carcinomas: An Exception to the Norm. J Cell Physiol 2007; 207: 581–588.

Nagel AM, Bock M, Hartmann C, Gerigk L, Neumann J-O, Weber M-A, et al. The Potential of Relaxation-Weighted Sodium Magnetic Resonance Imaging as Demonstrated on Brain Tumors. Invest Radiol 2011; 46: 539–547.

Neira JA, Ung TH, Sims JS, Malone HR, Chow DS, Samanamud JL, et al. Aggressive resection at the infiltrative margins of glioblastoma facilitated by intraoperative fluorescein guidance. J Neurosurg 2017; 127: 111–122.

Neto LPN, Madelin G, Sood TP, Wu C, Kondziolka D, Placantonakis D, et al. Quantitative sodium imaging and gliomas : a feasibility study. Neuroradiology 2018

Ohgaki H. Epidemiology of Brain Tumors. Humana Press; 2009

Ostrom QT, Gittleman H, Stetson L, Virk SM, Barnholtz-Sloan JS. Epidemiology of Gliomas. Cancer Treat Res 2015; 163: 1–14.

Ouwerkerk R, Bleich K, Gillen J. Tissue sodium concentration in human brain tumors as measured with 23 Na MR imaging. Radiology 2003; 23: 529–537.

Papadopoulos MC, Saadoun S, Binder DK, Manley GT, Krishna S, Verkman AS. Molecular mechanisms of brain tumor edema. Neuroscience 2004; 129: 1009–1018.

Prevarskaya N, Skryma R, Shuba Y. Ion channels and the hallmarks of cancer. Trends Mol Med 2010; 16: 107–121.

Riemer F, McHugh D, Zaccagna F, Lewis D, McLean MA, Graves MJ, et al. Measuring Tissue Sodium Concentration: Cross-Vendor Repeatability and Reproducibility of ^{23} Na-MRI Across Two Sites. J Magn Reson Imaging 2019: 1–7.

Riemer F, Solanky BSS, Stehning C, Clemence M, Wheeler-Kingshott CAMAM, Golay X.

Sodium (23Na) ultra-short echo time imaging in the human brain using a 3D-Cones trajectory. Magn Reson Mater Physics, Biol Med 2014; 27: 35–46.

Schuierer G, Ladebeck R, Barfuß H, Hentschel D, Huk WJ. Sodium-23 imaging of supratentorial lesions at 4.0 T. Magn Reson Med 1991; 22: 1–9.

Tamimi AF, Juweid M. Epidemiology and Outcome of Glioblastoma. In: Glioblastoma. 2017. p. 143–153

Thulborn KR, Lu A, Atkinson IC, Pauliah M, Beal K, Chan TA, et al. Residual Tumor Volume, Cell Volume Fraction and Tumor Cell Kill During Fractionated Chemoradiation Therapy of Human Glioblastoma using Quantitative Sodium MR imaging. Clin Cancer Res 2018: clincanres.2079.2018.

Vila-Carriles WH, Kovacs GG, Jovov B, Zhou ZH, Pahwa AK, Colby G, et al. Surface expression of ASIC2 inhibits the amiloride-sensitive current and migration of glioma cells. J Biol Chem 2006; 281: 19220–19232.

W. J. Youden. Index for rating diagnostic tests. Cancer 1950: 32–35.

Weber M, Henze M, Tuttenberg J, Stieltjes B, Meissner M, Zimmer F, et al. Biopsy targeting gliomas: do functional imaging techniques identify similar target areas? Invest Radiol 2010; 45: 755–768.

Wen PY, Macdonald DR, Reardon D a., Cloughesy TF, Sorensen a. G, Galanis E, et al. Updated response assessment criteria for high-grade gliomas: Response assessment in neuro-oncology working group. J Clin Oncol 2010; 28: 1963–1972.

Metabolic phenotyping of glioblastoma with Magnetic Resonance Imaging of hyperpolarized [1-^{13}C]pyruvate.

UNIVERSITY OF CAMBRIDGE

Chapter 5

Metabolic phenotyping of glioblastoma with Magnetic Resonance Imaging of hyperpolarized [1-^{13}C]pyruvate.

Glioblastomas (GBMs) are the most common and aggressive adult-onset primary malignant brain tumours accounting for 16% of all primary brain tumours (Dolecek *et al.*, 2013; Ostrom *et al.*, 2015; Tamimi and Juweid, 2017). Prognosis for newly diagnosed GBMs remains dismal with a median survival of 12-15 months despite the combination of maximal surgical resection, chemotherapy and targeted radiotherapy (or radiosurgery) (Ostrom *et al.*, 2015; CRUK, 2019). Furthermore, the cumulative incidence rate of brain tumours in the UK increased by around 34% since the early 1990s, thus becoming a pressing health burden (CRUK, 2019). GBMs are extremely heterogeneous, both morphologically and biologically, which contributes to a very poor prognosis. The intralesional heterogeneity seen at pathology is characterized by foci of necrosis commonly surrounded by cellular pseudopalisades and areas of microvascular hyperplasia (Rong *et al.*, 2006; Vartanian *et al.*, 2014). Those characteristics of an aggressive growth pattern help in differentiating GBM from lower-grade gliomas (LrGG). Moreover, the heterogeneity extends beyond the boundaries of the lesion into the so-called peritumoral brain zone (PBZ). This is defined on Magnetic Resonance Imaging (MRI) as the area surrounding the lesion that does not show contrast enhancement after gadolinium (Gd) administration on the T_1-weighted (T_1W) images and it is commonly hyperintense in the T_2-weighted (T_2W) images (Lemée *et al.*, 2015a). At pathology, this area contains a plethora of different cells, including reactive

astrocytes and inflammatory cells. Tumour cells are commonly identified in a third of biopsies from the PBZ that are considered as normal both on MRI and following surgical inspection; however, the histological characteristics of these invasive cell populations may differ from the cells isolated from the primary mass suggesting that only some clonal populations are able to migrate outside the boundaries of the lesion (Lemée *et al.*, 2015a, b). According to the so-called "go or grow" hypothesis, subpopulations of GBM cells have different metabolic and biological behaviour, with some cells exhibiting a tendency to favour migration whilst in contrast, other subpopulations preferentially proliferate (Giese *et al.*, 2003; Kathagen-Buhmann *et al.*, 2016). Metabolic reprogramming is believed to be one of the major driving forces in determining this behaviour (Corbin *et al.*, 2017).

Otto Warburg was the first to describe aerobic glycolysis (termed the Warburg effect), the non-oxidative metabolism of glucose even in the presence of oxygen. Although his assumption that the switch away from the tricarboxylic acid (TCA) cycle was derived by defective mitochondria has been confirmed only in selective cases, such as in a subset of cancers in which succinate dehydrogenase (SDH) and/or fumarate hydratase (FH) are mutated, the Warburg effect still constitutes the foundation stone of metabolic reprogramming in cancer (Warburg, 1925, 1956; Corbin *et al.*, 2017). Despite its metabolic inefficiency in terms of produced ATP molecules (aerobic glycolysis leads to the production of 2 molecules of ATP per pyruvate whilst the TCA produces up to 38 molecules of ATP), aerobic glycolysis produces NADH, used to fuel energy production, and lactate, that contributes in acidifying the microenvironment promoting cells invasion (Vander *et al.*, 2015; Strickland and Stoll, 2017).

The pentose phosphate pathway (PPP) also plays a significant and complementary role to aerobic glycolysis in the metabolism of GBM. Enzymes of the PPP are upregulated in highly proliferative, non-migrating cells to generate ribose-5-phospate and NADPH for DNA, RNA and fatty acid synthesis, and are downregulated in the hypoxic cellular pseudopalisades (Kathagen *et al.*, 2013; Kathagen-Buhmann *et al.*, 2016). On contrast, glycolytic enzymes are downregulated in highly proliferative, non-migrating cells and upregulated in the cell clones that favour migration (Kaur *et al.*, 2005; Kathagen *et al.*, 2013; Kathagen-Buhmann *et al.*, 2016). Moreover, glioma stem cells,

which may play a significant role in tumour recurrence, are less glycolytic when compared to differentiated cancer cells and this preservation of the mitochondrial capacity has been correlated to radio-resistance (Vlashi *et al.*, 2011; Strickland and Stoll, 2017).

The metabolic alterations in glioblastoma have been shown to promote cancer growth and invasiveness whereas previously they were thought to be solely a consequence of tumour development (Vartanian *et al.*, 2014; Corbin *et al.*, 2017). Therefore, metabolic reprogramming could represent a target for novel therapeutic strategies aimed at disrupting cancer-specific metabolic pathways (Corbin *et al.*, 2017; Strickland and Stoll, 2017). To date there have been several attempts to use pharmacological methods to alter tumour metabolism both in GBMs and other cancers and although some have shown initial promise, none are used routinely; examples include dichloroacetate which stimulates flux of pyruvate through pyruvate dehydrogenase within mitochondria. Exploring the intratumoral, peritumoral and intertumoral metabolic heterogeneity *in vivo* may help to identify why some patients are responding to these agents and may help with the discovery of novel therapeutic strategies (Michelakis *et al.*, 2010; Marin-Valencia *et al.*, 2012; Corbin *et al.*, 2017). Hyperpolarised ^{13}C Magnetic Resonance Spectroscopic Imaging (HP ^{13}C MRSI; also commonly called Hyperpolarised ^{13}C Magnetic Resonance Imaging, HP ^{13}C MRI) is based on the principles of dynamic nuclear polarization (DNP) and is a novel technique that allows the *in vivo* non-invasive assessment of the metabolism of hyperpolarized (HP) ^{13}C-labelled molecules (Zaccagna *et al.*, 2018). The process of DNP involves polarizing the nuclear spin in the solid state at temperatures close to absolute zero and in a strong magnetic field: polarization is transferred from the electrons to the nuclear spins by microwave irradiation; this method can result in a >10,000-fold enhancement of the nuclear polarization with a significant increase of the signal-to-noise (SNR) ratio when measured with ^{13}C MRS in the liquid-state (Ardenkjaer-Larsen *et al.*, 2003). The technique allows the possibility of *in vivo* detection of tissue metabolism through imaging the spatial distribution on injected ^{13}C-labelled cell substrates and their metabolites. The development of the method has spawned a new research area and several compounds have been evaluated in the pre-clinical setting (Kurhanewicz *et al.*, 2011). Among all the potential compounds, [1-^{13}C]pyruvate

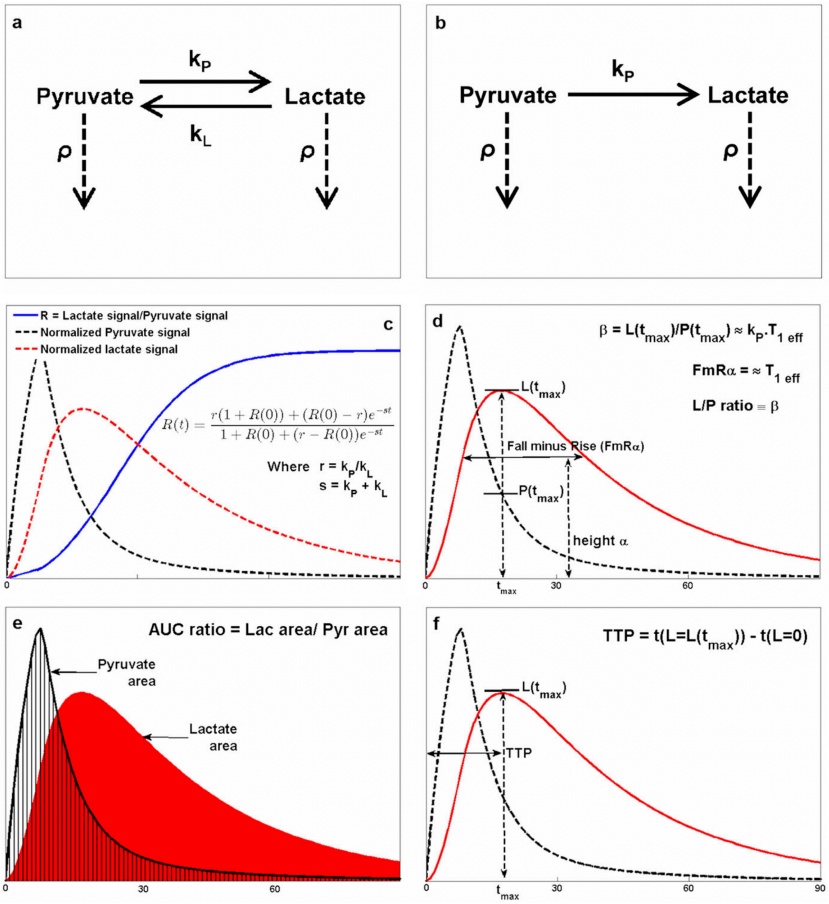

Figure 5.1: Schematic diagrams for models and model-free methods.

Schematic diagrams showing some of the models and model-free methods proposed for the analysis of HP ^{13}C MRI data. In (a) interactions accounted for in the two-way differential/ integral models; k_P is the forward reaction rate constant, k_L is the backward reaction rate constants, ρ is the inverse of the effective spin–lattice relaxation. In (b) interactions for one-way integral model; k_P is the forward reaction rate constant, ρ is the inverse of the effective spin–lattice relaxation. In (c) example metabolite time courses demonstrating the ratiometric model. (d) fall-minus-rise time at height α (FmR α) approach and L/P ratio method. (e) Lactate-to-pyruvate AUC ratio. (f) Lactate time to peak (TTP). Figures adapted from Daniels et al. (Daniels et al., 2016).

(refered to simply as pyruvate here) has been the most studied due to technical reasons (relatively long polarization half-life, forms a glass suitable for polarisation when frozen, is at a high concentration in liquid form) and biological reasons (rapid distribution and uptake, ability to explore the Warburg effect in cancer) (Zaccagna *et al.*, 2018; Kurhanewicz *et al.*, 2019). Pyruvate sits at a metabolic crossroad and plays a major role in many metabolic pathways (Brindle *et al.*, 2011; Lumata *et al.*, 2015). While the first clinical study of the technique used a preclinical device modified for human use, a clinical polarizer for sterile use intent was developed in 2011 which allowed the technique to be

translated more widely into the clinical arena (Ardenkjaer-Larsen *et al.*, 2011). The work described here has utilised one of the early devices to study metabolism in glioma.

Parallel to the development of hyperpolarised compounds, several methods to quantify the exchange between pyruvate and lactate have been proposed. Figure 5.1 illustrates the most widely used approaches to date. Kinetic models applied to spectroscopic data have been widely applied to derive the apparent build-up rate forward constant k_{PL} which expresses the constant conversion rate between pyruvate and lactate catalysed by the enzyme lactate dehydrogenase (Day *et al.*, 2007; Zierhut *et al.*, 2010; Witney *et al.*, 2011). Over the years, different approaches, based on simpler post-processing techniques have also been proposed. For instance, model-free parameters as the area under the curve for each metabolite (Hill *et al.*, 2013; Daniels *et al.*, 2016) or ratios of the metabolite signal peaks (Schroeder *et al.*, 2008; Seth *et al.*, 2011). Nevertheless, at present there is not a consensus on which method to use for the post-processing of HP [1-^{13}C]pyruvate MRI data. Our group is using a kinetic modelling of the exchange between the labelled pyruvate and its products based on a two-site exchange kinetic modelling with

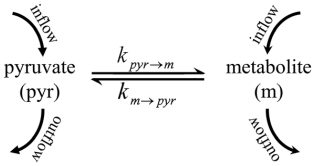

Figure 5.2: Schematic diagram of a two-site exchange model.
The diagram shows the two-site exchange model of pyruvate metabolism adopted in this study.
Figures adapted from Khegai et al. (Khegai et al., 2014).

a frequency-domain approach (Khegai *et al.*, 2014) as represented in figure 5.2.

Translation, feasibility and safety of the technique in a clinical setting were achieved in 2013 with the first-in-man study in patients with prostate cancer by Nelson and colleagues (Nelson *et al.*, 2013). Subsequently, images of the heart in healthy volunteers and the first-in-human renal cell carcinoma have been reported (Cunningham *et al.*, 2016; Tran *et al.*, 2019). Pyruvate has also been shown to cross the blood-brain barrier with the conversion of

pyruvate to [1-^{13}C]lactate (termed lactate) demonstrated both in healthy subjects and in primary and secondary brain tumours (Miloushev *et al.*, 2018; Park *et al.*, 2018; Grist *et al.*, 2019). Grist et al. demonstrated the conversion of hyperpolarized pyruvate to lactate and bicarbonate in the healthy human brain in the context of an intact blood-brain barrier (Grist *et al.*, 2019). This first study of healthy volunteers also measured the peak of pyruvate and lactate at 12 s and 16 s respectively, whilst the peak of labelled-bicarbonate was seen at 26 s (Grist *et al.*, 2019). Grist et al. also reported the first quantification of kPL and

Inclusion criteria
- 18 years or older; - Be scheduled for biopsy or resection of a presumed glioma of any grade (based on imaging features consisting with glioma); - Be aware of, and understand the diagnosis; - Be able to provide written informed consent according to ICH/GCP, national and local regulations; - Be willing and able to comply with scheduled visits, laboratory tests, imaging and other study procedure; - Patients of childbearing potential must have a negative urinary or blood pregnancy test prior to enrolment if there is a possibility they could be pregnant.
Exclusion Criteria
Clinical contraindications to MR imaging will apply to each patient and include, but are not limited to: - Pacemakers, non-MR compatible heart valves or cardiac stent or other vascular stent; - Renal impairment; - Known allergic reactions to Gd contrast agent; - Intracranial aneurysm clips that are not MR safe; - Intracranial programmable shunt; - History of intra-orbital metal fragments that have not been removed; - Inner ear implants; - Artificial joint/limb prosthesis not MR safe; - Neuro-stimulator or other under the skin devices; - False eye; - Claustrophobia; - Inability to give informed consent; - Diabetes or glucose deranging conditions.

Table 5.1: Inclusion and exclusion criteria for enrolment in the study.

kPB from the whole brain of healthy subjects; in that cohort, the kPL was 0.012 ± 0.006 s^{-1} and the kPB 0.02 ± 0.002 s^{-1}. Park *et al.* have reported 8 cases of previously diagnosed gliomas (grade II to IV) undergoing MRI follow-up using a 2D echo-planar spectroscopic sequence and paddle coils (Park *et al.*, 2018). They observed ^{13}C signal in all the cases but the experimental setup centred on a custom-built surface coil, as opposed to the dual-tuned birdcage coil used in this study, resulted in a 3- to 4- fold reduction of the signal intensity in the centre of the image with an almost complete lack of signal from the deep brain nuclei observed in those cases which is problematic for quantifying the metabolism of deep; the lactate peak was observed between 6 and 9 seconds after the pyruvate peak, potentially due to impaired exchange in the cancer cells (Park *et al.*, 2018). Miloushev *et al.* observed pyruvate conversion to lactate in 2 primary and secondary brain tumours; they also assessed repeatability in 1 patient (Miloushev *et al.*, 2018). Most of the published literature to date has demonstrated the feasibility and the safety of the technique in the human brain, with little information provided on the metabolic

Patient	Gender	Age (yrs)	Pathology (WHO 2016)	ATRX	MIB-1	Survival (days)
Patient 1	Male	66	GBM IDH-Wildtype	Lost	22	209
Patient 2	Female	53	GBM IDH-Wildtype	Retained	26	alive
Patient 3	Male	73	GBM IDH-Wildtype	Lost	38	257
Patient 4	Female	49	GBM IDH-Wildtype	Retained	18	alive
Patient 5	Male	48	GBM IDH-Wildtype	Retained	18	alive
Patient 6	Male	57	GBM IDH-Wildtype	Retained	19	alive
Patient 7	Male	74	GBM IDH-Wildtype	Lost	31	132

Table 5.2: Clinical characteristics

The monoclonal antibody MIB-1 was used to measure the Ki-67 expression which in turn determined the Ki-67 labelling index as a marker of proliferation as the clinical standard. Survival is expressed in days following the MRI.

exchange between the different metabolites. The work has shown that HP [1-^{13}C]pyruvate MRI is feasible and safe to use in humans with signal from the ^{13}C-labelled molecules clearly detectable in the human brain. This technique is extremely promising for the *in vivo* assessment of cellular metabolism in healthy and disease brain. Thus, the purpose of this study was to explore metabolic reprogramming in glioblastoma and in the surrounding microenvironment using. Moreover, this study explored the potential correlation between HP ^{13}C MRI and conventional, invasive, tissue biomarkers to increase our understanding of the underpinning metabolic changes of GBM.

5.1 Methods and materials

5.1.1 Patient selection, enrolment and clinical monitoring

This prospective study was approved by our local Research Ethics Committee (East of England, Cambridge South Research Ethics Committee, REC reference number 16/EE/0184). Between November 2016 and October 2018 eight treatment-naïve patients (6 males, 2 females; 60 $\pm$ 10.98 years) with a presumed diagnosis of GBM were recruited from the weekly Multidisciplinary Team (MDT) Meeting and/or from the Neuro-oncology clinic. Only patients scheduled for stereotactic biopsy or resection of a glioblastoma (based on consisting imaging features and MDT review) were screened to assess eligibility according to our inclusion and exclusion criteria (table 5.1). Considering the paucity of data relative to pyruvate injection in humans, a strictly conservative approach was chosen towards any disorder that may adversely affect by the injections of a high concentration of pyruvate (such as diabetes) or in presence of medications that may affect levels of pyruvate in the blood stream and, consequently, jeopardise the success of the scan. Clinical characteristics are displayed in table 5.2. During the Neuro-oncology clinic appointment, all the eligible patients received a detailed participant information sheet, describing the study rationale and procedure, and had a dedicated encounter with a member of the research team to discuss the study rationale, potential involvement and expected outcome. Written informed consent was signed by all the participants before enrolling in the study.

On the day of the scan, vital signs and laboratory tests were collected before and after the scan to ensure the wellbeing of the patient and confirm the safety of the study. Blood pressure, pulse and saturation were recorded before and after the scan and monitored during the entire procedure; temperature and weight were collected before and after the scan. Blood tests included: Aspartate transaminase, Lactate dehydrogenase, Lactate, Serum Glucose, Urea, Albumin, Bicarbonate, Sodium, Potassium and Creatinine; those were performed before and after the scan. Vital signs and laboratory investigations were performed to ensure patient suitability for the study.

5.1.2 Pyruvate synthesis and hyperpolarization

MRI examinations were performed using a 3.0 T clinical scanner and a 12-channel head coil (Discovery MR750; GE Healthcare). Imaging included: 3D T_2-weighted imaging (T_2W; repetition time/echo time [TR/TE] 2500/79 ms; 248 slices; slice thickness 1.2 mm; acquisition matrix 320x320; field of view [FOV] 240x240 mm), 2D T_2W fluid-attenuated inversion recovery (FLAIR; TR/TE 8000/126ms; inversion time [TI] 2128 ms; slice thickness 6 mm; acquisition matrix 384x224; FOV 240x240 mm) and DWI (TR/TE 2841-3867/83.3-87.4 ms; slice thickness 5mm; b-values 0,1000 s/mm^2; matrix 128x128; FOV 240x240 mm). 3D T_1-weighted Fast SPoiled GRadient echo (T_1W FSPGR; 252 slices; 0.94x0.94x1.5 mm reconstructed to 0.94x0.94x1 mm; TR/TE 8.2/3.2; slice thickness 1.5 mm; matrix 256x256; FOV 240x240 mm) was performed before and after gadolinium-based contrast injection (Gadobutrol 1.0 mmol/mL; Schering). ADC maps were generated as per clinical standard.

5.1.3 ^{1}H and HP ^{13}C MRI acquisitions

Patients were imaged on a 3 T clinical scanner (Discovery MR750, GE Healthcare, Waukesha, WI, U.S.A.) using a dual-tuned ^{13}C/^{1}H quadrature transmit/receive head coil (Rapid Biomedical, Rimpar, Germany) for the HP ^{13}C MRI and a 12-channel head coil (GE Healthcare, Waukesha, WI, U.S.A.) for the ^{1}H imaging.

The HP ^{13}C MRI acquisition was performed using a dynamic Iterative Decomposition with Echo Asymmetry and Least squares estimation (IDEAL) spiral chemical shift imaging (CSI) sequence (FOV 240 x 240 mm, TR 500 ms, Flip angle 15°, acquisition time 60 s, temporal resolution 4 s, acquisition matrix 40 x 40, reconstruction matrix 128 x 128, slice thickness 30 mm). (Wiesinger *et*

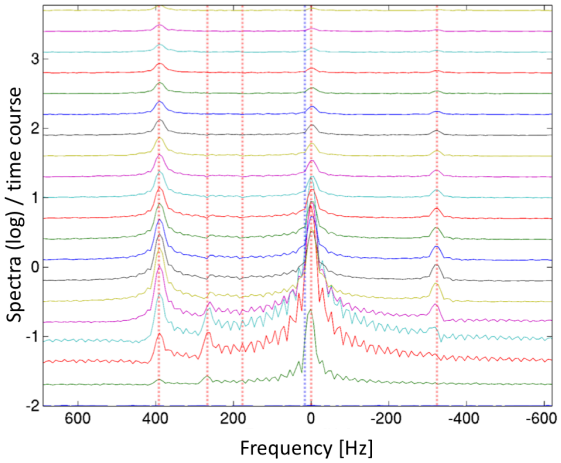

Figure 5.3: Representative spectra.
Dynamic ^{13}C spectra from a patient depicting the time course of pyruvate, lactate and bicarbonate.

al., 2012) A reference 3D T_1W Fast SPoiled GRadient echo (FSPGR; field of view [FOV] 240 x 240 mm, TR/TE 8.6/3.2 ms, acquisition matrix 256 x 224, reconstruction matrix 256 x 256; slice thickness 2mm) was acquired with the dual-tuned $^{13}C/^{1}H$ quadrature head coil within the same geometrical space to facilitate image registration for quantitative analysis.

The HP ^{13}C MRI acquisition was followed by conventional proton imaging including: 3D T_2W (repetition time/echo time [TR/TE] 2500/79 ms; 248 slices; slice thickness 1.2 mm; acquisition matrix 320 x 320; FOV 240 x 240 mm), 2D T_2W fluid-attenuated inversion recovery (T_2W FLAIR; TR/TE 8000/126 ms; inversion time [TI] 2128 ms; slice thickness 6 mm; acquisition matrix 384 x 224; FOV 240 x 240 mm) and Diffusion-Weighted Imaging (DWI, TR/TE 2841-3867/83.3-87.4 ms; slice thickness 5 mm; b-values 0, 1000 s/mm^2; matrix 128 x 128; FOV 240 x 240 mm). A 3D T_1W FSPGR (252 slices; 0.94 x 0.94 x1.5 mm reconstructed to 0.94 x 0.94 x 1 mm; TR/TE 8.2/3.2; slice thickness 1.5 mm; matrix 256 x 256; FOV 240 x 240 mm) was performed before and after gadolinium-based contrast injection (Gadobutrol 1.0 mmol/mL; Bayer AG, Leverkusen, Germany).

5.1.4 Image processing and analysis

The post processing was performed in Matlab (Matlab 2017a, the MathWorks, Natick, MA, U.S.A.) using in-house scripts allowing for the sum of the metabolites over the time course, iterative adjustment of a threshold for masking and estimation of noise-corrected ratio maps (lactate to pyruvate, bicarbonate to pyruvate and bicarbonate to lactate ratios). The kinetic modelling of the exchange between the labelled pyruvate and its products was estimated using a two-site exchange kinetic modelling with a frequency-domain approach (Khegai *et al.*, 2014). This fitting utilizes the entire acquired signal, from the pyruvate arrival until the polarization is decayed, avoiding an explicit time differentiation that could result in noise amplification. The apparent build-up rate forward constant k_{PL}, derived through the kinetic modelling, expresses the constant conversion rate between pyruvate and lactate catalysed by the enzyme lactate dehydrogenase (LDH) but also incorporates inflow and transport and hence is an apparent rate constant rather than a true rate constant. For the modelling, the backward conversion (expressed by the constant k_{LP}) and the spin lattice relaxation effects were combined as an effective relaxation term. Similarly, k_{PB} was defined as the apparent forward rate constant representing

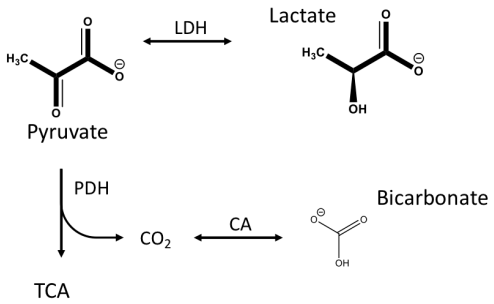

Figure 5.4: Diagram showing the conversion of pyruvate into lactate and bicarbonate. Abbreviations: LDH - lactate dehydrogenase, PDH - pyruvate dehydrogenase, CA - carbonic anhydrase, TCA – tricarboxylic acid cycle.

the conversion of pyruvate to carbon dioxide catalysed by the enzyme pyruvate dehydrogenase (PDH) and followed by exchange with bicarbonate, catalysed by the enzyme carbonic anhydrase (CA). Figure 5.4 shows the interplay between pyruvate, lactate and bicarbonate; a more comprehensive depiction of pyruvate metabolic fate is shown in Figure 2.2 in chapter 2.

A neuroradiologist with 7 years of experience in neuro-imaging outlined all the ROIs on the unenhanced 3D T_1W FSPGR sequence, acquired with the dual-tuned coil, using OsiriX (V.8.5.2, Pixmeo SARL, Bernex, Switzerland). The post gadolinium injection 3D T_1W FSPGR, the T_2W and the T_2W FLAIR images were used as additional guidance to define the different lesion components. Enhancing tumour was defined on the post-gadolinium T_1WI compared to pre-contrast T_1WI and excluding any area of haemorrhage. The necrotic components were defined as regions within the tumour that did not enhance and had a hyperintense signal on the corresponding T_2WI. ROIs were obtained for the whole tumour and the peritumoral region. To further assess the spatial heterogeneity within the lesion, a regional sub-analysis was performed selecting multiple circular ROIs in the medial, lateral, anterior and posterior aspects of the lesion; those ROIs were of the same area (1 cm^2) to avoid any potential confounding effects due to different volume of the ROIs. For comparison, the non-tumour bearing brain parenchyma (NTBP) was assessed in each hemisphere, each lobe and at the level of the basal ganglia. Furthermore, the lesion ROIs were mirrored on the contralateral side. Lastly, individual circular ROIs, identical to the ones drawn for the GBMs, were obtained in the lobes that were deemed normal at conventional imaging. The intra-patient heterogeneity was assessed computing histograms and scatter plots of metabolite concentrations and constants value in the GBMs and in the contralateral NTBP using in-house scripts in Matlab.

Apparent diffusion coefficient (ADC) maps were reconstructed from the DWI data. To ensure perfect matching of the ROIs, the ADC maps were registered to the unenhanced 3D T_1W FSPGR and the T_2W sequences using an in-house pipeline using FLIRT (FMRIB's Linear Image Registration Tool) as registration tool (Jenkinson and Smith, 2001; Jenkinson *et al.*, 2002). To account for the different slice thickness, the 6 ADC slices corresponding to the ^{13}C MRI slice were averaged. The ROIs drawn on the 3D T_1W FSPGR and the T_2W sequences, as detailed in the previous paragraph, were used to extrapolate the ADC values from the lesion and the mirrored contralateral region.

The same neuroradiologist performed a 3D manual segmentation of the GBMs using an open source dedicated software (ITK-SNAP v. 3.6;

www.itksnap.org) to obtain lesion volumes (Yushkevich *et al.*, 2006). As per the previously mentioned classification of the tumour components, the volume of the enhancing tissue and of the necrotic components were separately drawn and recorded. The total volume of the lesion was also computed as the sum of the two volumes. An example of segmented volume is shown in figure 5.1.

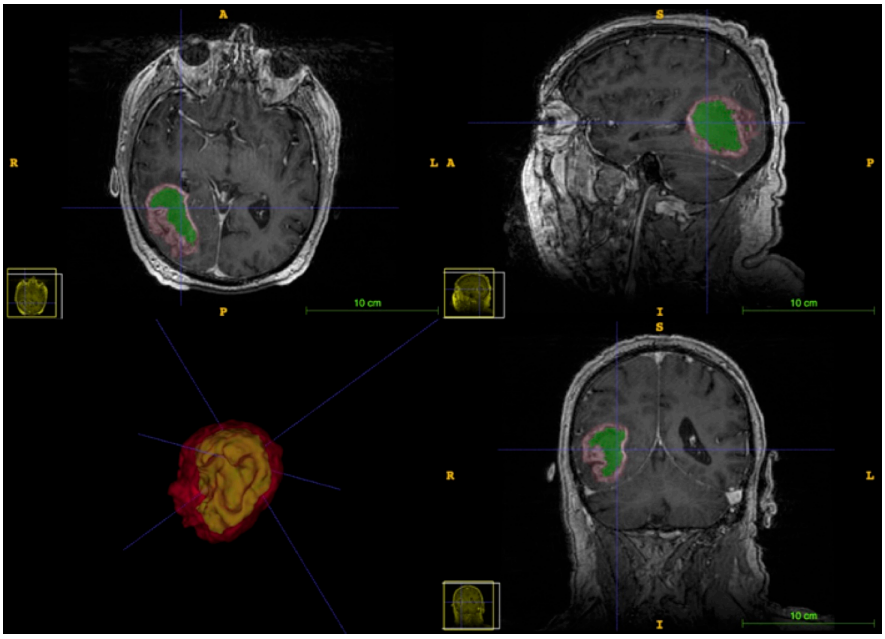

Figure 5.5: Example of volume segmentation.
Software used for the volumetric segmentation (ITK-SNAP v. 3.6; www.itksnap.org). Axial, sagittal and coronal images are reformatted from the 3D T_1W Fast SPoiled GRadient-echo (FSPGR). The segmentation is manually performed using the three planes to ensure maximum accuracy. The software also shows a 3D volume rendering of the lesion. Necrosis is displayed in green, enhancing tissue is displayed in red.

5.1.5 Histopathology, immunohistochemistry and western blot

5.1.5.1 Image-guided biopsy targeting and correlation with pathology

All the patients enrolled in this study were scheduled for maximal resection of their previously identified GBM. To explore the intratumoral heterogeneity of the lesions, several target areas for biopsies were identified prior to surgery for each patient with the aim of correlating imaging biomarkers with tissue-derived biomarkers. Identification of target areas was performed by the neuroradiologist in charge of the project on HP ^{13}C MR images and discussed with the operating neurosurgeon prior to surgery. For consistency, the same three sequences were used in all the cases: summed pyruvate,

summed lactate and lactate to pyruvate (LP) ratio. Those sequences were overlaid on the corresponding unenhanced axial T_1W FSPGR slice obtained with the dual-tuned coil. Targets were defined by a mismatch between summed pyruvate, summed lactate and LP ratio accounting also for eloquence of the adjacent tissue. If a potential target was deemed to be too close to a functional area of the brain (i.e. the motor cortex or the calcarine cortex) the location was discarded, and another suitable target identified. After the sampling plan was finalised; the proposed biopsy targets were recorded on the unenhanced and enhanced axial T_1W FSPGR. The neuroradiologist in charge of the study then discussed the sampling plan with the operating neurosurgeon prior to surgery, using both the annotated images and the full set of acquired images. Digital and printed copy of the annotated images were provided to the operating neurosurgeon to be used in the operating theatre. A member of the research team was present in theatre during surgery with a further copy of the sampling plan to assist with the targeted sampling. Tissue sampling was adapted during surgery if deemed necessary by the operating neurosurgery in consensus with the member of the research team present in the operating room. Screenshots of the neuronavigation system depicting the exact location of each biopsy were taken and stored for further image registration. After surgery, the exact areas from where the samples were taken were recorded on printed MRI images and on each sample to ensure future localization.

The direct comparison between imaging, pathological analysis and results from the western blots was performed by drawing circular ROIs of 1 cm^2 on the registered T_1WI, on areas corresponding to the biopsies location from which the tissue was obtained during surgery. Those ROIs were then transferred on the metabolic maps to obtain the concentration of the metabolites directly matched with the corresponding sample.

5.1.5.2 Histopathology and immunohistochemistry

A board-certified neuropathologist with 7 years of experience determined the tumour grade and type using the WHO-2016 classification (Louis *et al.*, 2016). Haematoxylin and eosin staining (H&E) was performed as per clinical standard; isocitrate dehydrogenase isozymes 1 (IDH1) mutation status and O[6]-methylguanine-DNA methyltransferase (MGMT) methylation status were

checked in all cases. As per standard of care, the antibody MIB-1, directed against the protein Ki-67 produced by the gene MKI67, was assessed on tumour photomicrographs from a x600 FOV and a fixed matrix of 184x138 μm using a semi-automated software (Image-Pro Insight, Media Cybernetics Inc, Maryland, U.S.A.) and expressed in percentage as a proliferation marker.

Tissue samples collected at surgery under image-guidance were fresh-frozen and stored in the Human Research Tissue Bank (HRTB) at -80 °C to allow for a subsequent quantitative and semi-quantitative analysis as per the research protocol. Additional Immunohistochemical (IHC) staining for research purposes was obtained for monocarboxylate transporter 1 (MCT1), monocarboxylate transporter 4 (MCT4), hypoxia-inducible factor 1-alpha (HIF1-a), carbonic anhydrase IX (CA IX), cluster of differentiation 31 (CD31), cluster of differentiation 4 (CD4), cluster of differentiation 8 (CD8), cluster of differentiation 68 (CD68), the antigen Ki67 and the antigen mast cell tryptase 1 (MCT). Samples were formalin-fixed and paraffin embedded (FFPE) after defrosting. Subsequently, de-waxing and re-hydration (as standard) prior to IHC were performed using an automated Leica ST5020 (Leica Biosystems Newcastle Ltd, Newcastle Upon Tyne, United Kingdom); 4 μm sections were obtained with a microtome.

The staining was done with a BOND-III fully automated immunohistochemistry (IHC) and in situ hybridization (ISH) stainer system (Leica Microsystems UK Ltd, Milton Keynes, United Kingdom). Pre-treatment of the formalin-fixed, paraffin-embedded tissue sections with heat-induced epitope retrieval (HIER) was performed for each monoclonal antibody for 20 minutes; Tris EDTA prepared at different pHs (6 to 9) was used in all the IHC procedures except for HIF1-α and CA IX (sodium citrate was used) and ki67 (no pre-treatment was performed). Endogenous peroxidase activity was blocked using 3-4% (v/v) hydrogen peroxide. Since all of the primary antibodies (listed in the following paragraph) are raised in rabbit, for antigen localisation all the slides were then incubated with a polymer anti-rabbit Poly-HRP-IgG (<25 μg/ml) containing 10% (v/v) animal serum in tris-buffered saline/0.09% ProClin™ 950 (Sigma-Aldrich, St. Louis, MO, U.S.A.). Diaminobenzidine tetrahydrochloride hydrate enhancer (DAB; AR9432; Leica Biosystems Newcastle Ltd, Newcastle

Upon Tyne, United Kingdom) was used for all the antibodies. The post-staining de-hydration and clearing were done on the automated Leica ST5020 (Leica Biosystems Newcastle Ltd, Newcastle Upon Tyne, United Kingdom). Finally, sections were mounted on a fully automated glass cover slipper CV5030 (Leica Biosystems Newcastle Ltd, Newcastle Upon Tyne, United Kingdom).

The antibodies used for staining were: HPA003324 (Atlas Antibodies, Bromma, Sweden) at a dilution of 1:500 for MCT1, HPA021451 (Atlas Antibodies, Bromma, Sweden) at a dilution of 1:500 for MCT4, ab51608 (Abcam, Cambridge, United Kingdom) at a concentration of 23.36 µg/ml for HIF1-α, NCL-L-CA IX (Leica Biosystems Newcastle Ltd, Newcastle Upon Tyne, United Kingdom) at a dilution of 1:100 for CA IX, M 0823 (Dako Denmark A/S, Glostrup, Denmark) at a dilution of 1:20 for CD31, PA0427-4B12 (Leica Biosystems Newcastle Ltd, Newcastle Upon Tyne, United Kingdom) for CD4 (no dilution required as this antibody is optimally diluted for use on the BOND systems), PA0183-4B11 (Leica Biosystems Newcastle Ltd, Newcastle Upon Tyne, United Kingdom) for CD8 (no dilution required as this antibody is optimally diluted for use on the BOND systems), M 0876 (Dako Denmark A/S, Glostrup, Denmark) at a dilution of 1:50 for CD68, M 7240 (Dako Denmark A/S, Glostrup, Denmark) at a dilution of 1:75 for Ki67 and PA0019-10D11 (Leica Biosystems Newcastle Ltd, Newcastle Upon Tyne, United Kingdom) and PA0019-10D11 (Leica Biosystems Newcastle Ltd, Newcastle Upon Tyne, United Kingdom) for MCT (no dilution required as this antibody is optimally diluted for use on the BOND systems).

After staining, brightfield scanning was performed to allow the high-resolution digitalised images to be quantitatively analysed using a dedicated image analysis platform for quantitative tissue analysis in digital pathology (HALO v2.2.1870.15; Indica Labs, Albuquerque, New Mexico, U.S.A).

The digital analysis of the slides was performed using dedicated algorithms able to quantify areas of staining according to their intensity (weak, moderate or strong). To facilitate the comparison across multiple samples and multiple staining the intensity was converted in percentage of staining relative to the whole area of the slide. The minimum optical densities used to cluster the voxels in weak, moderate and strong are as follow: MCT 1 0.482, 0.487 and 0.540; MCT 4 0.424, 0.487 and 0.54; CA IX 0.240, 0.319 and 0.478; CD31

Biomarker	Role and rationale for inclusion
MCT-1	Monocarboxylate transporter 1 is a membrane transporter with high affinity for pyruvate and responsible for its uptake and lactate import. Overexpression of MCT-1 in glioblastoma has been linked to worse survival.
MCT-4	Monocarboxylate transporter 4 is a membrane transporter with lactate as preferred substrate and mostly responsible for lactate export. MCT-4 is hypothesised to be overexpressed in hypoxic glioblastomas.
HIF1-α	Hypoxia Inducible Factor-1 alpha is involved in the induction of stem-like phenotype under hypoxia. Expression of HIF1-α is thought to be regulated by MCT-4 in glioblastoma.
CA IX	Carbonic anhydrase IX is a marker of hypoxia. CA IX is overexpressed in glioblastoma and associated with poor survival.
CD31	Cluster of differentiation 31, also known as Platelet endothelial cell adhesion molecule (PECAM-1), is expressed on platelets, inflammatory cells and endothelial cells. CD31 is overexpressed in glioblastomas and its expression correlates with HIF1-α.
CD4	Cluster of differentiation 4 is found on immune cells and dendritic cells. Tumour-infiltrating lymphocytes express CD4 and CD8, thus their quantification can inform on inflammation.
CD8	Cluster of differentiation 8 is found on immune cells (predominantly cytotoxic T cells), thymocytes and dendritic cells. Tumour-infiltrating lymphocytes express CD4 and CD8, thus their quantification can inform on inflammation.
CD68	Cluster of Differentiation 68 is expressed by monocytes and macrophages (including microglia). CD68 is a marker of inflammation.
Ki67	Ki67 is a cellular marker of proliferation.
LDH-A	Lactate dehydrogenase A is a key enzyme for the conversion of pyruvate into lactate. In glioblastoma, LDH-A has been shown to positively correlate with GBM development.
c-Myc	c-Myc is a transcription factor which expression is correlated with glioma grade and increases the expression of glycolytic enzymes.

Table 5.3: Tissue biomarkers

The table shows the tissue biomarkers assessed with immunohistochemistry and western blotting Their role and rationale for use is also provided.

0.244, 0.319 and 0.478. For CD4, CD8, CD68 and Ki67, cells were firstly identified and then classified as positive/negative stained; subsequently, the percentage of stained cells was computed. Mast cell tryptase 1 was not further analysed due to the complete lack of staining. A total of 290 individual slides from the 7 patients were analysed.

Western blotting was performed as described in Mair *et al* (Mair *et al.*, 2018). Briefly, proteins were extracted from tissue samples in Pierce RIPA buffer, containing protease inhibitor and EDTA (Thermo Fisher Scientific). Proteins were separated using gel electrophoresis in NuPage Bis-Tris precast gels (Thermo Fisher Scientific) and dry-blotted onto polyvinylidene difluoride (PVDF) membranes using an iBlot transfer stack (Thermo Fisher Scientific). Subsequent analysis was performed using an Odyssey Licor near-infrared digital fluorescence imaging system (LI-COR Biotechnology). Samples (n = 23) were analyzed in duplicate or triplicate and data from technical replicates were averaged. The antibodies for LDH-A and c-Myc were used at the dilution recommended by the manufacturer: LDHA–Cell Signaling Technology #3582 1:1,000 and c-Myc–Abcam ab32072 1:10,000, respectively.

5.1.6 Statistical Analysis

Anonymised data were recorded into multiple electronic spreadsheets (Microsoft Excel for Macintosh V. 16; Microsoft Corporation, Redmond, Washington, U.S.A.) for easy storage and analysis. The statistical analysis was performed using a mathematical analytical software (Matlab Statistics and Machine Learning Toolbox, Matlab 2017a; MathWorks, Natick, MA, United States), and two statistical dedicated packages, SPSS (SPSS 18.0 statistical package; SPSS Inc, Chicago, IL, USA) and RStudio version 1.1.463 (Rstudio Inc., Boston, MA, USA) for Macintosh based on R version 3.5.1 (The R Foundation for Statistical Computing Platform) as appropriate for the specific analysis to be undertaken. The Shapiro–Wilk test was used to test for normality of data. Continuous data are expressed as mean ± standard deviation [minimum – maximum] for normally distributed data and median ± median absolute deviation [minimum – maximum] for non-parametric data; categorical data are expressed an *n* (%).

Paired t-test, unpaired t-test and Wilcoxon signed rank test were used to compare the lactate to pyruvate ratio and kinetic values derived from the GBM and the NTBP as appropriate according to the distribution of the data. To further explore heterogeneity, in house developed scripts were used to generate histograms using the metabolites values and/or ADC to determine the bin width

and the number of voxels to determine the bin height. Values of pyruvate, lactate and bicarbonate were normalised for the contralateral non-tumour bearing brain parenchyma to account for inter-patient heterogeneity. Normalisation was not deemed necessary for the ratios (as ratios are intrinsically normalised) and for the modelled values (as they are mathematically derived using the same equations and thus the effects of the different SNRs is eliminated). In house scripts were also used to generate scatter plots of ADC and labelled metabolites both as per-voxel and per-patient. Volume of the entire lesion, the enhancing and the necrotic components were correlated with the LP and BP ratio using the Spearman's rho correlation coefficient and represented graphically using scatter plots. If present, all the fits have been obtained using a binomial derivate (linear fit). In-house scripts for the analysis are provided in the supplementary material at the end of the chapter.

To determine the statistical significance of all the tests, a base set value of $p = 0.05$ was initially chosen and subsequently corrected for multiple comparison. The false discovery rate (FDR) method using the Benjamini-Hochberg procedure was applied to test significance (Benjamini and Hochberg, 1995). The FDR represents the proportion of significant results that are actually false positives. Carefully consideration has been given to which proportion of false positive we were willing to accept for this study. An FDR of 5% is generally believed too low for many experiments having multiple correlations because this will be on top of a p value which is usually already chosen as low as 0.05 lead to an over rejection rate (McDonald, 2014).

Moreover, this is the first study correlating biological biomarkers with HP ^{13}C MRI in an exploratory fashion, thus, avoiding potential false negatives was deemed more important than the risk of including some false positives that might be disputed in future works. At the same time, the potential cost of disproving a too high number of false positive findings due to the expensive technique used in this study and the logistical difficulties in replicating the same setup, was considered when setting the FDR. All those considerations lead to a chosen value of 10%, however, we also decided to show the results of the analysis performed with a FDR of 5% as those results would be most likely to be significant in a confirmatory study. Of note, the p values that are presented in this study are raw p values and only the significance is stated according to the

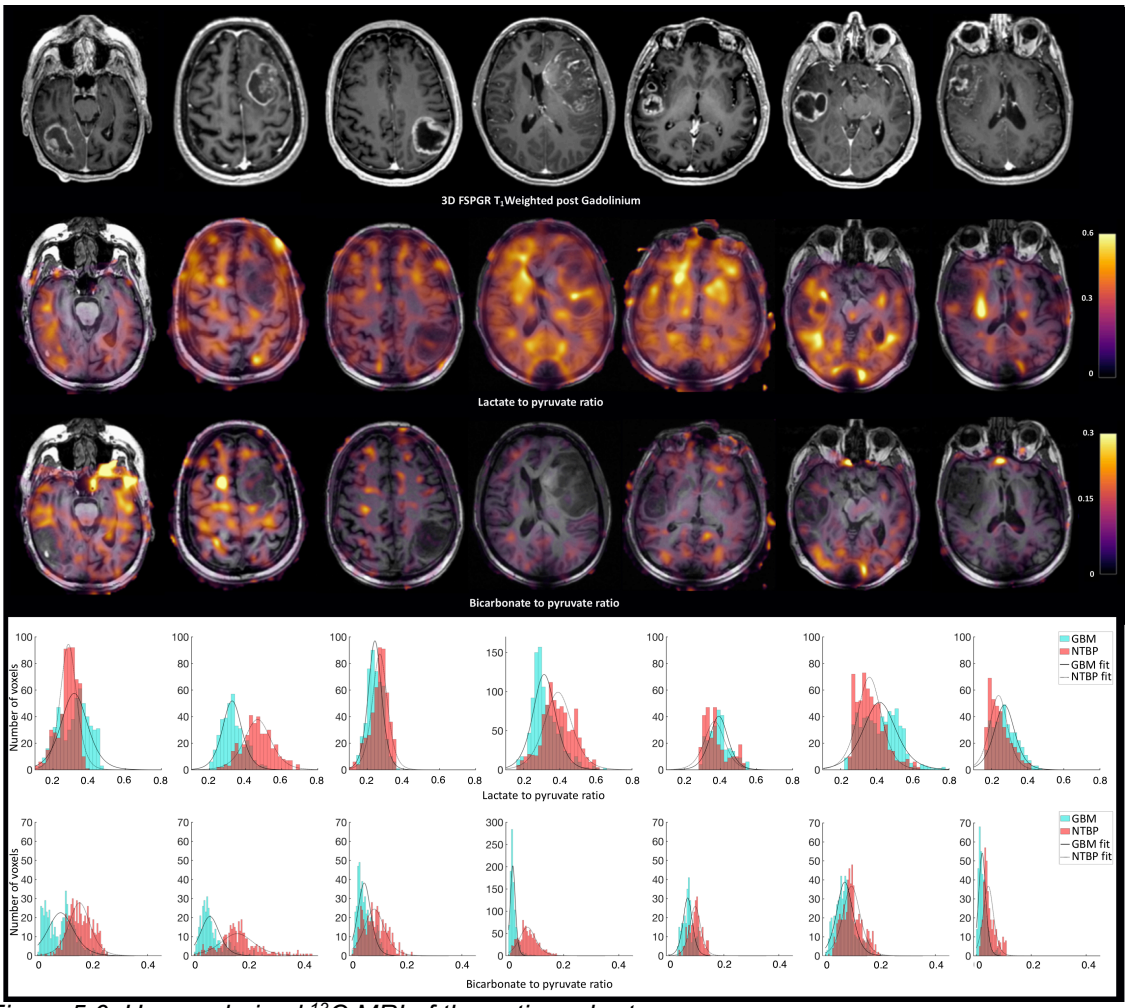

Figure 5.6: Hyperpolarised ^{13}C MRI of the entire cohort.

The first three rows show the 3D T_1W Fast SPoiled GRadient-echo (FSPGR), axial unenhanced T_1W overlaid with the lactate to pyruvate ratio and axial unenhanced T_1W overlaid with the bicarbonate to pyruvate ratio through the centre of the lesion for each patient. The last two rows show the histograms relative to the lactate to pyruvate ratio and bicarbonate to pyruvate ratio values for each voxel from the same slice; glioblastoma is shown in light blue, non-tumour bearing brain parenchyma is shown in light red.

Benjamini-Hochberg procedure. No Benjamini-Hochberg adjusted p values have been provided to avoid the potential confusion that those modified p values could generate when interposed with non-adjusted p values relating to other statistical procedures.

5.2 Results

5.2.1 Feasibility and technical success

Dynamic signal from hyperpolarized pyruvate, lactate, and bicarbonate was observed in the brain following intravenous injection of [1-^{13}C]pyruvate and

no adverse events were observed in the entire cohort. In 1 case the FoV was incorrectly acquired compared to the other cases and therefore this patient was excluded from the subsequent analysis to ensure homogeneity of the scans. Figure 5.2 shows LP and bicarbonate to pyruvate (BP) ratio maps for all the subjects.

Results from the QC report are shown in table 5.3. Briefly, the average polarization was 22.3 ± 3.9 % [16.3 – 28.0]; the pyruvate concentration was 256 ± 12 mmol/L [232 - 268] and pH was 7.7 ± 0.2 [7.3 – 8.0]. The time delay between dissolution and injection of pyruvate was 59 ± 4 s [54 - 65].

Patient	Polarization (%)	Pyruvate concentration (mmol/L)	EPA concentration (μM/L)	pH	Temperature (C)	QC module opening (s)	Injected volume (mL)
Patient 1	22.6	232	0.6	7.9	35	34	39
Patient 2	16.3	243	0.8	8	34	34	40
Patient 3	22.1	259	1	7.8	32.8	34	32
Patient 4	20.3	268	1.3	7.5	33.5	36	34.3
Patient 5	27.5	264	2	7.3	35.9	34	33.3
Patient 6	19.2	263	1.2	7.6	35.9	35	35
Patient 7	28	263	0.6	7.9	34.6	38	32.4
Entire cohort	22.3 ± 3.9 (16.3 - 28)	256 ± 12.3 (232 - 268)	1.1 ± 0.4 (0.6 - 2)	7.7 ± 0.2 (7.3 - 8)	34.5 ± 1.1 (32.8 - 35.9)	35 ± 1.4 (34 - 38)	35.1 ± 2.9 (32 - 40)

Table 5.4: Quality control of the hyperpolarized pyruvate.

The table shows the results from the quality control analyses of the hyperpolarized pyruvate obtained with the quality control (QC) monitor immediately after dissolution for each patient and as average ± standard deviation (minimum - maximum) for the entire cohort. Polarization is expressed in percentage of increase from the baseline, pyruvate concentration in the solution as mmol/L, the EPA concentration in μM/L, temperature in Celsius degree (C), the QC module refers to the time after dissolution when the door of the QC unlocks and is expressed in seconds, the injected volume of pyruvate is expressed in mL.

5.2.2 Pyruvate dynamics and metabolic heterogeneity

5.2.2.1 Comparison between the GBM and the contralateral side

The kinetic analysis of the GBMs demonstrated a high degree of variability in the concentrations of summed pyruvate, lactate and bicarbonate ranging, respectively, from 5.5 to 34.0 (average 18.6 ± 11.1), 1.7 to 10.6 (6.1 ± 3.6) and 0.28 to 2.74 (1.03 ± 0.84). This heterogeneity is best appreciated in the histograms shown in figures 5.5 and 5.6. Pyruvate and lactate summed over the entire time course were significantly higher in the GBM compared to the contralateral non-tumour bearing brain parenchyma, assessed using a mirrored ROI of the lesion (p = 0.010 and p = 0.036 respectively, paired samples t-test); table 5.4. However, the bicarbonate concentration summed over the time course was significantly lower in the tumour compared to contralateral non-tumour bearing brain parenchyma (p = 0.004, paired samples t-test); table 5.4.

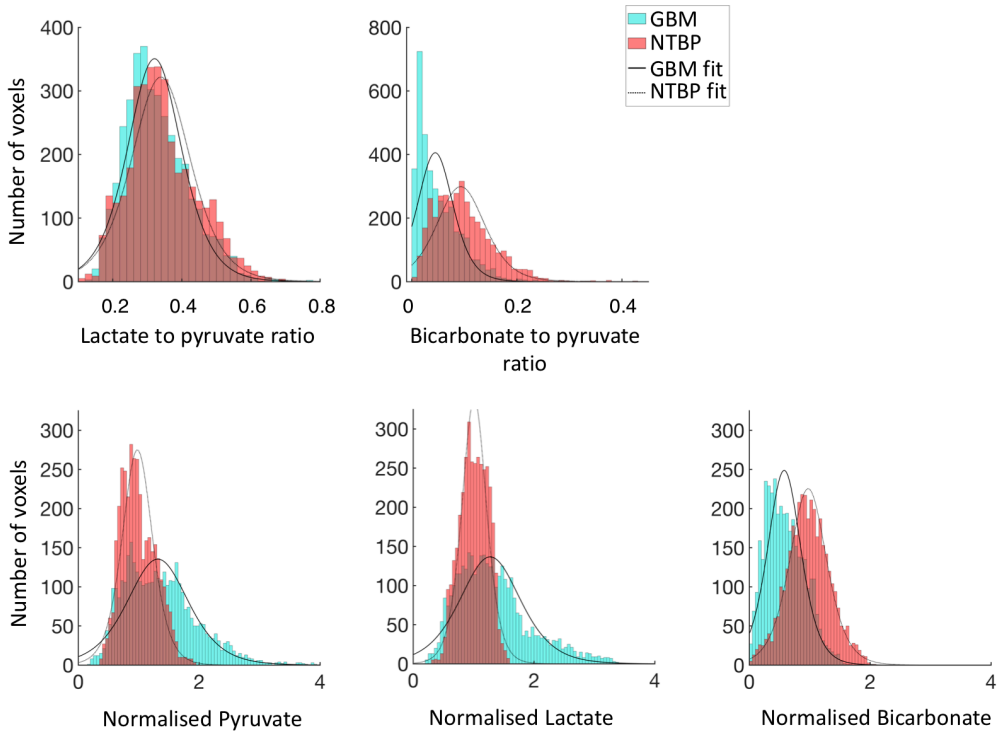

Figure 5.7: Hyperpolarised ^{13}C MRI metabolites in the entire cohort.
Histograms showing the pooled values in the entire cohort for lactate to pyruvate ratio, bicarbonate to pyruvate ratio, normalized pyruvate, normalized lactate and normalized bicarbonate. Normalisation is according to the non-tumour bearing brain parenchyma. Glioblastoma is shown in light blue, non-tumour bearing brain parenchyma is shown in light red.

The same trends were confirmed comparing the metabolic values of the GBMs with the metabolites obtained from multiple ROIs in the NTBP and from the entire contralateral hemisphere; tables 5.5 and 5.6.

As there are many experimental factors that may influence the summed pyruvate, lactate and bicarbonate signal, kinetic analysis was performed which corrects for these factors to generate more comparable data between patients. The kinetic analysis of the conversion between pyruvate and lactate showed a slightly lower LP ratio in the GBM compared with the corresponding area of the contralateral side; however, the difference was not statistically significant ($p = 0.382$, paired samples t-test); table 5.4. Similarly, there was not a statistically significant difference in the k_{PL} between the tumour and the contralateral side ($p = 0.730$, paired samples t-test); table 5.4. The lack of significant differences between the GBM and the NTBP was confirmed in the subanalyses with multiple ROIs and with the entire contralateral hemisphere; tables 5.5 and 5.6.

The assessment of the exchange between pyruvate and bicarbonate, revealed a BP ratio significantly lower in the GBM than in the contralateral side in all the subanalyses and unlike the LP ratio, this was significant (same region $p = 0.002$, paired samples t-test; multiple ROIs $p = 0.0002$, paired samples t-test; entire hemisphere $p = 0.016$, Wilcoxon signed rank test); tables 5.4, 5.5 and 5.6. The k_{PB} was lower in the GBM in all the sub analyses, however, the difference was significant only comparing the GBMs with multiple ROIs from the same contralateral region ($p = 0.0006$, paired sample t-test) and with the entire contralateral hemisphere ($p = 0.031$, Wilcoxon signed rank test); tables 5.5 and 5.6.

5.2.2.2 Intralesional heterogeneity

Visual inspection of the metabolic maps revealed intralesional heterogeneity in all the cases for all the analysed metabolites. In particular, LP and BP ratios show a high degree of intralesional heterogeneity. In all the 7 cases, areas of low LP ratio were demonstrated (representing high uptake of pyruvate in the GBM with slow exchange to lactate) as well as areas showing a high LP ratio (representing low pyruvate uptake and high lactate conversion). Similarly, tumour regions of both low BP ratio (representing high uptake of pyruvate with low exchange to bicarbonate) and high BP ratio (representing low

uptake of pyruvate and high exchange to bicarbonate) coexisted in all the cases. The intralesional heterogeneity is demonstrated in Figure 5.2; visually with the LP and BP ratio maps of all the 7 patients and quantitatively with the histograms showing the voxel intensity values for the two ratios.

The intralesional heterogeneity was assessed comparing the medial and the lateral side of the lesion. Pyruvate, lactate, bicarbonate and the BP ratio were significantly different across the lesion (p = 0.108, paired samples t-test; p = 0.028, Wilcoxon signed rank test; p = 0.034, Wilcoxon signed rank test; p = 0.0007, Wilcoxon signed rank test; respectively), table 5.7. There was no statistically significant difference in LP ratio (p = 0.774, paired sample t-test), k_{PL} (p = 0.497, paired sample t-test) or k_{PB} between the medial and lateral areas of the tumour (p = 0.055, Wilcoxon signed rank test).

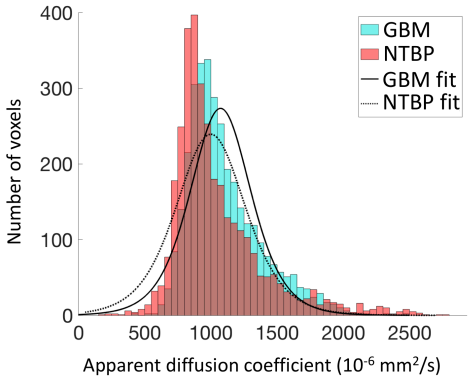

Figure 5.8: ADC values in the entire cohort.

Histograms showing the pooled ADC values in the entire cohort. Glioblastoma is shown in light blue, non-tumour bearing brain parenchyma is shown in light red.

5.2.2.3 Metabolic activity of the non-tumour bearing brain parenchyma

The comparison between the NTBP ipsilateral to the GBM and the contralateral NTBP demonstrated no statistically significant differences in pyruvate uptake (p = 0.119, paired sample t-test), lactate production (p = 0.100, paired sample t-test), LP ratio (p = 0.945, paired sample t-test) or k_{PL} (p = 0.772, paired sample t-test). Summed bicarbonate (p = 0.016, Wilcoxon signed rank test), BP ratio (p = 0.012, paired sample t-test) and k_{PB} (p = 0.029, paired sample t-test) were significantly lower in the ipsilateral side; table 5.9.

The kinetic analysis of the entire hemisphere confirmed significant differences in the exchange between pyruvate and bicarbonate, as

demonstrated by the summed bicarbonate signal (p = 0.001, Wilcoxon signed rank test), BP ratio (p < 0.001, Wilcoxon signed rank test) and k_{PB} (p = 0.044, Wilcoxon signed rank test). There was also a statistically significant difference in summed pyruvate signal (p = 0.030, paired sample t-test) and lactate signal (p = 0.040, paired sample t-test); table 5.10.

5.2.3 GBM cellularity, size and metabolic activity

The average tumour ADC was 1105.6 ± 282.3 x 10^{-6} mm^2/s (409.3 – 2483.9) for the GBMs and 1049.7 ± 348.4 x 10^{-6} mm^2/s (182.7 – 2782.5) for the contralateral area; there was no statistically significant difference between the two regions (p = 0.310; Wilcoxon signed rank test). Figure 5.7 shows the overlay between the histogram of ADC values in the tumour and those of the contralateral NTBP.

The scatter plots in figure 5.5 depict the distribution of ADC with LP and BP ratios. In the GBM, the ADC showed a slightly upward trend with increasing ADC values associated with an increase in both LP and BP ratios (r = 0.06, p < 0.001 and r = 0.18, p < 0.001, respectively), opposite to the trend showed by normal tissue that showed a decrease of ADC values with decrease of LP and BP ratios (LP ratio r = 0.15, p < 0.001 and BP ratio r = 0.1, p < 0.001). Higher r

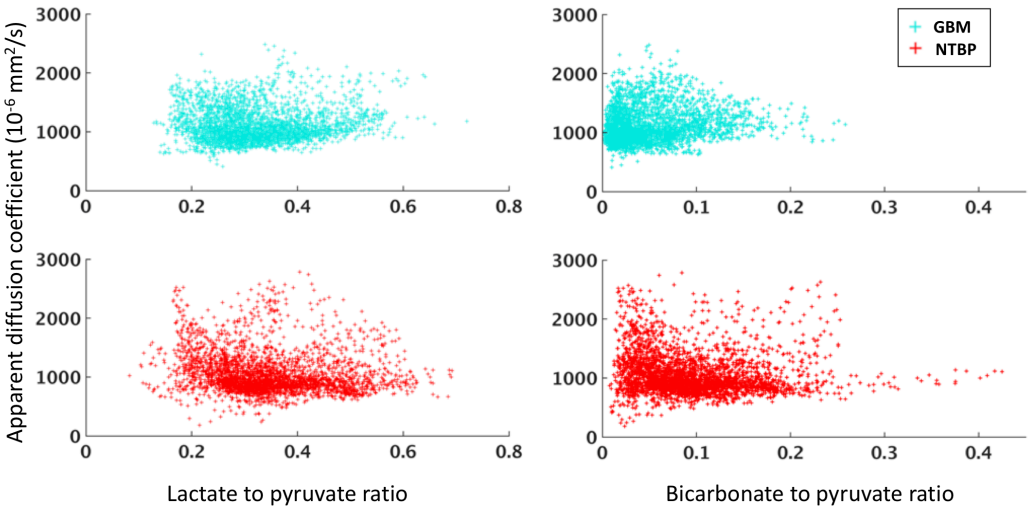

Figure 5.9: Relationship between ADC and hyperpolarized ^{13}C MRI.

The scatterplots show the relationship between ADC and lactate to pyruvate ratio (first column) and bicarbonate to pyruvate ratio (second column). Glioblastoma is shown in light blue, non-tumour bearing brain parenchyma is shown in light red.

values were found using a quadratic fit for both LP ratio (GBM r = 0.21, p < 0.001 and NTBP r = 0.23, p < 0.001) and BP ratio (GBM r = 0.2, p < 0.001 and NTBP r = 0.18, p < 0.001).

Figure 5.6 shows the relationship between the tumour volume and the LP and BP ratio. The average volume of the lesions was 43.4 ± 32.6 cm^3 (14.9 – 120.6), of which 27.6 ± 19.3 % (0.4 – 52.0) was frankly necrotic. A regression analysis demonstrated no statistically significant relationship between the LP ratio and: the entire lesion volume, the volume of the enhancing tissue, the volume of the necrosis and the percentage of the necrosis and (p = 0.770, p = 0.685, p = 0.503 and p = 0.356 respectively). This finding was corroborated by the Spearman's correlation coefficient analysis that showed no statistically significant correlation between the LP ratio and the tumour volume (p = 0.148 for the entire volume, p = 0.148 for the enhancing tissue, p = 0.819 for the necrosis and p = 0.819 for the percentage of necrosis).

The BP ratio showed a significant relationship with the entire lesion volume (r = 0.78, p = 0.038), the enhancing component (r = 0.84, p = 0.018) and the percentage of necrosis (r = 0.78, p = 0.038); there was no statistically significant relationship with the volume of necrosis (p = 0.138); figure 5.6. The Spearman's correlation coefficient analysis demonstrated a statistically significant correlation between BP ratio and necrosis both as volume (rho = 0.857, p = 0.014) and as a percentage (rho = 0.857, p = 0.014).

5.2.4 Relationship between HP ^{13}C MRI and tissue biomarkers

The concentration of LDH-A, as quantified by Western Blot, exhibited a linear positive relationship with the LP ratio (r = 0.43, p = 0.042; figure 5.7) which was statistically signficant (p = 0.0433; Spearman's correlation coefficient; figure 5.8). There were no statistically significant relationship nor correlation between LDH-A and the other HP ^{13}C MRI biomarkers; figure 5.7 and 5.8. The concentration of c-Myc did not show any statistically significant relationship or correlation with HP ^{13}C MRI biomarkers, figure 5.7 and 5.8. Figure 5.9 and figure 5.10 show the scatter plot, with the corresponding linear regressions, and the correlation matrix between IHC and the HP ^{13}C MRI. The regression analysis demonstrated a weak relationship between the

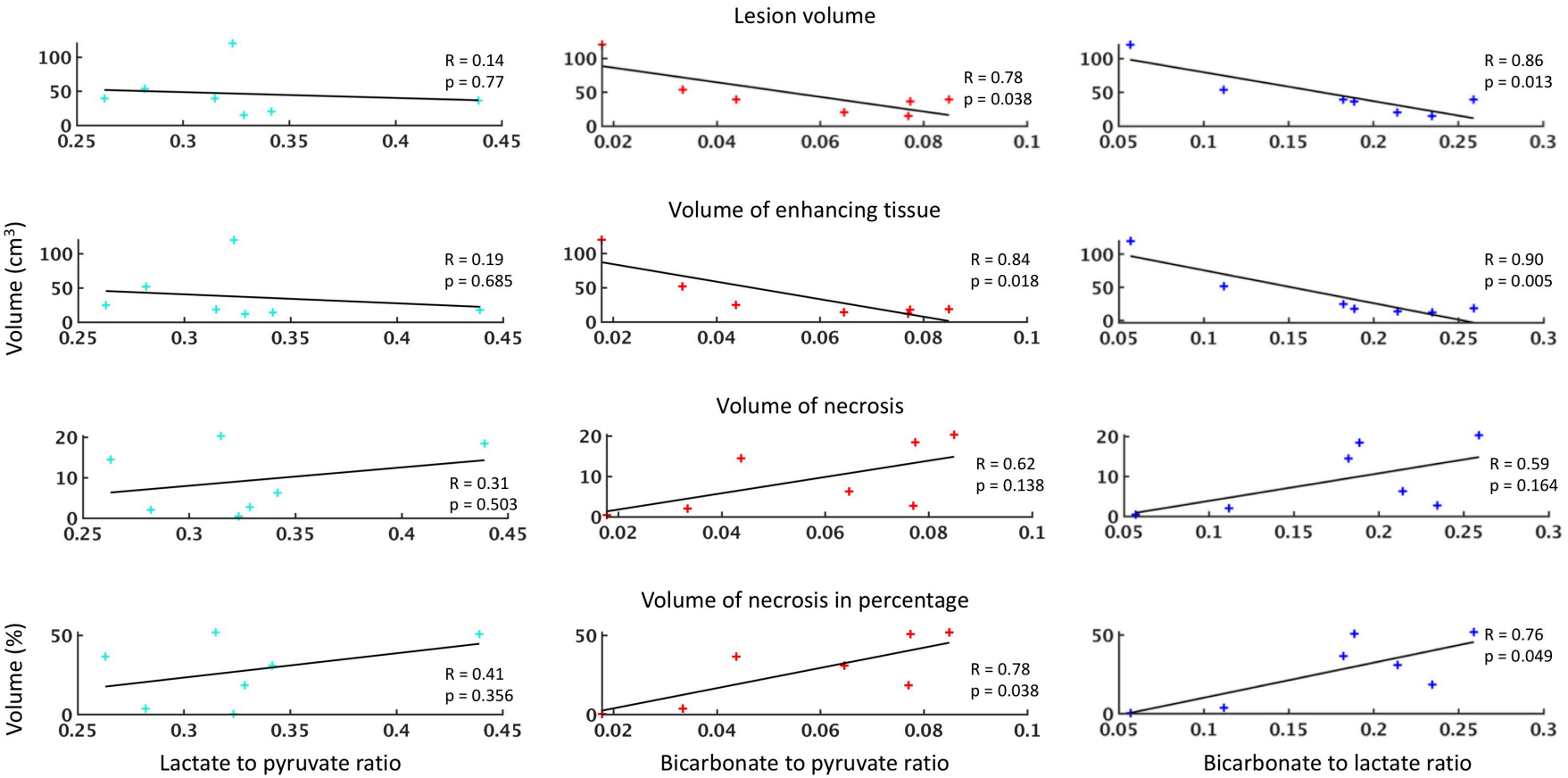

Figure 5.10: Relationship between the volume of the lesion and the hyperpolarized ^{13}C MRI.

The scatterplots show the relationship between the volume of the different components of the lesions and lactate to pyruvate ratio (first column), bicarbonate to pyruvate ratio (second column) and bicarbonate to lactate ratio (third column). Each marker represents a patient. The R and p for each regression are given in the figure. Level of significance was set at 0.05.

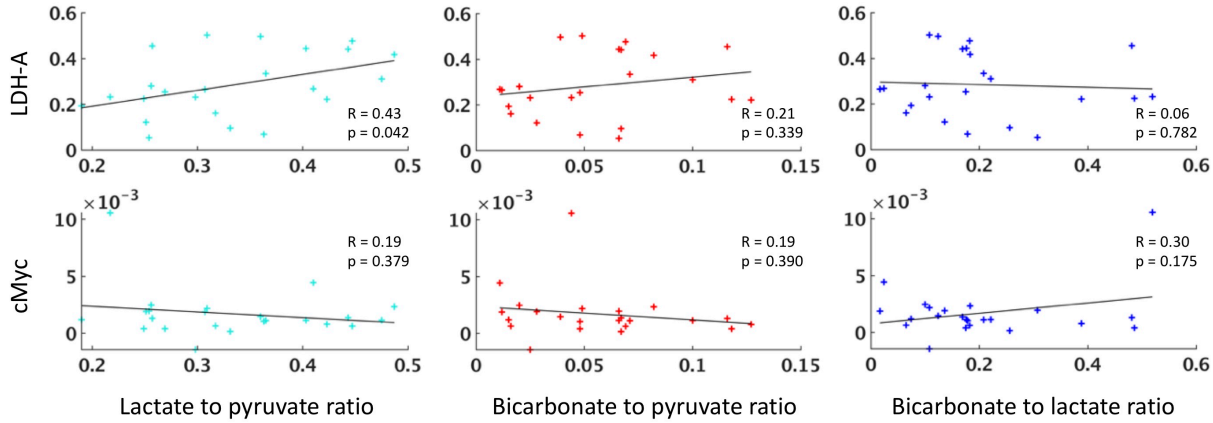

Figure 5.11: Relationship between the results of the western blots and the hyperpolarized ^{13}C MRI. The scatterplots show the relationship between cMyc and LDH-A expression and lactate to pyruvate ratio (first column), bicarbonate to pyruvate ratio (second column) and bicarbonate to lactate ratio (third column). Each marker represents a tissue sample. The R and p for each regression are given in the figure. Level of significance was set at 0.05.

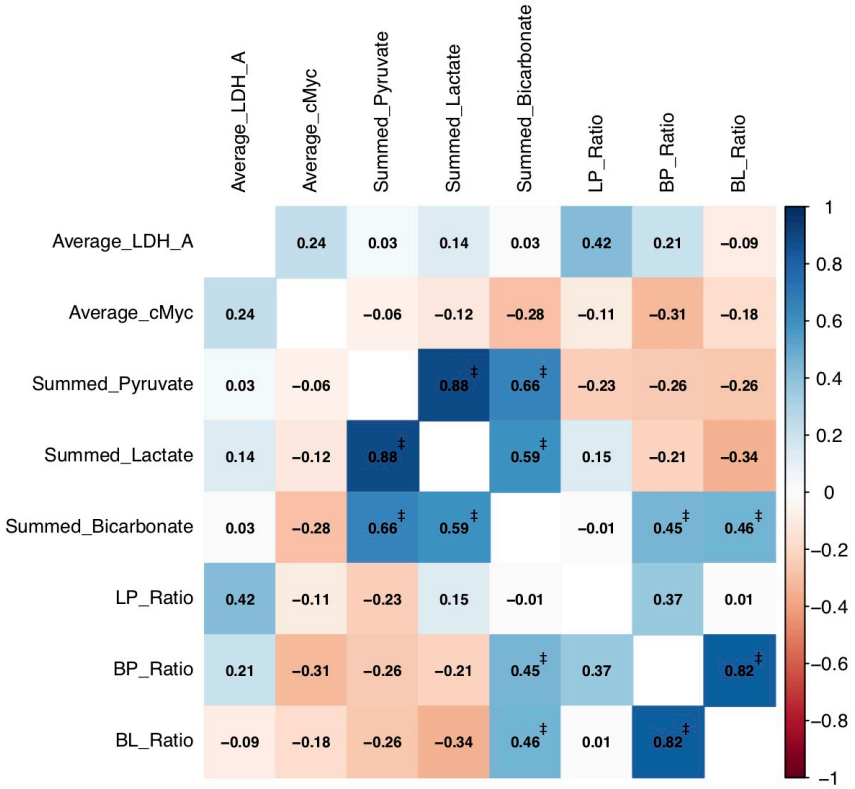

Figure 5.12: Correlation matrix between the results of the western blots and the hyperpolarized ^{13}C MRI. Correlation matrix between LDH-A and cMyc expression and summed pyruvate, summed lactate, summed bicarbonate, lactate to pyruvate ratio (LP_Ratio), bicarbonate to pyruvate ratio (BP_Ratio) and bicarbonate to lactate ratio (BL_Ratio). The numbers shown in each square represent the Spearman's correlation coefficient. Level of significance was set at 0.05 and corrected with the false discovery rate (FDR) method using the Benjamini-Hochberg procedure as described in the text. Significant differences, after correction, are represented with ‡.

immunohistochemical markers and the metabolites derived from the HP ^{13}C MRI. There was a significant linear positive relationship between CA IX and the BP ratio (r = 0.5, p = 0.005) and CD68 and BL ratio (r = 0.38, p = 0.043). The Spearman's correlation coefficient demonstrated several statistically significant correlations after correction with FDR at 10%. CA IX was significantly correlated with summed pyruvate (rho = - 0.59, p = 0.0007), summed lactate (rho = - 0.54, p = 0.003), BP ratio (rho = 0.51, p = 0.005) and BL ratio (rho = 0.48, p = 0.008). CD8 was significantly correlated with summed pyruvate (rho = -0.46, p = 0.011), summed lactate (rho = -0.43, p = 0.020), BP ratio (rho = 0.6, p = 0.0006) and BL ratio (rho = 0.59, p = 0.0007). CD68 was significantly correlated with BP ratio (rho = 0.55, p = 0.002) and BL ratio (rho = 0.53, p = 0.003). Lastly, MIB-1 was significantly correlated with LP ratio (rho = - 0.46, p = 0.013). With the FDR at 5%, CA IX was significantly correlated: with summed pyruvate, summed lactate and BP ratio; CD8 was correlated with BP ratio and BL ratio; and CD68 corelated with BL ratio and BP ratio.

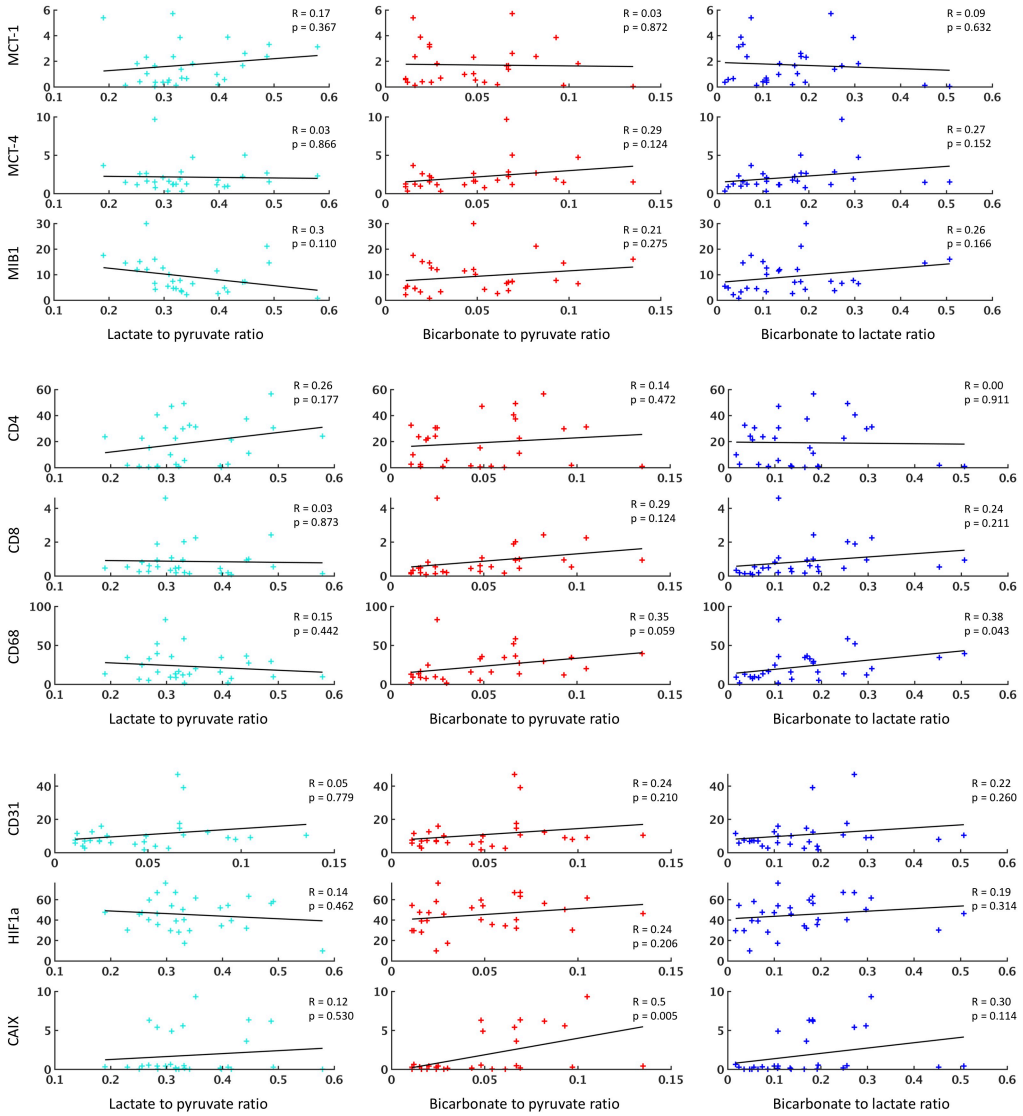

Figure 5.13: Relationship between the the results of the immunohistochemistry staining and the hyperpolarized ^{13}C MRI.

On the y axis: monocarboxylate transporter 1 (MCT1), monocarboxylate transporter 4 (MCT4), index of proliferation (MIB-1), cluster of differentiation 4 (CD4), cluster of differentiation 8 (CD8), cluster of differentiation 68 (CD68), cluster of differentiation 31 (CD31), hypoxia-inducible factor 1-alpha (HIF1-a) and carbonic anhydrase IX (CA IX).

On the x axis: lactate to pyruvate ratio (first column), bicarbonate to pyruvate ratio (second column) and bicarbonate to lactate ratio (third column). Each marker represents a tissue sample. The R and p for each regression are given in the figure. Level of significance was set at 0.05.

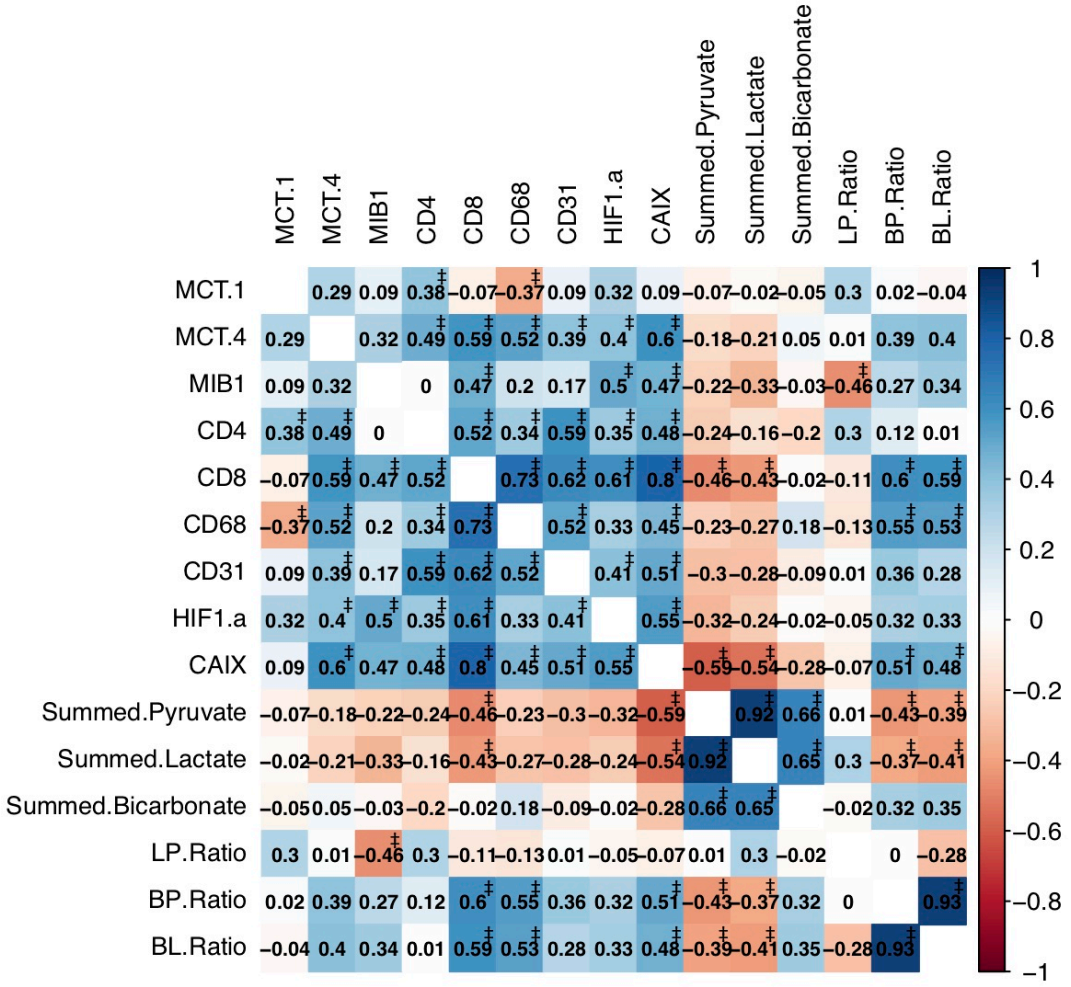

Figure 5.14: Correlation matrix between the results of the immunohistochemistry staining and the hyperpolarized ^{13}C MRI.

Immunohistochemistry staining are: monocarboxylate transporter 1 (MCT1), monocarboxylate transporter 4 (MCT4), cluster of differentiation 4 (CD4), cluster of differentiation 8 (CD8), cluster of differentiation 68 (CD68), cluster of differentiation 31 (CD31), hypoxia-inducible factor 1-alpha (HIF1-a) and carbonic anhydrase IX (CA IX). Hyperepolarised 13C MRI biomarkers are: summed pyruvate, summed lactate, summed bicarbonate, lactate to pyruvate ratio (LP_Ratio), bicarbonate to pyruvate ratio (BP_Ratio) and bicarbonate to lactate ratio (BL_Ratio). The numbers shown in each square represent the Spearman's correlation coefficient. Level of significance was set at 0.05 and corrected with the false discovery rate (FDR) method using the Benjamini-Hochberg procedure as described in the text. Significant differences, after correction, are represented with ‡.

5.3 Discussion

5.3.1 A novel tool for *in vivo* assessment of metabolic activity

This study has demonstrated the feasibility of imaging the conversion of hyperpolarized ^{13}C-labelled pyruvate to both lactate and bicarbonate in the human brain and in glioblastoma. Moreover, this study is the first of its kind correlating tissue biomarkers obtained through immunohistochemistry and western blots to the metabolic biomarkers obtained *in vivo* using HP ^{13}C MRI in patients with GBM.

There are only a small number of papers describing the use of HP ^{13}C MRI in the human brain. The initial reports in patients with brain tumours have focused on demonstrating its feasibility rather than attempting to correlate the signal with other measures of the metabolic activity of brain tumours. A total of five patients with GBM have been reported to date; however, the clinical history and characteristics are too varied to infer any significant conclusions (Miloushev *et al.*, 2018; Park *et al.*, 2018). More recently, Grist *et al.* demonstrated the feasibility of using HP ^{13}C MRI to acquire quantitative non-invasive measurements of pyruvate metabolism in a case series of 4 healthy volunteers applying the possibility of using these methods to study the diseased brain (Grist *et al.*, 2019). In this present study, we have confirmed the feasibility of the technique in the largest cohort of GBM patients to date with patients who are treatment naïve and have the same mutation profile (WHO 2016 GBM IDH-wildtype). The genetic and histological homogeneity of our cohort allows for interlesional comparison that has not been possible previously. Moreover, I assessed the correlation between HP ^{13}C MRI and the underlined biological features of GBMs. Confirming the biological correlates of the detected signal is key to understand how the technique may be used in clinical practice. MRI is already a key technique for the diagnosis, stratification and therapy assessment in GBM: however, the information that conventional imaging provides is insufficiently sensitive and specific and improved imaging techniques are required. Exploiting *in vivo* metabolic pathways with HP ^{13}C MRI may have a significant role in the future management of GBM if it could provide additional

biological and clinical information not accessible by other methods (Kurhanewicz *et al.*, 2019).

Together with Park et al. (Park *et al.*, 2018), this is the largest cohort of brain HP ^{13}C MRI scans reported so far. The technical success in all but one patient demonstrates that this technique is feasible in a clinical research setting. The single unsuccessful case reported here was due to a manual error during the set-up of the acquisition protocol and is accounted for by human error. The polarization levels of pyruvate were acceptable with values close to those reported previously (Grist *et al.*, 2019) and slightly lower when compared to the other reports on brain tumours imaging (Miloushev *et al.*, 2018; Park *et al.*, 2018). It is worthy to mention that the use of a birdcage coil, as opposed to a clamshell or pad coils, allows for a higher homogeneity of the acquired signal and resulting in better imaging.

5.3.2 Intra- and inter- lesional heterogeneity

Tumour heterogeneity, defined as the presence of different cancer cells within the same neoplasm, has been recognised as a distinctive characteristic of cancer (Dexter *et al.*, 1978; Heppner, 1984). The heterogeneity in gliomas was first described in the middle of the past century when Scherer noted different growing behaviours shown by different gliomas although at that time the term “heterogeneity” had not been ascribed to this (Scherer, 1940). Since then, mounting evidence has proved that malignant gliomas show a striking heterogeneity both at the cellular and molecular level, with authors claiming that a patient with glioblastoma may represent several distinct tumour subtypes within the same tumour (Aum *et al.*, 2014; Patel *et al.*, 2014). Indeed, several subclones with different genetic mutations and phenotypic characteristics (including different morphologies, proliferative properties, infiltrative capabilities and sensitivity to therapy) have been demonstrated (Stieber *et al.*, 2014; Soeda *et al.*, 2015). Interestingly, analysis of biopsies obtained from different locations within the same lesions have been classified into different glioblastoma molecular subgroups (Eder and Kalman, 2014). The high degree of intratumoral and intertumoral heterogeneity has been considered one of the key factors in determining a lack of effective therapeutic options for glioblastoma (Sottoriva *et*

al., 2013). This high degree of heterogeneity can jeopardise an accurate profiling of patients and contribute to a biased selection for single target therapies with consequent treatment failure or development of drug resistance. Therefore, a biomarker able to non-invasively characterize the metabolic phenotype of glioblastoma would be a significant contributor in the path to discover novel personalized therapies (Grande *et al.*, 2018).

Conventional imaging technique are limited in visualizing both the intratumoral and intertumoral heterogeneity in GBMs. Imaging the metabolic heterogeneity with HP ^{13}C MRI could represent a turning point for glioma imaging. At a visual inspection of the lactate to pyruvate and bicarbonate-to-pyruvate maps presented in this study (figure 5.2), the intralesional heterogeneity is immediately evident. Comparing those maps with the corresponding post-gadolinium T_1WI (figure 5.2), the capability of HP ^{13}C MRI in assessing the heterogeneity is even more striking. Indeed, whilst the post-gadolinium images show the extravasation of gadolinium in the lesion mostly due to the breakdown of the blood brain barrier, the carbon-13 images show the different metabolic activity in different clusters of the lesion, allegedly composed by different cellular populations. Of interest, the lactate-to-pyruvate and bicarbonate-to-pyruvate maps show a different distribution of clusters producing more lactate and/or more bicarbonate highlighting the capability of this technique to explore intralesional heterogeneity. Comparing the metabolic maps across patients, it is evident that some lesions are more metabolically active whilst other lesions are less metabolically active. This heterogenetiy is particularly significant for the lactate-to-pyruvate ratio.

A more quantitative assessment of the intralesional heterogeneity comes from the quantitative analysis of the metabolism within the lesions. The histogram in figure 5.2 shows both the intralesional and intrapatient heterogeneity. Comparing the distribution of the lactate-to-pyruvate across the patients, the different histogram patterns is notable. In some cases, GBMs exhibit lower LP values than the contralateral non-tumour bearing brain parenchyma; in other cases, the opposite is true. Also, the kurtosis of the histograms and the number of bins (representing how many voxels had the same LP or BP ratio) greatly vary between patients as did the number of voxels clustered in each bin. In contrast to the LP ratio, the bicarbonate-to-pyruvate

ratio showed a constant trend with values in the GBMs significantly lower than in the contralateral non-tumour bearing brain parenchyma, nonetheless, although once again, there was a high degree of heterogeneity within and between the lesions.

The lactate-to-pyruvate ratio and bicarbonate-to-pyruvate ratio maps showed a common pattern with one side of the lesion seemingly more metabolic active than the contralateral side. Although the biological explanation for this is not clear, it might relate to the grow or go theory described above (Giese *et al.*, 2003), I decided to arbitrarily compare the two sides to quantify this unusual intralesional heterogeneity. Interestingly, summed pyruvate, summed lactate, summed bicarbonate and the bicarbonate-to-pyruvate ratio were significantly different when the two sides were compared using evenly spaced and volumetrically identical region-of-interests (table 5.7). This result could be related to different perfusion characteristics of the medial and lateral component of the GBMs, for example a high number of perforating arteries and/or lenticulo-striate arteries adjacent to the lesion can determine a higher blood flow in the medial aspect of the lesion partially determining this behaviour. However, as this study was designed as a first, proof-of-concept study we do not have perfusion data available to disentangle a potential effect of the cerebral blood flow on the delivery of pyruvate and its subsequent metabolism. The information provided by the post-gadolinium T_1W images lack the dynamic component therefore they could not provide any more insights on this issue.

The correlation between LDH-A, c-Myc and the several immunohistochemistry staining we obtained from the tissue analysis unsurprisingly also highlighted the heterogeneity within the lesions. Indeed, both the correlation matrix for the western blots biomarkers and the immunohistochemistry staining included a series of correlations between the HP ^{13}C MRI metabolites. Due to the limited quantity of tissue available for each biopsy, the tissue samples used for the western blots and for the immunohistochemistry were different in almost all the cases.

The capability of HP ^{13}C MRI to detect intertumoral heterogeneity has significant implications for the management of patients with glioblastoma. Indeed, the ability to highlight regions with different metabolic activity and different metabolite concentrations, could be used to generate metabolic

habitats within the same lesion. Those topographic maps could be used in theatre to either guide needle biopsies in the areas with the presumed higher grade or to plan debulking and resection of lesions with a higher degree of confidence that the malignant tissue has been resected. In the context of lesions in close proximity to eloquent areas, the metabolic information could be used to study the potential aggressiveness of the tissue adjacent to the area in question, which could provide invaluable information to the surgeon to either push the boundaries of the resection to the highest possible safest margin or decide for a more conservative approach relying on other therapy approaches. Moreover, in the era of advanced image-guided targeting for radiotherapy treatment, a topographic map displaying the areas of higher metabolic activity could significantly alter the therapeutic plan (Burnet *et al.*, 2014).

5.3.3 The Warburg effect

The quantitative analysis of pyruvate, lactate and bicarbonate concentrations revealed a different behaviour of the GBMs as compared to the NTBP. Pyruvate and lactate were significantly higher in terms of absolute concentration; however, this did not translate into a significant increase in the lactate to pyruvate ratio nor the apparent forward rate constant k_{PL}, a modelled parameter expressing the conversion rate between pyruvate and lactate catalysed by the enzyme lactate dehydrogenase (LDH). The higher concentration of the two metabolites may reflect the known increase of perfusion in malignant gliomas or in the inflammation in the peritumoral brain zone (Lemée *et al.*, 2015a). Pyruvate concentration is influenced by blood perfusion and if more pyruvate is brought to the lesion, a concordant increase of lactate concentration is to be expected. Therefore, the increase in the absolute values of the two metabolites could potentially be partially attributed to the perfusion effect rather than an increase in aerobic glycolysis and GBMs have a high perfusion rate. This hypothesis is supported by the lactate to pyruvate ratio which partially corrects for perfusion effects and showed similar values in the tumour as compared to the contralateral side (0.34 ± 0.06 for the GBM versus 0.36 ± 0.10 for the contralateral side). The data here suggests that the aerobic glycolysis in GBMs is similar if not lower than in the non-tumour bearing brain

parenchyma. However, this agrees with the few clinical cases published to date: Park *et al.* showed lower aerobic glycolysis in patients with GBMs, whilst Miloushev *et al.* observed similar signal compared to the background in the sole GBM enrolled in their study (Miloushev *et al.*, 2018; Park *et al.*, 2018). These human results are somewhat surprising given the pre-clinical data in this area obtained from rats with orthotopic human glioblastoma xenografts : previous studies have shown an increased conversion of pyruvate in lactate in tumours as opposed to a lack of lactate production in normal brain parenchyma (Park *et al.*, 2010, 2013a, 2014). However, other pre-clinical reports have demonstrated a significant lactate production in the normal brain; these differences may represent interspecies variation or effects of anaesthesia on blood-brain barrier transport (Butt *et al.*, 2012; Park *et al.*, 2013b, 2016).

Our study confirmed, as previously shown by Grist *et al.*, that non-tumour bearing brain parenchyma has a significant conversion of pyruvate to lactate (Grist *et al.*, 2019). In the early nineties Magistretti *et al.* proposed the production of lactate in the normal brain as a key part in neurotransmission, with astrocytes being more glycolytic producing lactate and neurons being predominately oxidative and consuming lactate (Luc *et al.*, 1994; Bittar *et al.*, 1996; Magistretti *et al.*, 1999). Lactate shuttles the energy between astrocytes and neurons so that the latter can benefit from the high production rate of the former. More recently, MCT4 has been demonstrated in astrocytes and tanycytes (Pellerin *et al.*, 2005; Cortés-Campos *et al.*, 2011). Although tanycytes are only present in the fourth ventricle and hypothalamus, astrocytes are ubiquitous in the brain parenchyma, highlighting the importance of pyruvate and lactate metabolism in the normal brain. According to recent literature, MCTs have a key roles in several functions such as control the delivery of astrocyte-produced lactate to neurons, controlling the exchange of lactate and other monocarboxylates between several cells and promote angiogenesis (Pérez-Escuredo *et al.*, 2016). Indeed, alterations of MCT expression have been shown in a variety of diseases involving the central or the peripheral nervous systems such as neurodegenerative diseases or epilepsy (Pérez-Escuredo *et al.*, 2016). A reduction in MCTs expression, with consequent reduction in the lactate used to foster the metabolic activity of oligodendrocytes and neurons in general has been shown in animal models of Alzheimer’s disease, multiple sclerosis and

Parkinson's disease (Puchades *et al.*, 2013; Nijland *et al.*, 2014; Lu *et al.*, 2015).

Despite promising pre-clinical evidence that lactate labelling correlates with expression of LDH-A and c-Myc, in our cohort only the lactate-to-pyruvate ratio correlated with the expression of LDH-A (Mair *et al.*, 2018). The conversion from pyruvate to lactate is catalysed by LDH-A, therefore it was expected that the expression of LDH-A in cancer cells should directly correlate with the lactate-to-pyruvate ratio.

c-Myc is a promising biomarker for prognosis prediction and assessment of the metabolic activity in glioblastoma. In glioma, this proto-oncogene is involved in stem cell transformation and maintenance (Orian *et al.*, 1992; H. ZHENG, H. YING, H. YAN *et al.*, 2008). Moreover, c-Myc is deemed to drive the expression of key enzymes for the glycolytic pathway such as LDH-A. Overexpression of c-Myc has been strongly correlated with glioma grading and survival (Orian *et al.*, 1992; Chattopadhyay *et al.*, 1995; Herms *et al.*, 1999). Interestingly, c-Myc expression is also associated with mutant IDH1 expression known to be the most accurate predictor of survival and therapeutic response (Odia *et al.*, 2013). Besides its role as a potential biomarker, c-Myc is a potential therapeutic target in glioblastoma (Dang *et al.*, 2009). Preliminary data showed that c-Myc inhibition reduces proliferation, increases apoptosis and induces the formation of multinucleated cells that undergoes mitotic catastrophe (Annibali *et al.*, 2014). The increased glycolysis induced by c-Myc can also be a direct target. For instance, inhibition of the rate-limiting enzyme NAD^+ salvage pathway nicotinamide phosphoribosyl-transferase (NAMPT) induce cytotoxicity (Tateishi *et al.*, 2016). Therefore, c-Myc is of particular interest in glioblastoma and a non-invasive correlate of its expression would be desirable. Mair et al. demonstrated a positive correlation between lactate-to-pyruvate ratio and c-Myc (Mair *et al.*, 2018). Two of the patient-derived animal models exhibited a higher concentration of c-Myc and LDH-A, in those tumours the lactate-to-pyruvate ratio was significantly higher compared to the tumours with lower expression of c-Myc and LDH-A. Furthermore, to confirm that c-Myc was the driver of the lactate-to-pyruvate ratio increase, Mair et al. (Mair *et al.*, 2018) knocked down c-Myc expression in one of the models. This led to a reduction in expression of LDHA and subsequent decrease in lactate labelling. However, in our cohort

there was no correlation between c-Myc and any of the HP ^{13}C MRI biomarkers. An explanation for this could be that the pre-clinical studies were performed with either immortalized, commercially available single cell lines or PDX derived from single cell lines resulting in identical phenotypic and genotypic profiles. In our study biopsies were taken from different regions within the same cancer showing different metabolic behaviour. As glioblastomas are known to be extremely heterogenous and our samples have been obtained from different areas with different phenotypic characteristics, the lack of significance may be the result of the higher heterogeneity in our cohort. The locations for the biopsies were chosen according to their different metabolic behaviour with the aim of exploring the expression profile to further characterise those regions. Therefore, we can postulate that the lack of correlation could be ascribed to the heterogeneity of the clinical data or the homogeneity of the animal models. Potential future studies and mitigations strategies will be described in the section “limitations and future work”.

Immunohistochemistry was used to assess the drivers behind the metabolic phenotype in each case. Figure 5.9 shows the scatterplots for the immunohistochemistry biomarkers and the metabolic ratios. Pyruvate and lactate were significantly correlated with CA IX which is upregulated in hypoxia and can explain the increased lactate formation. The relationship between lactate and hypoxia highlights the potential role of HP ^{13}C MRI as a tool to study hypoxia in GBM. Pyruvate and lactate were significantly correlated also and CD8 which may reflect cytotoxic T cell immune infiltration, whilst the lactate-to-pyruvate ratio was significantly correlated with MIB-1. A positive linear relationship was observed between CA IX and the bicarbonate-to-pyruvate ratio and between CD68 on macrophages/microglia the and bicarbonate-to-lactate ratio but this was not present for the lactate to pyruvate ratio.

5.3.4 Reduced bicarbonate in GBM

A very consistent finding from these results is a reduced tumour bicarbonate signal which was unexpected. Bicarbonate has a key role in bioenergetics; it is produced by mitochondrial oxidative metabolism, through a reaction catalysed by PDH, and is a biomarker of inflammation and

mitochondrial dysfunction. Grist *et al.* recently demonstrated the presence of [1-^{13}C]bicarbonate throughout the brain in healthy subjects that underwent HP ^{13}C MRI (Grist *et al.*, 2019).

In this study the concentration of [1-^{13}C]bicarbonate and of the bicarbonate-to-pyruvate ratio were consistently lower in the GBMs when compared to the contralateral non-tumour bearing brain parenchyma. The lack of bicarbonate in the GBMs was also seen by Park *et al.* (Park *et al.*, 2018). A reduction in mitochondrial activity could be secondary to mitochondrial impairment in the cancer cells, an alteration in intracellular signalling pathways, or a consequence of local inflammation in the peritumoral microenvironment (Grist *et al.*, 2019).

The bicarbonate-to-pyruvate ratio is more informative than the absolute concentration of bicarbonate as the latter is affected by confounding factors such as the polarisation of the pyruvate or blood flow. Therefore, I assessed the relationship between bicarbonate-to-pyruvate ratio and other biomarkers to gain more insight on what is driving the downregulation of mitochondrial oxidative metabolism in the GBMs. Interestingly, the bicarbonate-to-pyruvate ratio showed an inverse relationship with the lesion volume and the volume of the enhancing tissue, whilst it showed a positive relationship with the percentage of necrosis. The data seems to suggest that an increase in necrosis is either the driving force of mitochondrial impairment or is secondary to it. CA IX, a known marker of hypoxia, was positively correlated with the BP ratio confirming that there is a relationship between hypoxia (or hypoxia-induced necrosis) and the production of bicarbonate. However, the bicarbonate-to-pyruvate ratio was also correlated with CD8 and CD68; know markers of inflammatory cells (the former is expressed by cytotoxic T cells and the latter by cells in the monocyte lineage and macrophages) The production of bicarbonate by inflammatory cells could explain the lack of bicarbonate observed in the GBMs as typically, the peritumoral region is where the inflammatory cells accumulate as a reaction to the pro-inflammatory status caused by the cancer, whilst there are rew inflammatory cells in the core. Moreover, both normal white and grey matter are producing bicarbonate, therefore the destruction of the normal microstructure in the GBM leads to the lack of neurons and astrocytes that are replaced by cancer cells with the consequent drop in bicarbonate production.

Although the actual reason for the lack of bicarbonate is still undetermined, in this study we demonstrated that bicarbonate production is clearly impaired in GBMs suggesting a reduction in mitochondrial function.

5.3.5 Lesion size and cellularity

We explored potential correlations between lesion size, cellularity and metabolic biomarkers to assess the relationship between tumour size and metabolism. The lactate-to-pyruvate ratio did not show any correlation with any volumetric measurements showing that size alone does not dictate metabolism. The metabolic phenotype in glioblastoma is the result of a highly heterogeneous environment with several habitats expressing different DNA mutations, having different protein expression profiles and therefore exhibiting different metabolic behaviour: therefore, heterogeneity is a greater driver of metabolism rather than the simple size of the lesion. The information provided by studying lactate dynamics are independent from what could be obtained with a conventional morphologic scan.

In this study, we observed a negative linear relationship between the bicarbonate-to-pyruvate ratio, the volume of the entire lesion and the volume of the enhancing component. In contrast, there was a positive linear relationship between bicarbonate-to-pyruvate ratio and necrosis both as volume and percentage, although the former was just a trend. This is in keeping with the assumption that larger lesions are more necrotic, due to the growth outpacing the angiogenesis, and more hypoxic, due to the lack of oxygenation. The correlation between the bicarbonate-to-pyruvate ratio and CA IX seems to support this hypothesis. However, despite an increase in pyruvate concentration and a reduction in bicarbonate production, there was not an increase in lactate-to-pyruvate ratio that remains unexplained.

The presence of diffuse and marked necrosis is one of the defining characteristics of Glioblastomas in the WHO classification of brain tumours. Cellularity is another key characteristic that also informs on prognosis and can be non-invasively explored with DWI. The utility of DWI in grading gliomas or assessing prognosis has been a matter of debate for more than two decades (Kono *et al.*, 2001; Zhang *et al.*, 2017). Here we used the ADC as a measure of

cellularity and compared it with HP ^{13}C MRI biomarkers to explore the presence of a direct relationship between cell density in the GBM and metabolism of pyruvate. There were correlations between ADC values, lactate-to-pyruvate and bicarbonate-to-pyruvate ratios. Of interest, we found a discrepancy between the linear regression and the correlation between lactate-to-pyruvate and bicarbonate-to-pyruvate ratio and ADC which points toward a non-linear relationship between HP ^{13}C MRI biomarkers and cellularity. This may be related to the complex GBM microenvironment which contains a wide variety of cell types. We envisage that the lactate concentration may be driven by cancer cells whilst bicarbonate concentration should be primarily due to inflammatory cells. A quadratic regression model was slightly better in predicting lactate-to-pyruvate and bicarbonate-to-pyruvate ratios given the ADC value of a certain voxel. In our cohort, the R values for the association between lactate-to-pyruvate and bicarbonate-to-pyruvate ratios with ADC were all in the lower spectrum suggesting a weak direct correlation between cellularity and metabolic activity.

In the GBM both the lactate-to-pyruvate and the bicarbonate-to-pyruvate ratios tend to increase as cellularity increases whilst the opposite is true in the non-tumour bearing white matter. The increase in cellularity in the GBM is given by a number of different factors including proliferation of cancer cells but inflammatory cells may also play a role. In particular, inflammation is significant at the boundaries of the lesion where cancer cells are spreading within the fibre bundles and the host is trying to resist to the invasion. In the non-tumour bearing brain parenchyma, lactate is predominantly produced within astrocytes and internalised in neurons for the back conversion to pyruvate. The bicarbonate-to-pyruvate ratio showed a difference when fit with a linear or quadratic model. With the quadratic model, the ratio decreases with increasing ADC values up to around 1000 x 10^{-6} mm^2/s, thereafter, it starts to steadily increase with cellularity.

5.3.6 Limitations and future work

This study has several limitations, mostly due to the preliminary exploratory nature of the study. First of all, only 8 patients were recruited and

only 7 successfully scanned. HP ^{13}C MRI is a very challenging technique and it is still at a very early stage with limited resources and lack of clinical-grade consumables. In particular, the production of the labelled pyruvate has to be undertaken manually by trained personnel in a sterile environment and the compound stored in a dedicated fluid path. The latter has been a hindrance to the recruitment because of limited availability, high failure rate and cost. During the course of this research project, more patients would have been eligible and willing to participate; however, the lack of fluid path halted the recruitment. This issue is partially been resolved by the vendor (GE) but the technique is some way from routine use. The availability of reliable fluid paths could significantly boost recruitment; indeed, my experience with recruiting patients with glioma into imaging study clearly demonstrated that the vast majority are willing to participate in research studies. A future study can aim to recruit a substantially higher number of patients to achieve numbers more fit for statistical analysis of results. Moreover, in this study I recruited only WHO 2016 GBM IDH-wildtype. Although this is the most common and most aggressive type of glioma, recruiting other subtypes would foster out understanding of glioma metabolic activity potentially discovering differences between grades not yet demonstrated.

Analysis-wise, the correlation with pathology is one of the strongest features of this study, however, at the same time, it is also a weak point. To explore the diverse aspects of metabolic activity and the tumour microenvironment, we collected data on expression of 1 enzyme, 1 proto-oncogene and stained for 9 protein markers. Despite the high number of biopsies collected from the 7 patients as part of the analysis, testing such a large set of biomarkers required a strict statistical correction of the results that may have led us to reject existing correlations and/or relationships. However, the results of this study may inform future studies to look into specific pathway in a focused fashion reducing the risk of false negative and increasing the power of the statistical analysis. Moreover, during the course of this study, liaising with neurosurgeons, the Department of Pathology, the Brain Tissue Bank and the histopathology core facility, I streamlined a procedure for target identification, tissue collection, storage, processing and analysis that can be the

platform around which build future studies to investigate the relationship between HP ^{13}C MRI and tissue biomarkers.

Variation in pyruvate signal are due to a combination of factors including delivery of pyruvate to the brain which may vary across patients and across brain regions. Perfusion-weighted MRI (PWI), including dynamic susceptibility-weighted contrast-enhanced imaging (DSC), dynamic contrast-enhanced imaging (DCE) and arterial spin labelling (ASL), is an established technique to assess perfusion in the brain. Glioblastomas are known to show an increase in the cerebral blood volume (Salama *et al.*, 2018); therefore, part of the increased pyruvate signal compared to non-tumour bearing brain parenchyma may be due to this increase in perfusion. The lack of a perfusion sequence in the present study is a limitation that could be rectified in future studies. Indeed, the information provided by perfusion maps could aid in disentangling the effect of pyruvate delivery from a true increased metabolic activity in glioblastomas.

Future studies may also explore more metabolites such as the bicarbonate-to-lactate ratio that was only partially explored in the current study. Indeed, the hyperpolarisation and delivery of pyruvate is a strong determinant of the concentration of lactate and bicarbonate. According to the fact that polarization is highly variable, as blood flow and volume are as well, pyruvate, lactate and bicarbonate concertation are unreliable as raw data. However, during the course of the study a reliable and easy pipeline to normalise the values with the contralateral non-tumour bearing brain parenchyma has been developed allowing for comparable data. Moreover, the addition of a perfusion sequence, with or without gadolinium, to the scan protocol would be beneficial in assessing the importance of the perfusion effect and to correct for it.

In summary, despite the limitations of the current study, I firmly believe that this preliminary project set the scene for a more comprehensive work to be carried out elucidating the relationship between HP ^{13}C-MRI, glioma heterogeneity and metabolism.

5.4 Conclusion

This study is the first comprehensive report to assess HP ^{13}C-MRI in glioma correlating imaging biomarkers with pathology to explore metabolic

activity in glioma. The results here presented demonstrate that HP ^{13}C-MRI can probe the metabolic activity of GBM *in vivo* and investigate both intratumoral and intertumoral heterogeneity. These results could deepen our understanding of metabolic reprogramming in GBM and the surrounding brain *in vivo*, which may enable improved stratification, tumour staging, and better monitoring of therapeutic response.

Additional tables

Metabolites and conversion constants	GBMs	Contralateral NTBP (area)	p values
Summed pyruvate	18.58 ± 11.12 (5.53 - 33.96)	13.65 ± 8.58 (4.40 - 27.34)	0.010‡
Summed lactate	6.14 ± 3.55 (1.72 - 10.60)	4.30 ± 2.04 (1.53 - 7.01)	0.036‡
Summed bicarbonate	1.03 ± 0.84 (0.28 - 2.74)	1.44 ± 1.00 (0.53 - 3.51)	0.004‡
Corrected Lactate to Pyruvate ratio	0.34 ± 0.06 (0.24 - 0.46)	0.36 ± 0.10 (0.25 - 0.53)	0.382
Corrected Bicarbonate to Pyruvate ratio	0.06 ± 0.03 (0.02 - 0.08)	0.10 ± 0.04 (0.05 - 0.16)	0.002‡
k_{PL}	0.0161 ± 0.0057 (0.0094 - 0.0277)	0.0165 ± 0.0073 (0.0078 - 0.0317)	0.730
k_{PB}	0.0017 ± 0.0013 (0.0003 - 0.0044)	0.0024 ± 0.0010 (0.0010 - 0.0044)	0.122

Table 5.5: Hyperpolarised ^{13}C MRI metabolites in the glioblastoma and in the contralateral non-tumour bearing parenchyma - Mirrored ROI.

The table shows the hyperpolarised 13C MRI metabolites within the glioblastoma and in a specular region of interest in the contralateral non-tumour bearing *brain parenchyma.*

Normally-distributed continuous values are shown as mean ± standard deviation (minimum - maximum), non-parametric continuous values are shown as median ± median absolute dispersion (minimum - maximum). The level of significance between the glioblastoma and the contralateral non-tumour bearing *parenchyma has been assessed with paired sample t-test (*) for normally distributed data and with the Wilcoxon signed rank test (⋆) for non-normally distributed figures. Level of significance was set at 0.05 and corrected with the false discovery rate (FDR) method using the Benjamini-Hochberg procedure as described in the text. Significant differences, after correction, are represented with ‡.*

Metabolites and conversion constants	**GBMs**	**Contralateral NTBP (ROIs)**	**p values**
Summed pyruvate	18.34 ± 11.42 (3.86 - 33.96)	12.83 ± 7.58 (4.40 - 23.18)	0.017‡
Summed lactate	6.01 ± 3.70 (1.60 - 10.60)	4.11 ± 1.99 (1.44 - 6.72)	0.048‡
Summed bicarbonate	1.00 ± 0.86 (0.28 - 2.74)	1.52 ± 1.10 (0.52 - 3.86)	0.004‡
Corrected Lactate to Pyruvate ratio	0.33 ± 0.05 (0.24 - 0.42)	0.35 ± 0.07 (0.25 - 0.44)	0.449
Corrected Bicarbonate to Pyruvate ratio	0.05 ± 0.02 (0.02 - 0.08)	0.12 ± 0.03 (0.06 - 0.16)	0.0002‡
k_{PL}	0.0152 ± 0.0041 (0.0094 - 0.0213)	0.0156 ± 0.0053 (0.0061 - 0.0226)	0.71
k_{PB}	0.0014 ± 0.0008 (0.0003 - 0.0025)	0.0030 ± 0.0008 (0.0016 - 0.0044)	0.0006‡

Table 5.6: Hyperpolarised ^{13}C MRI metabolites in the glioblastoma and in the contralateral non-tumour bearing parenchyma - Multiple ROIs.

The table shows the hyperpolarised 13C MRI metabolites within the glioblastoma and in a multiple circular region of interests of the same size drawn in the contralateral non-tumour bearing *brain parenchyma.*

Normally-distributed continuous values are shown as mean ± standard deviation (minimum - maximum), non-parametric continuous values are shown as median ± median absolute dispersion (minimum - maximum). The level of significance between the glioblastoma and the contralateral non-tumour bearing *parenchyma has been assessed with paired sample t-test (*) for normally distributed data and with the Wilcoxon signed rank test (⋆) for non-normally distributed figures. Level of significance was set at 0.05 and corrected with the false discovery rate (FDR) method using the Benjamini-Hochberg procedure as described in the text. Significant differences, after correction, are represented with ‡.*

Metabolites and conversion constants	GBMs	Contralateral hemisphere	p values
Summed pyruvate	18.58 ± 11.12 (5.53 - 33.96)	13.64 ± 7.25 (5.16 - 22.96)	0.044‡
Summed lactate	6.14 ± 3.55 (1.72 - 10.60)	4.09 ± 1.84 (1.58 - 6.16)	0.036‡
Summed bicarbonate	1.03 ± 0.84 (0.28 - 2.74)	1.50 ± 1.13 (0.49 - 3.88)	0.013‡
Corrected Lactate to Pyruvate ratio	0.34 ± 0.06 (0.24 - 0.46)	0.33 ± 0.05 (0.27 - 0.42)	0.704
Corrected Bicarbonate to Pyruvate ratio	0.06 ± 0.03 (0.02 - 0.08)	0.08 ± 0.03 (0.06 - 1.04)	0.016★‡
k_{PL}	0.0161 ± 0.0057 (0.0094 - 0.0277)	0.0152 ± 0.0045 (0.0071 - 0.0212)	0.600
k_{PB}	0.0022 ± 0.0009 (0.0003 - 0.0044)	0.0028 ± 0.0013 (0.0014 - 0.2940)	0.031★‡

Table 5.7: Hyperpolarised ^{13}C MRI metabolites in the glioblastoma and in the contralateral non-tumour bearing parenchyma – Hemisphere.

The table shows the hyperpolarised 13C MRI metabolites within the glioblastoma and in the contralateral hemisphere.

Normally-distributed continuous values are shown as mean ± standard deviation (minimum - maximum), non-parametric continuous values are shown as median ± median absolute dispersion (minimum - maximum). The level of significance between the glioblastoma and the contralateral non-tumour bearing *parenchyma has been assessed with paired sample t-test (*) for normally distributed data and with the Wilcoxon signed rank test (★) for non-normally distributed figures. Level of significance was set at 0.05 and corrected with the false discovery rate (FDR) method using the Benjamini-Hochberg procedure as described in the text. Significant differences, after correction, are represented with ‡.*

Metabolites and conversion constants	**Lateral**	**Medial**	**p values**
Summed pyruvate	19.81 ± 12.14 (3.15 - 50.57)	17.27 ± 13.42 (4.17 - 49.01)	0.108‡
Summed lactate	5.77 ± 1.91 (1.44 - 10.64)	3.51 ± 1.87 (1.82 - 18.64)	0.028$^{★‡}$
Summed bicarbonate	0.86 ± 0.78 (0.22 - 1.43)	1.13 ± 1.14 (0.41 - 1.09)	0.034$^{★‡}$
Corrected Lactate to Pyruvate ratio	0.32 ± 0.08 (0.18 - 0.40)	0.31 ± 0.09 (0.35 - 0.47)	0.774
Corrected Bicarbonate to Pyruvate ratio	0.03 ± 0.02 (0.02 - 0.06)	0.06 ± 0.04 (0.01 - 0.09)	0.0007$^{★‡}$
k_{PL}	0.0141 ± 0.0045 (0.0083 - 0.0230)	0.0150 ± 0.0081 (0.0201 - 0.0320)	0.497
k_{PB}	0.0011 ± 0.0006 (0.0002 - 0.0026)	0.0020 ± 0.0015 (0.0001 - 0.0048)	0.055$^{★}$

Table 5.8: Hyperpolarised ^{13}C MRI metabolites in the glioblastoma.

The table shows the hyperpolarised 13C MRI metabolites within the glioblastoma comparing ROIs obtained from the lateral and medial part of the lesion. Normally-distributed continuous values are shown as mean ± standard deviation (minimum - maximum), non-parametric continuous values are shown as median ± median absolute dispersion (minimum - maximum). The level of significance between the glioblastoma and the contralateral non-tumour bearing *parenchyma has been assessed with paired sample t-test (*) for normally distributed data and with the Wilcoxon signed rank test (★) for non-normally distributed figures. Level of significance was set at 0.05 and corrected with the false discovery rate (FDR) method using the Benjamini-Hochberg procedure as described in the text. Significant differences, after correction, are represented with ‡.*

Metabolites and conversion constants	Ipsilateral hemisphere	Contralateral hemisphere	p values
Summed pyruvate	14.84 ± 8.89 (5.15 - 30.81)	12.83 ± 6.63 (5.16 - 22.96)	0.119
Summed lactate	4.76 ± 2.50 (1.57 - 8.39)	4.09 ± 1.83 (1.58 - 6.16)	0.100
Summed bicarbonate	1.09 ± 0.60 (0.43 - 3.40)	1.25 ± 0.53 (0.49 - 3.88)	0.016$^{\star ‡}$
Corrected Lactate to Pyruvate ratio	0.34 ± 0.05 (0.28 - 0.40)	0.34 ± 0.06 (0.27 - 0.42)	0.945
Corrected Bicarbonate to Pyruvate ratio	0.08 ± 0.02 (0.05 - 0.11)	0.10 ± 0.03 (0.06 - 0.16)	0.012‡
k_{PL}	0.0158 ± 0.0045 (0.0076 - 0.0228)	0.0156 ± 0.0046 (0.0071 - 0.0212)	0.772
k_{PB}	0.0022 ± 0.0008 (0.0012 - 0.0038)	0.0027 ± 0.0008 (0.0014 - 0.0042)	0.029‡

Table 5.9: Hyperpolarised ^{13}C MRI metabolites in the non-tumour bearing brain parenchyma - cancer slice.

The table shows the hyperpolarised 13C MRI metabolites in the non-tumour bearing *brain parenchyma assessed in the slice containing the glioblastoma. Normally-distributed continuous values are shown as mean ± standard deviation (minimum - maximum), non-parametric continuous values are shown as median ± median absolute dispersion (minimum - maximum). The level of significance between the glioblastoma and the contralateral* non-tumour bearing *parenchyma has been assessed with paired sample t-test (*) for normally distributed data and with the Wilcoxon signed rank test (⋆) for non-normally distributed figures. Level of significance was set at 0.05 and corrected with the false discovery rate (FDR) method using the Benjamini-Hochberg procedure as described in the text. Significant differences, after correction, are represented with ‡.*

Metabolites and conversion constants	Ipsilateral hemisphere	Contralateral hemisphere	p values
Summed pyruvate	14.50 ± 7.15 (4.12 - 30.81)	13.37 ± 5.70 (3.71 - 22.96)	0.030‡
Summed lactate	4.49 ± 2.14 (1.57 - 8.39)	4.19 ± 1.76 (1.58 - 6.94)	0.040‡
Summed bicarbonate	1.17 ± 0.55 (0.43 - 3.40)	1.25 ± 0.53 (0.46 - 3.88)	0.001★‡
Corrected Lactate to Pyruvate ratio	0.33 ± 0.08 (0.15 - 0.51)	0.34 ± 0.08 (0.18 - 0.52)	0.427
Corrected Bicarbonate to Pyruvate ratio	0.09 ± 0.03 (0.04 - 1.00)	0.10 ± 0.03 (0.05 - 1.04)	0.000002★‡
k_{PL}	0.0153 ± 0.0052 (0.0074 - 0.0305)	0.0154 ± 0.0051 (0.0071 - 0.0305)	0.669
k_{PB}	0.0022 ± 0.0006 (0.0012 - 0.3266)	0.0027 ± 0.0005 (0.0014 - 0.2940)	0.044★‡

Table 5.10: Hyperpolarised ^{13}C MRI metabolites in the ipsilateral and contralateral hemisphere.

The table shows the hyperpolarised 13C MRI metabolites in the non-tumour bearing *brain parenchyma assessed in the slice containing the glioblastoma. Normally-distributed continuous values are shown as mean ± standard deviation (minimum - maximum), non-parametric continuous values are shown as median ± median absolute dispersion (minimum - maximum). The level of significance between the glioblastoma and the contralateral* non-tumour bearing *parenchyma has been assessed with paired sample t-test (*) for normally distributed data and with the Wilcoxon signed rank test (★) for non-normally distributed figures. Level of significance was set at 0.05 and corrected with the false discovery rate (FDR) method using the Benjamini-Hochberg procedure as described in the text. Significant differences, after correction, are represented with ‡.*

References

Annibali D, Whitfield JR, Favuzzi E, Jauset T, Serrano E, Cuartas I, et al. Myc inhibition is effective against glioma and reveals a role for Myc in proficient mitosis. Nat Commun 2014; 5: 1–11.

Ardenkjaer-Larsen JH, Fridlund B, Gram A, Hansson G, Hansson L, Lerche MH, et al. Increase in signal-to-noise ratio of > 10,000 times in liquid-state NMR. Proc Natl Acad Sci U S A 2003; 100: 10158–63.

Ardenkjaer-Larsen JH, Leach AM, Clarke N, Urbahn J, Anderson D, Skloss TW. Dynamic nuclear polarization polarizer for sterile use intent. NMR Biomed 2011; 24: 927–932.

Aum DJ, Kim DH, Beaumont TL, Leuthardt EC, Dunn GP, Kim AH. Molecular and cellular heterogeneity: The hallmark of glioblastoma. Neurosurg Focus 2014; 37: 1–11.

Benjamini Y, Hochberg Y. Controlling the False Discovery Rate : A Practical and Powerful Approach to Multiple Testing. J R Stat Soc 1995; 57: 289–300.

Bittar PG, Charnay Y, Bouras C, Pellerin L, Magistretti PJ. Selective Distribution of Lactate Dehydrogenase Isoenzymes in Neurons and Astrocytes of Human Brain. J Cereb Blood Flow Metab 1996; 16: 1079–1089.

Brindle KM, Bohndiek SE, Gallagher FA, Kettunen MI. Tumor imaging using hyperpolarized ^{13}C magnetic resonance spectroscopy. Magn Reson Med 2011; 66: 505–519.

Burnet NG, Jena R, Burton KE, Tudor GSJ, Scaife JE, Harris F, et al. Clinical and practical considerations for the use of intensity-modulated radiotherapy and image guidance in neuro-oncology. Clin Oncol 2014; 26: 395–406.

Butt SA, Søgaard L V., Magnusson PO, Lauritzen MH, Laustsen C, Keson P, et al. Imaging cerebral 2-ketoisocaproate metabolism with hyperpolarized 13 C Magnetic Resonance Spectroscopic Imaging. J Cereb Blood Flow Metab 2012; 32: 1508–1514.

Chattopadhyay P, Banerjee M, Sarkar C, Mathur M, AK, Mohapatra A, Sinha S. Infrequent alteration of the c-myc gene in human glial tumours associated with increased numbers of c-myc positive cells. Oncogene 1995; 11: 2711–4.

Corbin Z, Spielman D, Recht L. A Metabolic Therapy for Malignant Glioma Requires a Clinical Measure. Curr Oncol Rep 2017; 19

Cortés-Campos C, Elizondo R, Llanos P, Uranga RM, Nualart F, Garća MA. MCT expression and lactate influx/efflux in tanycytes involved in glia-neuron metabolic interaction. PLoS One 2011; 6

CRUK. Brain, other CNS and intracranial tumours incidence statistics | Cancer Research UK [Internet]. 2019[cited 2019 Mar 24] Available from: https://www.cancerresearchuk.org/health-professional/cancer-statistics/statistics-by-cancer-type/brain-other-cns-and-intracranial-tumours/incidence#collapseTen

Cunningham CH, Lau JYC, Chen AP, Geraghty BJ, Perks WJ, Roifman I, et al. Hyperpolarized ^{13}C Metabolic MRI of the Human Heart: Initial Experience. Circ Res 2016; 119: 1177–1182.

Dang C V., Le A, Gao P. MYC-induced cancer cell energy metabolism and therapeutic opportunities. Clin Cancer Res 2009; 15: 6479–6483.

Daniels CJ, Mclean MA, Schulte RF, Robb FJ, Gill AB, Mcglashan N, et al. A comparison of quantitative methods for clinical imaging with hyperpolarized ^{13}C-pyruvate. NMR Biomed 2016; 29: 387–399.

Day SE, Kettunen MI, Gallagher FA, Hu D-E, Lerche M, Wolber J, et al. Detecting tumor response to treatment using hyperpolarized ^{13}C magnetic resonance imaging and spectroscopy. Nat Med 2007; 13: 1382–1387.

Dexter DL, Kowalski HM, A. BB, Z. F, Vogel R, Heppner GH. Heterogeneity of tumor cells from a single mouse mammary tumor. Cancer Res 1978; 38: 3174–3181.

Dolecek TA, Propp JM, Stroup NE, Kruchko C. CBTRUS Statistical Report: Primary Brain and Central Nervous System Tumors Diagnosed in the United States in 2005 – 2009. Neuro Oncol 2013; 15: ii1–ii56.

Eder K, Kalman B. Molecular Heterogeneity of Glioblastoma and its Clinical Relevance. Pathol Oncol Res 2014; 20: 777–787.

Giese A, Bjerkvig R, Berens ME, Westphal M. Cost of migration: Invasion of malignant gliomas and implications for treatment. J Clin Oncol 2003; 21: 1624–1636.

Grande S, Palma A, Ricci-Vitiani L, Luciani AM, Buccarelli M, Biffoni M, et al. Metabolic Heterogeneity Evidenced by MRS among Patient-Derived Glioblastoma Multiforme Stem-Like Cells Accounts for Cell Clustering and Different Responses to Drugs. Stem Cells Int 2018; 2018: 1–16.

Grist JT, McLean MA, Riemer F, Schulte RF, Deen SS, Zaccagna F, et al. Quantifying normal human brain metabolism using hyperpolarized [1–^{13}C]pyruvate and magnetic resonance imaging. Neuroimage 2019; 189: 171–179.

H. ZHENG, H. YING, H. YAN ACK, HILLER DJ, A.-J. CHEN SRP, G. TONON GCC, Z. DING, J.M. STOMMEL, K.L. DUNN, R.WIEDEMEYER MJY, C. BRENNAN ΛYAW, et al. Pten and p53 Converge on c-Myc to Control Differentiation , Self-renewal , and Transformation of Normal and Neoplastic Stem Cells in Glioblastoma. Cold Spring Harb Symp Quant Biol 2008; LXXIII: 427–437.

Heppner G. Tumor heterogeneity. Cancer Res 1984; 44: 2259–2265.

Herms JW, Von Loewenich FD, Behnke J, Markakis E, Kretzschmar HA. C-MYC oncogene family expression in glioblastoma and survival. Surg Neurol 1999; 51: 536–542.

Hill DK, Orton MR, Mariotti E, Boult JKR, Panek R, Jafar M, et al. Model Free Approach to Kinetic Analysis of Real-Time Hyperpolarized ^{13}C Magnetic Resonance Spectroscopy Data. PLoS One 2013; 8: 1–9.

Jenkinson M, Bannister P, Brady M, Smith S. Improved optimization for the robust and accurate linear registration and motion correction of brain images. Neuroimage 2002; 17: 825–841.

Jenkinson M, Smith S. A global optimisation method for robust affine registration of brain images. Med Image Anal 2001; 5: 143–156.

Kathagen-Buhmann A, Schulte A, Weller J, Holz M, Herold-Mende C, Glass R, et al. Glycolysis and the pentose phosphate pathway are differentially associated with the dichotomous regulation of glioblastoma cell migration versus proliferation. Neuro Oncol 2016; 18: 1219–1229.

Kathagen A, Schulte A, Balcke G, Phillips HS, Martens T, Matschke J, et al. Hypoxia and oxygenation induce a metabolic switch between pentose phosphate pathway and glycolysis in glioma stem-like cells. Acta Neuropathol 2013; 126: 763–780.

Kaur B, Devi SN, Hunter SB, Cohen C, Hammond EH, Brat DJ, et al. Pseudopalisades in Glioblastoma Are Hypoxic, Express Extracellular Matrix Proteases, and Are Formed by an Actively Migrating Cell Population. Cancer Res 2005; 64: 920–927.

Khegai O, Schulte RF, Janich MA, Menzel MI, Farrell E, Otto AM, et al. Apparent rate constant mapping using hyperpolarized [1-^{13}C]pyruvate. NMR Biomed 2014; 27: 1256–1265.

Kono K, Inoue Y, Nakayama K, Shakudo M, Morino M, Ohata K, et al. The role of diffusion-weighted imaging in patients with brain tumors. AJNR Am J Neuroradiol 2001; 22: 1081–8.

Kurhanewicz J, Vigneron DB, Ardenkjaer-Larsen JH, Bankson JA, Brindle K, Cunningham CH, et al. Hyperpolarized ^{13}C MRI: Path to Clinical Translation in Oncology. Neoplasia (United States) 2019; 21: 1–16.

Kurhanewicz J, Vigneron DB, Brindle K, Chekmenev EY, Comment A, Cunningham CH, et al. Analysis of cancer metabolism by imaging hyperpolarized nuclei: prospects for translation to clinical research. Neoplasia 2011; 13: 81–97.

Lemée J-M, Clavreul A, Menei P. Intratumoral heterogeneity in glioblastoma: don't forget the peritumoral brain zone. Neuro Oncol 2015; 17: 1322–1332.

Lemée JM, Clavreul A, Aubry M, Com E, de Tayrac M, Eliat PA, et al. Characterizing the peritumoral brain zone in glioblastoma: a multidisciplinary analysis. J Neurooncol 2015; 122: 53–61.

Louis DN, Perry A, Reifenberger G, von Deimling A, Figarella-Branger D, Cavenee WK, et al. The 2016 World Health Organization Classification of Tumors of the Central Nervous System: a summary. Acta Neuropathol 2016; 131: 1–18.

Lu W, Huang J, Sun S, Huang S, Gan S, Xu J, et al. Changes in lactate content and monocarboxylate transporter 2 expression in Aβ<inf>25-35</inf>-treated rat model of Alzheimer's disease. Neurol Sci 2015; 36: 871–876.

Luc, Pellerin, Magistretti PJ. Glutamate uptake into astrocytes stimulates aerobic glycolysis: a mechanism coupling neuronal activity to glucose utilization. Proc Natl Acad Sci U S A 1994; 91: 10625–10629.

Lumata L, Yang C, Ragavan M, Carpenter N, DeBerardinis RJ, Merritt ME. Hyperpolarized ^{13}C Magnetic Resonance and its use in metabolic assessment of cultured cells and perfused organs [Internet]. 1st ed. Elsevier Inc.; 2015Available from: http://dx.doi.org/10.1016/bs.mie.2015.04.006

Magistretti PJ, Pellerin L, Rothman DL, Shulman RG. Energy on Demand. Science (80-) 1999; 283: 496 LP – 497.

Mair R, Wright AJ, Ros S, Hu D en, Booth T, Kreis F, et al. Metabolic imaging detects low levels of glycolytic activity that vary with levels of C-MyC expression in patient-derived xenograft models of glioblastoma. Cancer Res 2018; 78: 5408–5418.

Marin-Valencia I, Yang C, Mashimo T, Cho S, Baek H, Yang XL, et al. Analysis of tumor metabolism reveals mitochondrial glucose oxidation in genetically diverse human glioblastomas in the mouse brain in vivo - Supplementar material. Cell Metab 2012; 15: 827–837.

McDonald JH. Handbook of Biological Statistics. 3rd ed. Baltimore, Maryland: Sparky House Publishing; 2014

Michelakis ED, Sutendra G, Dromparis P, Webster L, Haromy A, Niven E, et al. Metabolic modulation of glioblastoma with dichloroacetate. Sci Transl Med 2010; 2: 1–9.

Miloushev VZ, Granlund KL, Boltyanskiy R, Lyashchenko SK, DeAngelis LM, Mellinghoff IK, et al. Metabolic imaging of the human brain with hyperpolarized^{13}C Pyruvate demonstrates ^{13}C lactate production in brain tumor patients. Cancer Res 2018; 78: 3755–3760.

Nelson SJ, Kurhanewicz J, Vigneron DB, Larson PEZ, Harzstark AL, Ferrone M, et al. Metabolic imaging of patients with prostate cancer using hyperpolarized [1-^{13}C]pyruvate. Sci Transl Med 2013; 5

Nijland PG, Michailidou I, Witte ME, Mizee MR, Van Der Pol SMA, Van Het Hof B, et al. Cellular distribution of glucose and monocarboxylate transporters in human brain white matter and multiple sclerosis lesions. Glia 2014; 62: 1125–1141.

Odia Y, Orr BA, Robert Bell W, Eberhart CG, Rodriguez FJ. CMYC expression in infiltrating gliomas: Associations with IDH1 mutations, clinicopathologic features and outcome. J Neurooncol 2013; 115: 249–259.

Orian JM, Vasilopoulos K, Yoshida S, Kaye AH, Chow CW, Gonzales MF. Overexpression of multiple oncogenes related to histological grade of astrocytic glioma. Br J Cancer 1992; 66: 106–112.

Ostrom QT, Gittleman H, Stetson L, Virk SM, Barnholtz-Sloan JS. Epidemiology of Gliomas. Cancer Treat Res 2015; 163: 1–14.

Park I, Hu S, Bok R, Ozawa T, Ito M, Mukherjee J, et al. Evaluation of heterogeneous

metabolic profile in an orthotopic human glioblastoma xenograft model using compressed sensing hyperpolarized 3D ^{13}C magnetic resonance spectroscopic imaging. Magn Reson Med 2013; 70: 33–39.

Park I, Larson PEZ, Gordon JW, Carvajal L, Chen H-Y, Bok R, et al. Development of methods and feasibility of using hyperpolarized carbon-13 imaging data for evaluating brain metabolism in patient studies. Magn Reson Med 2018; 80: 864–873.

Park I, Larson PEZ, Tropp JL, Carvajal L, Reed G, Bok R, et al. Dynamic hyperpolarized carbon-13 MR metabolic imaging of nonhuman primate brain. Magn Reson Med 2014; 71: 19–25.

Park I, Larson PEZ, Zierhut ML, Hu S, Bok R, Ozawa T, et al. Hyperpolarized ^{13}C magnetic resonance metabolic imaging: Application to brain tumors. Neuro Oncol 2010; 12: 133–144.

Park JM, Recht LD, Josan S, Merchant M, Jang T, Yen Y-F, et al. Metabolic response of glioma to dichloroacetate measured in vivo by hyperpolarized ^{13}C magnetic resonance spectroscopic imaging. Neuro Oncol 2013; 15: 433–441.

Park JM, Spielman DM, Josan S, Jang T, Merchant M, Hurd RE, et al. Hyperpolarized ^{13}C-lactate to ^{13}C-bicarbonate ratio as a biomarker for monitoring the acute response of anti-vascular endothelial growth factor (anti-VEGF) treatment. NMR Biomed 2016; 29: 650–659.

Patel AP, Tirosh I, Trombetta JJ, Shalek AK, Gillespie SM, Wakimoto H, et al. Single-cell RNA-seq highlights intratumoral heterogeneity in primary glioblastoma. Science (80-) 2014; 344: 1396–1402.

Pellerin L, Halestrap AP, Pierre K. Cellular and subcellular distribution of monocarboxylate transporters in cultured brain cells and in the adult brain. J Neurosci Res 2005; 79: 55–64.

Pérez-Escuredo J, Van Hée VF, Sboarina M, Falces J, Payen VL, Pellerin L, et al. Monocarboxylate transporters in the brain and in cancer. Biochim Biophys Acta - Mol Cell Res 2016; 1863: 2481–2497.

Puchades M, Sogn CJ, Maehlen J, Bergersen LH, Gundersen V. Unaltered lactate and glucose transporter levels in the MPTP mouse model of Parkinson's disease. J Parkinsons Dis 2013; 3: 371–385.

Rong Y, Durden DL, Van Meir EG, Brat DJ. 'Pseudopalisading' necrosis in glioblastoma: A familiar morphologic feature that links vascular pathology, hypoxia, and angiogenesis. J Neuropathol Exp Neurol 2006; 65: 529–539.

Salama GR, Heier LA, Patel P, Ramakrishna R, Magge R, Tsiouris AJ. Diffusion weighted/tensor imaging, functional MRI and perfusion weighted imaging in glioblastoma-foundations and future. Front Neurol 2018; 8: 1–11.

Scherer HJ. The forms of growth in gliomas and their practical significance. Brain 1940; 63: 1–35.

Schroeder MA, Cochlin LE, Heather LC, Clarke K, Radda GK, Tyler DJ. In vivo assessment of pyruvate dehydrogenase flux in the heart using hyperpolarized carbon-13 magnetic resonance. Proc Natl Acad Sci U S A 2008; 105: 12051–12056.

Seth P, Grant A, Tang J, Vinogradov E, Wang X, Lenkinski R, et al. On-target inhibition of tumor fermentative glycolysis as visualized by hyperpolarized pyruvate. Neoplasia 2011; 13: 60–71.

Soeda A, Hara A, Kunisada T, Yoshimura SI, Iwama T, Park DM. The evidence of glioblastoma heterogeneity. Sci Rep 2015; 5: 7979.

Sottoriva A, Spiteri I, Piccirillo SGM, Touloumis A, Collins VP, Marioni JC, et al. Intratumor heterogeneity in human glioblastoma reflects cancer evolutionary dynamics. Proc Natl Acad Sci U S A 2013; 110: 4009–14.

Stieber D, Golebiewska A, Evers L, Lenkiewicz E, Brons NHC, Nicot N, et al. Glioblastomas are composed of genetically divergent clones with distinct tumourigenic potential and variable stem cell-associated phenotypes. Acta Neuropathol 2014; 127: 203–219.

Strickland M, Stoll EA. Metabolic Reprogramming in Glioma. Front Cell Dev Biol 2017; 5

Tamimi AF, Juweid M. Epidemiology and Outcome of Glioblastoma. In: Glioblastoma. 2017.

p. 143–153

Tateishi K, Iafrate AJ, Ho Q, Curry WT, Batchelor TT, Flaherty KT, et al. Myc-Driven glycolysis is a therapeutic target in glioblastoma. Clin Cancer Res 2016; 22: 4452–4465.

Tran M, Latifoltojar A, Neves JB, Papoutsaki M-V, Gong F, Comment A, et al. First-in-human in vivo non-invasive assessment of intra- tumoral metabolic heterogeneity in renal cell carcinoma. BJR Case Rep 2019: 1–5.

Vander MG, Cantley LC, Thompson CB, Thompson CB, Heiden MG Vander, Cantley LC. Understanding The Metabolic the Warburg Effect : of Requirements Cell Proliferation. 2015; 324: 1029–1033.

Vartanian A, Singh SK, Agnihotri S, Jalali S, Burrell K, Aldape KD, et al. GBM's multifaceted landscape: Highlighting regional and microenvironmental heterogeneity. Neuro Oncol 2014; 16: 1167–1175.

Vlashi E, Lagadec C, Vergnes L, Matsutani T, Masui K, Poulou M, et al. Metabolic state of glioma stem cells and nontumorigenic cells. Proc Natl Acad Sci 2011; 108: 16062–16067.

Warburg O. The Metabolism of Carcinoma Cells. J Cancer Res 1925; 9: 148–163.

Warburg O. On the Origin of Cancer Cells. Science (80-) 1956; 123: 309–14.

Wiesinger F, Weidl E, Menzel MI, Janich MA, Khegai O, Glaser SJ, et al. IDEAL spiral CSI for dynamic metabolic MR imaging of hyperpolarized [1-^{13}C]pyruvate. Magn Reson Med 2012; 68: 8–16.

Witney TH, Kettunen MI, Brindle KM. Kinetic modeling of hyperpolarized ^{13}C label exchange between pyruvate and lactate in tumor cells. J Biol Chem 2011; 286: 24572–24580.

Yushkevich PA, Piven J, Hazlett HC, Smith RG, Ho S, Gee JC, et al. User-guided 3D active contour segmentation of anatomical structures: Significantly improved efficiency and reliability. Neuroimage 2006; 31: 1116–1128.

Zaccagna F, Grist JT, Deen SS, Woitek R, Lechermann LM, McLean MA, et al. Hyperpolarized carbon-13 magnetic resonance spectroscopic imaging: a clinical tool for studying tumour metabolism. Br J Radiol 2018; 2017: 20170688.

Zhang L, Min Z, Tang M, Chen S, Lei X, Zhang X. The utility of diffusion MRI with quantitative ADC measurements for differentiating high-grade from low-grade cerebral gliomas: Evidence from a meta-analysis. J Neurol Sci 2017; 375: 103–106.

Zierhut ML, Yen YF, Chen AP, Bok R, Albers MJ, Zhang V, et al. Kinetic modeling of hyperpolarized ^{13}C1-pyruvate metabolism in normal rats and TRAMP mice. J Magn Reson 2010; 202: 85–92.

Towards an integrated molecular imaging platform for glioma

UNIVERSITY OF CAMBRIDGE

Chapter 6

Towards an integrated molecular imaging platform for glioma

The work presented in this thesis is a selection of the projects I conducted in Cambridge studying towards my PhD under the phenomenal supervision and tutelage of Dr Ferdia A. Gallagher. Having the chance of working under Dr Gallagher guidance has been instrumental for my development as a researcher in molecular imaging, as a clinician and as a person. I choose to build my academic career in imaging because I strongly believe that novel imaging techniques have an unparalleled potential in neuro-oncology and will significantly shape this field. Currently, conventional proton MRI is a requisite for glioma detection, grading, assessment of tumour extension, monitoring and assessment of response to treatment. Moreover, image guidance is routinely used for biopsy, resection and radiotherapy targeting. However, MRI has significant limitations, for example in assessing response to treatment or monitoring disease progression. Novel techniques have the potential of overcoming such limitations providing functional, metabolic and micro-architectural information that can further exploit the underlying tumour biology. A new generation of superior imaging biomarkers could radically change the management of both lower-grade and high-grade tumours. In these final remarks I will summarise some of the content from the previous chapters to highlight how this thesis could foster a new generation of non-invasive biomarkers.

6.1 Grading, extension and tumour microenvironment

Current grading of glioma is largely based on tissue analysis which is invasive and can delay the diagnosis for several weeks. The time window

between the baseline MRI and subsequent surgery is very variable. Lesions can grow over this period of time, sometimes requiring a complete change in treatment plan; for example, a resection might be transformed following a stereotactic biopsy if the lesion grows to infiltrate eloquent areas. Also, the wait for surgery can be emotionally and psychologically devasting for patients and families. The three techniques presented in this thesis could all play a significant role in non-invasive detection, grading and assessment of infiltration of the surrounding tissue.

VERDICT MRI probes the tumour microstructure in an unprecedented way. The quantification of the intracellular and the combined extracellular/vascular volume is important on both a biological and a clinical level. I have shown that high-grade gliomas exhibit a higher intracellular volume fraction compared to lower-grade glioma and a corresponding smaller extracellular/vascular volume fraction. Also, cancer cells in high-grade glioma are larger than in lower-grade lesions and VERDICT is able to non-invasively assess the average size of cells in a given voxel. Combining this information in the future could be used to determine the area expressing the highest grade within the lesion, to predict the grade and to guide either biopsy and treatment.

I have demonstrated that tissue sodium concentration is increased in both lower-grade glioma and high-grade glioma but the ion is present in different compartments in the two. The development of a sequence to quantify the intracellular sodium concentration has demonstrated that the intracellular sodium concertation is significantly different between different grades, allowing for a quantitative tool to infer grading from imaging. Moreover, sodium MRI can assess the peritumoral zone highlighting foci of altered metabolism beyond the boundaries defined by conventional proton imaging.

Hyperpolarised carbon-13 MRI is the most challenging of the techniques presented in this thesis. Despite the challenges, it has been used to directly assess metabolic activity in cancer cells. In our cohort, the lack of a significant increase of the lactate to pyruvate ratio, the currently most used biomarker, challenged the concept that malignant cells are glycolytic. My data suggested that the aerobic glycolysis in glioblastoma is similar if not lower than in the normal appearing brain parenchyma which is surprising. Similarly,

I demonstrated a lack of bicarbonate production in the lesions. However, there was a high degree of heterogeneity both within and between the tumours: the heterogeneity can reflect different clusters of cells having a different metabolic behaviour, again opening up the possibility of improving the localization of the most malignant focus (or foci) for a more refined image guidance. Similarly to sodium MRI, hyperpolarised carbon-13 MRI provides metabolic information from the peritumoral zone facilitating the localization of cancer cells outside the conventional boundaries. Despite the small number of patients recruited for this study, we were able to demonstrate the presence of cancer cells in an area of normal signal intensity on proton imaging outside the tumour in one patient.

Ideally, a multiparametric MRI combining advanced proton imaging (such as DTI and perfusion imaging) with the above described techniques, could achieve better performance in the diagnosis of gliomas.

6.2 Treatment response and prognostication

The assessment of response to therapy is currently based on the revised RANO criteria using the assessment of post-gadolinium T_1-weighted imaging and T_2-weighted or FLAIR imaging. Relying on two-dimensional measurements in an era where volumetric analysis is increasingly automated seems anachronistic and prone to errors due to inter- and intra-operator variability. Nevertheless, the biggest limit of the RANO criteria is that the definition of true progression requires the follow-up to be undertaken 3 months following completion of chemoradiation unless the progression is outside the field of radiation of there is pathological confirmation. This time window is long considering that the survival for patients with glioblastoma is often below 12 months. Novel biomarkers are required to assess response earlier than this and in more reliable ways, potentially measuring the effects of the treatment directly.

Cytoreductive therapies induce necrosis in the target tissue. Notwithstanding the relative proportion of intracellular and extracellular volume at baseline, an increase in necrosis will lead to a decrease in the former and an increase in the latter. VERDICT MRI can reliable observe this

shift in relative volumes and could be used to detect necrosis as soon as it develops

An increase in necrosis could be easily and quickly detected by an increase in the tissue sodium concentration with a simultaneous decrease of the intracellular sodium concentration. Serial sodium scans can monitor the ion concentration and detect changes as early as a few hours after cells start to die. Moreover, this is a quantitative biomarker and semiautomatic software can be incorporated to obtain a numeric result at the time of the imaging test. In this thesis, sodium MRI has also been tested as a prognostic tool. Several biomarkers have been shown to successfully predict survival at baseline providing a useful information for treatment selection and modulation.

Hyperpolarised carbon-13 MRI may also play a significant role in assessing therapy response. Indeed, preclinical studies showed a decrease of metabolic activity, measured with the lactate to pyruvate ratio, within a few hours after starting treatment. This could be a very early imaging biomarker of response to therapy and could allow for immediate cessation of a non-responsive therapy and a switch to another approach within days rather than months.

6.3 The future of HP ^{13}C MRI

Hyperpolarised carbon-13 MRI has been the major focus of my research over the past 4 years. Many limitations have been overcome during that time, and a vast body of knowledge has been produced by the centres currently spearheading this technique. However, many open issues remain outstanding. I personally gained a fair amount of insight about this fascinating new tool that could potentially revolutionize the way we look at metabolic reprogramming in cancer and beyond. Therefore, a more detailed discussion of the future of the technique is provided below with some reflections made during my PhD.

6.3.1 MRI hardware developments for hyperpolarisation

Despite the large increase in signal-to-noise that is generated by DNP, both the hardware and acquisition sequences required have to be optimised

to avail of this increased signal. Dedicated ^{13}C coils are needed for the technology: current research being undertaken aims to optimize coil design and pulse sequences to maximize the signal acquired. For example, the use of multiple-channel coil arrays can enable parallel imaging techniques to accelerate acquisition while retaining sensitivity (Tropp *et al.*, 2011). Calibrationless methods have been shown to overcome the limitations of the short-lived hyperpolarized species in this context (Feng *et al.*, 2016).

There have been several different imaging schemes proposed for the acquisition of hyperpolarized ^{13}C data (Schmidt *et al.*, 2008; Durst *et al.*, 2015; Gordon *et al.*, 2017). A key component of most sequences is the use of single shot, multiple time point acquisition to acquire dynamic, metabolite-specific data (Gordon *et al.*, 2017). The differences mainly involve encoding efficiency, gradient demand and artefact behaviour: non-Cartesian trajectories are more efficient but are prone to artefacts (Durst *et al.*, 2015). The choice of the optimal sequence depends on the spatial and temporal resolution desired and the number of different chemical species to be resolved. Future developments in this area will involve assessing and improving intersite reproducibility of the data acquisition methods.

6.3.2 Pharmacy requirements and developments in formulation

The current approach for the consumables for the clinical polariser requires a local sterile production facility to fill pharmacy kits which can be costly to establish. A more practical approach may be the development of a large, centralised, filling facility where pharmacy kits could be frozen and transported to other sites. There are a number of country-specific regulatory issues that need to be addressed for the production and transport of these filled pharmacy kits at each site which needs to be considered before developing a programme of research locally.

If hyperpolarized ^{13}C-MRI is to be more widely used, it needs to be accessible for non-specialist centres. To improve availability, there is ongoing research in the area of long-lived polarised states and transport of pre-polarised molecules. Although this area is still in the early stages of

development and some way from clinical translation, it could potentially open up the possibility of hyperpolarizing molecules centrally and transporting them to the imaging site without the need for a local polariser.

6.3.3 New hyperpolarized tracers

Hyperpolarized ^{13}C-labelled tracers offer unique opportunities to probe many metabolic pathways. Although many hyperpolarized tracers have been developed, very few have the necessary biological, chemical and physical properties required for successful translation into human imaging. Table 6.1 summaries some of the tracers which have clinical potential and provide biologically useful information. As discussed above, [1-^{13}C]pyruvate has been used to probe LDH and PDH activity and similarly, [1-^{13}C]lactate can be used to probe LDH; however [1-^{13}C]pyruvate cannot be used to probe the tricarboxylic acid (TCA) cycle as the label is not incorporated into acetyl CoA (Chen *et al.*, 2008): [1-^{13}C]pyruvate oxidation mediated by PDH releases the hyperpolarized ^{13}C as $^{13}CO_2$ and therefore the production of acetyl CoA and incorporation into the Krebs cycle cannot be studied. In contrast, [2-^{13}C]pyruvate allows downstream metabolites such as acetyl carnitine, citrate and glutamate to be detected (Schroeder *et al.*, 2009, 2013) [2-^{13}C]pyruvate can assess metabolism in tissues where PDH activity is high such as the heart, by probing oxidative metabolism through the Krebs cycle rather than anaerobic glycolysis and lactate formation (Schroeder *et al.*, 2009).

^{13}C-Urea has been utilised to probe tissue perfusion but unlike conventional perfusion tracers, is a small endogenous molecule (Svensson, 2003; Svensson *et al.*, 2003). A number of potential issues has been identified with gadolinium-based contrast agents recently such as accumulation in the brain with repeated use (Kanda *et al.*, 2015; McDonald *et al.*, 2015); consequently, hyperpolarized urea may provide an alternative method to image tissue perfusion with a physiologically relevant molecule (Chen *et al.*, 2008). ^{13}C-Urea could also be used to study tissue oxygenation as has been shown in both the healthy and diabetic rat kidney (Reed *et al.*, 2014; Laustsen *et al.*, 2016) .

Tracer Name	Biological Relevance
[1-^{13}C]Pyruvate	LDH and PDH activity
[2-^{13}C]Pyruvate	LDH, PDH, TCA activity
[1-^{13}C]Lactate	LDH activity
[1-^{13}C]Acetate	TCA activity and fatty acid oxidation
[1-^{13}C]Glutamine	Glutaminolysis
[^{13}C]Urea	Tissue perfusion
[1,4-$^{13}C_2$]Fumarate	Cellular necrosis

Table 6.1: Some of the tracers currently being investigated and their biological relevance.

Hyperpolarized [1,4-$^{13}C_2$]fumarate has been proposed as a positive contrast agent for detecting successful treatment response and tissue necrosis. [1,4-$^{13}C_2$]fumarate is exchanged to [1,4-$^{13}C_2$]malate in the presence of the enzyme fumarase. The intracellular enzyme is released into the extracellular space following necrosis allowing enzymatic conversion of fumarate to malate (Gallagher *et al.*, 2009b) This has been demonstrated in tumours and in acute kidney injury (Nielsen *et al.*, 2017).

One important advantage of HP ^{13}C-MRI over PET imaging is that it allows multiple probes to be injected either sequentially or simultaneously so that several metabolic pathways can be studied at a single time point. Although dual PET probe injection has also been undertaken, the modelling required to differentiate these probes is complicated by perfusion, metabolism and excretion and is often impractical; furthermore, conversion into metabolic products cannot be detected (Ho *et al.*, 2007). In comparison, HP ^{13}C-MRI has the advantage of discriminating probes and their metabolites by virtue of differences in chemical shift: therefore, metabolism of molecules injected simultaneously can be directly compared. This has been demonstrated in several pre-clinical models and has the potential to be applied to humans in the future (Witney *et al.*, 2010).

6.3.4 Image analysis and quantification

Robust quantification of HP ^{13}C-MRI will be important for the repeatability and reproducibility of the technique. Given that the technique

probes exchange or flux between two metabolic pools, there are many analogies between the approaches taken for HP ^{13}C-MRI and those used in PET and DCE-MRI. Several methods have been proposed to reliably and reproducibly quantify the pyruvate-lactate exchange reaction: kinetic parameters can be fitted to model-based approaches such as the two-site exchange model which are the most accurate; simpler model-free approaches such as the area under the curve (AUC) of the lactate-to-pyruvate ratio and the lactate time-to-peak may adequately represent the reaction and may be more suitable for widespread clinical use (Day *et al.*, 2007; Daniels *et al.*, 2016; Siddiqui *et al.*, 2016). Further challenges of the technique include the segmentation of tumour from normal tissue which is compounded by the low resolution and SNR of the data. However, by fully utilising the 5-dimensional nature of HP ^{13}C MRI – including spatial, temporal and spectral information – segmenting areas of high metabolic exchange from low exchange can be greatly facilitated and these approaches could be used for automated and reproducible delineation of tumour regions in the future (Gallagher and Daniels, 2017).

6.3.5 Hyperpolarized ^{13}C-MRI with PET/MRI

Since its introduction in clinical practice, PET/CT has found many clinical applications due to the combination of metabolic (PET) and anatomical (CT) information (De Galiza Barbosa *et al.*, 2016). ^{18}F-FDG PET/CT is a powerful tool for staging and treatment response monitoring in a wide range of cancers such as lung cancer and lymphoma (Czernin *et al.*, 2013; Parodi, 2015). The recent creation of hybrid systems combining PET and MRI have capitalized on the inherent advantages of MRI over CT such as the lack of ionizing radiation, functional imaging capabilities, spectroscopy and improved soft-tissue contrast (Sotoudeh *et al.*, 2016; Ehman *et al.*, 2017). Several clinical applications have been proposed for PET/MRI (Nensa *et al.*, 2014; Fraum *et al.*, 2016): in oncology, examples include head and neck cancers, liver tumours and pelvic malignancies which may significantly benefit from the hybrid approach due to improvements in co-registration and reduction in movement artefact (Blechacz *et al.*, 2011; Cheung *et al.*, 2013; Lee *et al.*,

2014; Kang *et al.*, 2016; Schaarschmidt *et al.*, 2016) PET/MRI has also demonstrated potential in organs such as the lung where traditionally MRI has only had a limited role, highlighting the potential of the combination of those two techniques (Schmidt *et al.*, 2013; Fraioli *et al.*, 2014; Schaarschmidt *et al.*, 2017).

PET/MRI could provide a powerful tool for imaging tumour metabolism. While ^{18}F-FDG is a highly sensitive measure of metabolism and has many applications, it simply measures glucose uptake and phosphorylation and therefore provides only an indirect measure of the Warburg effect (Gambhir, 2002; Vaupel and Mayer, 2007; Binderup *et al.*, 2010). In contrast, hyperpolarized ^{13}C-MRSI is capable of monitoring the uptake of ^{13}C-pyruvate and its conversion into ^{13}C-lactate (or ^{13}C-alanine and ^{13}C-bicarbonate) enabling real-time *in vivo* imaging of metabolism and a more direct measure of the Warburg effect (Golman *et al.*, 2006; Kurhanewicz *et al.*, 2008; Gallagher *et al.*, 2009a). Combining PET/MRI with ^{13}C-MRI provides the opportunity to study cancer metabolism in conjunction with other MR measures of tumour structure, function and heterogeneity (Gutte *et al.*, 2015b). A recent study reported the simultaneous acquisition of ^{18}F-FDG PET and ^{13}C-MRI using a PET/MRI system in 10 dogs (Gutte *et al.*, 2015c). This demonstrated that, although there is a strong correlation between uptake of FDG and pyruvate conversion to lactate, there are areas of mismatch between the two techniques confirming the potential added value of combining the two techniques (Gutte *et al.*, 2015c, a). For instance, increased accumulation of ^{18}F-FDG with low lactate production would indicate oxidative metabolism, while increased accumulation of ^{18}F-FDG and high lactate production would indicate aerobic glycolysis secondary to the Warburg effect. Therefore, by combining the data of the two techniques the accuracy in disentangling oxidative inflammatory cell metabolism from reductive metabolism in cancer cells would be improved.

Simultaneous acquisition also provides the possibility of using data from one technique to improve the other. For instance, the use of MRI data has already been proven to enhance the spatial resolution of PET reconstructions (Bailey *et al.*, 2018) and the use of integrated PET/MR system has been proven to achieve better image registration, resulting in more

accurate anatomical localization (Sotoudeh *et al.*, 2016). In the clinical setting, PET is often used as a simple static scan to assess the steady state uptake of a target tissue e.g. by using the maximum standardised uptake value of a lesion. However, dynamic image acquisitions are feasible and provide additional information on the metabolic activity of the target tissue or lesion. Complex kinetic models are frequently used to estimate the wash in, metabolism, and wash out of the tracer, which may require dynamic blood sampling to quantify the concentration of the tracer in the blood; these approaches may cause discomfort and lack of compliance (La Fougère *et al.*, 2011). Perfusion MRI, with or without the intravenous administration of a gadolinium-based contrast agent, is a non-invasive technique to assess the perfusion dynamics of the normal brain and of gliomas. For instance, perfusion MRI can aid in differentiating true progression, pseudoprogression, pseudoresponse and radionecrosis (Suh *et al.*, 2018*a*), with the potential of being used as a decision-making tool in the clinical management of patients with glioblastoma (Suh *et al.*, 2018*b*). Acquiring a perfusion-weighted sequence shortly before the injection of the radiotracer provides valuable information on the blood flow reaching the lesion, the time the flow reaches its peak (time-to-peak) and the amount of blood volume contained within the lesion. This information could be used to model the kinetic of the radiotracer and of the hyperpolarised pyruvate improving the quantitative nature of those techniques and tailoring the models to the specific target tissue. Moreover, the simultaneous acquisition of PET and HP ^{13}C-MRI, and the potential use of a single MR perfusion acquisition to model the delivery of both probes could ensure that the metabolic state is unchanged between the two acquisition ensuring comparability. Glioblastomas for instance grow rapidly and have a high degree of hypoxia that influences the metabolic state and may change day-by-day. A hybrid acquisition ensures that PET and MRI information is obtained simultaneously, and would there is no potential bias due to changing metabolic states of the lesion.

Technically, acquiring HP ^{13}C-MRI simultaneously during the PET acquisition does not have any significant effect on the PET signal. A phantom study demonstrated that using a flip angle of 29º, the error estimation of PET quantitative data is < 2% (Hansen *et al.*, 2016). This flip angle corresponds to

the Ernst angle and was deliberately chosen as far larger than the flip angles actually used in the clinical studies. Our group have used flip angles between 10º and 15º for all the clinical studies and therefore the error is likely to be lower in a real clinical scenario.

Beside ^{18}F-FDG, a wide range of tracers could be used with this combined hyperpolarized ^{13}C-MRI/PET approach such as the amino acid analogues ^{11}C-methyl-L-methionine (MET) and O-(2-[^{18}F]fluoroethyl)-L-tyrosine (FET) in brain tumours for diagnosis and therapy assessment (Galldiks *et al.*, 2017). This combination could be important in the management of some cancers and certain population groups where longitudinal monitoring is required or where dose reduction is important such as children or women of reproductive age (Gutte *et al.*, 2015*c*). Combined hyperpolarized ^{13}C-MRI/PET studies are currently being undertaken at a number of sites.

As HP ^{13}C-MRI is in its infancy and rapidly evolving, the projected long-term costs of the technology are difficult to accurately evaluate. Hardware costs will reduce in time if there is increased demand for hyperpolarisation approaches. The author believes that in the future the costs for undertaking such studies could be similar to those currently for PET imaging. These costs could be defrayed by the clinical benefits and treatment cost savings if the technique is shown to have unique applications, particularly if ineffective but expensive therapies can be discontinued. Given that MRI is more widely available than PET in most hospitals, HP ^{13}C-MRI could become an important additional clinical tool if unique applications are revealed.

6.4 To infinity and beyond

Advances in imaging will pave the way for better outcomes from personalised care and identification of new targets. In particular, sodium MRI and hyperpolarised carbon-13 MRI can exploit the metabolic activity of tumours in ways that were not feasible previously. This can lead to the identification of overexpressed ion channels, that could be selectively target. Understanding *in vivo* tumour biology may become a new role for the imaging

of tomorrow, especially in cancers such as glioblastomas in which animal models are failing to represent the heterogeneity of the in human disease.

6.5 Future work

There is an urgent need for adoption of novel techniques into clinical trial design, to avoid under- or overestimation of response to treatment and to develop new drugs. The novel techniques presented here are exceptionally promising but more data is required for validation before a wider adoption could be promoted. Developing new techniques is technically challenging but I believe that the work conducted over the past 4 years has lead to a point where these techniques can be reliable used in a research setting. The sequences have been developed, tested and perfected over multiple iterations; similarly, the pipeline for post-processing and image analysis have been streamlined and it is now quite robust and reliable. Therefore, the next step must be trial setup with higher recruitment targets, a comprehensive pathological assessment and collection of follow-up data to confirm the preliminary findings of this thesis and validate the techniques.

Moreover, over the course of my PhD I come to realise that many other neurological and neurosurgical conditions would be ideal candidates for one or a combination of these techniques. Now that acquisition, post-processing and image analysis are robust enough, new areas of research should be explored. For instance, over the course of my PhD I assessed both sodium MRI and VERDICT MRI in other primary and secondary brain tumours as a proof of concept or simply because some presumed glioblastomas turned out to be metastases. Therefore, trials assessing brain metastases or other primary tumours of the central nervous system would be easy to implement.

Over the next few years I aim to continue working in molecular imaging both in neuro-oncology than in other neurological application. A pilot project on secondary brain tumours is pending ethics approval in my current institution and, hopefully, will start by the end of the year. Moreover, I hope to continue to oversee with Dr Gallagher the recruitment of high-grade glioma

into the MISSION:GliomaS study that has been developed in the first year of my PhD and allows for multinuclear imaging of patients with gliomas.

6.6 Concluding remarks

My PhD has been a long journey from the writing of the research protocol and submission to the Ethical Review Board to the final draft of this thesis, through development, validation and initial translation of novel MRI techniques for the assessment of patients with gliomas. The data presented in this thesis are a proof of that long journey from the first sodium MRI we undertook in Cambridge in 2015 to the 65th patient recruited in October 2018. I also explored other novel techniques in a very limited number of patients; those data are not featured in this thesis due to the limited nature of these proof of concept studies. Nevertheless, the three main pillar of my work presented in this thesis are the finish line of my PhD but also, and more importantly, the starting point of a new chapter for imaging research in glioma both in my career and, hopefully, in the wider field.

The legacy of this thesis are three promising novel techniques ready to be deployed on selected cohorts in Cambridge and elsewhere, to foster our understanding of gliomas and win the fight against one of the most aggressive cancer mankind can experience.

References

Bailey DL, Pichler BJ, Gückel B, Antoch G, Barthel H, Bhujwalla ZM, et al. Combined PET/MRI: Global Warming—Summary Report of the 6th International Workshop on PET/MRI, March 27–29, 2017, Tübingen, Germany. Mol Imaging Biol 2018; 20: 4–20.

Binderup T, Knigge U, Loft A, Federspiel B, Kjaer A. 18F-fluorodeoxyglucose positron emission tomography predicts survival of patients with neuroendocrine tumors. Clin Cancer Res 2010; 16: 978–985.

Blechacz B, Komuta M, Roskams T, Gores GJ. Clinical diagnosis and staging of cholangiocarcinoma. Nat Rev Gastroenterol Hepatol 2011; 8: 512–522.

Chen AP, Kurhanewicz J, Bok R, Xu D, Joun D, Zhang V, et al. Feasibility of using hyperpolarized [1-^{13}C]lactate as a substrate for in vivo metabolic ^{13}C MRSI studies. Magn Reson Imaging 2008; 26: 721–726.

Cheung TT, Ho CL, Lo CM, Chen S, Chan SC, Chok KSH, et al. 11C-Acetate and 18F-FDG PET/CT for clinical staging and selection of patients with hepatocellular carcinoma for liver transplantation on the basis of Milan criteria: surgeon's perspective. J Nucl Med 2013; 54: 192–200.

Czernin J, Allen-Auerbach M, Nathanson D, Herrmann K. PET/CT in Oncology: Current Status and Perspectives. Curr Radiol Rep 2013; 1: 177–190.

Daniels CJ, Mclean MA, Schulte RF, Robb FJ, Gill AB, Mcglashan N, et al. A comparison of quantitative methods for clinical imaging with hyperpolarized ^{13}C-pyruvate. NMR Biomed 2016; 29: 387–399.

Day SE, Kettunen MI, Gallagher FA, Hu D-E, Lerche M, Wolber J, et al. Detecting tumor response to treatment using hyperpolarized ^{13}C magnetic resonance imaging and spectroscopy. Nat Med 2007; 13: 1382–1387.

Durst M, Koellisch U, Frank A, Rancan G, Gringeri C V., Karas V, et al. Comparison of acquisition schemes for hyperpolarised ^{13}C imaging. NMR Biomed 2015; 28: 715–725.

Ehman EC, Johnson GB, Villanueva-Meyer JE, Cha S, Leynes AP, Larson PEZ, et al. PET/MRI: Where might it replace PET/CT? J Magn Reson Imaging 2017: 1–16.

Feng Y, Gordon JW, Shin PJ, von Morze C, Lustig M, Larson PEZ, et al. Development and testing of hyperpolarized ^{13}C MR calibrationless parallel imaging. J Magn Reson 2016; 262: 1–7.

La Fougère C, Suchorska B, Bartenstein P, Kreth FW, Tonn JC. Molecular imaging of gliomas with PET: Opportunities and limitations. Neuro Oncol 2011; 13: 806–819.

Fraioli F, Screaton NJ, Janes SM, Win T, Menezes L, Kayani I, et al. Non-small-cell lung cancer resectability: diagnostic value of PET/MR. Eur J Nucl Med Mol Imaging 2014; 42: 49–55.

Fraum TJ, Fowler KJ, McConathy J. PET/MRI: emerging clinical applications in oncology. Acad Radiol 2016; 23: 220–236.

De Galiza Barbosa F, Delso G, Ter Voert EEGW, Huellner MW, Herrmann K, Veit-Haibach P. Multi-technique hybrid imaging in PET/CT and PET/MR: What does the future hold? Clin Radiol 2016; 71: 660–672.

Gallagher FA, Daniels CJ. Unsupervised Segmentation of 5D Hyperpolarized Carbon-13 MRI Data Using a Fuzzy Markov Random Field Model. IEEE Trans Med Imaging 2017; 0062: 1–11.

Gallagher FA, Kettunen MI, Brindle KM. Biomedical applications of hyperpolarized ^{13}C magnetic resonance imaging. Prog Nucl Magn Reson Spectrosc 2009; 55: 285–295.

Gallagher FA, Kettunen MI, Hu D-E, Jensen PR, Zandt R In 't, Karlsson M, et al. Production of hyperpolarized [1,4-$^{13}C2$]malate from [1,4-$^{13}C2$]fumarate is a marker of cell necrosis and treatment response in tumors. Proc Natl Acad Sci 2009; 106: 19801–19806.

Galldiks N, Law I, Pope WB, Arbizu J, Langen KJ. The use of amino acid PET and conventional MRI for monitoring of brain tumor therapy. NeuroImage Clin 2017; 13: 386–394.

Gambhir SS. Molecular imaging of cancer with positron emission tomography. Nat Rev Cancer 2002; 2: 683–693.

Golman K, Zandt RI, Lerche M, Pehrson R, Ardenkjaer-Larsen JH. Metabolic imaging by hyperpolarized ^{13}C magnetic resonance imaging for in vivo tumor diagnosis. Cancer Res 2006; 66: 10855–10860.

Gordon JW, Vigneron DB, Larson PEZ. Development of a symmetric echo planar imaging framework for clinical translation of rapid dynamic hyperpolarized ^{13}C imaging. Magn Reson Med 2017; 77: 826–832.

Gutte H, Hansen A, Larsen M, Rahbek S, Johannesen H, Ardenkjaer-Larsen J, et al. In vivo phenotyping of tumor metabolism in a canine cancer patient with simultaneous ^{18}F-FDG-PET and hyperpolarized ^{13}C-pyruvate Magnetic Resonance Spectroscopic Imaging (hyperPET): mismatch demonstrates that FDG may not always reflect the Warburg effect. Diagnostics 2015; 5: 287–289.

Gutte H, Hansen AE, Henriksen ST, Johannesen HH, Ardenkjaer-Larsen J, Vignaud A, et al. Simultaneous hyperpolarized (13)C-pyruvate MRI and (18)F-FDG-PET in cancer (hyperPET): feasibility of a new imaging concept using a clinical PET/MRI scanner. Am J Nucl Med Mol Imaging 2015; 5: 38–45.

Gutte H, Hansen AE, Larsen MME, Rahbek S, Henriksen ST, Johannesen HH, et al. Simultaneous hyperpolarized ^{13}C-pyruvate MRI and 18F-FDG PET (HyperPET) in 10 dogs with cancer. J Nucl Med 2015; 56: 1786–1792.

Hansen AE, Andersen FL, Henriksen ST, Vignaud A, Ardenkjaer-Larsen JH, Højgaard L, et al. Simultaneous PET/MRI with ^{13}C magnetic resonance spectroscopic imaging (hyperPET): phantom-based evaluation of PET quantification. EJNMMI Phys 2016; 3: 7.

Ho C -l., Chen S, Yeung DWC, Cheng TKC. Dual-Tracer PET/CT Imaging in Evaluation of Metastatic Hepatocellular Carcinoma. J Nucl Med 2007; 48: 902–909.

Kanda T, Fukusato T, Matsuda M, Toyoda K, Oba H, Kotoku J, et al. Gadolinium-based contrast agent accumulates in the brain even in subjects without severe renal dysfunction: evaluation of autopsy brain specimens with inductively coupled plasma mass spectroscopy. Radiology 2015; 276: 228–32.

Kang B, Lee JM, Song YS, Woo S, Hur BY, Jeon JH, et al. Added value of integrated whole-body PET/MRI for evaluation of colorectal cancer: Comparison with contrast-enhanced MDCT. Am J Roentgenol 2016; 206: W10–W20.

Kurhanewicz J, Bok R, Nelson SJ, Vigneron DB. Current and Potential Applications of Clinical ^{13}C MR Spectroscopy. J Nucl Med 2008; 49: 341–344.

Laustsen C, Stokholm Nørlinger T, Christoffer Hansen D, Qi H, Mose Nielsen P, Bonde Bertelsen L, et al. Hyperpolarized ^{13}C urea relaxation mechanism reveals renal changes in diabetic nephropathy. Magn Reson Med 2016; 75: 515–518.

Lee SJ, Seo HJ, Cheon GJ, Kim JH, Kim EE, Kang KW, et al. Usefulness of Integrated PET/MRI in Head and Neck Cancer: A Preliminary Study. Nucl Med Mol Imaging (2010) 2014; 48: 98–105.

McDonald RJ, McDonald JS, Kallmes DF, Jentoft ME, Murray DL, Thielen KR, et al. Intracranial gadolinium deposition after contrast-enhanced MR Imaging. Radiology 2015; 275: 772–782.

Nensa F, Beiderwellen K, Heusch P, Wetter A. Clinical applications of PET/MRI: Current status and future perspectives. Diagnostic Interv Radiol 2014; 20: 438–447.

Nielsen PM, Eldirdiri A, Bertelsen LB, Jørgensen HS, Ardenkjaer-Larsen JH, Laustsen C. Fumarase activity: an in vivo and in vitro biomarker for acute kidney injury. Sci Rep 2017; 7: 40812.

Parodi K. Vision 20/20: Positron emission tomography in radiation therapy planning, delivery, and monitoring. Med Phys 2015; 42: 7153–7168.

Reed GD, Von Morze C, Bok R, Koelsch BL, Van Criekinge M, Smith KJ, et al. High resolution ^{13}C MRI with hyperpolarized urea: In vivo T 2 mapping and 15N labeling effects. IEEE Trans Med Imaging 2014; 33: 362–371.

Schaarschmidt BM, Grueneisen J, Metzenmacher M, Gomez B, Gauler T, Roesel C, et al. Thoracic staging with 18F-FDG PET/MR in non-small cell lung cancer - does it change therapeutic decisions in comparison to 18F-FDG PET/CT? Eur Radiol 2017; 27: 681–688.

Schaarschmidt BM, Heusch P, Buchbender C, Ruhlmann M, Bergmann C, Ruhlmann V, et al. Locoregional tumour evaluation of squamous cell carcinoma in the head and neck area: a comparison between MRI, PET/CT and integrated PET/MRI. Eur J Nucl Med Mol Imaging 2016; 43: 92–102.

Schmidt H, Brendle C, Schraml C, Martirosian P, Bezrukov I, Hetzel J, et al. Correlation of Simultaneously Acquired Diffusion-Weighted Imaging and 2-Deoxy-[18F] fluoro-2-D-glucose Positron Emission Tomography of Pulmonary Lesions in a Dedicated Whole-Body Magnetic Resonance/Positron Emission Tomography System. Invest Radiol 2013; 48: 247–255.

Schmidt R, Laustsen C, Jean-Nicolas D, Kettunen MI, Serrao EM, Marco-Rius I, et al. In vivo single-shot 13 C spectroscopic imaging of hyperpolarized metabolites by spatiotemporal encoding. J Magn Reson 2008; 3: 89–96.

Schroeder MA, Atherton HJ, Ball DR, Cole MA, Heather LC, Griffin JL, et al. Real-time assessment of Krebs cycle metabolism using hyperpolarized ^{13}C magnetic resonance spectroscopy. FASEB J 2009; 23: 2529–2538.

Schroeder MA, Lau AZ, Chen AP, Gu Y, Nagendran J, Barry J, et al. Hyperpolarized ^{13}C magnetic resonance reveals early- and late-onset changes to in vivo pyruvate metabolism in the failing heart. Eur J Heart Fail 2013; 15: 130–140.

Siddiqui S, Kadlecek S, Pourfathi M, Xin Y, Mannherz W, Hamedani H, et al. The use of hyperpolarized carbon-13 magnetic resonance for molecular imaging [Internet]. Adv Drug Deliv Rev 2016Available from: http://dx.doi.org/10.1016/j.addr.2016.08.011

Sotoudeh H, Sharma A, Fowler KJ, McConathy J, Dehdashti F. Clinical application of

PET/MRI in oncology. J Magn Reson Imaging 2016; 44: 265–276.

Suh CH, Kim HS, Jung SC, Choi CG, Kim SJ. Perfusion MRI as a diagnostic biomarker for differentiating glioma from brain metastasis: a systematic review and meta-analysis. Eur Radiol 2018; 28: 3819–3831.

Suh CH, Kim HS, Jung SC, Choi CG, Kim SJ. Multiparametric mri as a potential surrogate endpoint for decision-making in early treatment response following concurrent chemoradiotherapy in patients with newly diagnosed glioblastoma: A systematic review and meta-analysis. Eur Radiol 2018; 28: 2628–2638.

Svensson J. Contrast-enhanced magnetic resonance angiography. Development and optimization of techniques for paramagnetic and hyperpolarized contrast media [Internet]. 2003Available from: http://www.blackwell-synergy.com/links/doi/10.1034/j.1600-0455.44.s.429.1.x

Svensson J, Månsson S, Johansson E, Petersson JS, Olsson LE. Hyperpolarized ^{13}C MR angiography using trueFISP. Magn Reson Med 2003; 50: 256–262.

Tropp J, Lupo JM, Chen A, Calderon P, McCune D, Grafendorfer T, et al. Multi-channel metabolic imaging, with SENSE reconstruction, of hyperpolarized [1-^{13}C] pyruvate in a live rat at 3.0tesla on a clinical MR scanner. J Magn Reson 2011; 208: 171–177.

Vaupel P, Mayer A. Hypoxia in cancer: Significance and impact on clinical outcome. Cancer Metastasis Rev 2007; 26: 225–239.

Witney TH, Kettunen MI, Hu D, Gallagher FA, Bohndiek SE, Napolitano R, et al. Detecting treatment response in a model of human breast adenocarcinoma using hyperpolarised [1-^{13}C]pyruvate and [1,4-$^{13}C2$]fumarate. Br J Cancer 2010; 103: 1400–1406.

Zaccagna F, Grist JT, Deen SS, Woitek R, Lechermann LM, McLean MA, et al. Hyperpolarized carbon-13 magnetic resonance spectroscopic imaging: a clinical tool for studying tumour metabolism. Br J Radiol 2018; 2017: 20170688.

Achievements

UNIVERSITY OF CAMBRIDGE

Achievements

This chapter lists the publication and abstracts I have contributed at different level during my PhD.
A list of prizes, awards and grants is also provided.

Papers

1. Optic Chiasm Morphometric Changes in Multiple Sclerosis: Feasibility of a Simplified Brain MRI Measure of White Matter Atrophy. **Zaccagna F**, Matys T, Massoud T. Clinical Anatomy 2019 Aug 5. doi: 10.1002/ca.23446. [Epub ahead of print].
2. Impact of Integrated Whole Body ^{68}Ga PET/MR Imaging in Comparison with ^{68}Ga PET/CT in Lesions Detection and Diagnosis of Suspected Neuroendocrine Tumours. A Alshammari, M Masoomi, R Syed, E Skoura, S Michopoulou, **F Zaccagna**, J Bomanji, F Fraioli. American Journal of Internal Medicine 2019; 7(4): 102-111
3. Sodium homeostasis in the tumour microenvironment. Leslie TK, James AD, **Zaccagna F**, Grist JT, Deen S, Kennerley A, Riemer F, Kaggie JD, Gallagher FA, Gilbert FJ, Brackenbury WJ. Biochim Biophys Acta Rev Cancer. 2019 Jul 23. pii: S0304-419X(19)30062-9. doi: 10.1016/j.bbcan.2019.07.001. [Epub ahead of print]4.
4. Post-mortem computed tomography (PMCT) radiological findings and assessment in advanced decomposed bodies. G Cartocci, A Santurro, M Neri, **F Zaccagna**, C Catalano, R La Russa, E Turillazzi, V Panebianco, P Frati, V Fineschi. La Radiologia Medica 2019 June 18. Doi 10.1007/s11547-019-01052-6 [Epub ahead of print]
5. Non-invasive assessment of glioma microstructure using VERDICT MRI: correlation with histology. **F Zaccagna**, F Riemer, AN Priest, MA McLean, K Allinson, JT Grist, C Dragos, T Matys, JH Gillard, C Watts, SJ Price, MJ Graves,

FA Gallagher. Eur Radiol. 2019 Mar 19. doi: 10.1007/s00330-019-6011-8. [Epub ahead of print]

6. Multi-site repeatability and reproducibility of MR fingerprinting of the healthy brain at 1.5 and 3.0 T. Buonincontri G, Biagi L, Retico A, Cecchi P, Cosottini M, Gallagher FA, Gómez PA, Graves MJ, McLean MA, Riemer F, Schulte RF, Tosetti M, **Zaccagna F**, Kaggie JD. Neuroimage. 2019 Mar 25;195:362-372. doi: 10.1016/j.neuroimage.2019.03.047. [Epub ahead of print]
7. Measuring Tissue Sodium Concentration: Cross-Vendor Repeatability and Reproducibility of 23 Na-MRI Across Two Sites. Riemer F, McHugh D, **Zaccagna F**, Lewis D, McLean MA, Graves MJ, Gilbert FJ, Parker GJM, Gallagher FA. J Magn Reson Imaging. 2019 Mar 12. doi: 10.1002/jmri.26705. [Epub ahead of print]
8. Ossification of the Pterygoalar and Pterygospinous Ligaments: A Computed Tomography Analysis of Infratemporal Fossa Anatomical Variants Relevant to Percutaneous Trigeminal Rhizotomy. T Matys, T. Ali, **F. Zaccagna**, D.G. Barone, R.W. Kirollos, T.F. Massoud. Journal of Neurosurgery 2019 in press.
9. Evaluation of the sensitivity of R1ρ MRI to pH and macromolecular density. Ali SO, Fessas P, Kaggie JD, **Zaccagna F**, Houston G, Reid S, Graves MJ, Gallagher FA. Magn Reson Imaging. 2019 May;58:156-161. doi: 10.1016/j.mri.2019.02.004. [Epub ahead of print] PMID: 30771445
10. Quantifying normal human brain metabolism using hyperpolarized [1-^{13}C]pyruvate and magnetic resonance imaging. Grist JT, McLean MA, Riemer F, Schulte RF, Deen SS, **Zaccagna F**, Woitek R, Daniels CJ, Kaggie JD, Matys T, Patterson I, Slough R, Gill AB, Chhabra A, Eichenberger R, Laurent MC, Comment A, Gillard JH, Coles AJ, Tyler DJ, Wilkinson I, Basu B, Lomas DJ, Graves MJ, Brindle KM, Gallagher FA. Neuroimage. 2019 Apr 1;189:171-179. doi: 10.1016/j.neuroimage.2019.01.027 PMID: 30639333
11. In and around the optic chiasm: a pictorial review of neuroimaging. **F Zaccagna**, V Pizzuti, DG Barone, P Siotto, L Saba, E Raz, T Matys, TF Massoud. Neurographics Volume 9, Number 1, 1 February 2019, pp. 1-17(17)
12. Reorganization of brain networks following carotid endarterectomy: an exploratory study using resting state functional connectivity with a focus on the changes in Default Mode Network connectivity. Porcu M, Craboledda D, Garofalo P, Barberini L, Sanfilippo R, **Zaccagna F**, Wintermark M, Montisci R, Saba L. Eur J Radiol. 2019 Jan; 110:233-241. doi: 10.1016/j.ejrad.2018.12.007. Epub 2018 Dec 6. PMID: 30599866

13. Connectometry evaluation in patients undergoing carotid endarterectomy: an exploratory study. Porcu M, Craboledda D, Garofalo P, Columbano G, Barberini L, Sanfilippo R, **Zaccagna F**, Wintermark M, Montisci R, Saba L. Brain Imaging Behav. 2018 Dec 7. doi: 10.1007/s11682-018-0024-9. [Epub ahead of print] PMID: 30535626
14. Can unenhanced MRI of the breast replace contrast-enhanced MRI in assessing response to neoadjuvant chemotherapy? Cavallo Marincola B, Telesca M, **Zaccagna F**, Riemer F, Anzidei M, Catalano C, Pediconi F. Acta Radiol. 2019 Jan;60(1):35-44. doi: 10.1177/0284185118773512. Epub 2018 May 9. PMID: 29742918
15. Resting-state functional connectivity MRI analysis in Human Immunodeficiency Virus and Hepatitis C Virus co-infected subjects. A pilot study. Corgiolu S, Barberini L, Suri JS, Mandas A, Costaggiu D, Piano P, **Zaccagna F**, Lucatelli P, Balestrieri A, Saba L. Eur J Radiol. 2018 May;102:220-227. doi: 10.1016/j.ejrad.2018.03.022. Epub 2018 Mar 20. PMID: 29685540
16. Hyperpolarized carbon-13 MRI: a clinical tool for studying tumour metabolism. **Fulvio Zaccagna**, James T Grist, Surrin S Deen, Ramona Woitek, Laura M. T. Lechermann, Mary A McLean, Bristi Basu, and Ferdia A. Gallagher. Br J Radiol. 2018 Jan 19:20170688. doi: 10.1259/bjr.20170688. PMID: 29293376
17. Imaging intralesional heterogeneity of sodium concentration in multiple sclerosis: initial evidence from 23Na-MRI. JT Grist, F Riemer, MA McLean, T Matys, **F Zaccagna**, SF Hilborne, JP Mason, I Patterson, R Slough, J Kaggie, SS Deen, MJ Graves, JL Jones, AJ Coles, FA Gallagher. Journal of the Neurological Sciences 2018 2018 Apr 15; 387:111-114. doi: 10.1016/j.jns.2018.01.027. PMID: 29571845
18. Imaging techniques in ALS. **F Zaccagna**, G Lucignani, E Raz, C Colonnese. Arch Ital Biol. 2017 Dec 1;155(4):142-151. doi: 10.12871/00039829201745 PMID: 29405031.
19. Relationship between Carotid Computed Tomography Dual-Energy and Brain Leukoaraiosis. Saba L, Sanfilippo R, Balestrieri A, **Zaccagna F**, Argiolas GM, Suri JS, Montisci R. J Stroke Cerebrovasc Dis. 2017 Aug; 26(8): 1824-1830. doi: 10.1016/j.jstrokecerebrovasdis.2017.04.016.
20. Advanced magnetic resonance imaging in the study of primary intracranial brain tumors in adults: a state of art review. F Lavra, M Scartozzi, **F Zaccagna**, G Cartocci, L Saba. J Xiangya Med 2017; 2:56. doi: 10.21037/jxym.2017.06.01
21. Relationship between white matter hyperintensities volume and the circle of Willis configurations in patients with carotid artery pathology. Saba L, Sanfilippo R,

Porcu M, Lucatelli P, Montisci R, **Zaccagna F**, Suri JS, Anzidei M, Wintermark M. Eur J Radiol. 2017 Apr; 89:111-116. doi: 10.1016/j.ejrad.2017.01.031.

22. Qualitative analysis of small (≤2 cm) regenerative nodules, dysplastic nodules and well-differentiated HCCs with gadoxetic acid MRI. Di Martino M, Anzidei M, **Zaccagna F**, Saba L, Bosco S, Rossi M, Ginanni Corradini S, Catalano C. BMC Med Imaging. 2016 Nov 11;16(1):62.
23. Clinical neuroimaging markers of response to treatment in mood disorders. Porcu M, Balestrieri A, Siotto P, Lucatelli P, Anzidei M, Suri JS, **Zaccagna F**, Argiolas GM, Saba L. Neurosci Lett. 2016 Oct 11. pii: S0304-3940(16)30757-1. doi: 10.1016/j.neulet.2016.10.013. [Epub ahead of print] Review

Book Chapters

Neurological Disorders and Imaging Physics
Volume 1 - Application of multiple sclerosis
Luca Saba and Jasjit S Suri
OP Publishing Ltd, 2019. In press
Chapter 5: High field MR and neurological disorders
James T Grist, Frank Riemer, Tomasz Matys, Rhys Slough and Fulvio Zaccagna

Glioblastoma: State-of-the-Art Clinical Neuroimaging
Michael Iv, Max Wintermark, and Tarik F. Massoud
Nova Science Publishers, 2018. ISBN: 978-1-53614-588-5
Chapter 5: Imaging complications of Glioblastoma treatment
Tomasz Matys and Fulvio Zaccagna

Prizes and awards

- Guarantors of Brain Travel Grant — Apr ‘19
- International Society of Magnetic Resonance in Medicine trainee stipend — Apr ‘19
- Charles Freer award for Neuroradiology – University of Cambridge — Feb ‘19
- The William G. Negendank Third Place Award 2018 — Oct ‘18
- BEST Scholarship - IRCAD, Strasbourg — Jul ‘18
- E.G. Fearnsides Scholarship – University of — Feb ‘18

Cambridge

- Guarantors of Brain Travel Grant — Jan ‘18
- Radiological Society of North America (RSNA) Travel Award — Nov ‘17
- ESCR Young Abstract Presenter Programme (YAPP) — Jul ‘17
- European School of Radiology Asklepios Course Scholarship — May ‘17
- Royal Academy of Engineering Young Researcher — Sep ‘16
- Cambridge Cancer Centre Best poster in Translational Research — Jun ‘16
- International Society of Magnetic Resonance in Medicine trainee stipend — May ‘16
- Global Biotech Revolution Leader of Tomorrow in BioTech — Apr ‘16

Grants

Lundbeck Foundation - LIFE-GlioB — Dec ‘18

Co-Investigator for the University of Cambridge (local PI: Dr Ferdia Gallagher).

Other Centers: Aarhus University, Technical University of Denmark and GE

Total budget: DKK 9,320,400 (roughly USD 1,400,000)

Oral presentations at courses and congresses

EMIM 2019 – 14th European Molecular Imaging Meeting 2019; 19–22 March 2019, Glasgow, UK

1. Magnetic resonance spectroscopic imaging of hyperpolarized [1-^{13}C]pyruvate in glioblastoma: a promising tool for investigating tumor metabolism and heterogeneity. **F. Zaccagna**, J.T. Grist, M.A. McLean, C.J. Daniels, F. Riemer, J. Kaggie, S. Deen, R. Woitek, R. Schulte, K. Allinson, A. Chhabra, M.C. Laurent, A. Frary, T. Matys, I. Patterson, B. Do Carmo, S. Ursprung, I. Wilkinson, B. Basu, C. Watts, S.J. Price, S. Jefferies, J.H. Gillard, M.J. Graves, K.M. Brindle and F.A. Gallagher

XXI Symposium Neuroradiologicum 2018 – The World Congress of Neuroradiology; March 18th – 23rd 2018, Taipei, Taiwan

2. ^{23}Na-MRI demonstrates a sodium gradient within gliomas as a biomarker of tumour heterogeneity. **Zaccagna F**, Riemer F, McLean M, Grist J, Kaggie J, Schulte R, Matys T, Gillard J, Watts C, Price S, Graves M, Gallagher F

ECR 2018 – European Society of Radiology Annual Congress; February 28 - March 4, Vienna, Austria

3. ^{23}Na-MRI demonstrates a sodium gradient within gliomas as a biomarker of tumour heterogeneity. **F. Zaccagna**, F. Riemer, M.A. McLean, J.T. Grist, R. Schulte, C. Watts, S.J. Price, M.J. Graves, F.A. Gallagher

RSNA 2017 – 103rd Scientific Assembly and Annual Meeting of RSNA; Nov 26 – Dec 1 McCormick Place, Chicago, U.S.A.

4. CT Texture of Carotid Arteries identifies Vulnerable Plaque in Stroke and Transient Ischaemic Attack: a preliminary outcome study. **F Zaccagna**, B Ganeshan, M Rengo, M Arca, I Carbone, A Laghi, L Menezes

   Winner of RSNA 2017 Student Travel Award.

   This study was shortlisted for the RSNA Trainee Research Prize and for an individual press release. It was included in the press kit "because we believe your study is still important and newsworthy". The study was featured in the Daily Bulletin.

ESCR 2017 – European Society of Cardiovascular Radiology (ESCR) Annual Scientific Meeting 2017; 12-14 October 2017, Milan, Italy

5. CT Texture of Carotid Arteries identifies Vulnerable Plaque in Stroke and Transient Ischaemic Attack: a preliminary outcome study. **F. Zaccagna**, B. Ganeshan, M. Rengo, M. Arca, I. Carbone, A. Laghi, L. Menezes

CRUK & EPSRC Cancer Imaging Centre Summer School 2017; 5-7 September 2017, Cambridge, UK

6. ^{23}Na-MRI demonstrates a sodium gradient within gliomas as a biomarker of tumour heterogeneity. **F. Zaccagna**, F. Riemer, M.A. McLean, J.T. Grist, J. Kaggie, R. Schulte, T. Matys, J.H. Gillard, C. Watts, S. J. Price, M. J. Graves1, and F. A. Gallagher.

Young researchers' futures meeting; Royal Academy of Engineering – Panel for Biomedical Engineering; 7-9 Sept 2016, London, UK.

7. ^{23}Na-MRI in glioblastoma as a tool of assessing tumour microenvironment and heterogeneity: initial results. **Zaccagna F.**, Riemer F., McLean M., Grist J.T.,

Kaggie J., Schulte R.F., Hilborne S., Matys T., Gillard J.H., Price S.J., Graves M.J., Gallagher F.A.

VII Annual Meeting of ISMRM Italian Chapter - ISMRM; Feb 2016, Bologna, Italy.

8. ^{23}NA-MRI in glioblastoma as a tool of assessing tumour microenvironment and heterogeneity: initial results. **F. Zaccagna**, F. Riemer, M. McLean, J.T. Grist, J. Kaggie, Rolf Schulte, S. Hilborne, T. Matys, J.H. Gillard, S.J. Price, M.J. Graves, and F.A. Gallagher.

Posters presentations at courses and congresses

ISMRM 2019 – ISMRM 27th Annual Meeting & Exhibition, 11-16 May 2019, Montréal, QC.

1. Magnetic resonance spectroscopic imaging of hyperpolarized [1-^{13}C]pyruvate in glioblastoma: a promising tool for investigating tumor metabolism and heterogeneity. **Zaccagna F**, Grist J, McLean M, Daniels C, Riemer F, Kaggi, J, Deen S, Woitek R, Schulte R, Allinson K, Chhabra A, Laurent MC, Frary A, Matys T, Patterson I, Do Carmo B, Urpsrung S, Wilkinson I, Basu B, Watts C, Price S, Jefferies S, Gillard J, Graves M, Brindle K, Gallagher F.

ASNR 2019 - ASNR 57th Annual Meeting & The Foundation of the ASNR Symposium 2019; May 18-23, Boston, U.S.A.

2. Non-invasive assessment of glioma microstructure using VERDICT MRI: correlation with histology. **F. Zaccagna**, F. Riemer, A.N. Priest, M.A. McLean, K. Allinson, J.T. Grist, T. Matys, J H. Gillard, C. Watts, S.J. Price, M.J. Graves, F. A. Gallagher

BSNR 2018 – British Society of Neuroradiology 2018 annual meeting; 12-13 October, Dublin, Ireland

3. Non-invasive assessment of glioma microstructure using VERDICT MRI: correlation with histology. **F. Zaccagna**, F. Riemer, A.N. Priest, M.A. McLean, K. Allinson, J.T. Grist, T. Matys, J H. Gillard, C. Watts, S.J. Price, M.J. Graves, F. A. Gallagher

ISMRM 2018 Workshop on advances in multiscale cancer detection; 7-10 October, Dublin, Ireland

4. Hyperpolarized [1-^{13}C] pyruvate Magnetic Resonance Spectroscopic Imaging (HP ^{13}C MRSI) in glioblastoma: a promising tool to assess tumor metabolism. **F. Zaccagna**, J.T. Grist, M.A. McLean, C.J. Daniels, F. Riemer, J. Kaggie, S. Deen,

R. Woitek, R. Schulte, K. Allinson, A. Chhabra, M.C. Laurent, A. Frary, T. Matys, S. Ursprung, I. Wilkinson, B. Basu, C. Watts, S.J. Price, S. Jefferies, J.H. Gillard, M.J. Graves, K.M. Brindle and F.A. Gallagher

This paper won the The William G. Negendank Third Place Award 2018.

5. Non-invasive assessment of glioma microstructure using VERDICT MRI: correlation with histology. **F. Zaccagna**, F. Riemer, A.N. Priest, M.A. McLean, K. Allinson, J.T. Grist, T. Matys, J H. Gillard, C. Watts, S.J. Price, M.J. Graves, F. A. Gallagher

Joint annual meeting ISMR-ESMRMB 2018; 16-21 June 2018, Paris, France

6. 23Na-MRI demonstrates a sodium gradient within gliomas as a biomarker of tumor heterogeneity. **F Zaccagna**, F Riemer, MA McLean, JT Grist, J Kaggie, R Schulte, S Hilborne, T Matys, JH Gillard, C Watts, SJ Price, MJ Graves, and FA Gallagher.
7. Non-invasive assessment of glioma microstructure using VERDICT MRI with comparison to histopathology. **F Zaccagna**, F Riemer, AN Priest, MA McLean, JT Grist, T Matys, JH Gillard, C Watts, SJ Price, MJ Graves, and FA Gallagher.

ISMRM 2018 Workshop MR Imaging of ^{n}X-Nuclei (^{23}Na & Friends): From Controversies to Potential Clinical Applications; 07-10 April 2018, Dubrovnik, Croatia

8. ^{23}Na-MRI demonstrates a sodium gradient within gliomas as a biomarker of tumour heterogeneity. **F. Zaccagna**, F. Riemer, M.A. McLean, J.T. Grist, J. Kaggie, R. Schulte, T. Matys, J.H. Gillard, C. Watts, S. J. Price, M. J. Graves, and F. A. Gallagher.

XXI Symposium Neuroradiologicum 2018 – The World Congress of Neuroradiology; March 18th – 23rd 2018, Taipei, Taiwan

9. Non-invasive assessment of glioma microstructure using VERDICT MRI with comparison to histopathology. **F Zaccagna**, F Riemer, AN Priest, MA McLean, JT Grist, T Matys, JH Gillard, C Watts, SJ Price, MJ Graves, and FA Gallagher.

CRUK Cambridge Centre Annual Symposium 2017; 12th June 2017, CRUK Cambridge Institute, Cambridge, UK

10. ^{23}Na-MRI demonstrates a sodium gradient within gliomas as a biomarker of tumour heterogeneity. **F. Zaccagna**, F. Riemer, M. McLean, J.T. Grist, J. Kaggie, R. Schulte, S. Hilborne, T. Matys, J.H. Gillard, C. Watts, S.J. Price, M.J. Graves, and F.A. Gallagher.

CRUK Cancer Imaging Centre Annual Imaging Conference; 5th June 2017 London; UK

11. ^{23}Na-MRI demonstrates a sodium gradient within gliomas as a biomarker of tumour heterogeneity. **F. Zaccagna**, F. Riemer, M. McLean, J.T. Grist, J. Kaggie,

R. Schulte, S. Hilborne, T. Matys, J.H. Gillard, C. Watts, S.J. Price, M.J. Graves, and F.A. Gallagher.

ASNR 2017 – 55th Annual Meeting & The Foundation of the American Society of Neuroradiology Symposium; April 22nd – 27th, 2017. Long Beach, California, U.S.A.

12. The Optic Chiasm: A Comprehensive Pictorial and Educational Review of Common and Uncommon Abnormalities on Neuroimaging. **F Zaccagna**, T Matys, T. F. Massoud.

    This review has been invited for publication in Neurographics.

International Society of Magnetic Resonance in Medicine annual meeting 2017; 22nd – 27th April 2017 Honolulu, Hawaii, U.S.A.

13. ^{23}Na-MRI demonstrates a sodium gradient within gliomas as a biomarker of tumor heterogeneity. **F. Zaccagna**, F. Riemer, M.A. McLean, J.T. Grist, J. Kaggie, R. Schulte, S. Hilborne, T. Matys, J.H. Gillard, C. Watts, S.J. Price, M.J. Graves, and F.A. Gallagher.

    This poster has been selected for presentation in the X-Nuclei study group as well.

International Society of Magnetic Resonance in Medicine British Chapter – PostGrad meeting; 24th March 2017; London; UK

14. ^{23}Na-MRI in glioma as a tool of assessing tumour microenvironment and heterogeneity. **F. Zaccagna**, F Riemer, M.A. McLean, J.T. Grist, J. Kaggie, R. Schulte, T. Matys, J.H. Gillard, C. Watts, S. J. Price, M. J. Graves, and F. A. Gallagher.

WBIC 20th anniversary celebration; 24th Oct 2016; Cambridge; UK

15. ^{23}Na-MRI in glioma as a tool of assessing tumour microenvironment and heterogeneity: initial results. **F. Zaccagna**, F. Riemer, M. McLean, J.T. Grist, J. Kaggie, R. Schulte, S. Hilborne, T. Matys, J.H. Gillard, C. Watts, S.J. Price, M.J. Graves, and F.A. Gallagher.

Young Researchers' Futures Meeting 2016; 7th - 9th September, 2016; Imperial College London, London, UK

16. ^{23}Na-MRI in glioblastoma as a tool of assessing tumour microenvironment and heterogeneity: initial results. **F Zaccagna**, F Riemer, M McLean, JT Grist, J Kaggie, RF Schulte, S Hilborne, T Matys, JH Gillard, SJ Price, MJ Graves, and FA Gallagher

CRUK & EPSRC Cancer Imaging Centre in Cambridge and Manchester; From bench to bedside: validating and qualifying imaging biomarkers; 14 June 2016, Cambridge, UK

17. Diffusion kurtosis imaging (DKI) as a tool to probe tissue microstructure in brain. **F Zaccagna**, F Riemer, A Maiter, M McLean, AN Priest, JT Grist, J Kaggie, S Hilborne, T Matys, JH Gillard, C Watts, MJ Graves, SJ Price and FA Gallagher.

Cambridge Cancer Centre Annual Symposium 2016; 6th June 2016, CRUK Cambridge Institute, Cambridge, UK

18. 23NA-MRI in glioblastoma as a tool of assessing tumour microenvironment and heterogeneity: initial results. **F Zaccagna**, F Riemer, M McLean, JT Grist, J Kaggie, R Schulte, S Hilborne, T Matys, JH Gillard, C Watts, SJ Price, MJ Graves, F Gallagher.

    Winner of best poster prize in Translational Research.

International Society of Magnetic Resonance in Medicine annual meeting 2016; 7-13 May 2016 Singapore

19. Non-Gaussian measurements of water diffusion in glioma as a tool for probing tumor heterogeneity and grade. **F Zaccagna**, F Riemer, M McLean, AN Priest, JT Grist, J Kaggie, S Hilborne, T Matys, MJ Graves, JH Gillard, SJ Price and FA Gallagher.

VII Annual Meeting of ISMRM Italian Chapter - ISMRM; Feb 2016, Bologna, Italy

20. Non-gaussian measurements of water diffusion in glioma as a tool for probing tumor heterogeneity and grade. **F Zaccagna**, F Riemer, M McLean, AN Priest, JT Grist, J Kaggie, S Hilborne, T Matys, MJ Graves, JH Gillard, SJ Price and FA Gallagher.

EBI-Sanger-Cambridge PhD Symposium (eSCAMPS); 1st Feb 2016, Cambridge, UK

21. Non-Gaussian measurements of water diffusion in glioma as a tool for probing tumour heterogeneity and grade. **F. Zaccagna**, F. Riemer, M. McLean, A.N. Priest, J.T. Grist, J. Kaggie, S. Hilborne, T. Matys, M.J. Graves, J.H. Gillard, S.J. Price and F.A. Gallagher.

RSNA 2015 – 101st Scientific Assembly and Annual Meeting of RSNA; Nov 29 – Dec 4 McCormick Place, Chicago, U.S.A.

22. Radiation Induced Changes in the Brain and Spine: What the Radiologist Needs to Know. E Raz, L Saba, **F Zaccagna**, Sacconi, G M Fatterpekar.

Acknowledgements

A PhD is a long journey through science and life. After 4 years in Cambridge, I am definitely a different person compared with the young radiologist that matriculated in 2015. Many people joined me along this journey. Some were involved on the scientific side, some on the personal one and few had a profound impact on both. I hope I showed my sincere gratitude, respect and love to all the people I met during this journey; however, I feel that some deserve to be singled out.

Dr Ferdia Gallagher, you deserve my eternal gratitude. Working with you has been incredible. You are a terrific teacher, a bright mind and a special person. I learnt a lot just being at your side. Ferdia, you have also been a caring guide for my personal development, far beyond what was supposed to be your “job” as a tutor. Being part of your team has been more like being part of a family with a caring and loving father than an aseptic research group. You gave me freedom to pursue my ideas, right or wrong, and you have always been there to provide assistance, guidance and brainstorm any crazy idea. Thank you. I hope we will keep working together in the future.

Dr Frank Riemer, having you as daily guide during this journey has been a blessing. Not only for the never-ending teaching sessions and all the help you provided at the most unsocial time of the day and weekends, but also, and arguably more importantly, for having been a friend. I am sure distance will never break us apart Frank.

Prof Jonathan H. Gillard, since our first meeting back in 2012 you have been an invaluable mentor and a role model. You spent uncountable time advising me on how to become a successful academic neuroradiologist and you have

been an asset in shaping my path in Academia. Without your continuous support I would have never secured this PhD and both my personal and academic life would have been extremely different.

The stunning people of the CUH and University Departments of Radiology, Candice Anderson, Ralph Ball, Dr Tristan Barrett, Dr Charlie Daniels, Dr Surrin Deen, Rose Eichenberger, Sarah Hilborne, Amy Frary, Prof Fiona Gilbert, Dr Andrew Gill, Dr Martin Graves, Mr Ashley Grimmer, Dr James Grist, Dr Yuan Huang, Dr Josh Kaggie, Marie-Christine Laurent, Matthew Locke, Dr Roie Manavaki, Dr Tomasz Matys, Ilse Patterson, Wendy Philips, Dr Andrew Priest, Prof Evis Sala, Rhys Slough, Dr Leonardo Rundo, Mr Brian White, Dr Ramona Woitek and Dr Stephan Ursprung. You all have had a role in my PhD journey, and I will always keep all our shared moments in my memories. Thank you for having been so welcoming and supportive beyond belief.

Research is a multidisciplinary effort, and my PhD required the involvement of many brilliant minds from several departments who I deeply thank for all their help and support. Thanking all of them would be impossible in those few pages, however, some of them deserve special mention. First and foremost, the neuro-oncology team, Gemma Bullen, Mr Robert Morris, Ingela Oberg, Mr Richard Mair, Mr Stephen Price, Mr Tomas Santarius and Mr Colin Watts, for welcoming in their service as a member of their group and for their help with the recruitment. Dr Kieren Allinson for all the hours I spent in his office discussing pathology or looking at slides with him. Mrs Cara Brodie and the immunohistochemistry lab at the Cancer Research UK (CRUK) Cambridge Institute for keeping up with my emails and visits to the CI at the craziest times.

My friends, both in UK and in Italy. No man is an island and without such a net of loving people I would have never survived the PhD. Leaving all my loved one behind was difficult both for me and for them, but my extended Italian family and my team of like-minded crazy individual has been a constant throughout my life despite the miles between us. Thank you Stefano,

Damiano, Antonello, Valerio, Gianfranco, Pierluigi, Daniele, Martina, Elisa, Lara, Jacopo, Davide, Federica, Gaia, Chiara, Giulia, Pier Luigi, Federica, Luca, Diego, Damiano, Nikita, Claudio, Ferruccio, Edoardo, Francesca, Alessandro, Ismael, Danilo, Carmen, Concetta, Christian and all the others that I am lucky to share my life with.

Masha, you have been an incredible surprise. I will always remember the first day we met and how our lives became entangled. Thank you for being by my side and for your endless support.

My deepest gratitude to my mother, because seeing me leaving has been one of the worst days of her life, but she kept supporting me every single day since then and I know that she will always do. Thank you for your strength and for your love.

The patients who accepted to enrol in the studies part of this thesis notwithstanding the impact of the diagnosis on their life. Your contribution has been key to the success of these projects.

Lastly, I would like to thank the CRUK & EPSRC Cancer Imaging Centre in Cambridge and Manchester for my scholarship and for supporting my research.